Elucidating the Interfacial Molecular Interaction Mechanisms of Silicone Adhesive, Polymer Degradation and Polymer Bio-applications Using Advanced Spectroscopy

by

Ting Lin

A dissertation submitted in partial fulfillment
of the requirements for the degree of
Doctor of Philosophy
(Macromolecular Science and Engineering)
in the University of Michigan
2024

Doctoral Committee:

Professor Zhan Chen, Chair
Professor Joerg Lahann
Assistant Professor Abdon Pena-Francesch
Professor Anish Tuteja

Ting Lin

linting@umich.edu
ORCID iD: 0000-0002-3016-1492

© Ting Lin 2024

Dedication

This work is sincerely dedicated to my beloved family as well as those who love and support me along this journey.

Acknowledgements

As I near the completion of 23 years of education, I wish to seize this moment to extend my deepest appreciation to my mentors, colleagues, family, and friends.

First and foremost, I would like to express my sincere gratitude to my Ph.D. advisor Prof. Zhan Chen for his continuous support and instructive advice during my graduate school journey. His unwavering enthusiasm for research serves as a profound inspiration to me. He consistently took the time to engage in discussions, inspiring me in navigating complex problems. He not only aided in my professional growth as an independent researcher but also empowered me to complete this dissertation by unlocking my potential. I feel so honored and lucky to have him supervise both in research and in life.

Along with that, I am grateful to my dissertation committee members: Prof. Joerg Lahann, Prof. Anish Tuteja, Prof. Abdon Pena-Francesch for their detailed feedback and helpful discussion. I also want to thank my collaborators in Dow Chemical Company: Dr. Xiaoyun Chen, Dr. Carol Mohler, Dr. Nick Shephard, Dr. Dongchan Ahn, Dr. Elizabeth Santos, Dr. Frederic Gubbels for guiding the silicone project; Dr. Yuming Lai in Dow Chemical Company, Rachel Cable, Dr. Jessica Choi, and Prof. Melissa Duhaime in Ecology and Evolutionary Biology for Polyethylene degradation project. I also would like to thank the sources that funded my doctorate research: Dow Chemical Company University Project Initiatives, 3M fellowship, PPG fellowship, Rackham Predoctoral fellowship.

Also, I appreciate all my colleagues in Chen lab, especially: Dr. Minyu Xiao, Dr. Xingquan

Zou, Dr. Joshua Jasensky, Dr. Bolin Li, Dr. Daniel Rossi, Dr. John Andre, Dr. Tieyi Lu, Dr. Wen Guo, Dr. Ruiying Guo, Dr. Jun Zhao, Jinpeng Gao, Shuqing Zhang, Yuchen Wu for all the help and inspiring discussion in the past few years.

Finally, I am deeply grateful to my family who love and support me unconditionally. Without their encouragement and unfailing support, this thesis would not be possible, and I won't be who I am now. Simultaneously, I want to express my sincere gratitude to all those who provided invaluable support whenever I faced challenging moments throughout my Ph.D. endeavors.

Table of Contents

Dedication ii

Acknowledgements iii

List of Tables ix

List of Figures x

Abstract xiv

Chapter 1 Introduction 1

1.1 Motivation and Background 1

1.1.1 Introduction 1

1.1.2 Polymer – Biomolecule Interactions 2

1.1.3 Adhesion and Silicone Adhesives 2

1.1.4 Polyethylene Degradation Mechanisms under Simulated Solar Exposure 4

1.2 Sum Frequency Generation (SFG) Vibrational Spectroscopy 5

1.2.1 SFG Background and Basic Theory 5

1.2.2 SFG Instrumentation 7

1.2.3 Orientation Calculation of Buried Interfaces 8

1.3 Presented Research 9

1.4 Research Contributions 11

1.5 References 12

Chapter 2 Probing Biological Molecule Orientation and Polymer Surface Structure at the Polymer/Solution Interface in Situ 15

2.1 Introduction 15

2.2 Materials and Methods 18

2.2.1 Materials and Sample Preparation 18

2.2.2 Experimental Methods 20

2.3 Results and Discussion 23

2.3.1 Peptides Orientation 23

2.3.2 Phenyl Group Orientation 31

2.4 Conclusion 38

2.5 References 39

Chapter 3 Molecular Insights to Adhesion at a Buried Silica-filled Silicone/Polyethylene Terephthalate Interface 46

3.1 Introduction 46

3.2 Materials and Methods 49

3.2.1 Materials and Sample Preparation 49

3.2.2 Experimental Methods 52

3.3 Results and Discussion 54

3.3.1 Adhesion Strength Results 54

3.3.2 SFG Results 56

3.3.3 Correlation between SFG and Adhesion Measurement Results 78

3.4 Conclusion 80

3.5 References 81

Chapter 4 Probing Covalent Interactions at a Silicone Adhesive/Nylon Interface 87

4.1 Introduction 87

4.2 Materials and Methods 89

4.2.1 Materials and Sample Preparation 89

4.2.2 Experimental Methods 91

4.3 Results and Discussion 93

4.3.1 Buried Nylon/Silicone (with or without Adhesion Promoters) Interface: SFG N-H Stretching Signal 93

4.3.2 Group Contribution Solubility Parameter Estimation 98

4.3.3 Buried Nylon/Silicone (with or without Adhesion Promoters) Interface: SFG C=O Stretching Signal 101

4.3.4 Adhesion Test Results 104

4.4 Conclusion 107

4.5 References 108

Chapter 5 Elucidating the Changes in Molecular Structure at the Buried Interface of RTV Silicone Elastomers during Curing 115

5.1 Introduction 115

5.2 Materials and Methods 117

5.2.1 Materials and sample preparation 117

5.2.2 Experimental Methods 119

5.2.3 SFG Data Analysis Method 121

5.3 Results and Discussion 124

5.3.1 Time-dependent Methoxy SFG Results 124

5.3.2 Silylated Time-dependent Methoxy SFG Results 127

5.3.3 Humidity Comparison on Methoxy SFG Results 134

5.3.4 Adhesion Results 136

5.3.5 Peak Assignment of Ti Catalyst 138

5.4 Conclusion 139

5.5 References 140

Chapter 6 Analysis of Accelerated Weather Aging Effect on Polyethylene with Varied Densities Using a Combination of Analytical Techniques 144

6.1 Introduction 144

6.2 Materials and Methods 146

6.2.1 Materials and Sample Preparation 146
6.2.2 Experimental Methods 146
6.3 Results and Discussion (Ting Lin's work) 149
6.3.1 Raman spectroscopy 149
6.3.2 Grazing incident X-ray diffraction (GIXRD) 151
6.4 Results and Discussion (Shuqing Zhang's work) 153
6.4.1 ATR-FTIR 153
6.4.2 Nanoindentation 158
6.4.3 Water Contact Angle Measurement 160
6.5 Further Discussion 161
6.6 Conclusion 165
6.7 References 166
Chapter 7 Conclusions and Future Work 171
7.1 Conclusions and Future Work 171
7.2 References 177

List of Tables

Table 2.1 Number of amino acid of each type in each peptide investigated in this research 19

Table 2.2 Indices of refraction used in the Fresnel Coefficient calculations. 21

Table 2.3 Amide I peak fitting parameters 31

Table 2.4 Phenyl group C-D stretching vibrational peak fitting parameters. 35

Table 3.1 Silicone elastomer (SE) compositions. 51

Table 3.2 Compositions of the silicone adhesive samples investigated. 52

Table 3.3 SFG peak assignments [53-54, 64, 69, 74] 58

Table 3.4 Fitting parameter 77

Table 4.1 Compositions (in weight ratio) of the silicone adhesive samples investigated. More details about Part A and Part B can be found in ref. 48. 90

Table 4.2 Fedors group contribution parameters at 25.0 °C for Hildebrand solubility parameter estimates reported in this study.[71] 98

Table 5.1 Fitting parameters of the time-dependent SFG spectra collected from the MSA/silica interface before silylation as shown in Figure 5.3 125

Table 5.2 Tilt angles of methoxy group at SiO2/MSA interface with various curing times 126

Table 5.3 Fitting parameters of the time-dependent SFG spectra collected from the MSA/silica interface after silylation as shown in Figure 5.5 132

Table 5.4 Fitting parameters of the time-dependent SFG spectra collected from the MSA/silica interface before silylation at different humidity levels (30% and 80%) 135

Table 6.1 Polyethylene sample information 146

Table 6.2 Summary of change in carbonyl index and vinyl index for plaques after 4 weeks of simulated solar exposure 156

List of Figures

Figure 1.1 (a) SFG energy diagram, (b) schematic of the SFG experimental setup..... 6

Figure 2.1 SFG ssp and sps spectra collected from the d8-PS/PBS solution interface. 20

Figure 2.2 Fresnel Coefficients calculated as a function of the d8-PS film thickness for the CaF2/d8-PS interface and the d8-PS/peptide solution interface for SSP (a) and SPS (b) spectra.22

Figure 2.3 CD spectra of the wild-type hybrid peptide in PBS solution (a), the wild-type hybrid peptide on quartz (b), the wild-type hybrid peptide on PS (c), hybrid peptide mutant A2 on PS, and MSI-78 on PS..... 24

Figure 2.4 SFG ssp and ppp amide I spectra collected from the interfaces between d8-PS and solutions of the wild-type MSI-78 peptide (a) and the MSI-78 mutant (b). 26

Figure 2.5 SFG ssp and ppp amide I spectra collected from the interfaces between d8-PS and solutions of mutant B (a), wild-type hybrid peptide (b), mutant A (c), and mutant A2 (d). 29

Figure 2.6 Dependence of tilt angle on the SFG amide I signal ratio $\chi ppp/\chi ssp$ of an α-helical peptide with 26 amino acid residues. 30

Figure 2.7 Different C-D stretching modes for phenyl group (a), tilt angle and twist angle of a phenyl group in lab-fixed (x, y, z) coordinate system and molecule-fixed (x', y', z') coordinate system (b). 31

Figure 2.8 SFG ssp and sps spectra collected from the interfaces between d-PS and solutions of PBS buffer (a), mutant B (b), wild-type cecropin-melittin hybrid peptide (c), mutant A (d), and mutant A2 (e). 33

Figure 2.9 $\chi ssp,v2/\chi sps,v2$ ratio as a function of phenyl group tilt angle (assuming a δ-distribution of orientation)..... 35

Figure 2.10 SFG ssp and sps spectra collected from the interfaces between d-PS and solutions of MSI78 peptide (a), and MUMSI78 peptide (b). 38

Figure 3.1 SFG experimental sample geometry 53

Figure 3.2 Schematic of 90^{o} adhesion test. 53

Figure 3.3 Adhesion data collected from different silicone adhesives with silica filler: (a) all samples cured at 150 ^{o}C for 60 mins (b) all samples cured at 150 ^{o}C for 15 mins. All the silicone samples tested here contain fillers, indicated by (f) in the two figures..... 55

Figure 3.4 SFG spectra collected from buried interfaces between d4-PET and different silicone (with adhesion promoter) samples: (a) uncured and cured silica unfilled GPS/DMMVS silicone; (b) uncured and cured silica filled GPS/DMMVS silicone; (c) uncured and cured silica unfilled GPS/DMMVS/AC silicone; (d) uncured and cured silica filled GPS/DMMVS/AC silicone. The dots are experimental data and the lines are fitting results. 57

Figure 3.5 SFG spectra collected from buried interfaces between d4-PET and different silicone (with adhesion promotor of mixed DMMVS and methyl terminated silane OTMS or HTMS) samples: (a) uncured and cured OTMS/DMMVS/AC silicone with silica filler; (b) uncured and cured HTMS/DMMVS/AC silicone with silica filler. The compositions of samples OTMS/DMMVS/AC and HTMS/DMMVS/AC can be found in Table 3.2. 65

Figure 3.6 SFG spectra collected from buried interfaces between d4-PET and AC silicone with silica filler samples under different curing times at 150°C: (a) Uncured AC silicone with silica filler (0 mins); (b) Cured AC silicone with silica filler (15 mins); (c) Cured AC silicone with silica filler (60 mins); These samples do not contain the adhesion promoters..... 69

Figure 3.7 SFG spectra collected from buried interfaces between d4-PET and GPS/DMMVS/AC silicone with silica filler samples after curing for 15 min; (b) SFG spectra collected from buried interfaces between d4-PET and GPS/DMMVS silicone with silica filler samples after curing for 15min. The dots are experimental data and the lines are fitting results..... 70

Figure 3.8 Schematic of silicone methyl groups oriented at the d4-PET/silicone interface. θ and ψ are tilt and twist angles for a $Si(CH_3)_2$ group. 72

Figure 3.9 Dependence of tilt angle of the vector v versus the surface normal on the SFG methyl signal strength ratio $\chi ssp,s/\chi ssp,as$ 73

Figure 3.10 SFG spectra collected from buried interfaces between d-PET and different neat silicone samples: (a) uncured and cured neat silicone without silica filler; (b) uncured and cured neat silicone with silica filler; (c) uncured and cured silicone with silica filler and adhesion catalyst. 74

Figure 4.1 Schematics of SFG experiment and adhesion test: (a) SFG experimental sample geometry, (b) experiment configuration of 90^{o} adhesion test..... 92

Figure 4.2 SFG spectra in the N-H stretching frequency region collected from buried interfaces between nylon and silicone with different adhesion promoter samples: (a) uncured neat silicone; (b) uncured GPS/DMMVS/AC silicone; (c) uncured SA/DMMVS/AC silicone; (d) cured neat silicone; (e) cured GPS/DMMVS/AC silicone; (f) cured SA/DMMVS/AC silicone..... 94

Figure 4.3 SFG spectra in the C=O stretching frequency region collected from buried interfaces between nylon and silicone with different adhesion promoter samples: (a) uncured neat silicone;

(b) uncured GPS/DMMVS/AC silicone; (c) uncured SA/DMMVS/AC silicone; (d) cured neat silicone; (e) cured GPS/DMMVS/AC silicone; (f) cured SA/DMMVS/AC silicone..... 102

Figure 4.4 (a) Adhesion strengths measured from different nylon/silicone interfaces; (b) Photos of the cross sections of different silicone systems. 105

Figure 5.1 Schematic showing a methoxy group and the coordinate system chosen for orientation analysis. The methoxy group adopts a C3v symmetry. The xyz coordinate demonstrates the lab coordination frame. Θ is tilt angle of the vector v of the $SiOCH_3$ group. 123

Figure 5.2 χssp/χppp ratio as a function of the tilt angle of the net transition dipole of the methoxy C-H stretching (with respect to the surface normal)..... 124

Figure 5.3 SFG SSP (black) and PPP (red) spectra collected from the MSA/silica interface as a function of curing time of (a) 0 h, (b) 3 h, (c) 6 h, (d) 10 h, (e) 23 h. Dots: experimental data. Lines: fitting results. (f) Time-dependent SFG χssp/χppp ratio. (g) The time-dependent χssp, χppp, and the averaged values. 127

Figure 5.4 XPS spectra collected from the silica substrates (a) before and (b) after silylation, (c) SFG spectra before and after silylation, (d) water contact angle results before and after silylation. 129

Figure 5.5 SFG spectra collected from the MSA/silylated silica interface as a function of curing time: (a) 0 hr; (b) 3 hr; (c) 5 hr; (d) 23 hr; (e) 26 hr; (f) 57 hr; (g) Time-dependent SFG χssp/χppp ratio; (j) The time-dependent χssp, χppp, and the averaged values 130

Figure 5.6 (a) Schematic of molecule orientation difference on regular and silylated silica surfaces; (b) Schematic showing curing process in RTV silicone at silica substrate. 133

Figure 5.7 SFG spectra collected from the MSA/silica interface as a function of time when cured at different humidity levels: exposure of (a) 0 hr; (b) 1 hr; (c) 2 hr; (d) 5 hr to 30% humidity level; (f) 0 hr; (g) 1 hr; (h) 2 hr; (i) 5 hr to 80% humidity level; (e) Time-dependent SFG χssp/χppp ratio at 30% and 80% humidity levels. (j) Time-dependent χssp, χppp, and the averaged values at 30% and 80% humidity levels..... 134

Figure 5.8 Adhesion strength on silica substrate with and without silylation 136

Figure 5.9 Schematic of the curing process of RTV silicone. Initially curing occurs using the hydroxyl groups because it takes some time for moisture to diffuse to the interface. Top right: silylated silica/silicone interface. Bottom right: silica/silicone interface. Different objects in the figure were not drawn to scale.. 137

Figure 5.10 SFG spectrum from the MSA (with Ti catalyst but without MTMS)/silica interface (a), SFG spectrum from the MSA (wih MTMS but without Ti catalyst)/silica interface (b), SFG spectrum from the MSA (with both Ti catalyst and MTMS)/silica interface (c), Raman spectrum of Ti catalyst (d), IR spectrum of Ti catalyst (e)..... 138

Figure 6.1 Raman results of various LLDPE samples in pristine condition, after two and four weeks of UV exposure. a) LLDPE #5 crystalline region, b) LLDPE L crystalline region, c) LLDPE K crystalline region, d) LLDPE J crystalline region, e) LLDPE #5 amorphous region, f) LLDPE L amorphous region, g) LLDPE K amorphous region, h) LLDPE J amorphous region..... 149

Figure 6.2 Raman results of various HDPE samples in pristine condition, after two and four weeks of UV exposure. a) HDPE #6 crystalline region, b) HDPE G crystalline region, c) HDPE H crystalline region, d) HDPE #6 amorphous region, e) HDPE G amorphous region, f) HDPE H amorphous region..... 150

Figure 6.3 Raman intensity change of various samples as a function of the UV exposure time in the crystalline region (left) and the amorphous region (right). 151

Figure 6.4 GIXRD results of various PE samples in pristine condition, after two and four weeks of UV exposure. a) LLDPE L, b) LLDPE K, c) HDPE G, d) HDPE H, e) Summary of crystallinity change trend probed by GIXRD. 152

Figure 6.5 ATR-FTIR of LLDPE film #5 and HDPE film #6 in pristine condition (T0), after two and four weeks of simulated solar exposure. (a: 3100-3800 cm^{-1}, b: 1550-1900 cm^{-1}, c: 880-940 cm^{-1}) 153

Figure 6.6 Carbonyl index (a) and vinyl index (b) of LLDPE film #5 and HDPE film #6 in pristine condition (T0), after two and four weeks of simulated solar exposure. 154

Figure 6.7 ATR-FTIR of LLDPE plaques J, L in pristine condition (T0), after two and four weeks of simulated solar exposure. (a: 3100-3800 cm^{-1}, b: 1550-1900 cm^{-1}, c: 880-940 cm^{-1})..... 155

Figure 6.8 Carbonyl index (a) and vinyl index (b) of LLDPE plaques in pristine condition, after two and four weeks of simulated solar exposure. 155

Figure 6.9 ATR-FTIR of HDPE plaques G, H and LLDPE plaques J, L undergoing four weeks of simulated solar exposure. (a: 3100-3800 cm^{-1}, b: 1550-1900 cm^{-1}, c: 880-940 cm^{-1})..... 156

Figure 6.10 a) Schematic of different sample locations for testing. ATR-FTIR of HDPE plaques H (b, c, d) and LLDPE J (e, f, g) undergoing four weeks of simulated solar exposure at different locations. (b, e: 3100-3800 cm^{-1}, c, f: 1550-1900 cm^{-1} d, g: 880-940 cm^{-1})..... 157

Figure 6.11 Nanoindentation results: plaques G, H, J, K, L in pristine condition and after four weeks of simulated solar exposure. 159

Figure 6.12 Water contact angle measurement..... 160

Figure 6.13 Summary of the normalized difference between 4-week aged and pristine polyethylene samples: a) Raman deduced crystallinity, b) GIXRD deduced crystallinity, c) Carbonyl index, d) Vinyl index, e) Nanoindentation. 162

Figure 6.14 Correlations of the crystallinities measured from different samples with GIXRD and Raman spectroscopy. 164

Abstract

In the past, SFG research has primarily focused on simple model systems. This thesis highlights the potential of using SFG to study buried polymer interfaces of practically applicable and commercial polymers, such as silicone adhesives, developing a tool to investigate real-world interfaces relevant to many applications. Also, this thesis provides an in-depth study on silicone/polymer buried solid/solid interface like first time probing the interfacial chemical reactions *in situ* and orientation analysis during curing. The SFG methodologies developed in this thesis are widely applicable for many polymer systems.

High-performance adhesives become increasingly important across diverse applications due to the demand of energy efficiency. Adhesion is mediated by interfacial molecules and occurs at buried interfaces. Optimizing and controlling the adhesion often relies on understanding the interfacial molecular structure. However, it has always been challenging in both academia and industry to investigate such buried interfaces nondestructively. In this thesis, sum frequency generation (SFG) vibrational spectroscopy was applied to study molecular structures of buried interfaces to understand molecular mechanisms of polymer adhesion in situ.

High-temperature vulcanized (HTV) silicone is one of the most commonly used silicone and the HTV silicone mentioned in this work is mainly based on the hydrosilylation curing chemistry, which is the addition reaction of Si-H and Si-vinyl group catalyzed by platinum catalyst. SFG was applied to study buried interfaces of HTV silicone composite systems and the results were correlated to adhesion measurement data to understand the molecular adhesion mechanisms.

Silicone matrices with different added compositions such as adhesion promoters, fillers, and catalysts were investigated to understand the effects of various additives on the buried interfacial structure. The added filler appeared to reduce the interfacial segregation of the adhesion promoter at the silicone/substrate interface, while the adhesion catalyst can facilitate the interfacial segregation of adhesion promoter to enhance adhesion. SFG was also utilized to probe the interfacial chemical reaction between HTV silicone and polar polymer substrate in situ. This is the first time to directly monitor this process at buried interfaces of commercial silicone adhesive system. It illustrates that manipulating segregation and functionality of adhesion promoter, interfacial reaction, and surface composition at buried interfaces can substantially amplify silicone adhesion.

Besides HTV silicone, room temperature vulcanized (RTV) silicone based on condensation curing was also investigated by SFG. Here the RTV silicone indicates the silicone involving the formation of crosslinked networks through chemical reactions between silanol groups and other reactive groups in formulated products such as alkoxysilanes or acetoxysilanes.

This thesis also investigates the molecular interactions between biological molecules and polymer surfaces in situ. SFG was used to study molecular interactions between polystyrene and various peptides with different numbers of aromatic amino acids by monitoring the orientation changes of polystyrene phenyl groups and alpha-helical peptides during the interactions. It was found that the charge-charge interaction was the dominant interaction at the interface, which outperformed the π–π interaction.

Polyethylene weathering mechanism was investigated and such research was included in this thesis as well. With global plastic production exceeding 300 million tons per year since 2014, plastics accumulating in the environment are increasing at an alarming rate. Globally, only a small

portion of plastic waste is recycled. A comprehensive study on plastic degradation mechanisms can offer essential knowledge to ultimately understand the impact of the degraded materials, helping the development of strategies to mitigate such impact. Changes in the structure of polyethylene after exposure to UV irradiation depend on the exposure time and the polyethylene characteristics. This study employed multiple analytical tools and offered a systematic understanding of polyethylene degradation. This approach provides knowledge on how plastics behave in the environment and their degradation mechanisms.

Chapter 1 Introduction

1.1 Motivation and Background

1.1.1 Introduction

Polymer-based substances are widely used in many applications like biomedical implants, adhesives, coatings, and composites.[1-9] It is crucial to understand the surface and interfacial structures of these polymers as they dictate crucial interfacial characteristics such as biocompatibility, adhesion, chemical responsiveness, and interfacial stability.[10-11] Therefore it is important to study surface/interfacial structures of polymer materials. For instance, it is necessary to study the interfacial structure of organic adhesives because such structure influences the adhesion strength. Different interfacial structures of polymeric biomaterials would lead to various interactions with biological media leading to varied biocompatibility, thus investigating and understanding such interfacial structures is vital.

However, surface and interface only involve small numbers of molecules, which makes it extraordinarily difficult to probe them. In addition, many interfaces are buried, which lead to further difficulties to study. Traditional analytical techniques for studying surface structures like attenuated total reflectance infrared spectroscopy (ATR-FTIR) lack monolayer surface sensitivity. Other techniques like grazing incidence X-ray diffraction (GIXRD) and X-ray photoelectric spectroscopy (XPS) require the breakage of buried interface to produce two exposed surfaces to probe, which can likely destroy the original structure of the buried interface.

Benefiting from the advancements in high-power pulse laser techniques and nonlinear optical systems, nonlinear vibrational spectroscopies such as sum frequency generation (SFG) vibrational

spectroscopy have emerged as non-destructive techniques well-suited for probing buried interfaces at the molecular level without the interference from bulk materials. This thesis research applies laboratory-developed methods to study real-world materials and interfaces to address industrial adhesion issues and investigate biomolecule-polymer interactions.

In addition to the SFG research, this thesis also studied polyethylene degradation mechanisms after simulated solar exposure. The three research topics which will be covered in this thesis, including polymer–biological molecule interactions, silicone adhesives, and polyethylene degradation mechanisms, will be briefly introduced below. More detailed introductions of each topic will be presented in chapters 2 to 6.

1.1.2 Polymer – Biomolecule Interactions

Polymers are widely used for many applications involving interactions with biological molecules such as proteins and peptides, ranging from biomedical materials, marine antifouling coatings, membranes for biomolecule separation, to substrates for enzyme molecules for biosensing. For such applications, it is important to understand molecular interactions between biological molecules and polymer materials in situ in real time. Such understanding provides vital knowledge to manipulate biological molecule–polymer interactions and to optimize polymer surface structures to improve polymer performance. In chapter 2, SFG was applied to study interactions between peptides (serving as models for biological molecules) and deuterated polystyrene (d8-PS, serving as a model for polymer materials). The peptide conformations/orientations and polymer surface phenyl orientation during the peptide–d8-PS interactions were determined using SFG, providing important knowledge for the field of polymeric biomaterial.

1.1.3 Adhesion and Silicone Adhesives

An adhesive is a substance capable of holding materials together by surface attachment. Adhesives work by developing bonds with the materials they contact, allowing two different surfaces to resist separation. With global focus now on sustainability and environmental friendliness, adhesive research can help us develop new materials with better bonding capabilities, creating stronger, lighter, and more durable products across various industries.

The origin of adhesion, or the mechanisms through which different substances stick to each other, occurs generally due to four types of forces: mechanical, chemical, dispersive, and electrostatic interactions. Mechanical Interlocking: When the surfaces of two solids come into very close contact, such that the surface roughness of one surface falls into the valleys of the other surface, mechanical interlocking can occur. It is reliant on the surface roughness of the materials. Chemical Bonding: Adhesion can occur when the two surfaces chemically react with each other, forming a bond at the interface. This can be very strong but often requires specific conditions or pre-treatments. Dispersive Adhesion (Van der Waals forces): This happens due to physical interactions between the two surfaces. These weak attractions occur when polarized molecules interact, including dipoles, induced dipoles, and instantaneous dipoles. Electrostatic Forces: Electrostatic forces between charged bodies or between charged bodies and neutral bodies can also cause adhesion.

These mechanisms contribute to the adhesive's strength. The overall adhesion strength can be influenced by various factors, including the intrinsic properties of the adhesive material (like its mechanical properties and chemical bonding structure), the types of materials being adhered together, the roughness and cleanliness of the surfaces, and the environmental conditions (like temperature and humidity). Different applications may require optimizing different factors to maximize adhesion strength. For example, an adhesive for a wet or humid application may need

to be primarily chemically bonding to resist water interference, while an adhesive for a dry, rough surface may work most effectively by mechanical interlocking.

Silicone adhesives are widely used in many important applications in aviation, automotive, construction, and electronics industries.[12-14] Thus, understanding the correlation between the interfacial structure of silicone adhesive systems and adhesion is needed for understanding silicon adhesion mechanisms. The research in this thesis specifically investigated the molecular behaviors of silicone adhesives at buried interfaces in situ. Such investigations were divided into three parts in this thesis research. The first part was the study on the impact of fillers and adhesion catalyst on interfacial structures of silicone adhesive system in contact with PET. The second part was the examinations of interfacial chemical reactions between polymer and silicone adhesive to uncover the adhesion promotion mechanism and the adhesion promoter selection strategy. The studies in the first two parts focused on the HTV hydrolyzation based silicone chemistry. The research in the third part elucidated the molecular behavior of adhesion promoters at the buried interface of RTV condensation silicone elastomers during curing. The research on silicone adhesives not only sheds light on the molecular behaviors/interactions of silicone adhesives but also provides a framework applicable to study interfaces of a wide array of complex polymer-based systems in practical applications. The research results on silicone adhesives were presented in chapters 3 to 5.

1.1.4 Polyethylene Degradation Mechanisms under Simulated Solar Exposure

Polyethylene, the most commonly utilized plastic globally, contributes significantly to the mounting volume of solid waste, posing a rising threat to the natural environment. A deeper comprehension of how plastics break down can offer valuable insights into reducing the accumulation of plastic waste post-use. In this study, a variety of commercially available polyethylene materials with varied manufacturing parameters were exposed to simulated solar

exposure for different lengths of time. A combination of analytical techniques were employed to assess the chemical and physical alterations in these polyethylene materials following exposure.

1.2 Sum Frequency Generation (SFG) Vibrational Spectroscopy

1.2.1 SFG Background and Basic Theory

SFG, a second-order nonlinear optical process, involves the combination of two photons to produce a third photon with the combined energy of the incoming photons.[11-23] The selection rule for SFG specifies that this photon combination is restricted to media lacking inversion symmetry. Since most bulk media exhibit inversion symmetry, SFG signals cannot be generated from such environments. However, for surfaces and interfaces where inversion symmetry is broken, the SFG process occurs, making SFG spectroscopy a technique intrinsically specific to surfaces/interfaces.

In our SFG vibrational spectroscopic studies, the incoming beams consist of a visible beam at 532 nm and a frequency-tunable infrared (IR) beam. By adjusting the frequency of the IR beam, it is feasible to selectively examine various functional groups on a surface or at an interface. Control over the polarization of each incoming beam and the generated SFG beam enables the determination of the surface/interfacial orientation of these functional groups.

Recent advancements in SFG research underscore its potency in exploring surfaces and interfaces across diverse systems, including biological systems, organic molecules, water, and polymer materials.[24-28] The energy diagram for an SFG process is depicted in Figure 1.1a. As mentioned above, SFG's surface/interfacial selectivity is due to its specific selection rule. The signal strength in SFG is directly linked to the square of the second-order nonlinear susceptibility, $\chi^{(2)}$, of a material (under the electric dipole approximation). $\chi^{(2)}$, being a polar third-rank tensor, undergoes a sign change when subjected to an inversion operation: $\chi^{(2)}(r) = -\chi^{(2)}(-r)$. In materials that possess inversion symmetry, $\chi^{(2)}$ remains unchanged under such an operation: $\chi^{(2)(}r) = \chi^{(2)}(-r)$.

Consequently, the only feasible solution for these conditions is $\chi^{(2)} = 0$, implying the absence of an SFG signal for materials with inversion symmetry under the electric dipole approximation.

Most bulk polymer materials, including polymer solutions, melts, and solid polymer systems, exhibit inversion symmetry because their functional groups are typically randomly oriented. Thus, they do not produce SFG signals. At a surface or interface where inversion symmetry is disrupted, the situation changes as molecules or functional groups exhibit a discrepancy between $\chi^{(2)}(r)$ and $\chi^{(2)}(-r)$. In such cases, $\chi^{(2)}$ does not necessarily equate to zero, enabling the detection of SFG signals from surfaces and interfaces. The inherent surface/interface sensitivity of SFG, with a capability to detect submonolayer properties, is a result of the selection rule.[29-38]

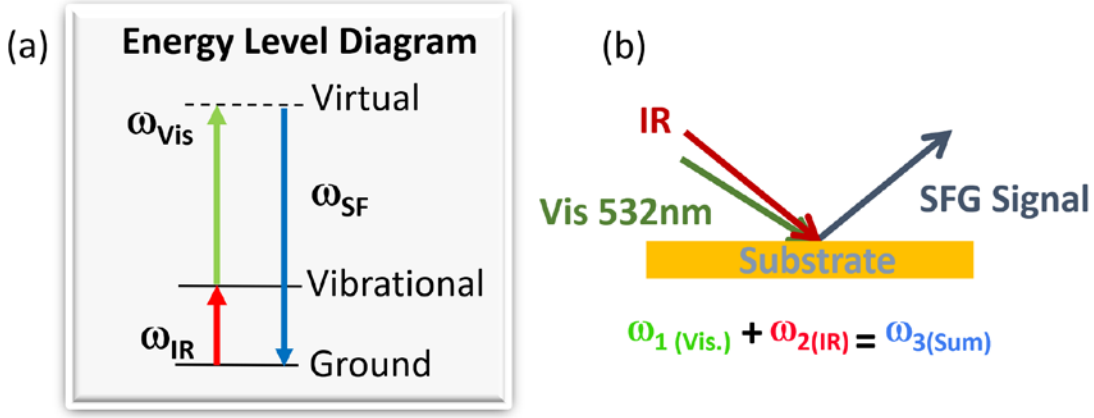

Figure 1.1 (a) SFG energy level diagram, (b) schematic of the SFG experimental sample setup

Clearly, the sensitivity of SFG to surfaces/interfaces is not contingent upon the penetration depth of the incident laser beams into the sample. Even if the laser beams penetrate the entire sample volume, only molecules situated on the surface or at the interface contribute to the signal due to the governing SFG selection rule.

SFG signal intensity can be expressed as:

$$I_{SFG} \propto |\chi_{eff}^{(2)}|^2 I_{IR} I_{vis} \qquad \textbf{eq. 1.1}$$

Where $\chi_{eff}^{(2)}$ is the effective second-order nonlinear optical susceptibility that can be measured by our SFG experiment. I_{IR} and I_{vis} represent the intensities of the input IR and visible beams, respectively. For the $\chi_{eff}^{(2)}$**,** it can be expressed as below:

$$\chi_{eff}^{(2)} = \chi_{nr} + \sum_q \frac{A_q}{\omega_2 - \omega_q + i\Gamma_q} \qquad \textbf{eq. 1.2}$$

Where χ_{nr} is the non-resonant contribution. The qth resonant contribution has frequency ω_q (peak center), signal amplitude A_q (related to intensity), and line width Γ_q. All the SFG spectra in this thesis are fitted with equation 1.2. $\chi_{eff}^{(2)}$ is the effective second-order nonlinear susceptibility tensor of the sample (e.g., a surface or an interface).

1.2.2 SFG Instrumentation

The SFG experiments reported in this thesis utilized a Nd:YAG laser (EKSPLA PL2251, Lithuania) to produce a picosecond fundamental output laser pulse at a wavelength of 1064 nm. This pulse was divided into two parts: one was frequency-doubled to create a fixed-frequency, visible (532 nm) beam (EKSPLA H500), while the remaining 1064 nm energy, along with part of the 532 nm energy, was employed to generate a frequency-tunable infrared (IR) input beam through optical parametric generation/amplification (OPG/OPA) and a difference frequency generation (DFG) process (EKSPLA PG501/DFG1P).

The visible and IR beams were directed at the buried interfaces from angles of 65° and 60°, respectively, relative to the surface normal. The region of overlap for these beams had a diameter of approximately 0.5 mm. The energies of the visible and IR pulses were roughly 30 μJ and 120 μJ, respectively, for the C-H and O-H stretching frequency range (2700-3800 cm^{-1}). In the carbonyl

C=O stretching frequency range (1550-1950 cm^{-1}), the energies were 30 μJ for the visible beam and 40 μJ for the IR beam at the sample interface. It is important to note that these energy values are specific to the instrument used in this study and may vary between instruments.

The generation of an output SFG beam occurred when spatially and temporally overlapped visible and IR beams interacted at a surface or a buried interface. The SFG sample geometry was shown in Figure 1.1b. The intensity of the SFG beam was recorded by a monochromator/PMT as a function of the IR frequency (wavenumber, cm^{-1}), resulting in the production of a vibrational spectrum.

1.2.3 Orientation Calculation of Buried Interfaces

In the lab-fixed coordinate system, the measured $\chi_{eff}^{(2)}$ can be correlated to the sample susceptibility components defined in the lab coordination system after accounting for the Fresnel coefficients:

$$\chi_{eff,ssp}^{(2)} = L_{yy}(\omega)L_{yy}(\omega_1)L_{zz}(\omega_2)\sin\beta_2\,\chi_{yyz}$$
$$\chi_{eff,ppp}^{(2)} = -L_{xx}(\omega)L_{xx}(\omega_1)L_{zz}(\omega_2)\cos\beta\cos\beta_1\sin\beta_2\,\chi_{xxz}$$
$$-L_{xx}(\omega)L_{zz}(\omega_1)L_{xx}(\omega_2)\cos\beta\sin\beta_1\cos\beta_2\,\chi_{xzx}$$
$$+L_{zz}(\omega)L_{xx}(\omega_1)L_{xx}(\omega_2)\sin\beta\cos\beta_1\cos\beta_2\,\chi_{zxx}$$
$$+L_{zz}(\omega)L_{zz}(\omega_1)L_{zz}(\omega_2)\sin\beta\sin\beta_1\sin\beta_2\,\chi_{zzz} \qquad \textbf{eq. 1.3}$$

Here, β_1 and β_2 are incident angles of the input visible and IR beams vs. the surface normal. L_{ii}'s (i = x, y, z) are Fresnel coefficients which are related to the refractive indices of materials forming the interface and input angles of the input beams.

The ratios of SFG second-order nonlinear optical susceptibility components (e.g., χ_{yyz} or χ_{zzz}) can be measured and connected to related elements of molecular hyperpolarizability via molecular orientations. Such connections for functional groups like methyl and methoxy groups that adapt C3v symmetry have been extensively reported.[39-42] The ratios of SFG second-order nonlinear

optical susceptibility components (e.g., χ_{yyz} or $\chi_{zzz)}$ can be measured and connected to the related elements of molecular hyperpolarizability via molecular orientations. For instance, in the case of the symmetric stretching mode of a methyl group:

$$\chi_{xxz,\mathrm{s}} = \chi_{yyz,\mathrm{s}} = \frac{1}{2} N_{\mathrm{s}} \beta_{ccc} [\cos\theta(1+r) - \cos^3\theta(1-r)]$$

$$\chi_{zzz,\mathrm{s}} = N_{\mathrm{s}} \beta_{ccc} [r\cos\theta + \cos^3\theta(1-r)] \qquad \textbf{eq. 1.4}$$

Where β_{aac} equals $r\beta_{ccc}$, and θ represents the angle formed between the principal axis of the methyl group and the z-axis aligned along the surface normal. The number density, N_s, represents the number density of molecules on surface or at interface and remains unchanged when different polarization combinations of the input and output beams are used in an SFG experiment. Consequently, valuable insights into molecular orientation can be derived from experimental measurements by analyzing the ratio of signal intensities obtained from two polarization combinations (such as ssp and ppp). This method eliminates the need for knowing the surface coverage because this factor cancels out in the signal strength ratio. When determining the orientation of methyl groups on a surface, the ssp and ppp signal strength ratio can be used to determine the orientation angle θ, assuming the orientation angles for all the groups (e.g., methyl groups) are the same or a delta angle distribution. In cases where surface/interface methyl groups display varied orientations (or have an orientation distribution), the terms of $\cos\theta$ and $\cos^3\theta$ shown in Eq. 1.4 should be replaced by $\langle\cos\theta\rangle$ and $\langle\cos^3\theta\rangle$ (“< >” meaning average). To comprehensively describe the orientation distribution and average orientation, knowing the surface coverage (N_s) might be necessary.[43]

1.3 Presented Research

Each thesis topic was briefly mentioned above. Here, in more detail, chapter 2 will focus on

using SFG to investigate molecular interactions between biological molecules and polymer surface in situ. Various peptides with different numbers of aromatic amino acids were used as models for biological molecules, and the d8-PS surface served as a model for polymer surfaces. The orientations of both the PS phenyl group and the peptides at the polymer/peptide solution interface were determined to understand the interfacial interactions especially the π–π interaction. This research shed lights on how the π–π interaction plays a role when biological media come in contact with polymer surfaces with aromatic functionality.

Chapters 3 and 4 investigated the molecular structures at the hydrolyzation HTV silicone/polar polymer (polyethylene terephthalate (PET) and nylon) interfaces to understand the adhesion mechanisms of silicone adhesives. Such research also sheds light on the effects of fillers and adhesion catalyst on the interfacial behavior of the adhesion promotion system for silicone elastomers as well as the related impact on adhesion. Chapter 3 focused on studying interfacial structures of silicone elastomeric adhesives in the presence of silica fillers and/or a zirconium(IV) acetylacetonate adhesion catalyst at the silicone/PET interface to understand their individual and synergistic effects. The interfacial structures obtained from the SFG study were correlated to the adhesion behavior of silicone adhesive to PET. The interfacial reactions of methoxy and epoxy groups of the adhesion promoter were found to play significant roles in enhancing the interfacial adhesion at the buried interface. Chapter 4 focused on studying the interfacial chemical reactions between nylon and two alkoxysilane adhesion promoters with varied functionalities (succinic anhydride (SA) and epoxy) formulated into silicone. Evidence of reactions between the organofunctional group of each silane and the reactive groups on the polyamide was found at the buried interface. SFG results elucidated the mechanisms of organo-silane adhesion promotion for silicone at the molecular level and mapped out the adhesion promoter selection strategy.

Chapter 5 aimed to elucidate the interfacial molecular structural changes and origins of interfacial

reactive hydroxyl groups in RTV condensation cured silicone during curing, focusing on the methoxy groups at interfaces and their relationship to adhesion. This study established the correlation between interfacial molecular structure changes of RTV silicones and their effect on adhesion strength. It also highlighted the power of SFG spectroscopy as a unique tool for studying chemical and structural changes at RTV silicone/substrate interfaces in situ and in real time during curing. This work provides valuable insights into the interfacial chemistry of RTV silicone and its implications for material performance and application development, aiding in the development of improved silicone adhesives.

Chapter 6 utilized a combination of analytical techniques to evaluate the chemical and physical changes in polyethylene materials subjected to simulated solar exposure, including water contact angle measurements, attenuated total reflection-Fourier transform infrared spectroscopy (ATR-FTIR), Raman spectroscopy, grazing incidence X-ray Diffraction (GIXRD) and nanoindentation tests. It was found that various polyethylene samples underwent structural changes under UV irradiation, leading to increased hydrophilicity, a greater number of polar groups, an increased degree of crystallinity, and higher elastic modulus. The structural changes of polyethylene are time-dependent and vary depending on the difference in their parameters. This research demonstrated that the combined use of various analytical tools in the study can provide a more complete picture of polyethylene degradation mechanisms for understanding the fate of plastics in the environment.

1.4 Research Contributions

Chapter 6 presents my joint research with another Ph.D. student, Shuqing Zhang, in our group. This research was completed by Shuqing Zhang and me. Shuqing collected ATR-FTIR, water contact angle, and nanoindentation data. I collected the Raman and GIXRD data. We both performed data analysis and worked on the conclusions from the results together. I want to acknowledge Shuqing’s effort on the research work in this chapter and for her assistance in presenting such results in this chapter.

1.5 References

1. Ramakrishna, S.; Mayer, J.; Wintermantel, E.; Leong, K. W., Biomedical Applications of Polymer-Composite Materials: A Review. *Compos. Sci. Technol.* **2001**, *61*, 1189-1224.
2. Hsissou, R.; Seghiri, R.; Benzekri, Z.; Hilali, M.; Rafik, M.; Elharfi, A., Polymer Composite Materials: A Comprehensive Review. *Compos. Struct.* **2021**, *262*, 113640.
3. Zhang, Q.; Li, T.; Duan, A.; Dong, S.; Zhao, W.; Stang, P. J., Formation of a Supramolecular Polymeric Adhesive Via Water–Participant Hydrogen Bond Formation. *J. Am. Chem. Soc.* **2019**, *141*, 8058-8063.
4. Matos-Pérez, C. R.; White, J. D.; Wilker, J. J., Polymer Composition and Substrate Influences on the Adhesive Bonding of a Biomimetic, Cross-Linking Polymer. *J. Am. Chem. Soc.* **2012**, *134*, 9498-9505.
5. Hong, Y.; Li, Y.; Wang, F.; Zuo, B.; Wang, X.; Zhang, L.; Kawaguchi, D.; Tanaka, K., Enhanced Thermal Stability of Polystyrene by Interfacial Noncovalent Interactions. *Macromolecules* **2018**, *51*, 5620-5627.
6. Nam, S.; Mooney, D., Polymeric Tissue Adhesives. *Chem. Rev.* **2021**, *121*, 11336-11384.
7. Pletincx, S.; Fockaert, L. L. I.; Mol, J. M. C.; Hauffman, T.; Terryn, H., Probing the Formation and Degradation of Chemical Interactions from Model Molecule/Metal Oxide to Buried Polymer/Metal Oxide Interfaces. *npj Materials Degradation* **2019**, *3*, 23.
8. Ohya, Y.; Takahashi, A.; Nagahama, K., Biodegradable Polymeric Assemblies for Biomedical Materials. In *Polymers in Nanomedicine*, Kunugi, S.; Yamaoka, T., Eds. Springer Berlin Heidelberg: Berlin, Heidelberg, 2012; pp 65-114.
9. Ding, B.; Jasensky, J.; Li, Y.; Chen, Z., Engineering and Characterization of Peptides and Proteins at Surfaces and Interfaces: A Case Study in Surface-Sensitive Vibrational Spectroscopy. *Acc. Chem. Res.* **2016**, *49*, 1149-1157.
10. Cai, C.; Azam, M. S.; Hore, D., Temperature-Dependent Chemical Functional Group Reorientation at Silicone Surfaces. *J. Phys. Chem. C* **2021**, *125*, 22214-22222.
11. Wang, J.; Wloch, G.; Lin, T.; Chen, Z., Investigating Thin Silicone Oil Films Using Four-Wave Mixing Spectroscopy and Sum Frequency Generation Vibrational Spectroscopy. *Langmuir* **2021**, *37*, 14540-14549.
12. Vázquez, A. V.; Shephard, N. E.; Steinecker, C. L.; Ahn, D.; Spanninga, S.; Chen, Z., Understanding Molecular Structures of Silanes at Buried Polymer Interfaces Using Sum Frequency Generation Vibrational Spectroscopy and Relating Interfacial Structures to Polymer Adhesion. *J. Colloid Interface Sci.* **2009**, *331*, 408-416.
13. Chen, Z., Investigating Buried Polymer Interfaces Using Sum Frequency Generation Vibrational Spectroscopy. *Prog. Polym. Sci.* **2010**, *35*, 1376-1402.
14. Ye, H.; Gu, Z.; Gracias, D. H., Kinetics of Ultraviolet and Plasma Surface Modification of Poly(Dimethylsiloxane) Probed by Sum Frequency Vibrational Spectroscopy. *Langmuir* **2006**, *22*, 1863-1868.
15. Lu, X.; Shephard, N.; Han, J.; Xue, G.; Chen, Z., Probing Molecular Structures of Polymer/Metal Interfaces by Sum Frequency Generation Vibrational Spectroscopy. *Macromolecules* **2008**, *41*, 8770-8777.
16. Lambert, A. G.; Davies, P. B.; Neivandt, D. J., Implementing the Theory of Sum Frequency Generation Vibrational Spectroscopy: A Tutorial Review. *Appl. Spectrosc.Reviews* **2005**, *40*, 103-145.

17. Geiger, F. M., Second Harmonic Generation, Sum Frequency Generation, and X(3): Dissecting Environmental Interfaces with a Nonlinear Optical Swiss Army Knife. *Annu. Rev. Phys. Chem.* **2009**, *60*, 61-83.
18. Chen, Z., Understanding Surfaces and Buried Interfaces of Polymer Materials at the Molecular Level Using Sum Frequency Generation Vibrational Spectroscopy. *Polym. Int.* **2007**, *56*, 577-587.
19. Kristalyn, C. B.; Lu, X. L.; Weinman, C. J.; Ober, C. K.; Kramer, E. J.; Chen, Z., Surface Structures of an Amphiphilic Tri-Block Copolymer in Air and in Water Probed Using Sum Frequency Generation Vibrational Spectroscopy. *Langmuir* **2010**, *26*, 11337-11343.
20. Lu, X.; Zhang, C.; Ulrich, N.; Xiao, M.; Ma, Y.-H.; Chen, Z., Studying Polymer Surfaces and Interfaces with Sum Frequency Generation Vibrational Spectroscopy. *Anal. Chem.***2016**, *89*, 466-489.
21. Lu, X.; Clarke, M. L.; Li, D.; Wang, X.; Xue, G.; Chen, Z., A Sum Frequency Generation Vibrational Study of the Interference Effect in Poly (N-Butyl Methacrylate) Thin Films Sandwiched between Silica and Water. *J. Phys. Chem. C* **2011**, *115*, 13759-13767.
22. FitzGerald, W. R.; Jena, K. C.; Hore, D. K., Effects of Single-Source Multiple Beam Interference in Vibrational Sum Frequency Generation Spectroscopy. *J. Mol. Struct.***2015**, *1084*, 368-373.
23. Sohrabpour, Z.; Kearns, P. M.; Massari, A. M., Vibrational Sum Frequency Generation Spectroscopy of Fullerene at Dielectric Interfaces. *J. Phys. Chem. C* **2016**, *120*, 1666-1672.
24. Okuno, M.; Ishibashi, T.-a., Heterodyne-Detected Achiral and Chiral Vibrational Sum Frequency Generation of Proteins at Air/Water Interface. *J. Phys. Chem. C* **2015**, *119*, 9947-9954.
25. Ho, J.-J.; Skoff, D. R.; Ghosh, A.; Zanni, M. T., Structural Characterization of Single-Stranded DNA Monolayers Using Two-Dimensional Sum Frequency Generation Spectroscopy. *J. Phys. Chem. B* **2015**, *119*, 10586-10596.
26. Li, Y.; Zhang, X.; Myers, J.; Abbott, N. L.; Chen, Z., Room Temperature Freezing and Orientational Control of Surface-Immobilized Peptides in Air. *Chem. Commun.* **2015**, *51*, 11015-11018.
27. Leng, C.; Hung, H.-C.; Sieggreen, O. A.; Li, Y.; Jiang, S.; Chen, Z., Probing the Surface Hydration of Nonfouling Zwitterionic and Poly(Ethylene Glycol) Materials with Isotopic Dilution Spectroscopy. *J. Phys. Chem. C* **2015**, *119*, 8775-8780.
28. Hu, D.; Chou, K. C., Re-Evaluating the Surface Tension Analysis of Polyelectrolyte-Surfactant Mixtures Using Phase-Sensitive Sum Frequency Generation Spectroscopy. *J. Am. Chem. Soc.* **2014**, *136*, 15114-15117.
29. Perry, A.; Neipert, C.; Space, B.; Moore, P. B., Theoretical Modeling of Interface Specific Vibrational Spectroscopy: Methods and Applications to Aqueous Interfaces. *Chem. Rev.* **2006**, *106*, 1234-1258.
30. Yan, E. C. Y.; Fu, L.; Wang, Z.; Liu, W., Biological Macromolecules at Interfaces Probed by Chiral Vibrational Sum Frequency Generation Spectroscopy. *Chem. Rev.* **2014**, *114*, 8471-8498.
31. Perry, A.; Ahlborn, H.; Space, B.; Moore, P. B., A Combined Time Correlation Function and Instantaneous Normal Mode Study of the Sum Frequency Generation Spectroscopy of the Water/Vapor Interface. *J. Chem. Phys.J. Chem. Phys.* **2003**, *118*, 8411-8419.
32. Cong, X.; Poyton, M. F.; Baxter, A. J.; Pullanchery, S.; Cremer, P. S., Unquenchable Surface Potential Dramatically Enhances Cu2+ Binding to Phosphatidylserine Lipids. *J. Am. Chem. Soc.* **2015**, *137*, 7785-7792.

33. Kim, J.; Cremer, P. S., Ir−Visible Sfg Investigations of Interfacial Water Structure Upon Polyelectrolyte Adsorption at the Solid/Liquid Interface. *J. Am. Chem. Soc.* **2000**, *122*, 12371-12372.
34. Su, X.; Cremer, P. S.; Shen, Y. R.; Somorjai, G. A., High-Pressure Co Oxidation on Pt(111) Monitored with Infrared−Visible Sum Frequency Generation (Sfg). *J. Am. Chem. Soc.* **1997**, *119*, 3994-4000.
35. Chen, Z.; Shen, Y. R.; Somorjai, G. A., Studies of Polymer Surfaces by Sum Frequency Generation Vibrational Spectroscopy. *Annu. Rev. Phys. Chem.* **2002**, *53*, 437-465.
36. Su, X.; Cremer, P. S.; Shen, Y. R.; Somorjai, G. A., Pressure Dependence of the Vibrational Spectra of Adsorbed Co on Pt(111) Studied by Sum Frequency Generation. *Phys. Rev. Lett.* **1996**, *77*, 3858-3860.
37. Wang, J.; Chen, C.; Buck, S. M.; Chen, Z., Molecular Chemical Structure on Poly(Methyl Methacrylate) (Pmma) Surface Studied by Sum Frequency Generation (Sfg) Vibrational Spectroscopy. *J. Phys. Chem. B* **2001**, *105*, 12118-12125.
38. Shen, Y. R., Surface Properties Probed by Second-Harmonic and Sum-Frequency Generation. *Nature* **1989**, *337*, 519-525.
39. Wang, J.; Paszti, Z.; Even, M. A.; Chen, Z., Measuring Polymer Surface Ordering Differences in Air and Water by Sum Frequency Generation Vibrational Spectroscopy. *J. Am. Chem. Soc.* **2002**, 124, 7016-7023.
40. Chen; Wang, J.; Even, M. A.; ChenChen, Z., Sum Frequency Generation Vibrational Spectroscopy Studies on "Buried" Polymer/Polymer Interfaces. *Macromolecules* **2002**, 35, 8093-8097.
41. Wang, J.; Chen, C.; Buck, S. M.; Chen, Z., Molecular Chemical Structure on Poly(Methyl Methacrylate) (Pmma) Surface Studied by Sum Frequency Generation (Sfg) Vibrational Spectroscopy. *J. Phys. Chem. B* **2001**, 105, 12118-12125.
42. Chen, C.; Wang, J.; Chen, Z., Surface Restructuring Behavior of Various Types of Poly(Dimethylsiloxane) in Water Detected by Sfg. *Langmuir* **2004**, 20, 10186-10193.
43. Simpson, G. J., Nonlinear Optical Polarization Analysis in Chemistry and Biology. Cambridge University Press: Cambridge, **2017**.

Chapter 2 Probing Biological Molecule Orientation and Polymer Surface Structure at the Polymer/Solution Interface in Situ

Adapted with permission from *Langmuir* **2020**, 36 (26), 7681-7690 (Copyright 2020 American Chemical Society).

2.1 Introduction

Polymer materials have been extensively used as biomaterials in a variety of biomedical applications because of their excellent properties.[1-2] They are highly biocompatible, customizable, and/or biodegradable. Polymers are compatible to biological tissues because they have carbon-based chemistry - Many polymers and their degradation products would not present toxicity after being implanted ***in vivo***. Also, polymers are flexible and easy to fabricate into multiple shapes and three-dimensional structures, which is beneficial for cell attachment and growth.[3] As a result, polymers are promising materials used as tissue scaffolds for tissue engineering.[4] Polymers are available in a wide range of forms (films, gels, fibers, bulk solids, etc.) and properties, which can be used as drug delivery vehicles and separation membranes to collapse or swell when responding to temperature and pH.[5-7] Certain functional groups (anhydride, ester, carbonate) in polymers can be degraded by hydrolysis or enzymatic degradation. This makes polymers as ideal materials for "working" inside the body for only a period of time and then disappear without the need to have any second surgery.[8-9]

For better use as biomaterials, extensive research has been performed to modify or tailor polymer bulk and surface structures to improve their functions - e.g., by incorporating different

backbone functionalities and altering sidechains flexibility.[10-12] However, there are still many unanswered questions. Biomedical polymers are implanted materials, therefore they have extensive interactions with biological media. Knowledge about such interactions is needed for developing biomedical polymer materials with better performance. Proteins are one of the most common biological materials to adsorb onto implanted polymer materials, while peptides are commonly used as models for proteins since they have protein secondary structures. Extensive research has been carried out to understand interactions between polymers and proteins/peptides, but most of such research focused on the behavior of biological molecules.[13-23] We believe that when studying the interactions between proteins/peptides and polymers, it is also important to consider how the "soft" polymer surface structure changes during the course of biological molecule adsorption and interaction, since such changes on the polymer surface structure could greatly influence interactions between polymers and adsorbed biomolecules.

Many polymer biomaterials contain conjugated functionalities such as aromatic rings in the backbones or sidechains. Such aromatic groups could entitle polymers with better electronic properties for various biological processes such as inter-/intra-cellular synchronization and neurophysiological communication.[24] These optoelectronic and electron conductive biomaterials will facilitate the development of biomedical devices and sensors used in vivo.[25] Besides, out of the twenty naturally occurred amino acids in proteins/peptides, five contain aromatic functionality. When proteins and peptides interact with a surface, the pi-pi interaction between the aromatic functional groups in amino acids and the surface aromatic structure have been considered to be one of the major interactions.[26-30] Our previous study has revealed that pi-pi interaction can dominate in the peptide-surface interaction. For example, we found that on graphene, whether a peptide can stand up or lie down is mainly determined by the pi-pi interaction because graphene

has extensive pi electrons on the surface.[31] However, hydrophobic or charge interaction can outweigh the pi-pi interaction for some other cases when the surface lacks aromatic structure. For example, for peptides on MoS_2 (another widely studied 2D material[32-33]), pi-pi interaction does not play a significant role.[34] Instead, charged amino acids on one terminus of the peptide enable the peptide to stand up on the MoS_2 surface in water.[34] To the best of our knowledge, there is limited study on the pi-pi interactions between polymers and biological molecules like peptides and proteins and on how to control such interactions. Therefore, it is necessary to investigate how the pi-pi interaction plays a role when biological media contact with polymer surfaces with aromatic functionality.

It is challenging to probe polymer – biological molecule interactions because such interactions occur at solid/liquid interfaces. As discussed in chapter 1, SFG is a second-order nonlinear optical spectroscopic technique with sub-monolayer surface/interface selectivity, which can be applied to study molecular structures of many buried interfaces including solid/liquid interfaces.[16,-23, 31, 34-73] We have extensively applied SFG to investigate detailed structural information of interfacial biological molecules, such as proteins and peptides, while interacting with various materials[14-23, 34-52] including polymers.[19, 21, 42-45] SFG can probe the amide I signals from interfacial peptides and proteins using different polarizations of the beams and determine their orientations. Interfacial ordering and time-dependent structural changes of biological molecules on polymer surfaces have also been examined using SFG.[19, 45] In addition, we applied SFG to study polymer surface changes after protein adsorption, focusing on methyl groups.[50]

To study biological molecule – polymer interactions, in this work, we used deuterated polystyrene (d8-PS) as a model aromatic polymer, and wild-type MSI-78 and its mutant with two less aromatic amino acids as model biomolecules. In addition, wild-type cecropin–melittin hybrid

peptide (we will refer this peptide to hybrid peptide below in this thesis) and its mutants were also used as model biomolecules. The wild-type hybrid peptide and the mutants studied here have similar (but not identical) amino acid sequences, with different numbers of amino acids with aromatic groups, as presented in more detail below. SFG vibrational spectroscopy was applied to study the phenyl group orientation on the polymer surface and the peptide orientation at the polymer/peptide solution interface to understand the interfacial interactions including the pi-pi interaction.

2.2 Materials and Methods

2.2.1 Materials and Sample Preparation

All peptide samples were purchased from Peptide 2.0. The sequences of the studied peptides are: N-terminus cysteine-modified MSI-78 (MSI-78(C1)): CGIGK FLKKA KKFGK AFAKQ LKK; mutant MSI-78(C1): CGIGK FLKKA KK**A**GK A**A**AKQ LKK. Wild-type hybrid peptide: KWKLF KKIGI GAVLK VLTTG LPALI S; mutant A: KWK**F**F KKIGI GAVLK VLTTG LPALI S; mutant A2: KWK**F**F KK**F**GI GAVLK VLTTG LPALI S; and mutant B: K**A**KL**A** KKIGI GAVLK VLTTG LPALI S. All the peptide solutions used have a same concentration of 5.0 μM, prepared by dissolving the peptide in phosphate buffered saline (PBS) (pH 7.4).

In this paper, amino acids were assigned into different groups in order to better describe the effect of each part of peptides. A wild-type hybrid peptide has 26 amino acids in total (see the peptide sequence presented above), including 1 proline (with a ring structure and electron rich nitrogen in the ring – may have favorable interaction with the PS phenyl group), 1 kind of charged amino acid (K), 5 kinds of non-aromatic hydrophobic amino acids (L, I, G, A, V), 2 kinds of hydroxyl-containing hydrophilic amino acids (T, S), and 2 kinds of aromatic hydrophobic amino acids (W, F). The 9 amino acids in the N-terminus region of the hybrid peptide contain 2 aromatic

amino acids, 3 hydrophobic (non-aromatic) residues, and 4 charged residues. The number of amino acids of each type in each peptide investigated in this research is listed in **Table 2.1**.

Fully deuterated polystyrene (d8-PS, Mn=575,000, Mw/Mn=1.09) was obtained from Polymer Source, Inc. The deuterated polystyrene was used here to avoid the spectral confusion of C-H vibrational signals from the peptides. Right-angle CaF_2 prisms were purchased from Altos Photonics (Bozeman, MT).

Table 2.1 Number of amino acid of each type in each peptide investigated in this research

Peptide	Charged (K)	Hydrophilic (T, S, Q)	Hydrophobic (L, I, G, A, V, C)	Aromatic (W, F)
Hybrid	5	3	15	2
Mutant A	5	3	14	3
Mutant A2	5	3	13	4
Mutant B	5	3	17	0
MSI-78	9	1	10	3
MSI-78 mutant	9	1	12	1

CaF_2 prisms were used as substrates for d8-PS thin films for SFG studies. Before polymer film deposition, these prisms were cleaned by soaking in toluene and acetone respectively, for 10 hours and then washed with detergent and DI water multiple times. After drying with nitrogen gas, the CaF_2 prisms were exposed to air plasma treatment for 3 min. The d8-PS sample was dissolved in toluene (2.5%, w/w) and d8-PS films were prepared by spin-coating the solution at 2000 rpm for 30 seconds onto CaF_2 prisms. All the d8-PS thin films were annealed in the oven at 100℃ for three hours before SFG experiment. With this preparation condition, d8-PS films with a thickness of 165 nm were obtained (The thickness was measured by a Dektak profilometer). We chose this

thickness of the d8-PS films for study because based on our Fresnel coefficient calculation (see **Section 3.2.2.1**), at this film thickness, the SFG signal from the buried d8-PS/CaF_2 interface can be minimized. Therefore, SFG spectra collected from the d8-PS film in contact with peptide solution were only contributed by the d8-PS/peptides solution interface (See **Section 2.2.2.1**).

2.2.2 Experimental Methods

2.2.2.1 SFG Experiment

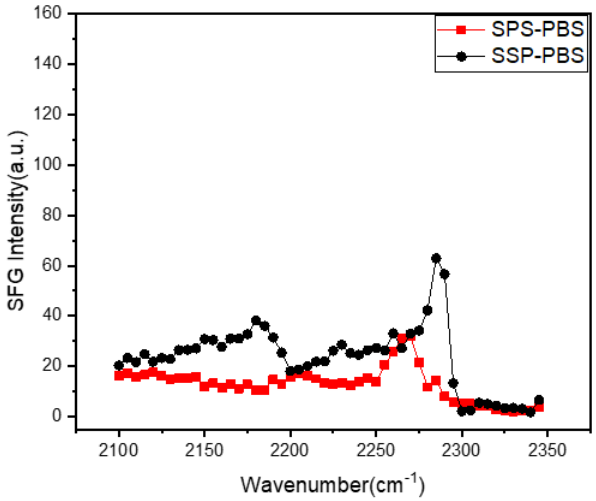

Figure 2.1 SFG ssp and sps spectra collected from the d8-PS/PBS solution interface.

For SFG experiment in this research, a peptide solution (5 μM) was placed in contact with the bottom of a CaF_2 prism (with d8-PS thin film deposited), and SFG signal was monitored as a function of time until equilibrium was reached (no further signal change). After using PBS solutions to replace the peptide solution several times in order to wash off weakly adsorbed peptides, SFG spectra were collected with different polarization combinations of the input visible, input IR, and generated SFG beams, including ssp (s-polarized SFG signal, s-polarized visible input, and p polarized input IR), ppp and sps. The SFG spectra for each sample was collected and averaged by 5 scans for each trial and 4 trials for each peptide.

SFG C-D stretching signal collected from the d8-PS/peptide solution interface may also

contain the contribution from the d8-PS/CaF_2 prism interface. To minimize the signal contribution from the d8-PS/CaF_2 interface, it is necessary to choose the optimal d8-PS film thickness. The thickness dependent Fresnel Coefficients of the d8-PS/CaF_2 interface and d8-PS/solution interfaces were calculated using the method published previously[80-82] (**Figure 2.2**). The refractive indices used in calculation are listed in **Table 2.2**. We chose 165 nm for the d8-PS film thickness in this study to minimize the signal contribution from the d8-PS/CaF_2 prism interface.

Table 2.2 Indices of refraction used in the Fresnel Coefficient calculations

	474 nm	532 nm	4366 nm, (2290 cm^{-1})
CaF_2 prism	1.44	1.44	1.40
d8-PS	1.61	1.60	1.57
Peptide solutions	1.33	1.33	1.33
CaF_2 Prism/d8-PS	1.52	1.52	1.49
d8-PS/Peptide solutions	1.48	1.47	1.45

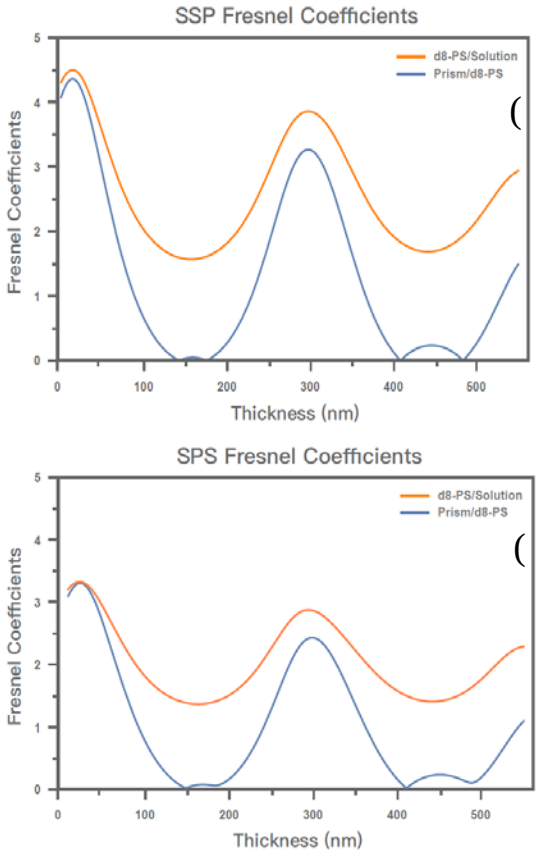

Figure 2.2 Fresnel Coefficients calculated as a function of the d8-PS film thickness for the CaF_2/d8-PS interface and the d8-PS/peptide solution interface for SSP (a) and SPS (b) spectra.

2.2.2.2 Circular Dichroism (CD) Experiment

To support the SFG amide I study, we used the Circular Dichroism (CD) spectroscopy to characterize secondary structures of various peptides adsorbed onto the d8-PS surface. The CD spectrometer applied here is a J-1500 CD spectrometer from Jasco Inc., Japan. All the CD spectra were collected by a continuous scanning mode from 190 nm to 240 nm at room temperature. The polystyrene (PS, M_w=593500, M_w/M_n=1.04) thin films were prepared by spin-coating PS solution (0.08 wt%) on high-quality quartz slides. The PS slides were placed in contact with various peptide solutions. The low concentration PS solution was used for preparing thin PS films to avoid high

UV absorbance by PS films. After peptide adsorption on PS, CD spectrum was collected at 1 nm resolution and 50 nm/min scanning rate. Each spectrum was averaged by 3 scans and 4 slides were stacked together in order to increase the signal to noise ratio.

2.3 Results and Discussion

2.3.1 Peptides Orientation

To investigate the molecular interactions between d8-PS and peptides, we studied an antimicrobial peptide, MS-78, and a mutant of MSI-78. The sequences of these two peptides were presented above in the previous section. The MSI-78 mutant studied here has two different amino acids compared to the wild-type MSI-78, with the two phenylalanine residues in MSI-78 replaced by alanine. In our previous SFG study on interactions between peptides and graphene, we found that MSI-78 lies down on the graphene surface, due to the strong pi-pi interaction between the three aromatic amino acids (Phe5, Phe12, Phe16) along the MSI-78 molecule and the pi electrons in graphene.[31] With two phenylalanine amino acids (Phe12 and Phe16) replaced by alanine, the mutant MSI-78 tilts (stands up) on the graphene surface instead of lying down.[31] Due to the reduced pi-pi interaction with graphene, the mutant MSI-78 does not need to lie down on the surface, but tilts instead. In the current research, instead of graphene, we want to study the interaction of d8-PS with MSI-78 and the MSI-78 mutant to understand whether pi-pi interaction plays a significant role in peptide – polymer interactions.

When a monolayer graphene sheet is deposited on a surface, the ring structure in graphene lies down on the surface, which enables MSI-78 on graphene to lie down on the surface as well due to the pi-pi interaction between the graphene and the MSI-78 aromatic amino acids. Before we present the SFG results on the MSI-78 interaction with d8-PS, we want to discuss whether the aromatic structure (phenyl group) on d8-PS is standing up or lying down on the surface. **Figure**

2.1 shows the SFG ssp and sps spectra collected from the d8-PS/PBS buffer solution interface in the C-D stretching frequency region. Compared to the SFG C-D stretching signals collected from the d8-PS/peptide solution interfaces which will be presented later, here SFG signals are much weaker. It was found from orientation analysis that the phenyl groups are more or less lying down on the d8-PS, which will be discussed in more detail below.

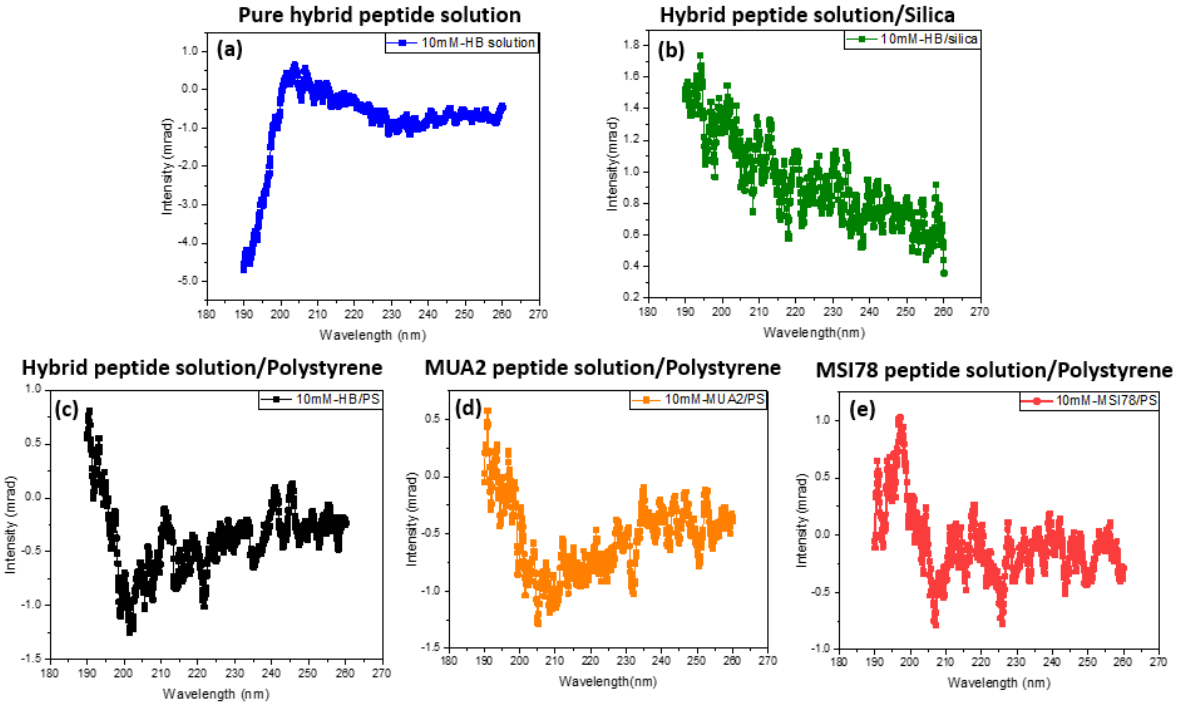

Figure 2.3 CD spectra of the wild-type hybrid peptide in PBS solution (a), the wild-type hybrid peptide on quartz (b), the wild-type hybrid peptide on PS (c), hybrid peptide mutant A2 on PS, and MSI-78 on PS.

By comparing the CD spectra in **Figure 2.3** with the CD spectrum reference of each secondary structure,[83, 84] we can identify the secondary structure of various peptides in each case. The wild type hybrid peptide has a random coil structure in the phosphate buffered saline (PBS) solution (as shown in **Figure 2.3a)**. The spectra displayed in **Figures 2.3c, d, and e** show two negative peaks at 208 nm and 222 nm, indicating that these peptides adopt alpha-helical structures on the PS surface. Differently, the spectrum in **Figure 2.3b** shows that the wild-type hybrid peptide does not

adopt an alpha-helical structure on quartz. The CD results of peptides on PS are well correlated to the SFG amide I signals presented below.

Figure 2.4 shows the SFG ssp and ppp spectra collected from the d8-PS/peptide (MSI-78 or MSI-78 mutant) solution interfaces. All the SFG spectra showed a strong amide I peak at ~1650 cm^{-1}, indicating that both peptides adopt an α-helical structure on the d8-PS surface. This conclusion matched the CD data shown above.

The observed SFG results are different from those collected from the graphene/peptide solution interfaces for MSI-78 and MSI-78 mutant.[31] MSI-78 lies down on graphene due to strong pi-pi interaction, leading to no detectable SFG amide I signal.[31] SFG amide I signal can be observed from the graphene/MSI-78 mutant solution interface because the mutation of the aromatic amino acid phenylalanine residues in MSI-78 with alanine reduced the pi-pi interaction between the MSI-78 mutant and graphene.[31] Here, SFG signals can be clearly seen from MSI-78 on d-PS, showing that MSI-78 does not lie down on the d8-PS surface. As we reported previously, using SFG amide I signal strengths detected using different polarization combinations of the input and output beams such as ppp and ssp (or χ_{ppp}/χ_{ssp} ratio), the tilt angle of the α-helical peptides versus the surface normal can be determined.[34, 48-49] According to the measured χ_{ppp}/χ_{ssp} ratio here, MSI-78 more or less stands up on the d8-PS surface, with a tilt angle of 4 degree vs. the surface normal. From the χ_{ppp}/χ_{ssp} ratio measured from the MSI-78 mutant, it was found that the MSI-mutant adopts a similar orientation compared to the wild-type MSI-78 – tilting at 11 degrees vs. the surface normal. Therefore, both MSI-78 and MSI-78 mutant stand up more or less on the d8-PS surface. Likely the pi-pi interaction does not play an important role in the peptide – d8-PS interactions for MSI-78 and MSI-78 mutant, otherwise they should adopt vastly different orientations on d-PS, with similar behavior on graphene surface.

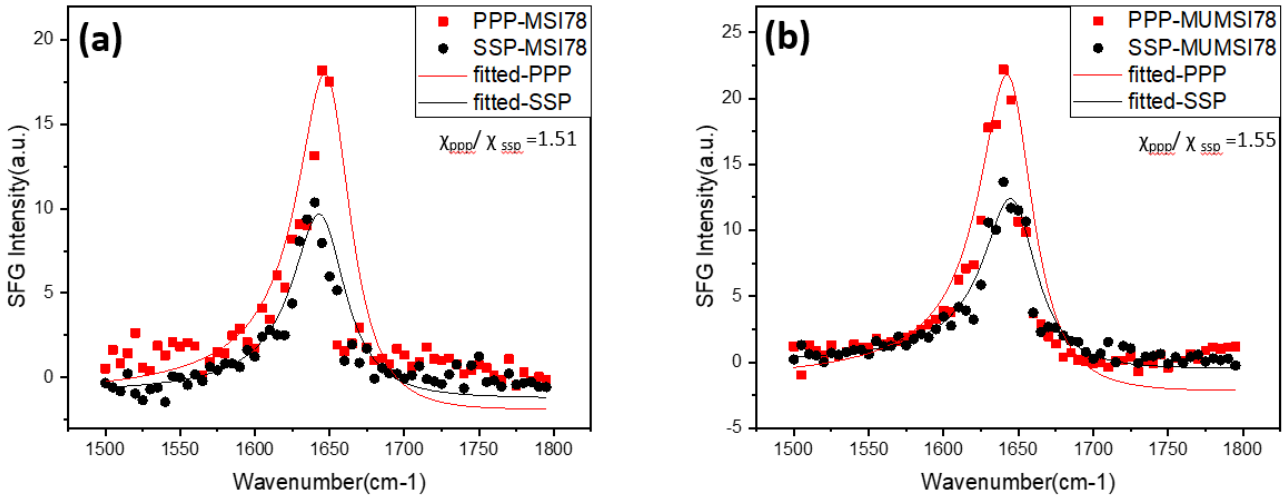

Figure 2.4 SFG ssp and ppp amide I spectra collected from the interfaces between d8-PS and solutions of the wild-type MSI-78 peptide (a) and the MSI-78 mutant (b).

To further understand the molecular interactions between peptides and d8-PS as well as the effects of pi-pi interactions, we also studied the hybrid peptide and its mutants. By studying the hybrid peptide and its mutants as models, we can well control the number of the aromatic amino acids in the peptide without varying other factors to investigate the effects of pi-pi interactions between PS and the peptides. The hybrid peptide studied here is an excellent antimicrobial peptide with better antibacterial activity and selectivity than its parental peptides. SFG ssp and ppp spectra in the amide I frequency region collected from the interfaces between d8-PS and the wild-type hybrid peptide and its mutant solutions are shown in **Figure 2.5**. Again, all the collected SFG spectra exhibit a distinct amide I peak centered at around 1650 cm^{-1}, indicating that all these peptides adopt an α-helical structure on the d8-PS surface, which was further verified by CD data presented in **Figure 2.3** above.

A wild-type hybrid peptide has 26 amino acids in total (see the peptide sequence presented above). There are 9 amino acid residues in the C-terminus region, including 1 proline (with a ring structure and electron rich nitrogen in the ring – may have favorable interaction with the PS phenyl

group), 5 non-aromatic hydrophobic amino acids, and 3 hydroxyl-containing hydrophilic amino acid residues. The 9 amino acids in the N-terminus region of the hybrid peptide contain 2 aromatic amino acids, 3 hydrophobic (non-aromatic) residues, and 4 charged residues.

In addition to the wild-type hybrid peptide, we also studied three different hybrid peptide mutants: mutant A, mutant A2 and mutant B. From the peptide sequences presented above, we know that the mutant A was mutated one non-aromatic amino acid in the wild-type hybrid peptide to aromatic amino acid and thus there is one more aromatic functionality in mutant A than the wild-type hybrid peptide. Mutant A2, which has 4 aromatic amino acids in total in the N-terminus, has 2 more aromatic residues than the wild-type hybrid peptide. Differently, the mutant B has less aromatic amino acids than the wild type hybrid peptide, and there is no aromatic residue on the N-terminus. For the C-terminus, the composition of all the three mutants are the same, and also the same as the wild-type hybrid peptide. If the pi-pi interaction plays a dominant role in the peptide - polymer surface interaction here, different peptides with different numbers of the aromatic amino acids should have different pi-pi interaction strengths with d8-PS, leading to varied peptide orientations. Therefore the stronger interaction between the peptide with more aromatic amino acids and the surface would occur, likely leading to a more tilted peptide orientation.

Figure 2.5 shows strong SFG amide I signals collected from the interfaces between the d8-PS and peptide solutions for wild-type hybrid peptide and all the three mutants, indicating that none of the peptide lies down on the d8-PS surface, regardless of the number of the aromatic amino acids in the N-terminus. The deduced χ_{ppp}/χ_{ssp} ratios from the spectral fitting parameters (**Table 2.3**) of the SFG spectra from the four peptides are similar, only varied slightly from 1.13 to 1.23 (**Figure 2.5**), showing that the peptides adopt similar orientations at the d8-PS/peptide solution interfaces. Such results demonstrate two possibilities: one is that here the pi-pi interaction does not

play a significant role, the other one is that all the peptides lie down onto the interfaces which is the special case of the first possibility. Here we believe the first case is more likely to happen. Because if all the peptides lie down on the surface the net dipole of α-helical peptides will be along with the interface, which will lead to very weak SFG signal. However, strong Amide I SFG signal can be observed here. Therefore, these results indicate different peptides adopt similar orientation but not lying down on d-PS surface. This conclusion matches the result obtained from the study on the interactions between d8-PS and MSI-78 as well as MSI-78 mutant presented above.

Our previous study showed that when the pi-pi interaction does not play an important role, charged amino acids on one terminus could enable the peptide to stand up on a hydrophobic surface.[34] For example, we showed that the hybrid peptide and the above three mutants can stand up on a 2D material MoS_2 surface at the MoS_2/peptide solution interfaces.[34] MoS_2 is different from graphene, which does not have aromatic functionality, therefore no strong pi-pi interaction exists between the peptides and the MoS_2 surface. The charged amino acid residues have more favorable interactions with water than the hydrophobic MoS_2 surface, enabling the peptides to stand up (or tilt) on the MoS_2 surface. Here likely similar situations occurred. For the wild-type hybrid peptide and all the three mutants, the more hydrophobic C-terminus interacts with the d8-PS surface, while the N-terminus interacts with water due to the favorable interactions between the charged amino acids on the N-terminus and water.

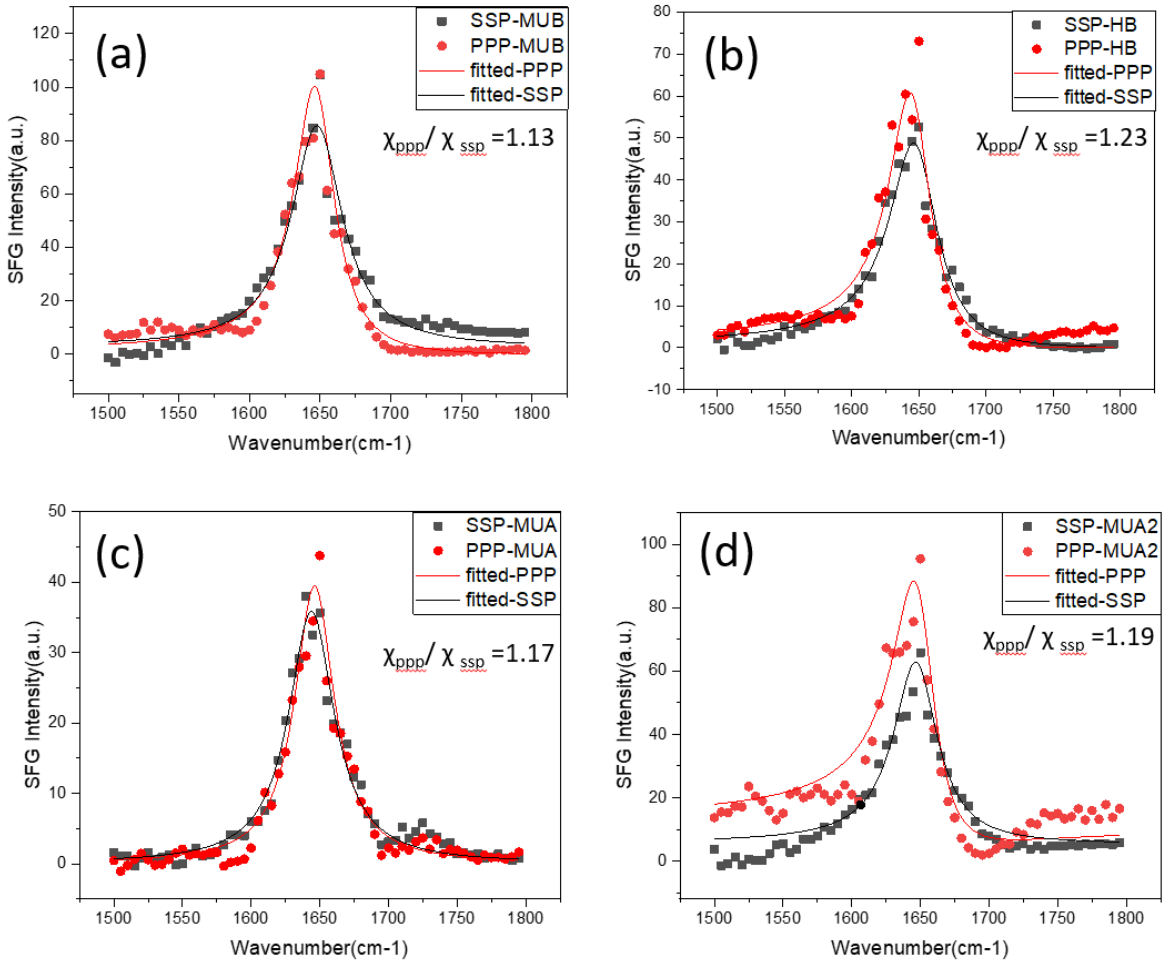

Figure 2.5 SFG ssp and ppp amide I spectra collected from the interfaces between d8-PS and solutions of mutant B (a), wild-type hybrid peptide (b), mutant A (c), and mutant A2 (d).

It is impossible to determine a tilt angle for any of the above four types of peptides at the d8-PS/peptide solution interfaces using the measured χ_{ppp}/χ_{ssp} ratios by assuming a delta or Gaussian orientation distribution, because the ratios are out of the possible range (**Figure 2.6**). One possibility is that the hybrid peptide and its three mutants studied here may not adopt a straight helical conformation. As we reported previously, the SFG orientation determination method for a bent helix is different from that for a single helix.[38] Therefore for interfacial hybrid peptide and

mutants investigated here, we cannot use the method for single helix for orientation determination. Another possibility is that even if the peptides are straight helical structures, they may adopt multiple orientations.[18, 52] Nevertheless, we do not have enough measured parameters to determine the orientation of bent helix or multiple orientations. Since the measured χ_{ppp}/χ_{ssp} ratios are more or less the same for all the four peptides, we believe that different peptides adopt similar orientations regardless of the number of aromatic amino acids in the peptide. Therefore likely the pi-pi interaction does not play a major role for the interfacial interaction occurred here.

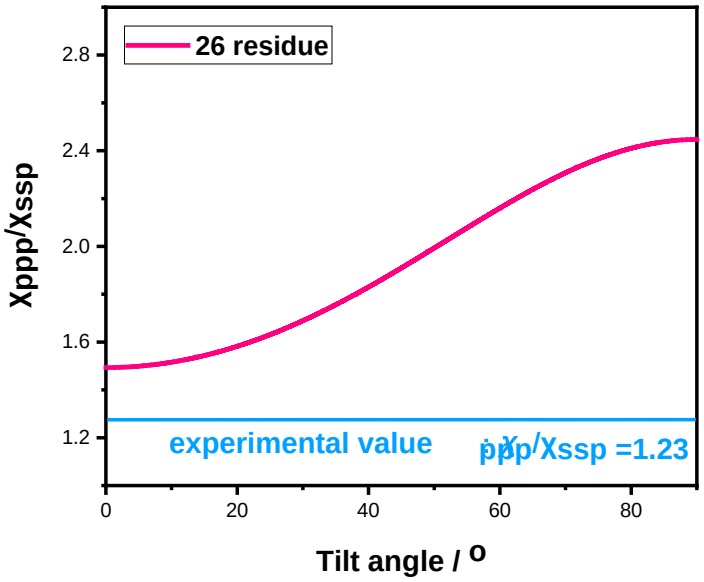

Figure 2.6 Dependence of tilt angle on the SFG amide I signal ratio χppp/χssp of an α-helical peptide with 26 amino acid residues.

Table 2.3 Amide I peak fitting parameters

	Mutant B	Hybrid	Mutant A	Mutant A2	MSI-78	MSI-78 mutant
Amplitude PPP, Aq (a.u.)	178.8	146.1	111.4	162.8	79.0	106.7
Wavenumber PPP, ωi (cm^{-1})	1647.3	1646.6	1646.1	1650.1	1650.3	1646.2
Width PPP, Γi (cm^{-1})	17.5	19.1	17.7	18.5	22.3	22.8
Amplitude SSP, Aq (a.u.)	201.3	152.5	121.9	145.5	72.4	78.2
Wavenumber SSP, ωi (cm^{-1})	1648.0	1648.1	1644.9	1647.1	1647.9	1647.5
Width SSP, Γi (cm^{-1})	22.1	22.1	20.4	19.5	22.1	21.9

The above results were corrected with the Fresnel coefficients and the detailed Fresnel coefficient calculation method has been discussed in a previous publication.[85]

2.3.2 Phenyl Group Orientation

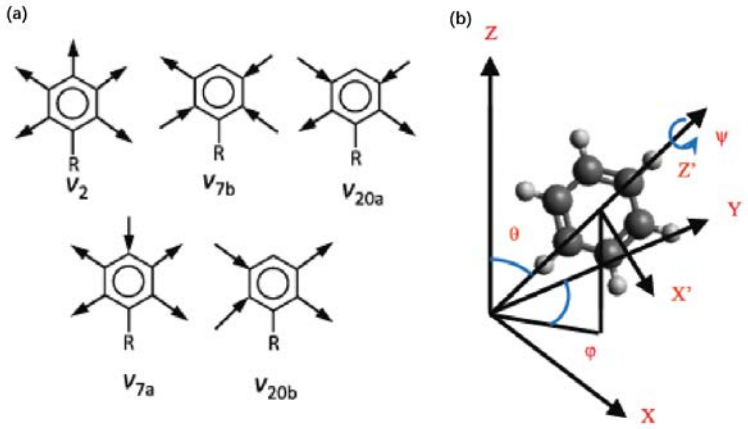

Figure 2.7 Different C-D stretching modes for phenyl group (a), tilt angle (θ) and twist angle (ψ) of a phenyl group in lab-fixed (x, y, z) coordinate system (the molecule-fixed system is (x', y', z')) (b).

As we discussed in the introduction section, upon biomolecule adsorption, the polymer surface can be restructured, as we showed previously.[50] In order to better understand the molecular interactions between polymer d8-PS and various peptides, we want to probe the surface structural

changes of d8-PS upon various peptides' adsorption, including wild-type hybrid peptide, mutants A, A2, and B. The vibrational modes of C-D stretching of a phenyl group and the phenyl orientation angle definition are shown in **Figure 2.7**. To monitor the d8-PS surface structural changes, SFG spectra were collected from the d8-PS/peptide solution interfaces in the C-D stretching frequency region, as shown in **Figure 2.8**. For comparison purpose, the SFG spectra collected from the d8-PS/PBS buffer interface are re-plotted. **Figure 2.8** shows that the SFG spectra collected from various d8-PS/peptide solution interfaces are quite similar, which are well correlated to the similar SFG amide I signals collected from different peptides on d8-PS. The d8-PS surface is mainly covered by phenyl groups, evidenced by strong SFG C-D stretching signals from the phenyl C-D stretching modes. The C-D signals from d8-PS have peaks centered at around 2265 cm^{-1}, 2275 cm^{-1}, and 2288 cm^{-1}, which can be assigned to the phenyl C-D stretching vibrational modes (**Figure 2.7**) of v_{7a}, v_{7b} and v_2, [77-78] respectively. For the PS/buffer interface, a peak at around 2175 cm^{-1} in the ssp SFG spectrum comes from the backbone CD_2 antisymmetric C-D stretching mode.[79] To quantitatively determine the orientation angles of the aromatic ring of the interfacial d8-PS molecule, SFG spectra were fitted and the fitting parameters are presented in the **Table 2.4**. However, not all the vibrational modes can provide reliable signal intensities for orientation analysis of phenyl groups. We decided to use the signal intensities of the v_2 mode for quantitative analysis. Although the orientation of a planar phenyl group is defined by a tilt and a twist angle, in this study only the tilt angle is determined. The χ_{yyz}/χ_{yzy} ratio of the v_2 vibrational mode measured in the ssp and sps spectra was used to deduce the tilt angle (by assuming the twist angle is random and can be averaged).

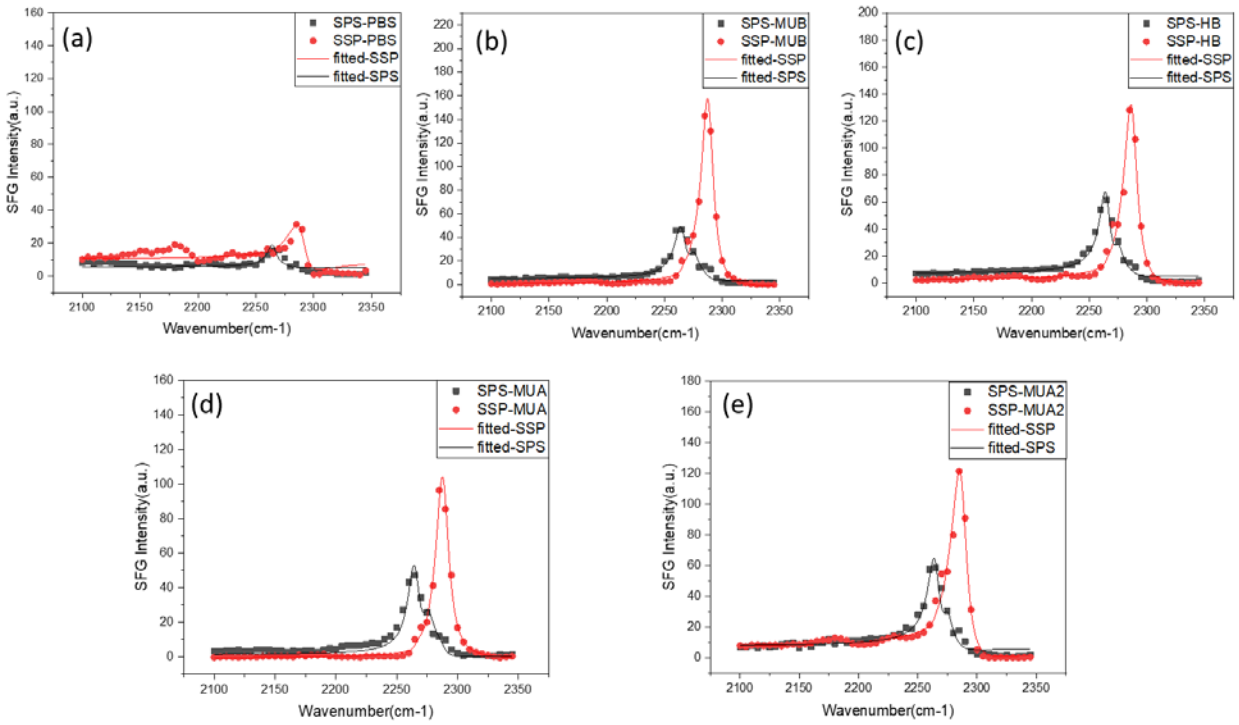

Figure 2.8 SFG ssp and sps spectra collected from the interfaces between d-PS and solutions of PBS buffer (a), mutant B (b), wild-type cecropin-melittin hybrid peptide (c), mutant A (d), and mutant A2 (e).

The phenyl group orientation analysis was reported in previous publications. [86-89] Here we will briefly discuss the tilt angle determination based on the fitting parameter listed in **Table 2.4.** To determine the tilt angle of the phenyl group on the d8-PS/solution interfaces, first it is necessary to use the Fresnel coefficient for local field correction.[90] The v_2 vibration mode belongs to the A_1 irreducible representation, the relationships between the measured χ_{zzz}, χ_{xxz}, χ_{xzx} terms and molecular hyperpolarizability components are listed below:

A_1: $$\chi_{zzz} = N(\beta_{x'x'z'} < cos\theta\ sin^2\theta\ cos^2\varphi > + \beta_{z'z'z'} < cos^3\theta >)$$

A_1: $$\chi_{xxz} = \frac{N}{8}(\beta_{x'x'z'} < cos\theta(3 + \cos 2\theta - 2sin^2\theta\ cos2\varphi) > + 4\beta_{z'z'z'} < cos\theta sin^2\theta >)$$

A_1: $$\chi_{xzx} = -\frac{N}{2}(\beta_{x'x'z'} < cos\theta\ sin^2\theta\ cos^2\varphi) > - \beta_{z'z'z'} < cos\theta sin^2\theta >) \quad (1)$$

According to the literature[91], the hyperpolarizability ratio $\rho=\beta_{z'z'z'}/\beta_{x'x'z'}$ can be obtained by density functional theory (DFT) calculation. For the v_2 vibrational mode, the value of ρ is equal to 1.13. From the fitting parameters of the SFG spectra, we can deduce χ_{xxz} and χ_{xzx}. For the v_2 mode and after averaging the twist angle, we have:

$$\frac{\chi_{xxz,v2}}{\chi_{xzx,v2}} = \frac{9.83\ cos\theta - cos3\theta}{cos\theta - cos3\theta} \quad (2)$$

After considering the Fresnel Coefficients, we can convert equation (2) into equation (3)

$$\frac{\chi_{eff,ssp,v2}}{\chi_{eff,sps,v2}} = 0.81 * \frac{9.83\ cos\theta - cos3\theta}{cos\theta - cos3\theta} \quad (3)$$

Figure 2.9 shows that the tilt angle of the phenyl groups at the d8-PS/peptide solution interfaces falls in a narrow range for various peptides. The tilt angles are 44°, 51°, 52°, and 47°, respectively, at the interfaces between d8-PS and solutions of mutant B, wild-type hybrid peptide, mutant A, and mutant A2. With increased number of aromatic amino acids of the peptides on d8-PS, the tilt angle of phenyl groups does not change substantially, indicating that the number of the peptide aromatic residues is irrelevant to the interaction between the hybrid peptide or its mutants and d8-PS. This result is consistent with that obtained from the peptide orientation analysis presented above. Also as we stated above, the much weaker SFG signals collected from the d8-PS/PBS buffer interface compared to those of the d8-PS/peptide solution interfaces indicated that the phenyl groups more or less lie down at the d8-PS/buffer interface. Here we quantitatively deduced the phenyl group orientation at the d8-PS/buffer solution interface. It was found that the phenyl tilt angle at this interface is 68° versus the surface normal, indicating that the phenyl rings

lie down more towards the interface compared to those at the polymer/peptide solution interfaces.

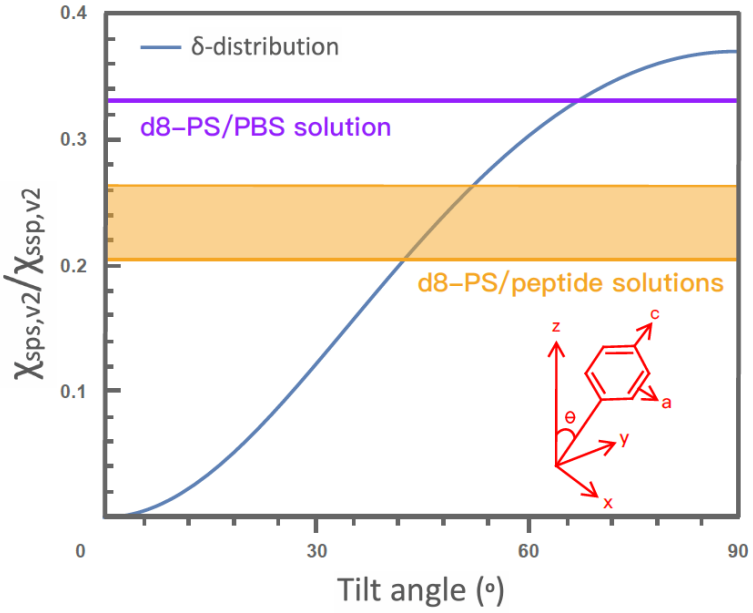

Figure 2.9 $\chi_{ssp,v2}/\chi_{sps,v2}$ ratio as a function of phenyl group tilt angle (assuming a δ-distribution of orientation)

Table 2.4 Phenyl group C-D stretching vibrational peak fitting parameters.

PBS-SSP			**PBS-SPS**			
ωi (cm$^-$	Γi (cm$^-$	Aq	ωi (cm$^-$	Γi (cm$^-$	Aq (a.u.)	assignme
2265	5	-1	2265	5	-17	v7a
2275	5	-1.1	2273	5	-3	V7b
2290	7.7	29.8	2288	7.2	9.4	v2
Mutant B-SSP			**Mutant B-SPS**			
ωi (cm$^-$	Γi (cm$^-$	Aq	ωi (cm$^-$	Γi (cm$^-$	Aq (a.u.)	assignme
2265	5.2	-4.1	2265	6.1	-36	v7a
2273	5	-3	2275	5.2	-17.5	V7b
2288	6.3	78.5	2288	7.1	18	v2
Hybrid-SSP			**Hybrid-SPS**			
ωi (cm$^-$	Γi (cm$^-$	Aq	ωi (cm$^-$	Γi (cm$^-$	Aq (a.u.)	assignme
2268	5.4	-3.3	2268	5.7	-39.8	v7a
2273	5	-2.9	2275	5.2	-17.5	V7b
2288	6.8	77.6	2288	6.9	20.3	v2
Mutant A-SSP			**Mutant A-SPS**			
ωi (cm$^-$	Γi (cm$^-$	Aq	ωi (cm$^-$	Γi (cm$^-$	Aq (a.u.)	assignme
2268	5	-3.3	2265	6	-40.4	v7a
2275	5	-2.5	2275	5	-15.1	V7b

2288	6.4	65.7	2288	7	20.2	v2
Mutant A2-SSP			**Mutant A2-SPS**			
ωi (cm^{-}	Γi (cm^{-}	Aq	ωi (cm^{-}	Γi (cm^{-}	Aq (a.u.)	assignme
2265	5.6	-3.5	2265	6	-40	v7a
2273	5	-2.8	2275	5.2	-18	V7b
2287	7.4	77.9	2288	7.1	18	v2
MSI78-SSP			**MSI78-SPS**			
ωi (cm^{-}	Γi (cm^{-}	Aq	ωi (cm^{-}	Γi (cm^{-}	Aq (a.u.)	assignme
2265	5.6	-1.4	2267	5.6	-17.2	v7a
2275	5.2	-3.1	2275	5.1	-6.3	V7b
2290	7.4	34.3	2290	7.5	9.6	v2
MUMSI78-SSP			**MUMSI78-SPS**			
ωi (cm^{-}	Γi (cm^{-}	Aq	ωi (cm^{-}	Γi (cm^{-}	Aq (a.u.)	assignme
2267	5.6	-1.2	2265	5.6	-15.0	v7a
2275	5.1	-2.1	2275	5	-10.2	V7b
2290	7.5	33.5	2290	7.4	10.3	v2

The similar SFG spectra collected from the various d8-PS/peptide solution interfaces in the C-D stretching frequency region led to similar polymer surface structure while in contact with different peptides, further confirming the similar interactions between d8-PS and peptides with different numbers of the aromatic amino acids. This shows that the pi-pi interaction does not play a major role here for the interactions between d8-PS and peptides. This conclusion is consistent with that obtained from SFG studies in the amide I frequency region above. This is very different from the interactions between graphene and peptides,[31] but more similar to those between MoS_2 and peptides.[34] As we reported, for MoS_2 – peptide interactions, charged amino acids on a peptide terminal are important to ensure that the peptide would not lie down on the surface. Here the wild-type hybrid peptide and the three mutants investigated all have multiple charged amino acids on the N-terminus, therefore SFG amide I signals were detected from all the peptides on d8-PS, because these peptides do not lie down at the interface.

To further verify this conclusion, we also collected the C-D stretching spectra from the d8-PS/MSI-78 and d8-PS/MSI-78 mutant solution interfaces (**Figure 2.10**) to examine whether the

pi-pi interaction is the dominant interaction between peptides and the d8-PS surface. Similar to the results obtained from the hybrid peptide and its mutants presented above, the SFG spectra collected from these two interfaces in **Figure 2.10** are very similar, which is consistent with the results acquired from the SFG study of the two peptides in the amide I frequency region. Using the spectra fitting results, the tilt angles of the phenyl ring at the d8-PS/MSI-78 and d8-PS/MSI-78 mutant solution interfaces were deduced to be 52^{o} and 54^{o}, respectively. Again, the increased number of the aromatic amino acids did not substantially change the interfacial molecular structure of the phenyl group on d8-PS, showing that the pi-pi interaction is not the dominating interaction between the peptide and PS surface, otherwise the PS phenyl orientation should be different when interacting with peptides of different amino acid numbers.

As we discussed above, the aromatic phenyl ring tilts towards the d8-PS surface at the polymer/PBS solution interface. This is because water is hydrophilic, while d8-PS is hydrophobic, the unfavorable interaction between water and polymer pushes phenyl groups to lie down more. This is similar to the methyl groups in air and in water on a polymer surface, as we reported previously.[51] After peptides were adsorbed, the d8-PS phenyl groups stand up more, due to the peptide - polymer interaction. Peptides have hydrophobic amino acids - they are much more hydrophobic than water. The hydrophobic interactions between the peptide and polymer enable the aromatic phenyl groups to orient more towards the peptides, leading to more standing-up orientation and stronger SFG C-D stretching signals.

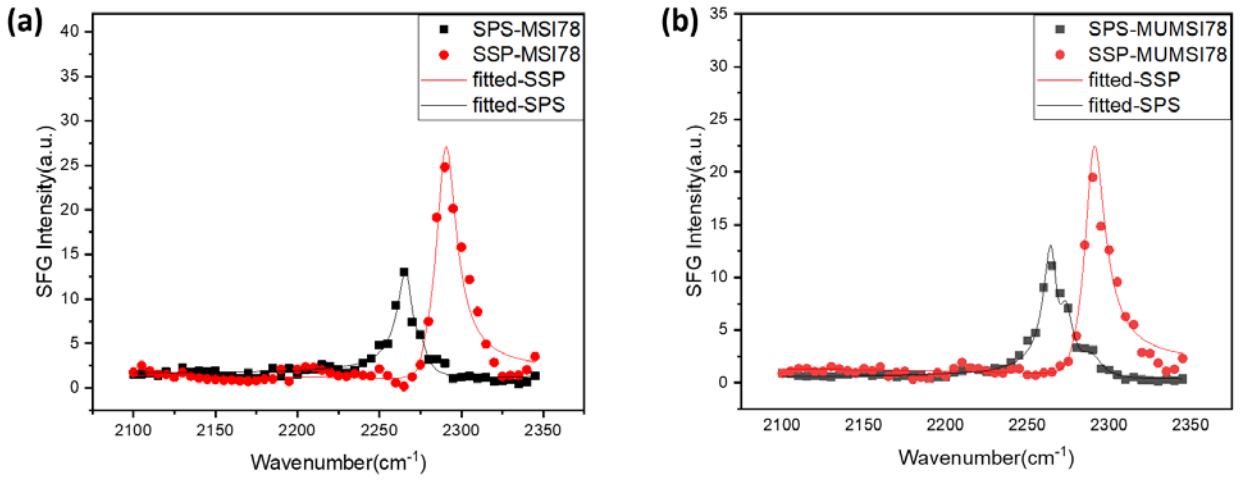

Figure 2.10 SFG ssp and sps spectra collected from the interfaces between d-PS and solutions of MSI78 peptide (a), and MUMSI78 peptide (b).

2.4 Conclusion

In this study, we applied SFG to investigate molecular interactions between biological molecules and polymer surfaces in situ. Various peptides with different numbers of aromatic amino acids were used as models for biological molecules, and d8-PS surface was served as a model for polymer surfaces.

Interactions between d8-PS and MSI-78 as well as its mutant with two less aromatic amino acids were investigated. It was found that the two peptides adopt similar orientations at the d8-PS/peptide solution interfaces, which indicates that the pi-pi interaction does not play a major role in determining peptide – d8-PS interactions, otherwise the peptides should adopt different orientations, as what was observed on a graphene surface.[31]

SFG studies on hybrid peptide and three mutants with different numbers of aromatic amino acid residues show that all the peptides adopt a similar orientation on d8-PS surface, regardless of the aromatic amino acid number in the peptide. This is again different from the peptide - graphene

interaction, where the number of the aromatic amino acids influences the peptide orientation due to the fact that the pi-pi interaction dominates the interfacial interactions. The observations from these four peptides at the d8-PS/peptide solution interfaces are similar to those from the MoS_2/peptide solution interfaces, where the pi-pi interaction is not important. We believe that on the d8-PS surface, the pi-pi interaction does not play an important role, which is well correlated to the results obtained from the studies on the interactions between d8-PS and MSI-78 as well as the MSI-78 mutant.

SFG studies on the phenyl orientation on the d8-PS surface while in contact with various peptide solutions in the C-D stretching frequency region produced compatible results to the above SFG amide I studies on interfacial peptides. Phenyl orientations on the d8-PS surface while contacting peptides with different numbers of aromatic amino acids are similar, showing that the pi-pi interaction between the surface phenyl group and the peptide aromatic groups are not dominating.

Molecular interactions between polymer surfaces and biological molecules are important for many applications involving biomedical polymers, antifouling polymer coatings, polymer membranes for bio-separation, and surface immobilized proteins or peptides for biosensing. SFG is a powerful tool to probe such interactions at buried solid/liquid interfaces in situ at the molecular level. The knowledge obtained from such studies helps the development of polymers with improved performance.

2.5 References

1. Thomas, S.; Balakrishnan, P.; Sreekala, M. S., Fundamental Biomaterials: Ceramics. **2018**, 1-20.
2. Tanzi, M. C.; Farè, S., Characterization of Polymeric Biomaterials. **2017**, 38-51.
3. Hutmacher, D. W., Scaffolds in tissue engineering bone and cartilage. *Biomaterials* **2000**, 21 (24), 2529-2543.

4. Landry, M. J.; Rollet, F. d. r.-G.; Kennedy, T. E.; Barrett, C. J., Layers and multilayers of self-assembled polymers: tunable engineered extracellular matrix coatings for neural cell growth. *Langmuir* **2018**, 34 (30), 8709-8730.
5. Kumar, A.; Srivastava, A.; Galaev, I. Y.; Mattiasson, B., Smart polymers: physical forms and bioengineering applications. *Prog. Polym. Sci.* **2007**, 32 (10), 1205-1237.
6. Bromberg, L. E.; Ron, E. S., Temperature-responsive gels and thermogelling polymer matrices for protein and peptide delivery. *Adv. Drug Delivery Rev.* **1998**, 31 (3), 197-221.
7. Stamatialis, D. F.; Papenburg, B. J.; Girones, M.; Saiful, S.; Bettahalli, S. N.; Schmitmeier, S.; Wessling, M. J., Medical applications of membranes: drug delivery, artificial organs and tissue engineering. *J. Membr. Sci.* **2008**, 308 (1-2), 1-34.
8. Vroman, I.; Tighzert, L., *Biodegradable polymers. Materials* **2009**, 2 (2), 307-344.
9. Nair, L. S.; Laurencin, C. T., Biodegradable polymers as biomaterials. *Prog. Polym. Sci.* **2007**, 32 (8-9), 762-798.
10. Huang, J.; Xiao, S.; Unger, M. A., Polymer surface modification. U.S. Patent No. 7,368,163. 6 May 2008.
11. Green, J. J.; Elisseeff, J. H., Mimicking biological functionality with polymers for biomedical applications. *Nature* **2016**, 540 (7633), 386-394.
12. Carter, S.; Rimmer, S.; Sturdy, A.; Webb, M., Highly branched stimuli responsive poly [(N-isopropyl acrylamide)-co-(1, 2-propandiol-3-methacrylate)]s with protein binding functionality. *Macromol. Biosci.* **2005**, 5 (5), 373-378.
13. Weidner, T.; Breen, N. F.; Li, K.; Drobny, G. P.; Castner, D. G., Sum frequency generation and solid-state NMR study of the structure, orientation, and dynamics of polystyrene-adsorbed peptides. *Proc. Natl. Acad. Sci.* **2010**, 107 (30), 13288-13293.
14. Wang, J.; Chen, X.; Clarke, M. L.; Chen, Z., Detection of chiral sum frequency generation vibrational spectra of proteins and peptides at interfaces in situ. *Proc. Natl. Acad. Sci.* **2005**, 102 (14), 4978-4983.
15. Chen, X.; Wang, J.; Sniadecki, J. J.; Even, M. A.; Chen, Z., Probing α-helical and β-sheet structures of peptides at solid/liquid interfaces with SFG. *Langmuir* **2005**, 21 (7), 2662-2664.
16. Chen, X.; Chen, Z., SFG studies on interactions between antimicrobial peptides and supported lipid bilayers. Biochim. *Biophys. Acta, Biomembr.* **2006**, 1758 (9), 1257-1273.
17. Chen, X.; Boughton, A. P.; Tesmer, J. J.; Chen, Z., In situ investigation of heterotrimeric G protein βγ subunit binding and orientation on membrane bilayers. *J. Am. Chem. Soc.* **2007**, 129 (42), 12658-12659.
18. Chen, X.; Wang, J.; Boughton, A. P.; Kristalyn, C. B.; Chen, Z., Multiple orientation of melittin inside a single lipid bilayer determined by combined vibrational spectroscopic studies. *J. Am. Chem. Soc.* **2007**, 129 (5), 1420-1427.
19. Clarke, M. L.; Wang, J.; Chen, Z., Conformational changes of fibrinogen after adsorption. *J. Phys. Chem. B* **2005**, 109 (46), 22027-22035.
20. Wang, J.; Even, M. A.; Chen, X.; Schmaier, A. H.; Waite, J. H.; Chen, Z., Detection of amide I signals of interfacial proteins in situ using SFG. *J. Am. Chem. Soc.* **2003**, 125 (33), 9914-9915.
21. Wang, J.; Clarke, M. L.; Chen, X.; Even, M. A.; Johnson, W. C.; Chen, Z., Molecular studies on protein conformations at polymer/liquid interfaces using sum frequency generation vibrational spectroscopy. *Surf. Sci.* **2005**, 587 (1-2), 1-11.

22. Wang, J.; Paszti, Z.; Clarke, M. L.; Chen, X.; Chen, Z., Deduction of structural information of interfacial proteins by combined vibrational spectroscopic methods. *J. Phys. Chem. B* **2007**, 111 (21), 6088-6095.
23. Wang, J.; Lee, S.-H.; Chen, Z., Quantifying the ordering of adsorbed proteins in situ. *J. Phys. Chem. B* **2008**, 112 (7), 2281-2290.
24. Deng, M.; Nair, L. S.; Nukavarapu, S. P.; Kumbar, S. G.; Jiang, T.; Krogman, N. R.; Singh, A.; Allcock, H. R.; Laurencin, C. T., Miscibility and in vitro osteocompatibility of biodegradable blends of poly [(ethyl alanato)(p-phenyl phenoxy) phosphazene] and poly (lactic acid-glycolic acid). *Biomaterials* **2008**, 29 (3), 337-349.
25. Muskovich, M.; Bettinger, C. J., Biomaterials‐based electronics: polymers and interfaces for biology and medicine. *Adv. Healthcare Mater.* **2012**, 1 (3), 248-266.
26. Flocco, M. M.; Mowbray, S. L. J., Planar stacking interactions of arginine and aromatic side-chains in proteins. *J. Mol. Biol.* **1994**, 235 (2), 709-717.
27. Hughes, Z. E.; Tomásio, S. M.; Walsh, T. R., Efficient simulations of the aqueous bio-interface of graphitic nanostructures with a polarisable model. *Nanoscale* **2014**, 6 (10), 5438-5448.
28. Duan, G.; Smith, V. H.; Weaver, D. F., Characterization of aromatic− amide (side-chain) interactions in proteins through systematic ab initio calculations and data mining analyses. *J. Phys. Chem. A* **2000**, 104 (19), 4521-4532.
29. Tóth, G.; Murphy, R. F.; Lovas, S., Stabilization of local structures by π–CH and aromatic–backbone amide interactions involving prolyl and aromatic residues. *Protein Eng.* **2001**, 14 (8), 543-547.
30. Burley, S.; Petsko, G. A., Aromatic-aromatic interaction: a mechanism of protein structure stabilization. *Science* **1985**, 229 (4708), 23-28.
31. Zou, X.; Wei, S.; Jasensky, J.; Xiao, M.; Wang, Q.; Brooks III, C. L.; Chen, Z., Molecular interactions between graphene and biological molecules. *J. Am. Chem. Soc.* **2017**, 139 (5), 1928-1936.
32. Li, H.; Li, Y.; Aljarb, A.; Shi, Y.; Li, L. J., Epitaxial growth of two-dimensional layered transition-metal dichalcogenides: growth mechanism, controllability, and scalability. *Chem. Rev.* **2017**, 118 (13), 6134-6150.
33. Cai, Z.; Liu, B.; Zou, X.; Cheng, H. M., Chemical vapor deposition growth and applications of two-dimensional materials and their heterostructures. *Chem. Rev.* **2018**, 118 (13), 6091-6133.
34. Xiao, M.; Wei, S.; Li, Y.; Jasensky, J.; Chen, J.; Brooks, C. L.; Chen, Z., Molecular interactions between single layered MoS 2 and biological molecules. *Chem. Sci.* **2018**, 9 (7), 1769-1773.
35. Ye, S.; Nguyen, K. T.; Le Clair, S. V.; Chen, Z., In situ molecular level studies on membrane related peptides and proteins in real time using sum frequency generation vibrational spectroscopy. *J. Struct. Biol.* **2009**, 168 (1), 61-77.
36. Ding, B.; Chen, Z., Molecular interactions between cell penetrating peptide Pep-1 and model cell membranes. *J. Phys. Chem. B* **2012**, 116 (8), 2545-2552.
37. Thennarasu, S.; Huang, R.; Lee, D.-K.; Yang, P.; Maloy, L.; Chen, Z.; Ramamoorthy, A. J. B., Limiting an antimicrobial peptide to the lipid− water interface enhances its bacterial membrane selectivity: a case study of MSI-367. *Biochemistry* **2010**, 49 (50), 10595-10605.
38. Ding, B.; Soblosky, L.; Nguyen, K.; Geng, J.; Yu, X.; Ramamoorthy, A.; Chen, Z., Physiologically-relevant modes of membrane interactions by the human antimicrobial peptide, LL-37, revealed by SFG experiments. *Sci. Rep.* **2013**, 3 (1), 1-8.

39. Ding, B.; Jasensky, J.; Li, Y.; Chen, Z., Engineering and characterization of peptides and proteins at surfaces and interfaces: a case study in surface-sensitive vibrational spectroscopy. *Acc. Chem. Res.* **2016**, 49 (6), 1149-1157.
40. Ding, B.; Panahi, A.; Ho, J.-J.; Laaser, J. E.; Brooks III, C. L.; Zanni, M. T.; Chen, Z., Probing site-specific structural information of peptides at model membrane interface in situ. *J. Am. Chem. Soc.* **2015**, 137 (32), 10190-10198.
41. Soblosky, L.; Ramamoorthy, A.; Chen, Z., lipids, p. o., Membrane interaction of antimicrobial peptides using E. coli lipid extract as model bacterial cell membranes and SFG spectroscopy. *Chem. Phys. Lipids* **2015**, 187, 20-33.
42. Chen, Z.; Ward, R.; Tian, Y.; Malizia, F.; Gracias, D. H.; Shen, Y.; Somorjai, G. A., Interaction of fibrinogen with surfaces of end-group-modified polyurethanes: A surface-specific sum-frequency-generation vibrational spectroscopy study. *Biomaterials* **2002**, 62 (2), 254-264.
43. Liu, Y.; Jasensky, J.; Chen, Z., Molecular interactions of proteins and peptides at interfaces studied by sum frequency generation vibrational spectroscopy. *Langmuir* **2012**, 28 (4), 2113-2121.
44. Leng, C.; Hung, H.-C.; Sun, S.; Wang, D.; Li, Y.; Jiang, S.; Chen, Z., interfaces, Probing the surface hydration of nonfouling zwitterionic and PEG materials in contact with proteins. *ACS Appl. Mater. Interfaces* **2015**, 7 (30), 16881-16888.
45. Wang, J.; Chen, X.; Clarke, M. L.; Chen, Z., Vibrational spectroscopic studies on fibrinogen adsorption at polystyrene/protein solution interfaces: hydrophobic side chain and secondary structure changes. *J. Phys. Chem. B* **2006**, 110 (10), 5017-5024.
46. Nguyen, K. T.; Le Clair, S. V.; Ye, S.; Chen, Z., Molecular interactions between magainin 2 and model membranes in situ. *J. Phys. Chem. B* **2009**, 113 (36), 12358-12363.
47. Han, X.; Liu, Y.; Wu, F.-G.; Jansensky, J.; Kim, T.; Wang, Z.; Brooks III, C. L.; Wu, J.; Xi, C.; Mello, C. M., Different interfacial behaviors of peptides chemically immobilized on surfaces with different linker lengths and via different termini. *J. Phys. Chem. B* 2**014**, 118 (11), 2904-2912.
48. Nguyen, K. T.; Le Clair, S. V.; Ye, S.; Chen, Z., Orientation determination of protein helical secondary structures using linear and nonlinear vibrational spectroscopy. *J. Phys. Chem. B* **2009**, 113 (36), 12169-12180.
49. Ye, S.; Nguyen, K. T.; Boughton, A. P.; Mello, C. M.; Chen, Z., Orientation difference of chemically immobilized and physically adsorbed biological molecules on polymers detected at the solid/liquid interfaces in situ. *Langmuir* **2010**, 26 (9), 6471-6477.
50. Clarke, M. L.; Chen, Z., Polymer surface reorientation after protein adsorption. *Langmuir* **2006**, 22 (21), 8627-8630.
51. Wang, J.; Paszti, Z.; Even, M. A.; Chen, Z., Measuring polymer surface ordering differences in air and water by sum frequency generation vibrational spectroscopy. *J. Am. Chem. Soc.* **2002**, 124 (24), 7016-7023.
52. Yang, P.; Ramamoorthy, A.; Chen, Z., Membrane orientation of MSI-78 measured by sum frequency generation vibrational spectroscopy. *Langmuir* **2011**, 27 (12), 7760-7767.
53. Shen, Y. R., Phase-sensitive sum-frequency spectroscopy. *Annu. Rev. Phys. Chem.* **2013**, 64, 129-150.
54. Gracias, D.; Chen, Z.; Shen, Y. R.; Somorjai, G. A., Molecular characterization of polymer and polymer blend surfaces. Combined sum frequency generation surface vibrational spectroscopy and scanning force microscopy studies. *Acc. Chem. Res.* **1999**, 32 (11), 930-940.
55. Gopalakrishnan, S.; Liu, D.; Allen, H. C.; Kuo, M.; Shultz, M. J., Vibrational spectroscopic studies of aqueous interfaces: salts, acids, bases, and nanodrops. *Chem. Rev.* **2006**, 106 (4), 1155-1175.

56. Wang, Z.; Fu, L.; Yan, E. C., C–H stretch for probing kinetics of self-assembly into macromolecular chiral structures at interfaces by chiral sum frequency generation spectroscopy. *Langmuir* **2013**, 29 (12), 4077-4083.
57. Sagle, L. B.; Cimatu, K.; Litosh, V. A.; Liu, Y.; Flores, S. C.; Chen, X.; Yu, B.; Cremer, P. S., Methyl groups of trimethylamine N-oxide orient away from hydrophobic interfaces. *J. Am. Chem. Soc.* **2011**, 133 (46), 18707-18712.
58. Malyk, S.; Shalhout, F. Y.; O'Leary, L. E.; Lewis, N. S.; Benderskii, A. V., Vibrational sum frequency spectroscopic investigation of the azimuthal anisotropy and rotational dynamics of methyl-terminated silicon (111) surfaces. *J. Phys. Chem. C* **2013**, 117 (2), 935-944.
59. Li, Q.; Hua, R.; Cheah, I. J.; Chou, K. C., Surface structure relaxation of poly (methyl methacrylate). *J. Phys. Chem. B* **2008**, 112 (3), 694-697.
60. Perry, A.; Neipert, C.; Space, B.; Moore, P. B., Theoretical modeling of interface specific vibrational spectroscopy: Methods and applications to aqueous interfaces. *Chem. Rev.* **2006**, 106 (4), 1234-1258.
61. Premadasa, U. I.; Moradighadi, N.; Kotturi, K.; Nonkumwong, J.; Khan, M. R.; Singer, M.; Masson, E.; Cimatu, K. L., Solvent isotopic effects on a surfactant headgroup at the air–liquid interface. *J. Phys. Chem. C* **2018**, 122 (28), 16079-16085.
62. Wang, F.; Li, X.; Zhang, F.; Liu, X.; Hu, P.; Beke-Somfai, T.; Lu, X., Revealing interfacial lipid hydrolysis catalyzed by phospholipase A1 at molecular level via sum frequency generation vibrational spectroscopy and fluorescence microscopy. *Langmuir* **2019**, 35 (39), 12831-12838.
63. Richmond, G. L., Molecular bonding and interactions at aqueous surfaces as probed by vibrational sum frequency spectroscopy. *Chem. Rev.* **2002**, 102 (8), 2693-2724.
64. Chen, Z.; Shen, Y.; Somorjai, G. A., Studies of polymer surfaces by sum frequency generation vibrational spectroscopy. *Annu. Rev. Phys. Chem.* **2002**, 53 (1), 437-465.
65. Lu, X.; Zhang, C.; Ulrich, N.; Xiao, M.; Ma, Y.-H.; Chen, Z., Studying polymer surfaces and interfaces with sum frequency generation vibrational spectroscopy. *Anal. Chem.* **2017**, 89 (1), 466-489.
66. Li, X.; Ma, L.; Lu, X., Calcium ions affect water molecular structures surrounding an oligonucleotide duplex as revealed by sum frequency generation vibrational spectroscopy. *Langmuir* **2018**, 34 (49), 14774-14779.
67. Han, X.; Leng, C.; Shao, Q.; Jiang, S.; Chen, Z., Absolute orientations of water molecules at zwitterionic polymer interfaces and interfacial dynamics after salt exposure. *Langmuir* **2018**, 35 (5), 1327-1334.
68. Xiao, M.; Jasensky, J.; Gerszberg, J.; Chen, J.; Tian, J.; Lin, T.; Lu, T.; Lahann, J.; Chen, Z., Chemically immobilized antimicrobial peptide on polymer and self-assembled monolayer substrates. *Langmuir* **2018**, 34 (43), 12889-12896.
69. Jasensky, J.; Ferguson, K.; Baria, M.; Zou, X.; McGinnis, R.; Kaneshiro, A.; Badieyan, S.; Wei, S.; Marsh, E. N. G.; Chen, Z., Simultaneous observation of the orientation and activity of surface-immobilized enzymes. *Langmuir* **2018**, 34 (31), 9133-9140.
70. Leng, C.; Huang, H.; Zhang, K.; Hung, H.-C.; Xu, Y.; Li, Y.; Jiang, S.; Chen, Z., Effect of surface hydration on antifouling properties of mixed charged polymers. *Langmuir* **2018**, 34 (22), 6538-6545.
71. Xiao, M.; Mohler, C.; Tucker, C.; Walther, B.; Lu, X.; Chen, Z., Structures and adhesion properties at polyethylene/silica and polyethylene/nylon interfaces. *Langmuir* **2018**, 34 (21), 6194-6204.

72. Xiao, M.; Jasensky, J.; Foster, L.; Kuroda, K.; Chen, Z., Monitoring antimicrobial mechanisms of surface-immobilized peptides in situ. *Langmuir* **2018**, 34 (5), 2057-2062.
73. Han, X.; Zheng, J.; Lin, F.; Kuroda, K.; Chen, Z., Interactions between Surface-Immobilized Antimicrobial Peptides and Model Bacterial Cell Membranes. *Langmuir* **2018**, 34 (1), 512-520.
74. Hung, K.-K.; Stege, U.; Hore, D. K., IR absorption, raman scattering, and IR-Vis sum-frequency generation spectroscopy as quantitative probes of surface structure. *Appl. Spectrosc. Rev.* **2015**, 50 (4), 351-376.
75. Wang, H. F.; Gan, W.; Lu, R.; Rao, Y.; Wu, B. H., Quantitative spectral and orientational analysis in surface sum frequency generation vibrational spectroscopy (SFG-VS). *Int. Rev. Phys. Chem.* **2005**, 24 (2), 191-256.
76. Shen, Y. R., Surface properties probed by second-harmonic and sum-frequency generation. *Nature* **1989,** 337 (6207), 519-525.
77. Ulrich, N. W.; Li, X.; Myers, J. N.; Williamson, J.; Lu, X.; Chen, Z., Packaging; Technology, M., Distinct molecular structures of edge and middle positions of plasma treated covered polymer film surfaces relevant in the microelectronics industry. *IEEE Trans. Compon., Packag., Manuf. Technol.* **2017**, 7 (8), 1377-1390.
78. Briggman, K. A.; Stephenson, J. C.; Wallace, W. E.; Richter, L. J., Absolute molecular orientational distribution of the polystyrene surface. *J. Phys. Chem. B* 2001, 105 (14), 2785-2791.
79. Yang, C. S.-C.; Wilson, P. T.; Richter, L. J., Structure of polystyrene at the interface with various liquids. *Macromolecules* **2004**, 37 (20), 7742-7746.
80. Kristalyn, C. B.; Lu, X. L.; Weinman, C. J.; Ober, C. K.; Kramer, E. J.; Chen, Z., Surface Structures of an Amphiphilic Tri-Block Copolymer in Air and in Water Probed Using Sum Frequency Generation Vibrational Spectroscopy. *Langmuir* **2010,** *26* (13), 11337-11343.
81. Lu, X.; Shephard, N.; Han, J.; Xue, G.; Chen, Z., Probing molecular structures of polymer/metal interfaces by sum frequency generation vibrational spectroscopy. *Macromolecules* **2008,** *41* (22), 8770-8777.
82. Shen, Y. R., Optical second harmonic generation at interfaces. *Annu. Rev. Phys. Chem.* **1989,** *40* (1), 327-350.
83. Greenfield, N. J., Using circular dichroism spectra to estimate protein secondary structure. *Nat. Protoc.* **2006,** *1* (6), 2876.
84. Johnson Jr, W. C., Function,; Bioinformatics, Protein secondary structure and circular dichroism: a practical guide. *Proteins: Struct., Funct., Bioinf.* **1990,** *7* (3), 205-214.
85. Zou, X.; Wei, S.; Jasensky, J.; Xiao, M.; Wang, Q.; Brooks III, C. L.; Chen, Z., Molecular interactions between graphene and biological molecules. *J. Am. Chem. Soc.* **2017,** *139* (5), 1928-1936.
86. Lu, X.; Myers, J. N.; Chen, Z., Molecular ordering of phenyl groups at the buried polystyrene/metal interface. *Langmuir* **2014,** *30* (31), 9418-9422.
87. Lu, X.; Spanninga, S. A.; Kristalyn, C. B.; Chen, Z., Surface orientation of phenyl groups in poly (sodium 4-styrenesulfonate) and in poly (sodium 4-styrenesulfonate): poly (3, 4-ethylenedioxythiophene) mixture examined by sum frequency generation vibrational spectroscopy. *Langmuir* **2010,** *26* (17), 14231-14235.
88. Myers, J. N.; Zhang, C.; Chen, C.; Chen, Z.; science, i., Influence of casting solvent on phenyl ordering at the surface of spin cast polymer thin films. *J. Colloid Interface Sci.* **2014,** *423*, 60-66.

89. Hirose, C.; Akamatsu, N.; Domen, K., Formulas for the analysis of the surface SFG spectrum and transformation coefficients of cartesian SFG tensor components. *Appl. Spectrosc.* **1992,** *46* (6), 1051-1072.
90. Yang, C. S.-C.; Wilson, P. T.; Richter, L. J., Structure of polystyrene at the interface with various liquids. *Macromolecules* **2004,** *37* (20), 7742-7746.
91. Briggman, K. A.; Stephenson, J. C.; Wallace, W. E.; Richter, L. J., Absolute molecular orientational distribution of the polystyrene surface. *J. Phys. Chem. B* **2001,** *105* (14), 2785-2791.

Chapter 3 Molecular Insights to Adhesion at a Buried Silica-filled Silicone/Polyethylene Terephthalate Interface

Adapted with permission from *Langmuir* **2020**, 36 (49), 15128-15140 (Copyright 2020 American Chemical Society).

3.1 Introduction

Silicone elastomers, adhesives, sealants and coatings with poly(dimethyl siloxane) (PDMS) as the major component, are commonly used in the aviation, automotive, construction and electronics industries because of their ability to passivate and protect components from extremes in thermal, mechanical and environmental stresses.[1] The global market for silicones has increased rapidly and in 2021 is expected to be 20 billion U.S. dollars.[2] In many applications, the reliability and durability of the device, article or joint is reliant upon the adhesion of the cured silicone material to the underlying substrates.[3-6] Silicones excel over other elastomers when thermal and environmental resistance is required; they are able to retain their elasticity and other mechanical properties over time. Silicone adhesives are supplied as one- or two-part formulations, generally relying on room temperature vulcanization (RTV) products that crosslink by condensation reactions or high temperature vulcanization (HTV) products that crosslink by addition reactions. The latter relies predominantly on hydrosilylation chemistry, in which a vinyl terminated PDMS and a silicone-hydride functional siloxane oligomer crosslink in the presence of a platinum catalyst.[7] This addition-cured system is preferred when a rapid cure is desired with no leaving groups. Also, addition-cured silicones are good candidate adhesives for their outstanding

thermal stability and controllable curing process[1, 8-9]. Silicones, while fundamentally chemically inert, have low surface energy and are able to wet substrates exceptionally well. However, their non-polar nature and intrinsic lack of reactive organofunctional groups in addition-cured silicones lead to poor adhesion of these silicone adhesives to polymers.[10] To address this issue, plasma or corona surface treatments have been applied[11-12] but require extra processing steps and expense. Therefore, self-priming curable silicone formulations are most broadly sought after in most applications. In the past few decades, blending adhesion promoters into silicone matrices was utilized as an economic and efficient way to achieve good adhesion for addition-cured silicones.[13-19] Different organosilane-based coupling agents have been developed as adhesion promoters to improve silicone adhesion to various substrates such as metals and polymers by providing interfacial reactive functionalities.[20-21] Common classes of adhesion promoters or adhesion catalysts in silicone formulations include organosilanes, titanates, and zirconates, along with reactive organic small molecules and organosiloxane oligomers that typically have either an unsaturated group or SiH group to provide complementary coupling to the hydrosilylation cured matrix.

While adhesion involves a complex interplay of bulk and interfacial phenomena[22-25], adhesion of silicone to any substrates must originate at the buried silicone/polymer interfaces. Without a minimum of wetting and interfacial contact, no subsequent coupling to viscoelastic energy dissipation schemes can be invoked upon exposure to various stress fields. The understanding of adhesion mechanisms needed to accelerate the development of new adhesives therefore can be greatly assisted by probing the molecular interactions and structures present at silicone/polymer interfaces. Since such interfaces are buried interfaces between two solids, their structures are difficult to examine in situ nondestructively at the molecular level.

Unlike SFG[26-54], many traditional surface sensitive analytical techniques (e.g., XPS) require debonding of composite parts to obtain structural information of the original buried interface, which may destroy information about the original interface.[55] Practically, good adhesion is often defined by the observation of cohesive failure of the adhesive or substrate which occurs because the interface is sufficiently strong that it cannot be separated cleanly. This rules out the application of conventional destructive surface analytical techniques to successfully examine the adhesive joints. As mentioned above, in contrast, SFG can directly probe the interfacial structure of a buried interface in situ nondestructively.[56-62] This unique property makes SFG an excellent tool to study buried silicone adhesive/polymer substrate interfaces.[30]

Previously, we have carried out systematic studies to reveal the adhesion promotion mechanism of alkoxysilane-siloxane mixtures on aliphatic group deuterated polyethylene terephthalate (d4-PET) using SFG[51-54, 63-68]. The interfacial ordering of the three methoxy end groups of (3-glycidoxypropyl)trimethoxysilane (γ-GPS, which is an alkoxysilane, Scheme 3.1) was found to play important roles in determining adhesion strength at the silicone/PET interface. The addition of DMMVS (Hydroxyl terminated dimethyl methylvinyl co-siloxanol, Scheme 3.1) caused more ordering of the methoxy groups at the d4-PET/silicone interface before curing and, therefore, promoted the adhesion by the interfacial chemical reactions between methoxy groups and hydroxyl end groups of PET during the curing process.[64, 69]

Along with the alkoxysilane-siloxanol mixture adhesion promotion system, other components are introduced into silicone matrices to achieve better performance and properties for silicone elastomers. This current study focused on the effects of two common components on interfacial structures and adhesion of silicone adhesives: adhesion catalyst and filler. Adhesion catalyst is typically added to silicone adhesives to accelerate interfacial reactions involving the

alkoxysilane groups of γ-GPS or the silanol groups on DMMVS and enhance the adhesion. However, the detailed mechanism of adhesion catalyst still remains unclear. To improve the mechanical strength and toughness of silicone materials, inorganic silica fillers are widely used as additives in silicone elastomers. Nevertheless, any components added to the silicone system may change the interfacial molecular structure and then affect adhesion. For example, the introduction of high surface area silica fillers may create silica/silicone interfaces that also compete for reactive species needed for adhesion.

In this study, the interfacial structure of a silicone/d4-PET interface was investigated for a silicone elastomer containing a γ-GPS-DMMVS mixture. The SFG results were correlated to adhesion measurements to understand how the interfacial structure changes caused by the addition of silica filler and/or adhesion catalyst to silicone affect the interfacial adhesion.

3.2 Materials and Methods

3.2.1 Materials and Sample Preparation

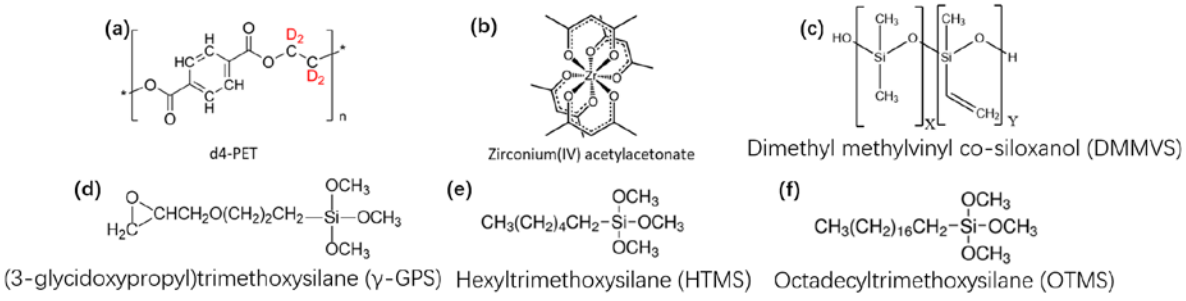

Scheme 3.1 Molecular structures of materials used: a) d4-PET, b) adhesion catalyst (AC), c) DMMVS, d) γ-GPS, e) HTMS, f) OTMS.

Aliphatic chain deuterated PET (d4-PET) was used as polymer substrate in this study to avoid spectral interference of the C-H stretching signals from PET. The d4-PET (Mv=72,000 g/mol, lot

number P3416) was obtained from Polymer Source, Inc and dissolved in the solvent 2-chlorophenol to prepare a d4-PET solution at 1.5 wt%. A polymer thin film was prepared by spin-coating the d4-PET solution on a fused silica prism at 2000 rpm for 30 seconds (VTC-100 spin-coater, MTI Corporation). The polymer films were placed in a vacuum oven and annealed at 150 ^{o}C for 14 hours to remove remaining solvent. Samples for adhesion testing were prepared using unreinforced 0.25 inch thick Ertalyte® PET-P (Boedeker Plastics Inc,).

The adhesion promoter γ-GPS was purchased from Millipore-Sigma, Inc. Hexyltrimethoxysilane (HTMS) and Octadecyltrimethoxysilane (OTMS) were purchased from Santa Cruz Biotechnology and Sigma-Aldrich, respectively. Hydroxyl terminated dimethyl methylvinyl co-siloxanol (DMMVS) and Zirconium (IV) acetylacetonate were supplied by Dow, along with all siloxane polymers. It should be noted that Zirconium (IV) acetylacetonate was supplied as a paste-like dispersion in a 1:1 (w/w) mixture with a vinyl-terminated PDMS (Vi-PDMS11) having a number average molecular weight (Mn) of about 11 kDa. This catalyst dispersion containing 50 wt% active metal coordination complexes is hereby referred to as adhesion catalyst (AC). The silica-filled silicone elastomer matrices (**Table 3.1**) were also provided by Dow, as a two-part kit. The molecular structures of the above chemicals and the d4-PET polymer are shown in **Scheme 3.1**.

The two-part platinum-catalyzed addition cured silicone elastomer was provided by Dow (**Table 3.1**). The fumed silica is trimethylsiloxy-surface treated by a high shear mixing process with the vinyl terminated PDMS matrix polymer (Vi-PDMS60) that has Mn of about 60 kDa. Part A of the silica-filled silicone elastomer contains SiVi-functional PDMS and the Karstedt's catalyst complex, which is also supplied as a dilute dispersion in Vi-PDMS1. This Karstedt's catalyst loading in Part A yields a total Pt level of about 9 ppm (w/w) for curing of the total formulation

when Parts A and B are mixed at a 1:1 (w/w) ratio. Part B contains both Vi-PDMS58 and a PDMS crosslinker that is about 40 mol% randomly substituted with methylhydridosiloxane units and has Mn of about 900 Da, and 1-ethylnyl-1-cyclohexanol (Sigma-Aldrich) as a catalyst inhibitor to permit working time before heat curing. Equivalent formulations without the treated silica filler were also provided by Dow.

Table 3.1 Silicone elastomer (SE) compositions.

Material	wt%	
	Part A	Part B
Treated silica	19.20	19.33
Vi-PDMS60	80.77	73.93
SiH-functional PDMS crosslinker	-	6.67
Karsedt's (Pt) catalyst complex dilution	0.027	-
Catalyst inhibitor	-	0.074

For control samples (no adhesion components), the two parts were mixed in a 1:1 ratio (w/w). Adhesion components, including γ-GPS, DMMVS, and AC were then added to the two parts to produce samples for studies exploring the effect of the additives on adhesion. Formulations are detailed in **Table 3.2**.

All formulations were mixed by manually stirring for 10 minutes. Thick films of silicone (around 5 mm) were dropped onto the d4-PET-coated prism and the assembly was cured in an oven under nitrogen gas at 150 ^{o}C for 1 hour.

Table 3.2 Compositions of the silicone adhesive samples investigated.

Sample	Part A	Part B	AC	DMMVS	γ-GPS	OTMS	H
SE	50.00	50.00	-	-	-	-	-
SE-AC	49.70	49.25	0.30	-	-	-	-
SE-GPS/DMMVS	49.70	49.25	-	0.15	0.60	-	-
SE-GPS/DMMVS/AC	49.70	49.25	0.30	0.15	0.60	-	-
SE-OTMS/DMMVS/AC	49.70	49.25	0.30	0.15	-	0.60	-
SE-HTMS/DMMVS/AC	49.70	49.25	0.30	0.15	-	-	0.

3.2.2 Experimental Methods

3.2.2.1 SFG Experiment

To gain molecular structure information at the silicone/PET interface and correlate structure-properties relationship, SFG experiments were conducted. As mentioned in chapter 1, SFG is a well-developed technique used for investigating molecular structures at buried interfaces and there are many publications in this realm[36, 47-50, 65-68, 70]. Detailed SFG theory and experimental procedures have been extensively published and will not be repeated here. [26-29, 60, 71-72] Previously, we have examined molecular structures at buried silicone (Sylgard 184) interfaces and performed qualitative and quantitative characterizations on adhesion[54, 63-64]. The sample geometry used in this study is shown in **Figure 3.1**. The silicone films used here were sufficiently thick to avoid penetration of the visible and IR beams to the other side of the silicone sample, so only the buried silicone/d4-PET interface contributes to the SFG aliphatic C-H stretching signal from silicone adhesives, and there is no need to consider the signal contribution from multiple interfaces.[73] Under the experimental condition used, there was no sample damage by the input laser beams. The SFG spectra were collected from the buried silicone/d4-PET interfaces using the SSP polarization combination of the input and output beams. Multiple samples were tested for each interface and

the SFG spectra are reproducible. Each spectrum shown below is the averaged data for at least six individual spectra.

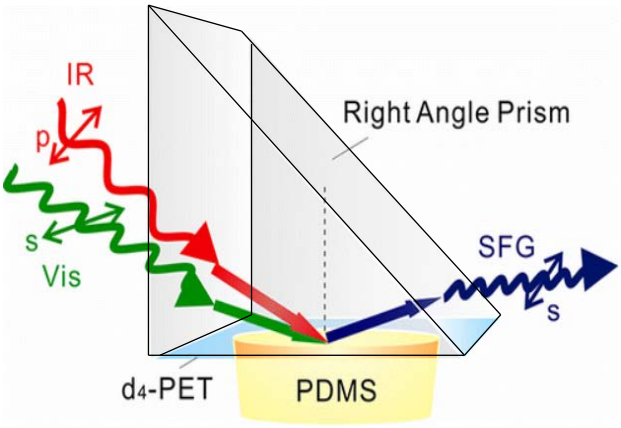

Figure 3.1 SFG experimental sample geometry to study d4-PET/silicone interfaces

3.2.2.2 Adhesion Strength Test

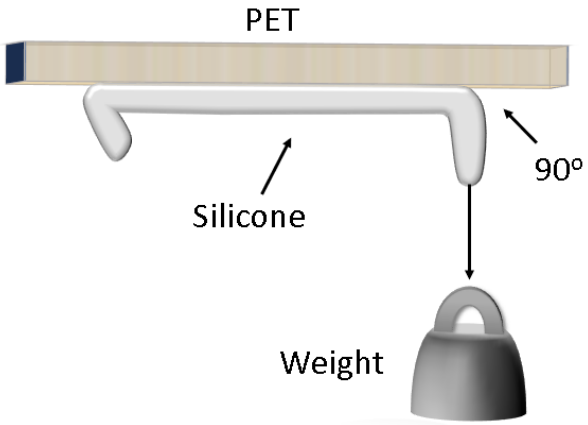

Figure 3.2 Schematic of 90º adhesion test.

In order to study the effects of silica filler and other components on adhesion strength of silicone elastomer on PET, 90-degree peeling test was conducted using the experimental configuration shown in **Figure 3.2**. By comparing the adhesion strengths of different sample

formulas and curing conditions, we can learn the adhesion promotion mechanism of silicone adhesives.

Samples were prepared by applying silicone stripes (10 cm long, 2 cm wide, 0.5 cm thick) onto PET plates. The samples were cured in an oven under various conditions specified below. Adhesion measurements were conducted at room temperature, after 12 hours of equilibration at ambient temperature.

A silicone stripe was peeled approximately 1 cm on one side for weight attachment. A clamp (not shown in **Figure 3.2**) was used to connect a stainless-steel hooked weight with the peeled section of the silicon stripe. The hooked weight was held manually to ensure that the angle between the hooked weight and the silicone stripe was about 90 degrees, and the hooked weight was released. If no adhesive failure between the silicone and PET occurred, additional weight was applied. This process was repeated until adhesion failure between silicone and PET occurred. The minimum weight to induce such a failure was recorded to characterize the adhesion strength. If the adhesion failure occurred during the first trial, the experiment was repeated with a new sample using a lighter hooked weight.

3.3 Results and Discussion

3.3.1 Adhesion Strength Results

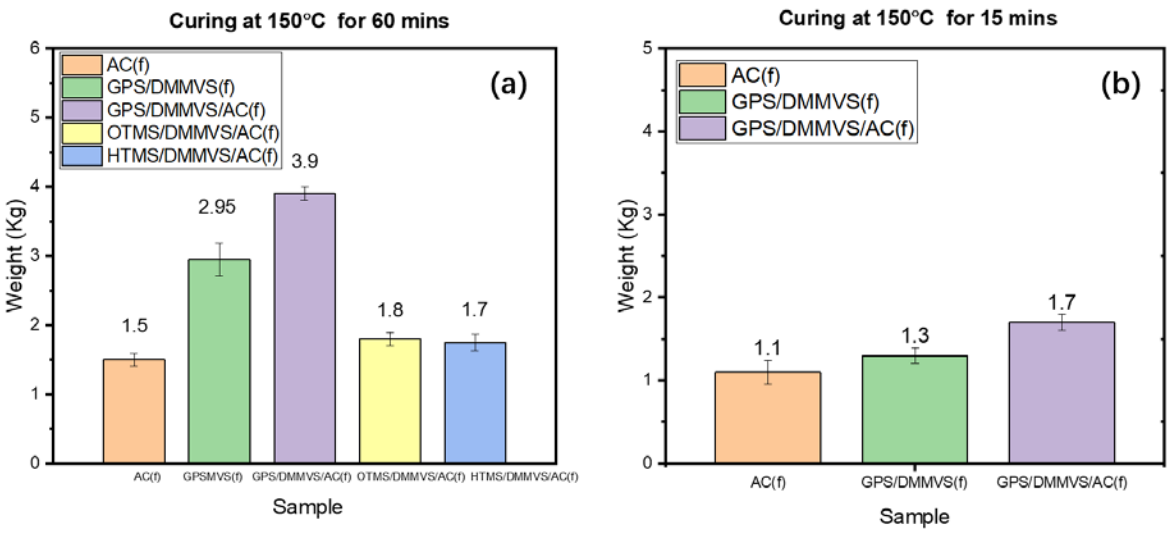

Figure 3.3 Adhesion data collected from different silicone adhesives with silica filler: (a) all samples cured at 150 ºC for 60 mins (b) all samples cured at 150 ºC for 15 mins. All the silicone samples tested here contain fillers, indicated by (f) in the two figures.

Figure 3.3 shows the measured adhesion strengths at polymer/silicone interfaces for various samples annealed at different temperatures with different annealing times. Because the silicone samples without silica are too soft and vulnerable even after curing, reliable adhesion data could not be obtained using the 90-degree peel test. Therefore, all the samples tested here are silica filled. The following results can be obtained from the adhesion testing experiments:

(1) The silicone samples containing the γ-GPS-DMMVS adhesion promoters (samples GPS/DMMVS/AC and GPS/DMMVS) have higher adhesion strength than the sample AC (which does not contain such adhesion promoters) at the silicone/polymer interface, as shown in **Figure 3.3a**. This indicates that the γ-GPS-DMMVS adhesion promoter is important for enhancing the silicone adhesion at interface.

(2) The adhesion strength of the silicone/polymer interface for the silicone sample containing γ-GPS-DMMVS adhesion promoters and AC is higher than that for the silicone sample containing γ-GPS-DMMVS adhesion promoters without AC (**Figure 3.3a,** GPS/DMMVS/AC vs.

GPS/DMMVS). This shows that AC facilitates interfacial adhesion.

(3) When the γ-GPS was replaced with a different silane without the epoxy end group, OTMS and HTMS, the adhesion strength was measured to be lower (**Figure 3.3a,** GPS/DMMVS/AC vs. OTMS/DMMVS/AC and HTMS/DMMVS/AC). This demonstrates the significance of the epoxy groups on silicone adhesion.

(4) Comparing the adhesion strengths of samples AC and OTMS/DMMVS/AC in **Figure 3.3a**, we can see that the addition of OTMS-DMMVS and HTMS-DMMVS increased the adhesion slightly (OTMS/DMMVS/AC and HTMS/DMMVS/AC vs. AC).

(5) Comparison between **Figure 3.3a** and **Figure 3.3b** shows that the adhesion strength increases as the curing time increases. Comparing to 60 mins annealing samples, the addition of γ-GPS-DMMVS adhesion promoter has little effect on promoting adhesion strength in 15 mins annealing samples, which is consistent with SFG study below (AC vs. γ–GPS/DMMVS/AC and γ–GPS/DMMVS in **Figure 3.3b**). The addition of AC has positive effect on facilitating γ-GPS-DMMVS adhesion promoter to enhance adhesion strength.

All the above observations from the adhesion measurements can be interpreted by SFG results presented below at the molecular level.

3.3.2 SFG Results

3.3.2.1 Interfacial Methoxy Behavior

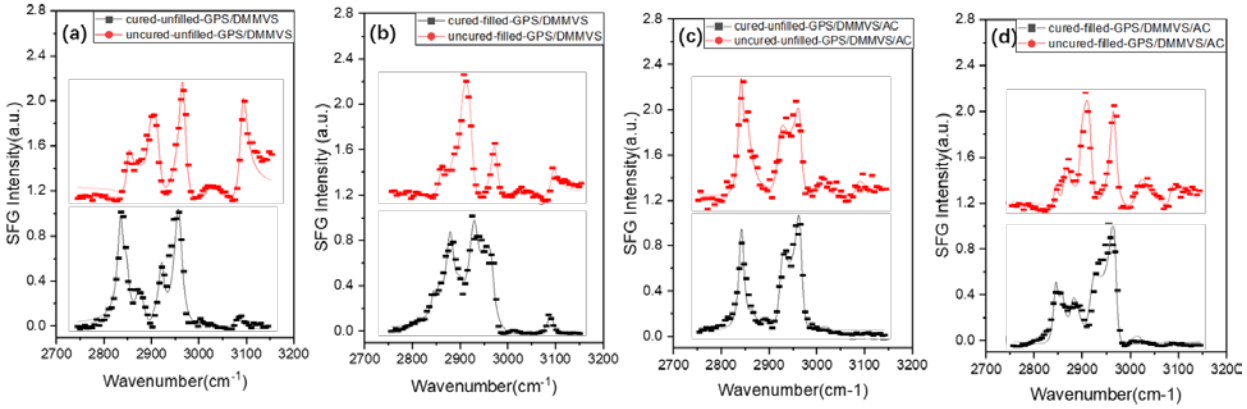

Figure 3.4 SFG spectra collected from buried interfaces between d4-PET and different silicone (with adhesion promoter) samples: (a) uncured and cured silica unfilled GPS/DMMVS silicone; (b) uncured and cured silica filled GPS/DMMVS silicone; (c) uncured and cured silica unfilled GPS/DMMVS/AC silicone; (d) uncured and cured silica filled GPS/DMMVS/AC silicone. The dots are experimental data and the lines are fitting results.

As reported in our previous studies on silicone adhesives with neither silica filler nor adhesion catalyst, the interfacial behavior of γ–GPS-DMMVS adhesion promoter plays a significant role in determining the adhesion strength of silicone.[53-54, 63-64, 68] This current research is focused on the effects of silica filler and adhesion catalyst on interfacial structure and adhesion at silicone/polymer interfaces. In **Section 3.3.2.4**, we presented the results on the effects of silica and adhesion catalyst on the interfacial structure of NEAT silicone (without γ–GPS-DMMVS adhesion promoter)/polymer interfaces (**Figure 3.10**). Here we investigate the effects of silica and adhesion catalyst on the interfacial structure of the silicone (with the γ–GPS-DMMVS adhesion promoter)/polymer interfaces. In our previous publications, we reported that strong adhesion of the silicone adhesives without silica fillers or adhesion catalyst is correlated to two SFG spectral observations from the silicone/polymer interface:[64] (1) ordered methoxy groups of γ–GPS at the uncured silicone/PET interface (evidenced by a strong SFG methoxy signal before curing), (2)

reaction between the methoxy groups and PET surface (evidenced by a decrease in SFG methoxy signal intensity). Therefore, we expect that the SFG methoxy signal collected from the silicone/polymer interface before and after curing in this research should also provide important information regarding adhesion.

Table 3.3 SFG peak assignments [53-54, 64, 69, 74]

Interfaces	Peak Center (cm^{-1})	Assignment
d4-PET/PDMS samples (cured, SSP)	2840	sym C-H stretching of methoxy (O-CH_3)
	2875	Sym C-H stretching of methylene(-CH_2)
	2910	sym C-H stretching of PDMS methyl (Si-CH_3)
	2925	asym C-H stretching of methylene(-CH_2)
	2965	asym C-H stretching of PDMS methyl (Si-CH_3)
	3010	Epoxy ring C-H stretching
	3085	Phenyl ring C-H stretching
d4-PET/PDMS samples (uncured, SSP)	2845	sym C-H stretching of methoxy (O-CH_3)
	2875	sym C-H stretching of methylene(-CH_2)
	2900	sym C-H stretching of PDMS methyl (Si-CH_3)
	2935	asym C-H stretching of methylene(-CH_2)
	2965	asym C-H stretching of PDMS methyl (Si-CH_3)
	3085	Phenyl ring C-H stretching

SFG spectra collected from the buried interfaces between d4-PET and silicone elastomers (with γ–GPS-DMMVS adhesion promoter), with and without adhesion catalyst, are shown in **Figure 3.4**. **Table 3.3** shows the SFG peak assignments. The 3085 cm^{-1} peak is assigned to the phenyl C-H stretching of d4-PET. The SFG peaks centered at ~2900 cm^{-1} and 2965 cm^{-1} are again assigned to the symmetric and anti-symmetric C-H stretching modes of Si-CH_3, respectively. The

symmetric Si-CH_3 stretching peak slightly shifts to 2910 cm^{-1} with the addition of adhesion catalyst in both uncured and cured system. The peak centered around 3000-3010 cm^{-1} is assigned to the epoxy C-H stretching of γ-GPS, indicating the presence of the epoxy end group of γ-GPS at the silicone/d4-PET interface with order[162]. The sharp peak at 2840-2845 cm^{-1} is assigned to the symmetric C-H stretching of the methoxy head group in γ–GPS.[64, 69] The peaks at 2875 cm^{-1} and 2925-2935 cm^{-1} are assigned to the symmetric and anti-symmetric -CH_2 stretching, respectively, from the backbone methylene groups of DMMVS and γ-GPS as well as the curing agent. **Table 3.4** shows the SFG spectra fitting parameters.

Silica filler effect:

SFG spectra displayed in Figure 3.4a were collected from the unfilled GPS/DMMVS silicone/d4-PET interface before and after curing. Methoxy group signals at the silicone interface are present in the SFG spectra before curing, which is consistent with the presence of the γ-GPS with order at the interface. After curing, the SFG signal from the methoxy group greatly increased, indicating that the interfacial methoxy groups have a higher interface coverage and/or becoming more ordered. This observation is quite different from the results obtained from our previous studies on silicone/d4-PET interfaces using SFG.[64] As we mentioned above, for a silicone/polymer interface with strong adhesion, our previous study indicates that SFG methoxy signal needs to be strong before curing (ordered methoxy groups at the uncured silicone/polymer interface).[64, 69] After curing, the SFG methoxy signal should greatly decrease, indicating the reaction between methoxy and the PET surface (likely hydroxyl end groups).[64, 69] However, here we observed the opposite trend – The SFG methoxy signal intensity was higher after curing. This is due to the different silicone samples we studied here from those used in previous investigations. The silicone sample used in this study contains a much smaller amount of γ-GPS (0.6 wt%) compared to that used in

the previous studies (1.5 wt%). Here at room temperature before curing it is difficult for methoxy groups of smaller amount of γ-GPS to segregate and order at the silicone/d4-PET interface. During the curing process, methoxy groups can be more efficiently diffuse to the silicone/polymer interface, increasing the SFG signal at 2840 cm^{-1}. At the same time, the interfacial methoxy groups could react, leading to lowering the SFG signal at 2840 cm^{-1}. The observed SFG signal increase is the overall effect from the methoxy diffusion and reaction, the details of which can be elucidated by time-dependent SFG studies. We performed such time-dependent studies for silica filled silicone systems which will be presented below but did not perform studies on unfilled silicone, because this research is focused on the filler and catalyst effects.

Comparing SFG spectra shown in Figure 3.4a with 3.4b, we can observe the effect of silica filler on the interfacial structure at the silicone/polymer interface. Much weaker SFG signals from methoxy groups at ~2840 cm^{-1} were detected from the silicone/polymer interfaces after the addition of the filler for both uncured and cured cases. The addition of silica to the silicone matrix increases the amount of interfacial area in the silicone matrix. Substantial amount of methoxy molecules may segregate and adsorb to such silicone/silica interfaces, which greatly reduces the amount of γ-GPS-DMMVS at the silicone/d4-PET interfaces. The presence of the lower concentration of methoxy groups at the silicone/d4-PET interface may generate the weaker SFG methoxy signal intensity for uncured sample for a given average orientation. This lower amount of methoxy groups at the silicone/d4-PET interface may result in poor adhesion. It might be expected that curing would facilitate migration of the methoxy groups to the silicon/polymer interface and cause a resultant increase in adhesion strength. The SFG methoxy signals are however also very weak in the cured system (Figure 3.4b), indicating the surface coverage/ordering of methoxy groups at the silicone/d4-PET interfaces are minimal with added

filler in the silicone matrix, regardless of curing. The decrease in coverage/ordering of the methoxy groups at the cured silicone/polymer interface may be due to the opposite effect of interfacial segregation (increasing the methoxy coverage) and interfacial chemical reaction (decreasing the methoxy coverage). This will be further studied by time-dependent curing experiment presented below.

The effect of the filler in the presence of the catalyst in the silicone matrix is shown by comparing the SFG spectra displayed in Figure 3.4c and 3.4d. Before curing, SFG methoxy signal from the unfilled silicone/polymer interface (Figure 3.4c) is larger than that collected from the filled silicone/polymer interface (Figure 3.4d). This is similar to what was observed when comparing Figure 3.4a with 3.4b in the absence of adhesion catalyst. This can be interpreted by the segregation of methoxy to the silica filler/silicone interfaces, as discussed above. Differently, after curing, the SFG methoxy signals are both large in Figure 3.4c and 3.4d, showing that filler does not substantially change the interfacial structure of adhesion promoters. This is different from the results in the absence of the catalyst. Apparently, the addition of catalyst to the silicone matric alters the effects of filler on the methoxy interfacial behavior, which will be discussed in more detail later.

Adhesion catalyst effect:

First, we want to study the effect of adhesion catalyst on the interfacial structure at the silicone/polymer interface in the absence of silica filler. Comparing the SFG spectra shown in **Figure 3.4a** with **3.4c**, we can see that the addition of the catalyst affects the interfacial behavior of methoxy groups, which is presumably expected to impact the silicone adhesion to PET. We discussed the methoxy SFG signal change before and after silicone curing without the presence of the catalyst in **Figure 3.4a** above. Here with the presence of catalyst, very strong methoxy signal

at 2840 cm^{-1} could be detected in **Figure 3.4c**, indicating that ordered methoxy groups cover the silicone/polymer interface before curing, which is one of the requirements for good adhesion. After curing, the methoxy signal intensity is still very large in **Figure 3.4c**. The large SFG methoxy signal after curing indicates that AC facilitates the interfacial segregation of the methoxy groups to ensue substantial methoxy interfacial coverage even after the interfacial reaction occurred. This should help to improve adhesion.

We then studied the effect of adhesion catalyst on interfacial methoxy behavior with the presence of filler in silicone. In order to do so, we compared SFG spectra plotted in **Figure 3.4b** with **3.4d**. Before curing, SFG methoxy signal from the uncured silicone (with filler and catalyst)/polymer interface is minimal, which is similar to that from the uncured silicone (with filler but without catalyst)/polymer interface. This shows that filler plays a dominating role to reduce the methoxy segregation at the silicone/polymer interface; the adhesion catalysts has little effect at the interface if the adhesion promoting species are adsorbed on filler surfaces. However, the SFG methoxy signal in **Figure 3.4b** is much larger than that in **3.4d**. As we discussed above, curing facilitates the methoxy interfacial segregation and interfacial reaction, which should have opposite effects on SFG signal changes. Here, even in the event of interfacial reaction of some of the methoxysilane groups, the methoxy SFG signal still increased after curing. One possible reason is that each γ-GPS molecule is comprised of three methoxy groups. Even if one or two react, there would still remain two or one residual methoxy group[75-76]. It is known that the first and second alkoxy groups hydrolyze and condense much faster than the third, so it is unlikely that all three are consumed simultaneously[77-78]. Thus, if one of the methoxy groups (or alternately, the epoxy tail) reacts directly with the substrate, this should induce a stronger orientation of the remaining alkoxy groups, relative to a "free" γ-GPS for which entropy would favor a more random orientation near

the interface. The fact that the adhesion catalyst is expected to facilitate reactions of the γ-GPS moieties suggest that it would favor stronger alignment of methoxy at the silicone/polymer interface. The rationale behind the combination of γ-GPS and DMMVS as an adhesion promoter system for Pt-cured silicones is that one of the alkoxysilane groups also couples to the Si-OH end of DMMVS which is able to tie into the silicone network through hydrosilylation of the pendant vinyl groups. Under this hypothesis, one should see a correlation to improved adhesion. More details of the methoxy interfacial behavior will be reported in the time dependent studies in **Section 3.3.2.3** below.

3.3.2.2 Interfacial Epoxy Behavior

After we discussed the interfacial behavior of methoxy groups, we want to study the behavior of epoxy groups at the interface. As we showed in **Figure 3.4** above, for all the silicone materials with γ-GPS-DMMVS adhesion promoter, before curing, the 3010 cm^{-1} peak could be clearly seen, indicating the interfacial coverage and ordering of the epoxy groups for all the samples. After curing, for all the four samples, the 3010 cm^{-1} peak disappeared. The disappearance of the SFG signals of epoxy after curing can be caused by the elimination or randomization of the interfacial epoxy groups. We believe that the interfacial epoxy groups have participated in the interfacial reaction during the curing process, leading to the disappearance of the SFG epoxy signals.

The ring-opening reaction of the epoxy functionality can be triggered by heat during the curing process (**Scheme 3.2**). On the other hand, the SFG signal intensities of CH_2 methylene peaks increased after curing (**Figure 3.4**), indicating increased coverage or ordering of interfacial methylene groups. The higher interfacial coverage/ordering of methylene groups may be caused by the methylene containing products generated from the network via hydrosilylation (**Scheme**

3.2), curing reaction (hydrosilylation groups on the polymer chains (**Scheme 3.2**)), and ring opening reaction of epoxy groups (**Scheme 3.2**).

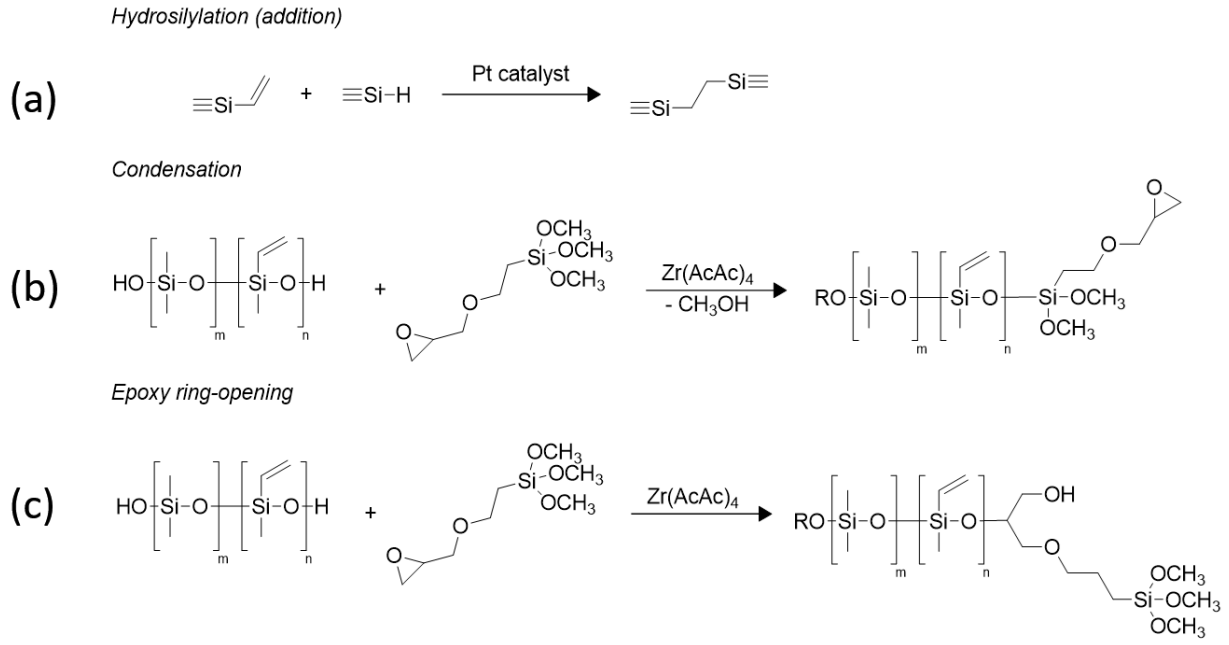

Scheme 3.2 Some possible reactions at the silicone/d4-PET interface during curing

Since all the epoxy signals disappeared for the cured samples, here we want to examine the effects of fillers and AC on the interfacial behavior of epoxy groups before curing. Comparing the SFG spectra collected from the uncured samples in **Figure 3.4a** to **3.4c**, and **3.4b** to **3.4d**, we can see that the addition of AC to the sample increased the epoxy signal, indicating that AC could help to segregate epoxy groups to the interface with order. Comparing the SFG spectra collected from the uncured samples in **Figure 3.4a** to **3.4b**, and **3.4c** to **3.4d**, we can see that the silica fillers did not substantial change the epoxy signals, which is different from above discussed effects of silica fillers on methoxy interfacial behavior. Especially for **Figures 3.4c** and **3.4d**, fillers decreased the SFG methoxy signal because of less methoxy (therefore also γ-GPS) coverage at the silicone/PET interface, but not the SFG epoxy C-H stretching signal. This shows that epoxy groups can be more ordered when there is less methoxy groups at the interface.

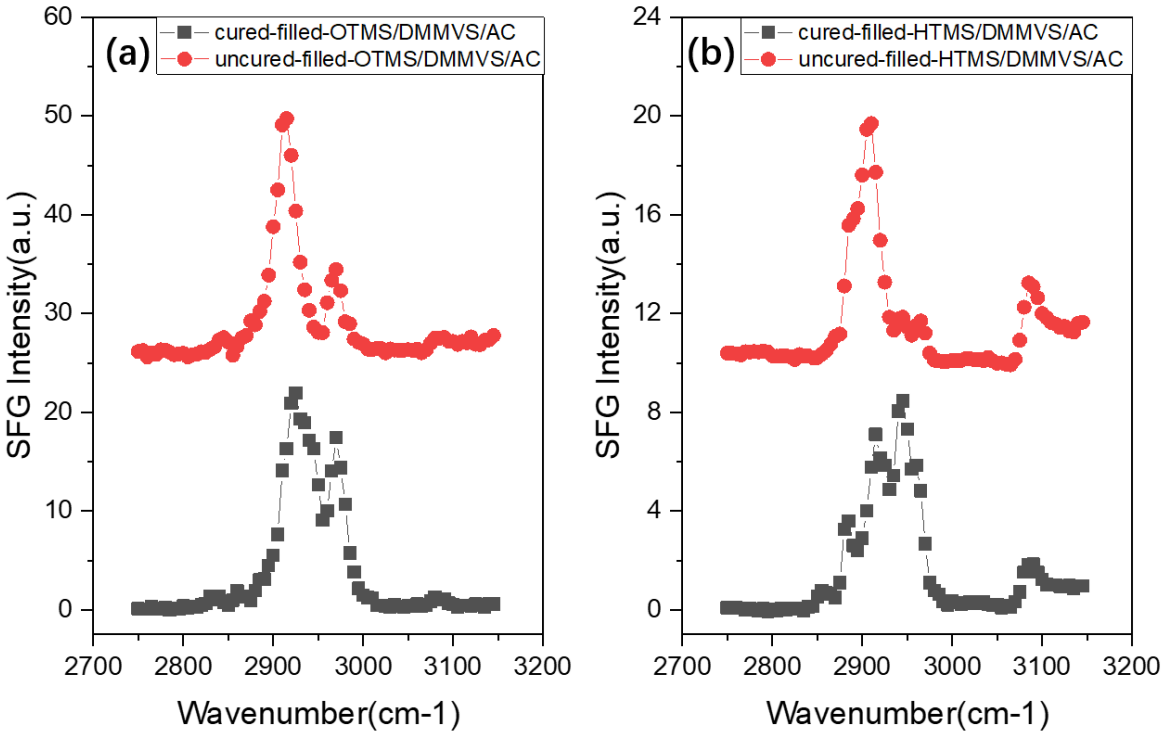

Figure 3.5 SFG spectra collected from buried interfaces between d4-PET and different silicone (with adhesion promotor of mixed DMMVS and methyl terminated silane OTMS or HTMS) samples: (a) uncured and cured OTMS/DMMVS/AC silicone with silica filler; (b) uncured and cured HTMS/DMMVS/AC silicone with silica filler. The compositions of samples OTMS/DMMVS/AC and HTMS/DMMVS/AC can be found in Table 3.2.

To further examine the effect of interfacial behavior of the γ-GPS end epoxy group at the silicone/polymer interface, we performed a set of control experiments by replacing γ-GPS with silanes of the same head methoxy groups but different end group, OTMS and HTMS, in the GPS/DMMVS/AC formula. The compositions of samples OTMS/DMMVS/AC and HTMS/DMMVS/AC can be found in **Table 3.2**. SFG spectra collected from the interfaces between d4-PET and silicone samples with OTMS and HTMS instead of γ-GPS are shown in **Figure 3.5**.

Comparing the SFG spectra in **Figure 3.5a** with those in **Figure 3.4d**, we can see that the silane end group in the promoting mixture influences the interfacial molecular structure at the

silicone/polymer interface. Without the epoxy group in OTMS, the SFG signal at 3010 cm^{-1} was absent in **Figures 3.5a**, which verifies our above peak assignment that the 3010 cm^{-1} peak is contributed by the C-H stretching mode of the epoxy group.

The influence of the silane end group on molecular structure of the silicone/polymer interface can also be seen from the methoxy interfacial behavior. Although for the uncured GPS/DMMVS/AC sample, the SFG signal of interfacial methoxy at 2845 cm^{-1} is weak in **Figure 3.4d**, it becomes much stronger after curing, indicating ordered methoxy at the cured silicone/polymer interface for the GPS/DMMVS/AC sample. Differently, only very weak SFG signals at 2845 cm^{-1}were detected from both uncured and cured OTMS/DMMVS/AC samples at the silicone/polymer interface in **Figure 3.5a**, indicating there are not many methoxy groups segregating to the interface with ordering.

The only difference between the GPS/DMMVS/AC and OTMS/DMMVS/AC samples is the different silane molecules used, γ-GPS vs. OTMS, which is only 0.6 wt% in each sample (**Table 3.2**). The different interfacial behavior of silane methoxy for GPS/DMMVS/AC and OTMS/DMMVS/AC at the silicone/polymer interface may be caused by three possible reasons: (1) The different silane end groups, epoxy in γ-GPS and methyl in OTMS, may have different effects on interfacial segregation/ordering of methoxy groups. (2) The OTMS molecule is much longer - The length of the silane molecule may affect the diffusion of the molecule to the interface with order. (3) The molecular weight of OTMS (374.67 Da) is 58.5% greater than that of γ-GPS (236.34 Da), such that for the same loading of 0.6 wt %, there would be less than half as many methoxy groups present in the OTMS system than γ-GPS. Let us examine these possibilities below.

To test the second and third possibilities mentioned above, we performed another control experiment by replacing OTMS with HTMS (**Scheme 3.1**), which has the same head groups and

the same end group as OTMS, but the length is much shorter than OTMS while comparable to γ-GPS. The formula weight of HTMS is 206.35 Da, or 14.5% lower than that of γ-GPS, such that the molar concentration of HTMS would be correspondingly higher at the constant weight loading of 0.6 wt% silane. As shown in **Figure 3.5b**, no SFG signal could be detected at 2845 cm^{-1} for both uncured and cured HTMS/DMMVS/AC samples at the silicone/polymer interface. Therefore, it is clear that the absence of methoxy with order at the silicone/polymer interface is not because of the length nor concentration of the methyl terminated silane, but likely due to the non-polar composition of the alkyl tail group.

This can be understood from the perspective of matrix compatibility differences among the three silane coupling agents by examining their solubility parameters. Using the group contribution method of Fedors to estimate solubility parameters[79], we obtain the following respective values for γ-GPS, OTMS and HTMS: 8.49 $(cal/cm^3)^{0.5}$, 8.14 $(cal/cm^3)^{0.5}$, and 7.76 $(cal/cm^3)^{0.5}$. For comparison, the same method yields a solubility parameter of 7.38 $(cal/cm^3)^{0.5}$ for PDMS, which is in good agreement with literature values.[80] Following the "like dissolves like" adage, smaller differences in solubility parameter between the silane and PDMS favor enhanced compatibility. Hence, γ-GPS can be expected to be significantly less compatible in PDMS and likely driven to interfaces by incompatibility in PDMS, as opposed to the alkylsilanes which, would tend to be less enthalpically dissatisfied to remain dispersed in the bulk of the PDMS matrix. This follows experimentally observed solution behavior, as hydrocarbons like n-alkanes are excellent solvents for even very high molecular weight PDMS, and unsurprisingly, the use of alkyl substituents is a simple way to enhance compatibility of organic compounds in PDMS.[80] Hence, both OTMS and HTMS will tend to be relatively compatible in PDMS. In contrast, γ-GPS contains both the strained three membered glycidyl ring, as well as an ether linkage, both of which introduce polarity and act

to reduce PDMS compatibility. It follows that the glycidoxypropyl tail of γ-GPS can promote segregation to the silicone/polymer interface. Orientational bias could then be induced by interfacial reactions with the substrate that occur on exposure to heat and may be accelerated by the adhesion catalyst, which is consistent with what we reported in our previous publication[53]. This study clearly shows that the synergistic behavior of the methoxy and epoxy groups on γ-GPS plays important roles in adhesion at the silicone/polymer interfaces, with evidence that suggest that both the methoxy and epoxy ends could be undergoing reactions. We note that the methoxy groups could react with the substrate or with the silanol termini of DMMVS, or undergo self-condensation reactions with either the methoxy or -OH groups (from epoxy ring opening) present on neighboring γ-GPS molecules.

Comparing **Figure 3.5a** to **3.5b**, we can tell that the silane molecule length affects the structure at the silicone/polymer interface. For HTMS/DMMVS/AC, methyl symmetric stretching signal at 2880 cm^{-1} can be detected from the uncured (as a shoulder) and cured (a distinct peak) silicone/polymer interface. For OTMS/DMMVS/AC samples, this signal was not detected. This indicates that methyl group is present and ordered at the silicone/polymer interface when HTMS was used to replace γ-GPS, which is not the case when OTMS was used.

3.3.2.3 Time Dependent Curing Studies

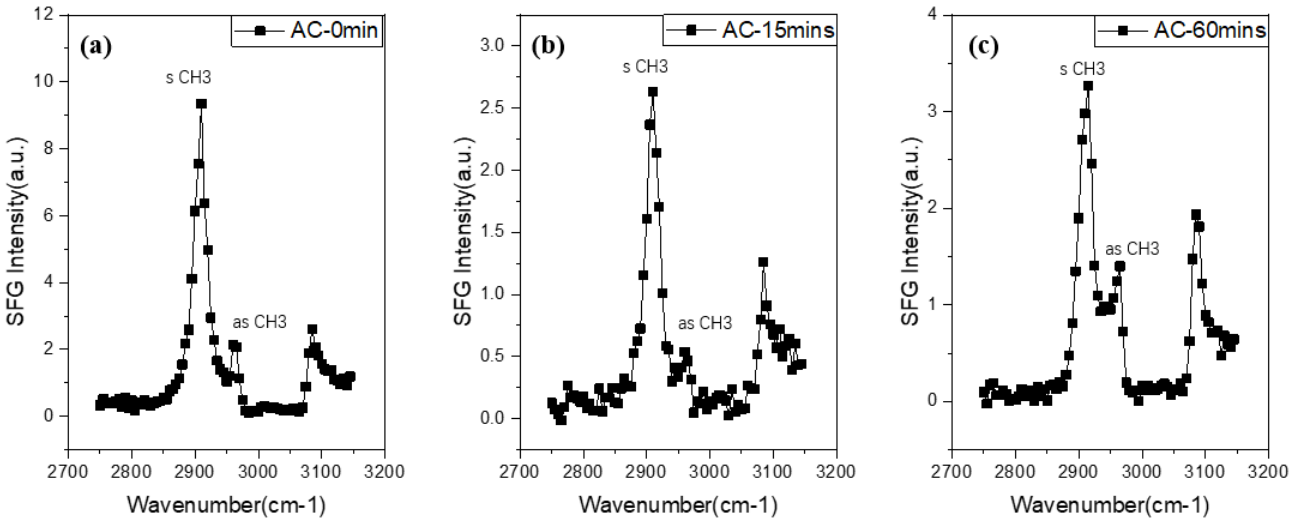

Figure 3.6 SFG spectra collected from buried interfaces between d4-PET and AC silicone with silica filler samples under different curing times at 150°C: (a) Uncured AC silicone with silica filler (0 mins); (b) Cured AC silicone with silica filler (15 mins); (c) Cured AC silicone with silica filler (60 mins); These samples do not contain the adhesion promoters.

Figure 3.6 shows SFG spectra collected from the silicone/polymer interface for AC silicone with silica filler with different curing times. As aforementioned, the peaks at 2910 cm^{-1} and 2965 cm^{-1} are assigned to the symmetric and asymmetric C-H stretching modes of Si-CH_3, and the peak centered at 3085 cm^{-1} is attributed to the phenyl C-H stretching from d4-PET. All the three spectra shown in **Figure 3.6** are similar; the only differences are the decreased ratio between the Si-CH_3 C-H symmetric/asymmetric stretching intensity and the increased signal from d4-PET phenyl C-H stretching as a function of the increased annealing time, caused by the interfacial orientation changes of Si-CH_3 (see **Section 3.3.2.4** for Si-CH_3 orientation discussion) and phenyl groups at the interface.

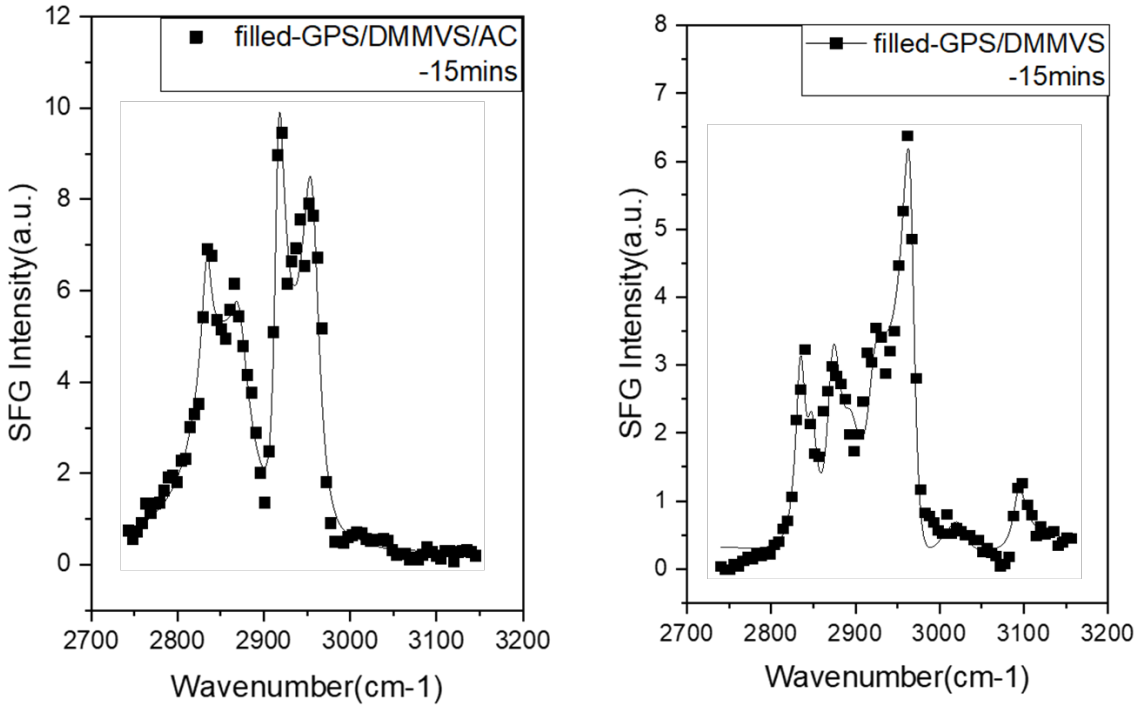

Figure 3.7 SFG spectra collected from buried interfaces between d4-PET and GPS/DMMVS/AC silicone with silica filler samples after curing for 15 min; (b) SFG spectra collected from buried interfaces between d4-PET and GPS/DMMVS silicone with silica filler samples after curing for 15min. The dots are experimental data and the lines are fitting results.

Before curing, only weak SFG methoxy signal at 2845 cm^{-1} could be detected (as a shoulder) from the d4-PET/GPS/DMMVS/AC filled silicone interface in **Figure 3.4d**, indicating that methoxy groups do not have substantial interfacial coverage or are not ordered at the interface. After curing for 60 minutes, the intensity of SFG methoxy signal at 2845 cm^{-1} increased (**Figure 3.4d)**, showing that more ordered methoxy group are present at the interface. We believe that methoxy groups diffused to the interface in the curing process and reacted at the interface to enhance adhesion. After curing for 15 minutes, strong SFG methoxy signals could be detected in **Figure 3.7a**. The methoxy C-H stretching signal intensity at 2845 cm^{-1} continued to increase from 15 to 60 min of the curing time (**Figure 3.4d**), showing that more methoxy groups were present

with order at the interface (even after some of the methoxy groups reacted at the interface). No SFG signal was detected at 3010 cm^{-1} in **Figure 3.7a**, suggesting that the epoxy groups may have already undergone ring opening with 15 min[81].

Before curing, no SFG methoxy signal at 2845 cm^{-1} could be detected from the d4-PET/GPS/DMMVS silica filled silicone interface in **Figure 3.4b**, indicating that methoxy groups are not present or not ordered at the interface. It is worth mentioning that the only difference between sample filled GPS/DMMVS silicone and the sample filled GPS/DMMVS/AC is that the filled GPS/DMMVS sample does not contain the AC component. After curing for 60 minutes, the intensity of the SFG methoxy signal at 2845 cm^{-1} only slightly increased as a shoulder (**Figure 3.4b)**, showing that small amount of ordered methoxy groups are present at the interface. As we discussed repeatedly, methoxy groups could diffuse to the interface in the curing process and react at the interface to enhance adhesion. After curing for 15 minutes, strong SFG methoxy signals could be detected in **Figure 3.7b**. Therefore, for the filled GPS/DMMVS silicone, initially methoxy groups are not present with order at the uncured silicone/polymer interface (**Figure 3.4b**). After curing for 15 minutes, methoxy groups diffused to the interface with order (some reacted as well), exhibiting a strong SFG methoxy signal at 2845 cm^{-1} (**Figure 3.7b**). Such interfacial methoxy groups reacted during the further curing process, leading to the decreased methoxy interface coverage, which reduced C-H stretching signal intensity at 2845 cm^{-1} (**Figure 3.4b**). The difference between **Figure 3.4b** and **3.4d** is due to the effect of AC on the silicone/polymer interfacial structure. AC promotes methoxy groups to continuously segregate to the interface, leading to strong methoxy SFG signal after curing the sample for 60 mins. Nevertheless, the methoxy interfacial segregation, ordering, and reaction play important roles in determining adhesion at the filled silicone/polymer interface, which can be observed using SFG.

3.3.2.4 Silicone Methyl (Si-CH3) Orientation Analysis

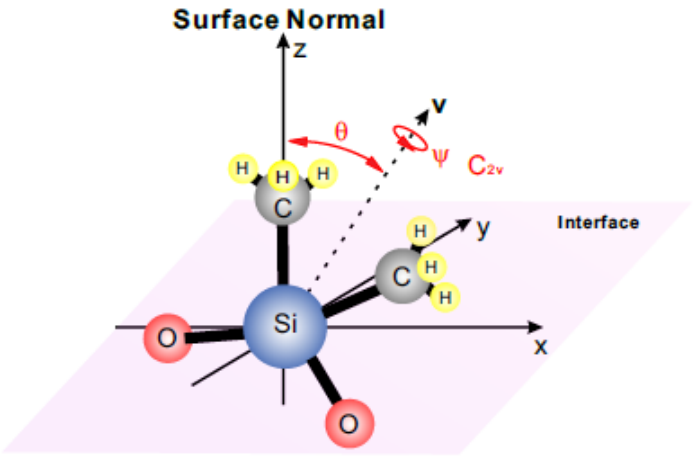

Figure 3.8 Schematic of silicone methyl groups oriented at the d4-PET/silicone interface. θ and ψ are tilt and twist angles for a $Si(CH_3)_2$ group.

Figure 3.8 displays the molecular structure and orientation of methyl groups in PDMS at interface. Note that **Θ** is the tilt angle and **Ψ** is the twist angle in the lab fixed coordination system. Although the individual methyl group belongs to **C3v** symmetry, the overall $Si(CH_3)_2$ group has a **C2v** symmetry. The vector **v** which is used to describe the orientation of two methyl groups, bisects between these two methyl groups. According to the previous publication, the average angle between the two neighboring methyl groups in PDMS is 112°. [82-83]

The "lying down" orientation of Si-CH_3 indicates a large tilt angle **Θ** versus the surface normal and the vector **v** leans more towards the interface. Likewise, the "standing up" orientation indicates a small tilt angle and the vector **v** tilts more away from the interface. To quantitatively analyze the orientation, the relationship between the tilt angle of the vector **v** and SFG methyl signal strength ratio $\chi_{ssp,s}/\chi_{ssp,as}$ was determined (**Figure 3.9**), which was reported in detail in the literature[82-84] and such details will not be discussed here. The twist angle was averaged in the calculation.

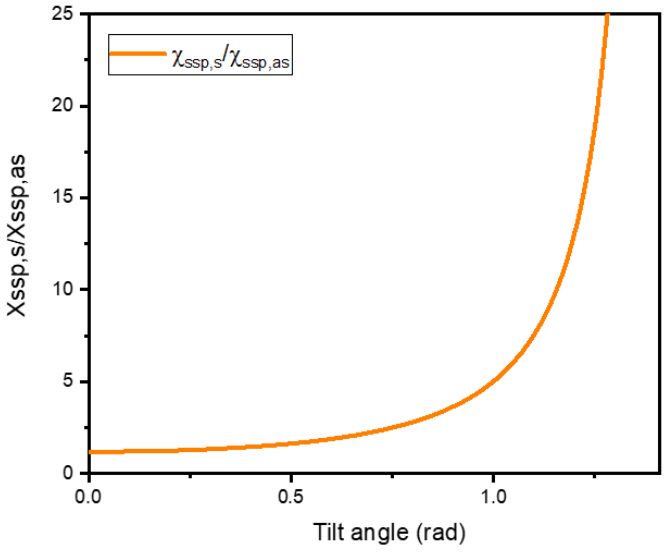

Figure 3.9 Dependence of tilt angle of the vector v versus the surface normal on the SFG methyl signal strength ratio $\chi_{ssp,s}/\chi_{ssp,as}$

In the text above, we mainly focused on the interfacial behavior of methoxy and epoxy groups. To understand the curing effect on other functional groups than methoxy/epoxy, e.g., the silicone Si-CH_3 structure at the silicone (with adhesion promoter)/d4-PET interface, we compared the SFG spectra displayed in **Figures 3.4a** and **3.4b**. It was found that the symmetric C-H stretching signal of the Si-CH_3 group decreased for both cases after curing, leading to much smaller intensity ratios between the symmetric and asymmetric stretching signals. The silicone methyl groups appear to stand up more at the interface after curing, similar to the neat silicone cases which will be presented below in **Figure 3.10**. By comparing **Figures 3.4c** and **3.4d**, we can see that the vector **v** between the two interfacial silicone methyl groups also stands up more at the interface after curing, similar to what was observed in other silicone systems.

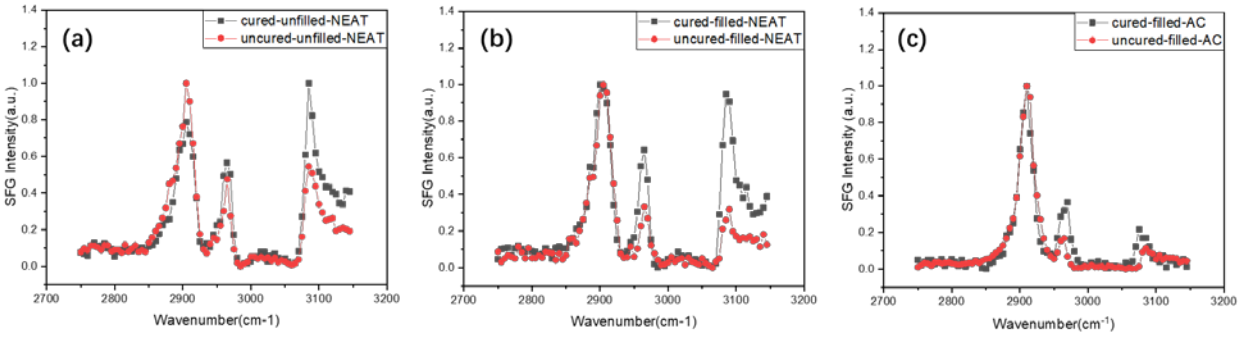

Figure 3.10 SFG spectra collected from buried interfaces between d-PET and different neat silicone samples: (a) uncured and cured neat silicone without silica filler; (b) uncured and cured neat silicone with silica filler; (c) uncured and cured silicone with silica filler and adhesion catalyst.

SFG spectra collected from the interfaces between d4-PET and neat PDMS, or neat PDMS with silica filler, or neat PDMS with both silica filler and AC are illustrated in **Figure 3.10**. These systems do not contain the adhesion promoting γ-GPS-DMMVS mixture. These spectra are very similar and dominated by three peaks, which can be assigned to the symmetric and anti-symmetric C-H stretching modes of the Si-CH_3 group at 2900 cm^{-1} and 2965 cm^{-1}, and the phenyl ring aromatic C-H stretching mode of d4-PET at 3085 cm^{-1}, respectively (**Table 3.2**).[84, 67-69] This indicates that the interfacial molecular structures as judged from the C-H stretching frequency region appear to be similar regardless of the addition of low levels of silica filler or zirconium adhesion catalyst.

Silica filler effect:

The individual effect of the addition of silica filler to silicone on the molecular structure at the silicone/d4-PET interface can be elucidated by comparing the spectra displayed in **Figure 3.10a** with **3.10b**. Since the 3085 cm^{-1} peak is from the d4-PET substrate, not from the silicone, we will not discuss this peak. As discussed above, in all four spectra, there are two peaks below 3000 cm^{-1}: They are centered around 2900 cm^{-1} and 2965 cm^{-1}, which are assigned to the C-H symmetric

and anti-symmetric stretching modes of the Si-CH_3 groups in the silicone matrix, respectively. [84, 67-69] The features of the SFG spectra collected from the systems with and without silica filler in silicone are very similar, indicating that there is no substantial change of interfacial molecular structure in the C-H stretching region at the uncured and cured silicone/d4-PET interfaces. If we compare the SFG spectra collected from the uncured silicone/d4-PET interfaces to those from the cured silicone/d4-PET interfaces, for both cases with and without filler, the intensity ratio of the symmetric Si-CH_3 stretching and anti-symmetric Si-CH_3 stretching decreases after curing. This indicates that for both cases the silicone methyl groups at interface tilt less towards the interface (or "standing up" more) after curing, indicating interfacial reconstruction upon curing. Nevertheless, for neat silicone samples without the adhesion promoting γ-GPS-DMMVS mixture, addition of silica filler to the silicone sample does not appear to have a substantial effect on the Si-CH_3 interfacial structure in the C-H stretching region at the silicone matrix/d4-PET interface.

Adhesion catalyst effect:

Similarly, by comparing SFG spectra displayed in **Figure 3.10b** with **3.10c,** the effect of adhesion catalyst on the interfacial molecular structure at the silicone/d4-PET interface before and after curing can be revealed. With the addition of the adhesion catalyst, the symmetric Si-CH_3 stretching peak center slightly shifted from 2900 cm^{-1} to 2910 cm^{-1}. In addition, the intensity ratio of the symmetric and asymmetric C-H stretching signals of Si-CH_3 groups increased for both uncured and cured silicone, indicating that the bisector angle between the two methyl groups (vector **v)** lies down more at the interface. Besides the slight spectral differences, there are no other significant differences between the SFG spectra collected from the silicone/d4-PET interfaces with and without adhesion catalyst. The added adhesion catalyst also does not appear to have a substantial effect on the interfacial structure in the C-H groups at the silicone/d4-PET interface.

With the added catalysts, the vector between the two silicone methyl groups stands up more at the interface after curing (**Figure 3.10c**). This is similar to the trend observed from the other two cases without adhesion catalyst in silicone as presented above.

In summary, the above three silicone/d4-PET interfaces were investigated, including the filled and unfilled NEAT silicone, and filled and unfilled AC silicone. The spectral features are similar, indicating similar interfacial structures. After curing, at the silicone/d4-PET interface for all the three silicone systems, the vector **v** between two silicone methyl groups stands up more at the interface. The addition of silica fillers to the silicone sample does not change the collected SFG spectra substantially, showing that fillers do not have strong effect on the interfacial structure. The addition of adhesion catalyst also does not substantially change the collected SFG spectra, only slightly shifting the band positions and intensity ratios, showing some small effect of the added adhesion catalyst on the interfacial structure of the silicone/d4-PET interface. This indicates that adhesion catalyst appears at or near the interface to slightly change the chemical environment, leading to small peak shift, which agrees with the purpose to add the catalyst to segregate to the interface to facilitate the reaction with the water moisture at the interface (**Scheme 3.2b**). **Scheme 3.2c** shows the catalyzed reaction between silicone and epoxy silane molecules.

Table 3.4 Fitting parameter

Fig. 3.4a-cured			**Fig. 3.4a-uncured**			
ωi (cm^-	Γi (cm^-	Aq	ωi (cm^-	Γi (cm^-	Aq (a.u.)	assignme
2840	7.2	6.7	2845	7.2	1.6	sym
2875	8.5	3.0	2875	8.0	5.8	sym CH_2
2910	8.0	0.5	2897	7.8	6.1	sym CH_3
2925	7.8	-5.6	2935	7.8	-14.3	asym
2965	10.6	-10.8	2965	10.6	-20.2	asym
3013	15.3	0.2	3010	15.0	9.8	Epoxy
3085	9.2	0.9	3085	9.3	15.0	Phenyl
Fig. 3.4b-cured			**Fig. 3.4b-uncured**			
ωi (cm^-	Γi (cm^-	Aq	ωi (cm^-	Γi (cm^-	Aq (a.u.)	assignme
2840	7.1	2.7	2845	7.2	0.4	sym
2875	8.2	6.1	2875	8.0	3.6	sym CH_2
2910	8.5	1.3	2898	7.8	6.2	sym CH_3
2925	7.7	-8.6	2935	7.8	-15.3	asym
2965	10.6	-6.8	2965	10.6	-11.0	asym
3013	15.3	0.2	3010	15.0	5.9	Epoxy
3085	9.2	1.2	3085	9.3	4.6	Phenyl
Fig. 3.4c-cured			**Fig. 3.4c-uncured**			
ωi (cm^-	Γi (cm^-	Aq	ωi (cm^-	Γi (cm^-	Aq (a.u.)	assignme
2840	7.2	13.5	2845	7.2	16.8	sym
2875	8.5	1.3	2875	8.0	2.5	sym CH_2
2910	7.9	0.2	2900	7.8	0.4	sym CH_3
2925	8.1	-14.3	2935	7.8	-15.1	asym
2965	10.6	-16.7	2965	10.6	-15.9	asym
3012	15.3	0.9	3010	15.0	9.0	Epoxy
3085	9.2	1.2	3085	9.3	4.7	Phenyl
Fig. 3.4d-cured			**Fig. 3.4d-uncured**			
ωi (cm^-	Γi (cm^-	Aq	ωi (cm^-	Γi (cm^-	Aq (a.u.)	assignme
2840	7.1	4.1	2845	7.2	0.7	sym
2875	8.5	3.5	2875	8.0	2.3	sym CH_2
2910	8.0	1.2	2901	7.9	8.5	sym CH_3
2925	7.8	-7.2	2935	8.3	-1.0	asym
2965	11.6	-9.8	2965	10.3	-7.9	asym
3013	15.9	3.3	3010	15.0	6.9	Epoxy
3085	9.2	1.1	3085	9.3	1.8	Phenyl
Fig. 7a			**Fig. 7b**			
ωi (cm^-	Γi (cm^-	Aq	ωi (cm^-	Γi (cm^-	Aq (a.u.)	assignme
2840	7.2	7.2	2845	7.2	3.2	sym
2875	8.5	6.8	2875	8.0	3.8	sym CH_2
2910	7.9	1.9	2900	7.8	1.9	sym CH_3
2925	7.8	-10.7	2935	7.8	-4.7	asym
2965	10.6	-8.9	2965	10.5	-7.6	asym
3012	15.3	2.3	3010	15.2	4.0	Epoxy

3085	9.4	0.9	3085	9.3	2.2	Phenyl

There is peak center shift in SFG spectra fitting. The degree of shift is within the resolution of the spectrometer (~6 cm^{-1}), which is reasonable.

3.3.3 Correlation between SFG and Adhesion Measurement Results

In **Section 3.3.1** above, we presented the adhesion measurement results of silica filled silicones on PET. In **Section 3.3.2** above, we discussed SFG results on silicone/d4-PET interfaces of both silicone samples with and without silica fillers. Here we will correlate the SFG and adhesion data for silica filled silicones.

3.3.3.1 Samples GPS/DMMVS/AC and GPS/DMMVS vs. sample AC

SFG results presented in **Figures 3.4b**, **3.4d**, **3.7a**, and **3.7b** show clearly that epoxy and methoxy groups of γ-GPS in samples GPS/DMMVS/AC and GPS/DMMVS segregated to the interfaces and reacted during the curing process. Such interfacial chemical reactions greatly strengthen the adhesion between d4-PET and silicone adhesives, as measured by adhesion testing experiments (**Figure 3.3a**). Differently, sample AC does not contain γ-GPS, and no chemical reaction can be detected from the epoxy and methoxy groups by SFG (**Figure 3.6**), leading to a much lower adhesion (**Figure 3.3a**).

3.3.3.2 Sample GPS/DMMVS/AC vs. GPS/DMMVS

Comparison of the SFG spectra shown in **Figure 3.4b** from sample GPS/DMMVS and the SFG spectra shown in **Figure 3.4d** from sample GPS/DMMVS/AC shows that AC facilitates the interfacial segregation of the methoxy and epoxy groups, which were involved in the interfacial

reactions. Therefore, the adhesion of GPS/DMMVS/AC is stronger than that of GPS/DMMVS (**Figure 3.3a**).

3.3.3.3 Sample GPS/DMMVS/AC vs. OTMS/DMMVS/AC

OTMS does not contain epoxy group, therefore no epoxy signal can be detected from the uncured silicone/d4-PET interface (**Figure 3.5a**). Comparison between **Figure 3.4d** and **3.5a** shows that the epoxy group in γ-GPS facilitates the interfacial segregation and order of the methoxy groups. The lack of interfacial epoxy reaction and the less ordered methoxy groups at the interface lead to much lower adhesion at the silicone adhesive/d4-PET interface for the sample OTMS/DMMVS/AC compared to GPS/DMMVS/AC (**Figure 3.3a**).

3.3.3.4 Sample AC vs. AC/DMMVS/OTMS

Small SFG signals of methoxy groups can be detected from the interface between d4-PET and the sample OTMS/MVA/AC (**Figure 3.5a**), but not from the d4-PET/sample AC interface (**Figure 3.6**). The interfacial reaction of methoxy groups leads to slightly higher adhesion at the interface between d4-PET and OTMS/DMMVS/AC compared to that between d4-PET and the sample AC (**Figure 3.3a**).

3.3.3.5 Time-dependence

Figure 3.3 shows that longer annealing time increased adhesion for all the three samples AC, GPS/DMMVS, and GPS/DMMVS/AC. **Figure 3.6** shows that the adhesion increase for the sample AC is likely because the interfacial orientation change of the Si-CH_3 and d4-PET phenyl groups after a longer annealing time. For samples GPS/DMMVS and GPS/DMMVS/AC, a longer annealing time facilitates the interfacial segregation and chemical reaction of the methoxy groups (**Figures 3.4b**, **3.4d**, and **3.7**), leading to stronger adhesion.

From the above discussions we can see that the adhesion measurement results presented in **Figure 3.3** can be fully interpreted by the SFG data on interfacial structures.

3.4 Conclusion

SFG was used to investigate molecular structures at buried silicone/d4-PET interfaces before and after silicone curing, in an *in situ* nondestructive manner. Silicone matrices with different added compositions such as adhesion promoters, filler, and catalysts were investigated to understand the effects of various additives on the buried interfacial structure. SFG results were compared to adhesion data to understand the molecular mechanisms of adhesion of silicone adhesives.

With adhesion promoter in the silicone matrix, the added filler appeared to reduce the interfacial segregation and ordering of methoxy groups of the adhesion promoter at the silicone/polymer interface before curing. During the curing process, methoxy groups can segregate with order to the interface and then react at the interface. The adhesion catalyst appears to promote the segregation of methoxy groups to the silicone/polymer interface, especially in the absence of silica filler. With the filler in the silicone matrix, with the high curing temperature, adhesion catalyst can also facilitate the segregation and ordering of methoxy groups, which helps to enhance the silicone adhesion.

In addition to the methoxy group, we also studied the effect of epoxy end group of γ-GPS in the adhesion promoting mixture on interfacial structures and adhesion at the silicone/polymer interface. The interfacial epoxy groups appeared to participate in the chemical reaction at the interface, enhancing the adhesion. In addition, the epoxy groups may facilitate the segregation with ordering of methoxy groups at the silicone/polymer interface. These results suggest the epoxy groups also play significant roles in enhancing the silicone/polymer adhesion.

For the first time, this research provides direct mechanistic insights to the role of functional groups responsible for adhesion of silicone adhesives to PET with silica filler at the molecular level. It was found that interfacial behavior of both methoxy and epoxy groups plays significant roles in determining silicone adhesion to polymer surfaces. Such interfacial behavior is greatly influenced by the composition of the adhesion promoter and the addition of the silica fillers as well as the adhesion catalyst. Such knowledge offers important direction for optimizing the design of silicone adhesive interfacial structure by varying the compositions in the silicone matrix to improve adhesion to polymeric substrates such as polyesters. This research elucidated the interfacial behavior of adhesion promoters and the impacts of fillers and catalysts in silicone on such behavior qualitatively. We believe that by systematically studying silicone adhesives with different amounts of adhesion promoters added in the future, we should be able to quantitatively correlate the silicone adhesion strength to SFG spectral fitting parameters, providing quantitative understanding on silicone adhesion effect to polymer materials.

3.5 References

1. Brinson, H. F.; Dostal, C.; Woods, M.; Ronke, A.; Henry, S.; Daquila, J.; O'Keefe, K., Engineered Materials Handbook Volume 3 Adhesives and Sealants. *ASM Intern.* **1990**, 33-38.
2. Research, Z. M. Global industry perspective, comprehensive analysis and forecaset 2015−2021 https://www.zionmarketresearch.com/report/silicone-market.
3. Wong, C., High-Performance Silicone Gel as Integrated-Circuit-Device Chip Protection: Cure Study and Electrical Reliability. ACS Publications: 1989.
4. Goff, D.; Yuan, E.; Long, H.; Neuhaus, H., Polymers for Electronic Packaging and Interconnection (Am. Chem. Soc., Symp. Ser. 407) ed JH Lupinski, RS Moore. Washington, DC: American Chemical Society) p: 1989.
5. Hampshire, W.; Dostal, C., Electronic Materials Handbook, Volume 1 Packaging. *ASM Intern.* **1989**.
6. Teisala, H.; Baumli, P.; Weber, S. A.; Vollmer, D.; Butt, H.-J. r., Grafting Silicone at Room Temperature—a Transparent, Scratch-resistant Nonstick Molecular Coating. *Langmuir* **2020,** *36* (16), 4416-4431.
7. Brook, M. A., *Silicon in organic, organometallic, and polymer chemistry*. Wiley New York:

2000; Vol. 123.
8. Kinloch, A., Adhesion and adhesives: science and technology" eng in. London: Chapman and Hall: 1987.
9. Yacobi, B.; Martin, S.; Davis, K.; Hudson, A.; Hubert, M., Adhesive bonding in microelectronics and photonics. *J. Appl. Phys.* **2002,** *91* (10), 6227-6262.
10. Ahn, D.; Shephard, N. E.; Rolley, P. A.; McMillan, C. S., Correlating adhesion with local composition at silicone elastomer-polymer interfaces. *Polym. Prepr.***2005,** *46* (1).
11. Hall, J. R.; Westerdahl, C. A.; Devine, A. T.; Bodnar, M. J., Activated gas plasma surface treatment of polymers for adhesive bonding. *J. Appl. Polym. Sci.* **1969,** *13* (10), 2085-2096.
12. O'Neill, L.; Shephard, N.; Leadley, S.; O'Hare, L.-A., Atmospheric pressure plasma polymerised primer to promote adhesion of silicones. *J. Adhes.* **2008,** *84* (6), 562-577.
13. Mine, K.; Nishio, M.; Sumimura, S., Heat curable organopolysiloxane compositions containing adhesion additives. Google Patents: 1977.
14. Schulz, J. R., Self-adhering silicone compositions and preparations thereof. Google Patents: 1978.
15. Suzuki, T.; Kasuya, A., Adhesion of addition-reaction type silicone elastomers. *J. Adhes. Sci. Technol.* **1989,** *3* (1), 463-473.
16. Gellman, A.; Naasz, B.; Schmidt, R.; Chaudhury, M.; Gentle, T., Secondary neutral mass spectrometry studies of germanium-silane coupling agent-polymer interphases. *J. Adhes. Sci. Technol.* **1990,** *4* (1), 597-601.
17. Gentle, T.; Schmidt, R.; Naasz, B.; Gellman, A.; Gentle, T., Organofunctional silanes as adhesion promoters: direct characterization of the polymer/silane interphase. *J. Adhes. Sci. Technol.* **1992,** *6* (2), 307-316.
18. Gray, T. E.; Lutz, M. A., Curable organopolysiloxane compositions with improved adhesion. Google Patents: 1997.
19. Ahn, D.; Rolley, P. A., Adhesives having improved chemical resistance and curable silicone compositions for preparing the adhesives. Google Patents: 2006.
20. Thiedmanu, W.; Tolan, F.; Pearce, P.; Morris, C., Silane coupling agents as adhesion promoters for aerospace structural film adhesives. *J. Adhes.* **1987,** *22* (3), 197-210.
21. Walker, P., Organosilanes as adhesion promoters. *J. Adhes. Sci. Technol.* **1991,** *5* (4), 279-305.
22. Gent, A.; Schultz, J., Effect of wetting liquids on the strength of adhesion of viscoelastic material. *J. Adhes.* **1972,** *3* (4), 281-294.
23. Andrews, E.; Kinloch, A. J., Mechanics of adhesive failure. II. *Proceedings of the Royal Society of London. A. Mathematical and Physical Sciences* **1973,** *332* (1590), 401-414.
24. Ahn, D.; Shull, K. R., Effects of methylation and neutralization of carboxylated poly (n-butyl acrylate) on the interfacial and bulk contributions to adhesion. *Langmuir* **1998,** *14* (13), 3637-3645.
25. Gong, L.; Xiang, L.; Zhang, J.; Chen, J.; Zeng, H., Fundamentals and Advances in the Adhesion of Polymer Surfaces and Thin Films. *Langmuir* **2019,** *35* (48), 15914-15936.
26. Shen, Y., Surface properties probed by second-harmonic and sum-frequency generation. *Nature* **1989,** *337* (6207), 519-525.
27. Bain, C. D., Sum-frequency vibrational spectroscopy of the solid/liquid interface. *J. Chem. Soc., Faraday Trans.* **1995,** *91* (9), 1281-1296.
28. Buck, M.; Himmelhaus, M., Vibrational spectroscopy of interfaces by infrared–visible sum frequency generation. *J. Vac. Sci. Technol. A* **2001,** *19* (6), 2717-2736.

29. Lambert, A. G.; Davies, P. B.; Neivandt, D. J., Implementing the theory of sum frequency generation vibrational spectroscopy: a tutorial review. *Appl. Spectrosc. Rev.***2005,** *40* (2), 103-145.
30. Ahn, D.; Dhinojwala, A., Sum frequency generation vibrational spectroscopy of silicone surfaces & interfaces. In *Silicone Surf. Sci.*, Springer: 2012; pp 23-58.
31. Roy, S.; Freiberg, S.; Leblanc, C.; Hore, D. K., Surface structure of acrylate polymer adhesives. *Langmuir* **2017,** *33* (8), 1763-1768.
32. Li, B.; Zhou, J.; Xu, X.; Yu, J.; Shao, W.; Fang, Y.; Lu, X., Solvent quality affects chain conformational order at the polymer surface revealed by sum frequency generation vibrational spectroscopy. *Polymer* **2013,** *54* (7), 1853-1859.
33. Yu, T.; Zhou, G.; Hu, X.; Ye, S., Transport and organization of cholesterol in a planar solid-supported lipid bilayer depend on the phospholipid flip-flop rate. *Langmuir* **2016,** *32* (44), 11681-11689.
34. Tan, J.; Zhang, J.; Luo, Y.; Ye, S., Misfolding of a Human Islet Amyloid Polypeptide at the Lipid Membrane Populates through β-Sheet Conformers without Involving α-Helical Intermediates. *J. Am. Chem. Soc.***2019,** *141* (5), 1941-1948.
35. Lovering, K. A.; Bertram, A. K.; Chou, K. C., Transient phase of ice observed by sum frequency generation at the water/mineral interface during freezing. *J. Phys. Chem. Lett.***2017,** *8* (4), 871-875.
36. Nonkumwong, J.; Erasquin, U. J.; Sy Piecco, K. W.; Premadasa, U. I.; Aboelenen, A. M.; Tangonan, A.; Chen, J.; Ingram, D.; Srisombat, L.; Cimatu, K. L. A., Successive Surface Reactions on Hydrophilic Silica for Modified Magnetic Nanoparticle Attachment Probed by Sum-Frequency Generation Spectroscopy. *Langmuir* **2018,** *34* (43), 12680-12693.
37. Obiles, R.; Premadasa, U. I.; Cudia, P.; Erasquin, U. J.; Berger, J. M.; Martinez, I. S.; Cimatu, K. L. A., Insights on the Molecular Characteristics of Molecularly Imprinted Polymers as Monitored by Sum Frequency Generation Spectroscopy. *Langmuir* **2019,** *36* (1), 180-193.
38. Han, X.; Leng, C.; Shao, Q.; Jiang, S.; Chen, Z., Absolute orientations of water molecules at zwitterionic polymer interfaces and interfacial dynamics after salt exposure. *Langmuir* **2018,** *35* (5), 1327-1334.
39. Xiao, M.; Jasensky, J.; Gerszberg, J.; Chen, J.; Tian, J.; Lin, T.; Lu, T.; Lahann, J.; Chen, Z., Chemically immobilized antimicrobial peptide on polymer and self-assembled monolayer substrates. *Langmuir* **2018,** *34* (43), 12889-12896.
40. Chen, X.; Sagle, L. B.; Cremer, P. S., Urea orientation at protein surfaces. *J. Am. Chem. Soc.***2007,** *129* (49), 15104-15105.
41. Peng, Q.; Chen, J.; Ji, H.; Morita, A.; Ye, S., Origin of the overpotential for the oxygen evolution reaction on a well-defined graphene electrode probed by in situ sum frequency generation vibrational spectroscopy. *J. Am. Chem. Soc.***2018,** *140* (46), 15568-15571.
42. Ye, H.; Abu-Akeel, A.; Huang, J.; Katz, H. E.; Gracias, D. H., Probing organic field effect transistors in situ during operation using SFG. *J. Am. Chem. Soc.***2006,** *128* (20), 6528-6529.
43. Zhang, C.; Parada, G. A.; Zhao, X.; Chen, Z., Probing Surface Hydration and Molecular Structure of Zwitterionic and Polyacrylamide Hydrogels. *Langmuir* **2019,** *35* (41), 13292-13300.
44. Perera, H. G.; Lu, T.; Fu, L.; Zhang, J.; Chen, Z., Probing the Interfacial Interactions of Monoclonal and Bispecific Antibodies at the Silicone Oil–Aqueous Solution Interface by Using Sum Frequency Generation Vibrational Spectroscopy. *Langmuir* **2019,** *35* (44), 14339-14347.
45. Zuo, B.; Inutsuka, M.; Kawaguchi, D.; Wang, X.; Tanaka, K., Conformational relaxation of poly (styrene-co-butadiene) chains at substrate interface in spin-coated and solvent-cast films. *Macromolecules* **2018,** *51* (6), 2180-2186.

46. Nguyen, H. K.; Sugimoto, S.; Konomi, A.; Inutsuka, M.; Kawaguchi, D.; Tanaka, K., Dynamics gradient of polymer chains near a solid interface. *ACS Macro Lett.***2019,** *8* (8), 1006-1011.
47. Bhattacharyya, D.; Montenegro, A.; Dhar, P.; Mammetkuliyev, M.; Pankow, R. M.; Jung, M. C.; Thompson, M. E.; Thompson, B. C.; Benderskii, A. V., Molecular orientation of poly-3-hexylthiophene at the buried interface with fullerene. *J. Phys. Chem. Lett.***2019,** *10* (8), 1757-1762.
48. Lu, X.; Zhang, C.; Ulrich, N.; Xiao, M.; Ma, Y.-H.; Chen, Z., Studying polymer surfaces and interfaces with sum frequency generation vibrational spectroscopy. *Anal. Chem.***2017,** *89* (1), 466-489.
49. Xiao, M.; Lu, T.; Lin, T.; Andre, J. S.; Chen, Z., Understanding Molecular Structures of Buried Interfaces in Halide Perovskite Photovoltaic Devices Nondestructively with Sub-Monolayer Sensitivity Using Sum Frequency Generation Vibrational Spectroscopy. *Adv. Energy Mater.* **2020,** *10* (26), 1903053.
50. Xiao, M.; Mohler, C.; Tucker, C.; Walther, B.; Lu, X.; Chen, Z., Structures and adhesion properties at polyethylene/silica and polyethylene/nylon interfaces. *Langmuir* **2018,** *34* (21), 6194-6204.
51. Chen, C.; Wang, J.; Chen, Z., Surface restructuring behavior of various types of poly (dimethylsiloxane) in water detected by SFG. *Langmuir* **2004,** *20* (23), 10186-10193.
52. Chen, C.; Wang, J.; Loch, C. L.; Ahn, D.; Chen, Z., Demonstrating the feasibility of monitoring the molecular-level structures of moving polymer/silane interfaces during silane diffusion using SFG. *J. Am. Chem. Soc.***2004,** *126* (4), 1174-1179.
53. Loch, C. L.; Ahn, D.; Chen, C.; Chen, Z., Polymer-silane interactions probed by sum frequency generation vibrational spectroscopy. *J. Adhes.* **2005,** *81* (3-4), 319-345.
54. Loch, C. L.; Ahn, D.; Chen, Z., Sum frequency generation vibrational spectroscopic studies on a silane adhesion-promoting mixture at a polymer interface. *J. Phys. Chem. B* **2006,** *110* (2), 914-918.
55. Ahn, D.; Shephard, N. E.; Olney, P. A.; McMillan, C. S., Thermal gradient enabled XPS analysis of PDMS elastomer adhesion to polycarbonate. *Macromolecules* **2007,** *40* (11), 3904-3906.
56. Chen, C.; Wang, J.; Even, M. A.; Chen, Z., Sum frequency generation vibrational spectroscopy studies on “buried” polymer/polymer interfaces. *Macromolecules* **2002,** *35* (21), 8093-8097.
57. Chen, Z., Understanding surfaces and buried interfaces of polymer materials at the molecular level using sum frequency generation vibrational spectroscopy. *Polym. Int.* **2007,** *56* (5), 577-587.
58. Lu, X.; Li, D.; Kristalyn, C. B.; Han, J.; Shephard, N.; Rhodes, S.; Xue, G.; Chen, Z., Directly probing molecular ordering at the buried polymer/metal interface. *Macromolecules* **2009,** *42* (22), 9052-9057.
59. Chen, Z., Investigating buried polymer interfaces using sum frequency generation vibrational spectroscopy. *Prog. Polym. Sci.* **2010,** *35* (11), 1376-1402.
60. Wang, H.; Gan, W.; Lu, R.; Rao, Y.; Wu, B., Quantitative spectral and orientational analysis in surface sum frequency generation vibrational spectroscopy (SFG-VS). *Int. Rev. Phys. Chem.* **2005,** *24* (2), 191-256.
61. Chen, Z.; Shen, Y.; Somorjai, G. A, Studies of polymer surfaces by sum frequency generation vibrational spectroscopy. *Annu. Rev. Phys. Chem.* **2020,** *53* (1), 437-465.
62. Shen, Y. J. N., Surface properties probed by second-harmonic and sum-frequency

generation. **1989,** *337* (6207), 519-525.
63. Loch, C. L.; Ahn, D.; Vázquez, A. V.; Chen, Z., Diffusion of one or more components of a silane adhesion-promoting mixture into poly (methyl methacrylate). *J. Colloid Interface Sci.* **2007,** *308* (1), 170-175.
64. Vázquez, A. V.; Shephard, N. E.; Steinecker, C. L.; Ahn, D.; Spanninga, S.; Chen, Z., Understanding molecular structures of silanes at buried polymer interfaces using sum frequency generation vibrational spectroscopy and relating interfacial structures to polymer adhesion. *J. Colloid Interface Sci.* **2009,** *331* (2), 408-416.
65. Zhang, C.; Hankett, J.; Chen, Z., Molecular level understanding of adhesion mechanisms at the epoxy/polymer interfaces. *ACS Appl. Mater. Interfaces.***2012,** *4* (7), 3730-3737.
66. Zhang, C.; Myers, J. N.; Chen, Z., Molecular behavior at buried epoxy/poly (ethylene terephthalate) interface. *Langmuir* **2014,** *30* (42), 12541-12550.
67. Myers, J. N.; Chen, Z., Surface plasma treatment effects on the molecular structure at polyimide/air and buried polyimide/epoxy interfaces. *Chin. Chem. Lett.* **2015,** *26* (4), 449-454.
68. Vázquez, A. V.; Holden, B.; Kristalyn, C.; Fuller, M.; Wilkerson, B.; Chen, Z., Surface and buried interfacial structures of epoxy resins used as underfills studied by sum frequency generation vibrational spectroscopy. *ACS Appl. Mater. Interfaces.***2011,** *3* (5), 1640-1651.
69. Vazquez, A. V.; Boughton, A. P.; Shephard, N. E.; Rhodes, S. M.; Chen, Z., Molecular structures of the buried interfaces between silicone elastomer and silane adhesion promoters probed by sum frequency generation vibrational spectroscopy and molecular dynamics simulations. *ACS Appl. Mater. Interfaces.***2010,** *2* (1), 96-103.
70. Tse, M. F., Adhesion of maleic anhydride functionalized polyolefins and blends. *J. Appl. Polym. Sci.* **2014,** *131* (3).
71. Shen, Y., Surfaces probed by nonlinear optics. *Surf. Sci.* **1994,** *299*, 551-562.
72. Shen, Y., The Principles of Nonlinear Optics (Wiley, New York, 1984). *Google Scholar W. Lee Smith, Opt. Eng* **1978,** *17*, 489.
73. Zhang, L.; Tan, J.; Pei, Q.; Ye, S., Film Thickness and Surface Plasmon Tune the Contribution of the SFG Signals from Buried Interface and Air Surface. *Chin. J. Chem. Phys.* **2020,** *33*, 532–539.
74. Zhang, C.; Chen, Z., Probing molecular structures of poly (dimethylsiloxane) at buried interfaces in situ. *J. Phys. Chem. C* **2013,** *117* (8), 3903-3914.
75. Kozerski, G. E.; Gallavan, R. H.; Ziemelis, M. J., Investigation of trialkoxysilane hydrolysis kinetics using liquid chromatography with inductively coupled plasma atomic emission spectrometric detection and non-linear regression modeling. *Anal. Chim. Acta* **2003,** *489* (1), 103-114.
76. Surivet, F.; My, L. T.; Pascault, J. P.; Tho, P. Q., Organic-inorganic hybrid materials. 1. Hydrolysis and condensation mechanisms involved in alkoxysilane-terminated macromonomers. *Macromolecules* **1992,** *25* (17), 4309-4320.
77. Yang, L.; Feng, J.; Zhang, W.; Qu, J.., Experimental and computational study on hydrolysis and condensation kinetics of γ-glycidoxypropyltrimethoxysilane (γ-GPS). *Appl. Surf. Sci.* **2010,** *257* (3), 990-996.
78. Britt, D. W.; Hlady, V., Protonation, hydrolysis, and condensation of mono-and trifunctional silanes at the air/water interface. *Langmuir* **1999,** *15* (5), 1770-1776.
79. Fedors, R. F., A method for estimating both the solubility parameters and molar volumes of liquids. *Polym Eng. Sci.* **1974,** *14* (2), 147-154.
80. Lee, J. N.; Park, C.; Whitesides, G. M., Solvent compatibility of poly (dimethylsiloxane)-

based microfluidic devices. *Anal. Chem.***2003,** *75* (23), 6544-6554.
81. Hao, W.; Hu, J.; Chen, L.; Zhang, J.; Xing, L.; Yang, W., Isoconversional analysis of non-isothermal curing process of epoxy resin/epoxide polyhedral oligomeric silsesquioxane composites. *Polym. Test.* **2011,** *30* (4), 349-355.
82. Kataoka, S.; Cremer, P. S., Probing molecular structure at interfaces for comparison with bulk solution behavior: Water/2-propanol mixtures monitored by vibrational sum frequency spectroscopy. *J. Am. Chem. Soc.* **2006,** *128* (16), 5516-5522.
83. Zheng, P.; McCarthy, T. J., Rediscovering silicones: Molecularly smooth, low surface energy, unfilled, uv/vis-transparent, extremely cross-linked, thermally stable, hard, elastic pdms. *Langmuir* **2010,** *26* (24), 18585-18590.
84. Zhang, C.; Chen, Z., Probing molecular structures of poly (dimethylsiloxane) at buried interfaces in situ. *J. Phys. Chem. C* **2013,** *117* (8), 3903-3914.

Chapter 4 Probing Covalent Interactions at a Silicone Adhesive/Nylon Interface

Adapted with permission from *Langmuir* **2022,** *38 (8), 2590-2600* (Copyright 2020 American Chemical Society).

4.1 Introduction

The research presented in this chapter will also focus on silicone adhesives. Compared to mechanical fasteners, polymeric adhesives can offer advantages in more uniform stress distribution, lighter weight construction, streamlined processing, and lower energy consumption for joining materials. The demand of bonding technologies is projected to reach $66.44bn by 2027 with increasing applications of adhesives across the global aerospace, automotive, construction, electronics, and medical sectors.[1] As discussed in the previous chapter, silicone elastomers, typically with poly(dimethyl siloxane) (PDMS) as the major component, represent a common and commercially important class of polymeric adhesives. The advantages of addition-cured silicones include their extreme heat and UV stability, low temperature flexibility, water repellency, controllable curing process and low surface energy that provides exceptional wetting characteristics.[2-7] However, due to their non-polar nature and intrinsic lack of reactive organofunctional groups, many addition-cured silicone adhesives exhibit poor adhesion to common polymers.[8] To address this issue, blending organo-silanes as adhesion promoters into curable self-priming silicone elastomer formulations offers an efficient and cost-effective alternative to the use of primers or pretreatments on polymer surfaces such as plasma, flame or corona surface treatments.[9-10] The introduction of a small amount of these organo-silane molecules

into silicone or the substrate surface introduces functionalities at the interface which can form covalent bonds between polymer substrates and silicone matrix, and enhance the silicone adhesion strength, as we presented in the previous chapter.[11-25]

In the previous chapter, SFG was applied to study buried silicone/PET interface.[26-47] Here, SFG was utilized to investigate the interfacial molecular structure at buried silicone interface with nylon 6,6/6 copolymer (Ultramid C33-02 from BASF) in situ. SFG was shown to be effective for investigating buried polymer interfaces, including silicone elastomer/thermoplastic interfaces.[127, 136, 148-151, 198-201] However, most of the silicone elastomer interfacial studies have focused on the orientation, alignment and reactivity of alkoxysilane groups, and none have studied adhesion of silicone elastomers to polyamides, which are widely used as engineering thermoplastics both in textiles and in structural components because of their excellent strength, toughness and heat resistance. The semi-crystalline nature of common polyamides such as nylon makes them a challenge for developing adhesion. In this work, SFG was used to provide detailed interfacial structure information at the molecular level between a silicone elastomer and nylon copolyamide PA 6/66 before and after the elastomer is cured. SFG results provide evidence of the interfacial chemical reactions that occur at the buried polymer interfaces, helping to elucidate the adhesion mechanisms of different silanes in addition-cured silicone systems. These results were shown to correlate to adhesion properties.

In previous work we have examined the molecular interactions between poly(ethylene terephthalate) (PET) and silicone with silane adhesion promoters, and successfully detected interfacial reactions involving methoxy and epoxy groups.[48] To the best of our knowledge, the interfacial chemical reactions between nylon and silane-containing silicone have not been examined and the related molecular adhesion promotion mechanisms are not yet well understood.

Here we studied two silicone adhesives, both containing trialkoxysilane coupling agents, but with different organofunctional groups. Specifically, we studied the [3-(trimethoxysilyl) propyl] succinic anhydride silane with succinic anhydride (SA) end group and (3-glycidoxypropyl)trimethoxy (γ-GPS) silane with an epoxy end group. The organofunctionality of the silane coupling agent was found to influence the interfacial structural changes after the interfacial chemical reactions probed by SFG. The resulting adhesion property changes were examined by the 90^{o} peeling test, which can be correlated to SFG results.

4.2 Materials and Methods

4.2.1 Materials and Sample Preparation

The molecular structures of the relevant species of interest to our adhesion studies are presented in **Scheme 4.1**. The nylon studied here was Ultramid C33 nylon-02 (copolyamide PA 6/66) which was obtained from BASF. The nylon thin film was prepared by spin-coating with nylon/m-cresol (5 mg/mL) solution onto the CaF_2 prism at 2000 rpm for 60 seconds (VTC-100 spin-coater, MTI Corporation). The nylon film thickness is around 15 nm, measured by ellipsometry. Samples for adhesion testing were prepared using high molecular weight commercial grade nylon 6/66 natural sheet (Boedeker Plastics Inc.).

The adhesion promoters γ-GPS and [3-(trimethoxysilyl) propyl] succinic anhydride silane (described as SA silane below) were purchased from Millipore-Sigma and Gelest, respectively. Hydroxyl terminated dimethyl methylvinyl co-siloxanol (DMMVS) and Zirconium (IV) acetylacetonate were supplied by Dow Chemical Company, and are thought to function as co-adhesion promoter and adhesion catalyst, respectively. The two-part platinum-catalyzed addition cured silicone elastomer with a base vinyl-terminated PDMS having number average molecular weight (Mn) of about 60 kDa was provided by Dow Chemical Company.[48] Part A contains

Karstedt's catalyst complex and SiVi-functional PDMS. Part B contains SiVi-functional PDMS, cross-linker with methylhydridosiloxane, and catalyst inhibitor. More detailed formulation can be found in Ref. 48. Neat silicone free of adhesion promoting compounds was used for benchmark study as a control. Two fully formulated silicone formulas with different functional silanes were compared. In the following, SA/DMMVS/AC silicone and GPS/DMMVS/AC silicone refer to the silicone materials containing SA silane and γ-GPS silane respectively, substituted in a 1:1 molar ratio; compositions can be found in **Table 4.1**. For SE and SE-GPS/DMMVS/AC samples, the sum of the weight ratios of different components is 100, therefore the weight ratios are weight percentages. The sample SE-SA/DMMVS/AC has the same composition as SE-GPS/DMMVS/AC, except the silane. To facilitate the comparison of the two samples, the weight ratios of various components were kept the same except the silanes (because of the different molecular weights of SA silane and γ-GPS silane). Thus the sum of the weight ratios of different components in SE-SA/DMMVS/AC is higher than 100. All formulations were prepared by manually mixing different components for 10 minutes and degassed in vacuum for 15 minutes at ambient laboratory temperature.

Table 4.1 Compositions (in weight ratio) of the silicone adhesive samples investigated. More details about Part A and Part B can be found in ref. 48.

Sample (weight ratio)	PartA	Part B	AC	DMMVS	γ-GPS	SA
SE	50.00	50.00	-	-	-	-
SE-GPS/DMMVS/AC	49.70	49.25	0.30	0.15	0.60	-
SE-SA/DMMVS/AC	49.70	49.25	0.30	0.15	-	0.77

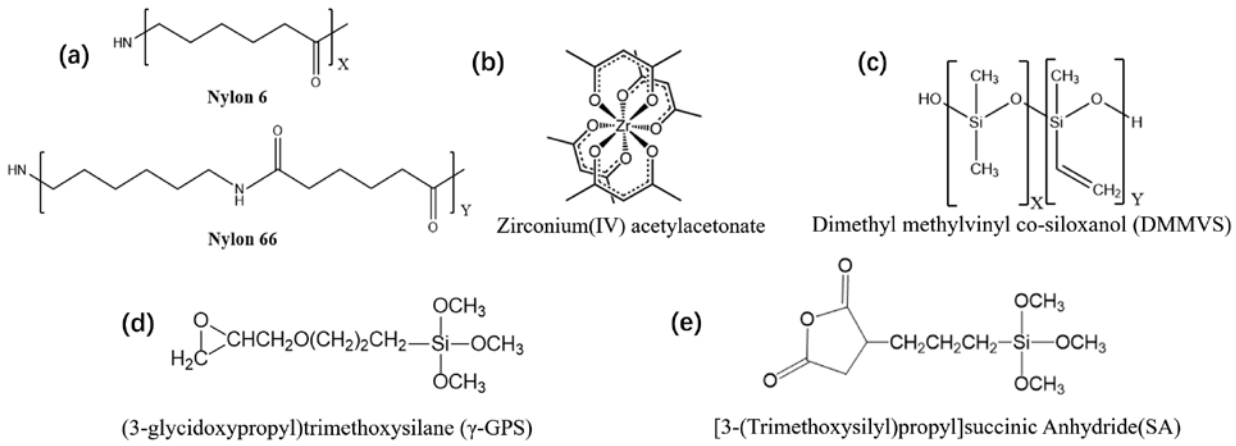

Scheme 4.1 Molecular structures of materials used in this research: a) nylon, b) adhesion catalyst (AC), c) DMMVS, d) γ-GPS, e) SA silane.

4.2.2 Experimental Methods

4.2.2.1 SFG Experiment

A thick semi-opaque film of silicone (around 5 mm thick) was applied by scraper onto the nylon-coated prism for SFG study. The silicone film is sufficiently thick so that no SFG signals could be produced from the air/silicone interface on the other side. The silicone samples for SFG experiments and adhesion experiments were cured in air oven at 150 ^{o}C for 1 hour. Both SSP (S-polarized sum frequency beam, S- polarized visible beam, P- polarized IR beam) and PPP polarization combinations of the input and output beams were used in SFG spectra collection.

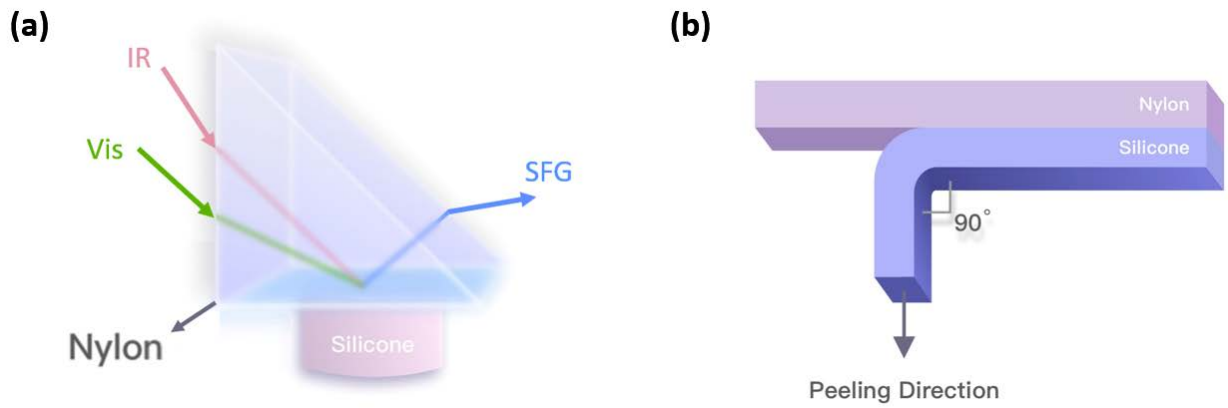

Figure 4.1 Schematics of SFG experiment and adhesion test: (a) SFG experimental sample geometry, (b) experiment configuration of 90º adhesion test.

4.2.2.2 Adhesion Strength Test

A 90-degree static loaded peel test was conducted to determine the adhesion strength between the silicone elastomer and nylon, as shown in **Figure 4.1b**. The adhesion data provides correlations between macroscopic adhesion property and microscopic interfacial molecular structures detected by SFG. Adhesion testing samples were prepared by spreading 0.4 cm thick silicone layer onto 6 cm long, 2.4 cm wide nylon plates and cured in air oven at 150 ºC for 1 hour. Before the peel test, samples were stored at ambient temperature in air for 12 hours after removal from the curing oven to reach equilibrium.

Each sample used for the adhesion test was manually peeled back along the nylon/silicone interface about 1 cm from one end to expose a tab for attachment of a weight. We then clamped a weight to the exposed silicone tab and allowed it to freely hang vertically relative to the substrate which was supported on each end in a horizontal orientation as shown in **Figure 4.1b**. The suspended weight was gradually increased until adhesion failure occurred at the silicone/nylon interface. All the failures were observed to be adhesive (interfacial) failures. The minimum weight to induce failure normalized by the width of the peel specimen was recorded as the adhesion

strength. If the adhesion failure occurred during the first trial, the experiment was repeated with a new sample using a lighter weight.[48]

4.3 Results and Discussion

4.3.1 Buried Nylon/Silicone (with or without Adhesion Promoters) Interface: SFG N-H Stretching Signal

SFG spectra collected in the N-H stretching frequency region (3000 - 3500 cm^{-1}) from the nylon/neat uncured silicone (without adhesion promoter) interface and the interfaces between nylon and formulated uncured silicones with different adhesion promoters (SA/DMMVS/AC silicone and GPS/DMMVS/AC silicone) are shown in **Figure 4.2**. In each of the SFG SSP and PPP spectra collected before curing, a broad peak centered at around 3300 cm^{-1} was observed, which can be assigned to the N-H stretching mode of nylon (since these silicone elastomer systems do not contain any NH groups).[46-47, 76-77] SFG spectra collected from nylon in contact with different silicone samples are varied, due to different interactions between nylon and silicone or different adhesion promoters. The thin nylon film used in the study has two interfaces: one is the nylon/CaF_2 prism interface, and the other is the nylon/silicone interface. Both interfaces may generate SFG signals from nylon. As we demonstrated previously, the nylon/CaF_2 interface does not generate detectable SFG signals.[45-47] Likely this is due to a random orientation distribution of the nylon molecules at the nylon/prism interface. Also, if the signals were dominated by the contributions from the nylon/CaF_2 interface, the SFG spectra collected from the nylon films in contact with different silicone samples should be similar, which was not what we observed. **Figure 4.1** shows clearly that SFG spectra collected from nylon in contact with different silicone samples vary in peak center locations and intensity ratios between the SSP and PPP signals, further confirming that

the SFG N-H stretching signals collected from nylon film in contact with silicone are mainly contributed from the nylon/silicone interface, not the nylon/CaF_2 interface.

The SFG N-H stretching signals from the uncured silicone sample shown in **Figure 4.2** are thought to originate from NH_2 (amine end groups of nylon) or NH (amide groups in the nylon backbone). The detected SFG signals show that the NH_2 and/or NH groups are ordered and not lying down at the nylon/silicone interface. As evidenced from the N-H stretching PPP/SSP signal intensity ratios of the various samples, it can be concluded that NH_2 and/or NH groups of nylon orient differently at the interface in each system.[78-79] From these differences, it can be inferred that the Nylon NH_2 and NH moieties' orientations are affected by the interfacial environments created by the various silicone systems through different interactions (e.g., hydrogen bonding interactions, hydrophobic interactions, etc.).

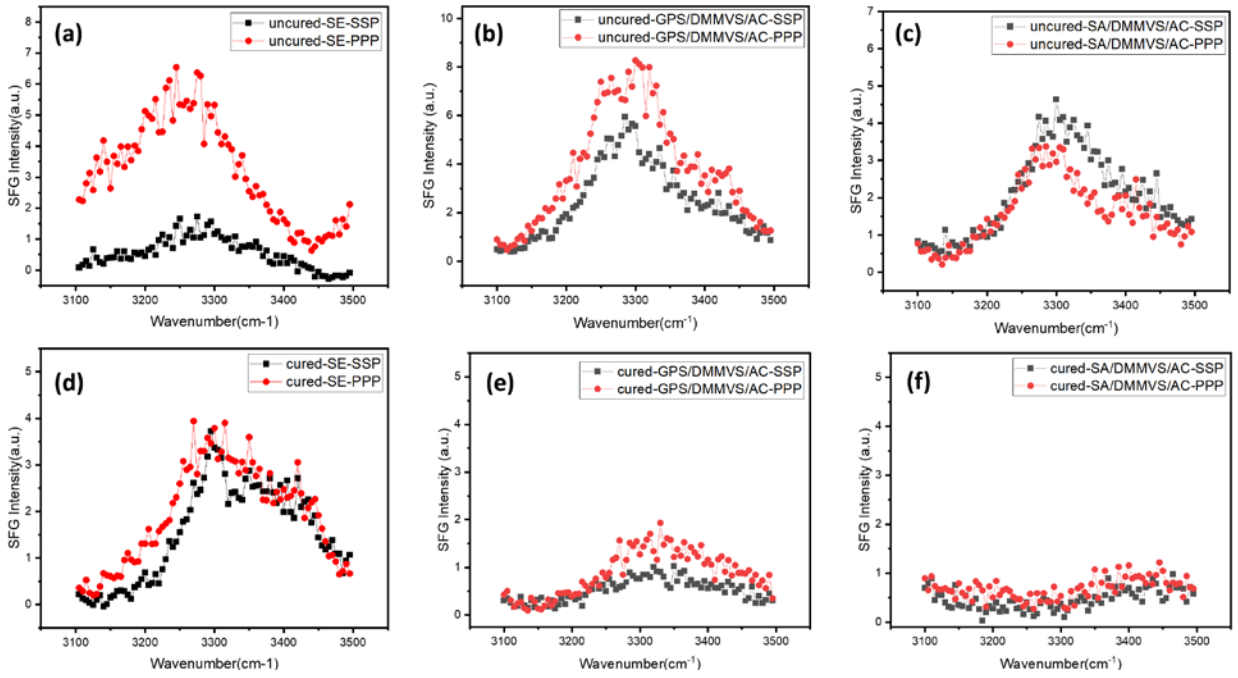

Figure 4.2 SFG spectra in the N-H stretching frequency region collected from buried interfaces between nylon and silicone with different adhesion promoter samples: (a) uncured neat silicone; (b) uncured GPS/DMMVS/AC silicone; (c) uncured SA/DMMVS/AC silicone; (d) cured neat silicone; (e) cured GPS/DMMVS/AC silicone; (f) cured SA/DMMVS/AC silicone. Black and red spectra are SFG SSP and PPP spectra, respectively.

After curing, strong SFG N-H stretching signals could still be detected from the nylon/neat silicone interface but with an obviously different PPP/SSP intensity ratio. This indicates that the NH_2 and/or NH groups are still present and ordered at the nylon/neat silicone interface after curing. This is anticipated because the silicone elastomer does not contain any functionality which is expected to be reactive with nylon NH_2 and/or NH groups. The PPP/SSP intensity ratio change shows that the average tilt angle of NH_2 and/or NH groups changed at the neat silicone/nylon interface after curing. This is reasonable because nylon could have varied interactions with uncured and cured neat silicone at the interface, leading to different interfacial orientations of NH/NH_2 groups. Such varied interactions also led to the spectral feature changes (e.g., through hydrogen bonding strength changes due to different interfacial environments) after curing the sample.

In contrast, after curing much weaker SFG N-H stretching signals were detected from the nylon/GPS/DMMVS/AC silicone interface, and no N-H stretching signals were observed from the nylon/SA/DMMVS/AC silicone interface. The disappearance of SFG signal could result from two situations: one is that the NH_2 and/or NH groups were not present at the interface anymore, the other is that they were still present at the interface but with random orientation (or disordered). Comparing with the neat silicone case, if the interfacial interactions between nylon and silicone are the dominating interfacial interactions, strong SFG signals should still be detected from the NH_2 and/or NH groups. The vastly different SFG signals observed here demonstrate that the adhesion promoters in SA/DMMVS/AC and GPS/DMMVS/AC silicones substantially influenced the interactions between nylon and silicone, changing the interfacial NH_2 and/or NH behavior. As shown below, the silane adhesion promoters can react with nylon NH_2 and/or NH groups, leading to the decrease or disappearance of the SFG N-H stretching signals.

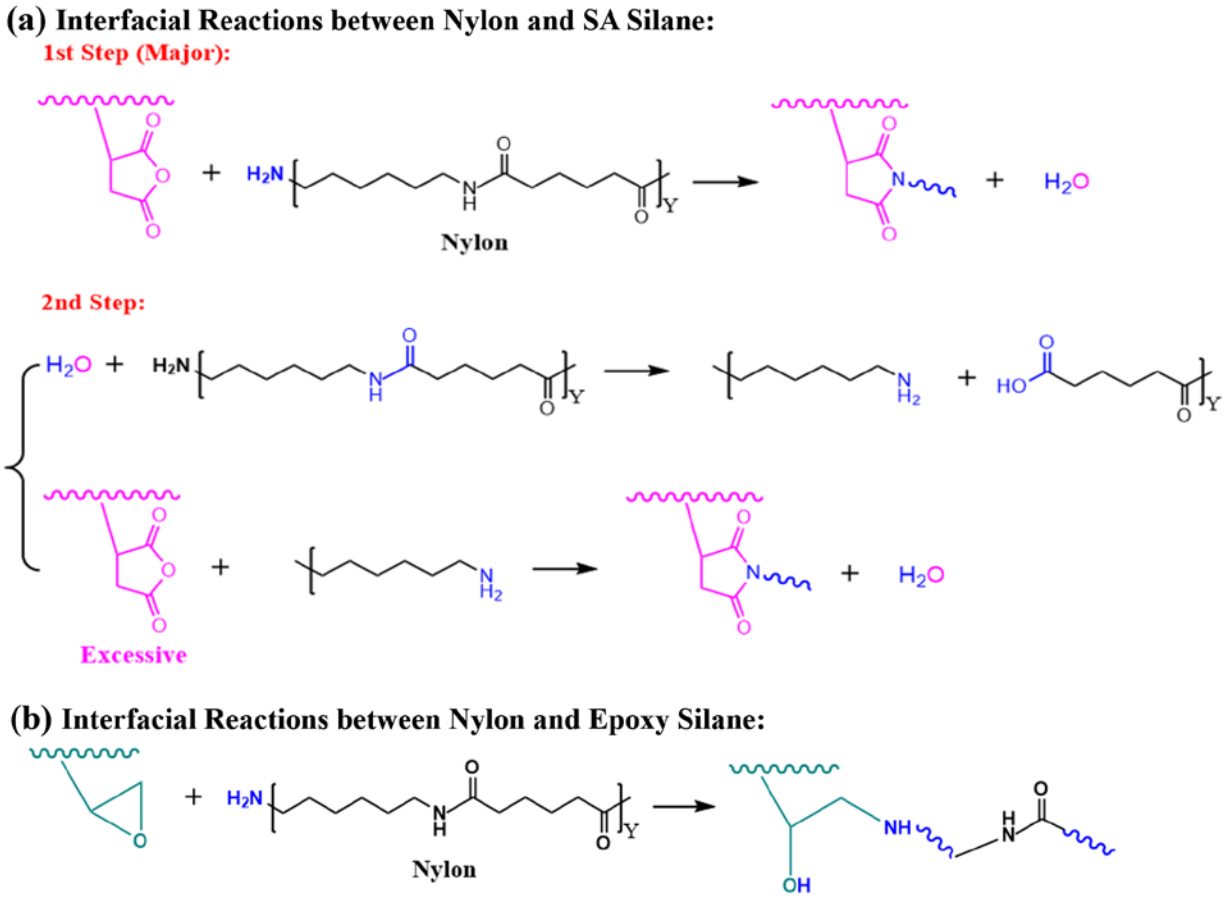

Scheme 4.2 Two reaction mechanisms at the buried nylon/silicone interfaces: (a) nylon/SA/DMMVS/AC silicone interface, (b)nylon/GPS/DMMVS/AC silicone interface.

It is well known that the SA groups and epoxy groups in the two silanes we studied can react with nylon NH_2 groups. The reaction mechanisms have been extensively reported in the literature.[80-90] SA can also react with nylon NH groups.[85] We believe the reduction or disappearance of the SFG N-H stretching signals is due to the consumption of the interfacial NH_2 or NH groups by chemical reactions. **Scheme 4.2** shows possible chemical reactions between nylon and two silanes in silicone. In our previous study, it was found that SA groups could directly react with nylon NH_2 end groups at the buried interface between nylon and SA-grafted polyolefin layers, producing imide linkages and amic acid moieties as reaction intermediates and water as a by-product.[47] This reaction happens readily, and the conversion rate can be very high - up to 99% at 180 ^oC for 2

minutes.[91] The produced water molecules may hydrolyze the amide groups in the nylon backbone to produce additional NH_2 groups. If there is excess SA in the system, the second reaction between the produced NH_2 groups and excess SA might happen. This likely occurred at the nylon/SA/DMMVS/AC silicone interface because nylon with high molecular weight which we used do not have many NH_2 end groups. Using the group contribution method of Fedors to estimate solubility parameters,[92] we obtain the following values: 8.49 $(cal/cm^3)^{0.5}$ for γ-GPS, 9.43 $(cal/cm^3)^{0.5}$ for SA silane, and 7.38 $(cal/cm^3)^{0.5}$ for PDMS. More details about the solubility parameter calculations will be present in the next section. Due to the "like dissolves like" rule, substances with similar solubility parameter have better compatibility. Therefore, SA silane is more likely to drive to an interface because of less compatibility in PDMS. Even though the amount of SA silane is only 0.77 wt% in the silicone adhesive, SA may be very interfacially active and thus an excess amount of SA groups could be present at the interface after all the nylon NH_2 end groups have reacted. In contrast, although the epoxy rings of γ-GPS silane could react with NH_2 groups, no water by-product would be produced, as shown in **Scheme 4.2.** Thus no reaction of NH band is observed at the buried interface.

The SFG observations in the N-H stretching frequency region can be explained as following: For the nylon/neat silicone interface, no reactive groups from neat silicone can react with the nylon NH_2 or NH groups. As a result, stronger SFG signals would be detected from the interface before and after curing. At the nylon/GPS/DMMVS/AC silicone interface, SFG results show that the interfacial aggregated epoxy end groups of the γ-GPS silane could react with the nylon NH_2 amine end groups, but not the amide NH groups. Therefore, strong SFG N-H stretching signals would be collected before curing, but weak signals were detected after curing (from the amide NH groups). At the nylon/SA/DMMVS/AC silicone interface, the interfacial aggregated silane SA groups

reacted with both NH_2 groups at molecular chain ends and NH groups in the backbone. As a result, strong SFG N-H stretching signals could be detected before curing, but no N-H signals could be seen in both SSP and PPP SFG spectra after curing. The SFG results in the C=O stretching frequency region which will be presented below further confirm these conclusions.

4.3.2 Group Contribution Solubility Parameter Estimation

The Hildebrand solubility parameters (δ) of 8.49 $(cal/cm^3)^{0.5}$ for γ-GPS, 9.43 $(cal/cm^3)^{0.5}$ for SA silane, and 7.38 $(cal/cm^3)^{0.5}$ for PDMS were obtained using the method of Fedors,[71] which is based upon the cohesive energy density relationship of Equation 4.1

$$\delta = \sqrt{\frac{\Delta E_v}{V}} = \sqrt{\frac{\sum_i \Delta e_i}{\sum_i \Delta v_i}} \qquad \textbf{Eq. 4.1}$$

in which ΔE_v is the energy of vaporization, and Δe_i and Δv_i are the group contributions of the i sub-structural unit that comprises a given molecule. All the group contribution parameters used were taken from **Table 4.2** of Fedors, which provides a list of Δe_i and Δv_i for many of the most commonly occurring and useful structural units found in polymers, including siloxanes.

Table 4.2 Fedors group contribution parameters at 25.0 °C for Hildebrand solubility parameter estimates reported in this study.[71]

Group	**Δe_i (cal / mol)**	**Δv_i (cm^3 / mol)**	**Δfw (Da)**
a) Si	810	0.0	28.090
b) O	800	3.8	16.000
c) CH_3	1125	33.5	15.034
d) CH_2	1180	16.1	14.027
e) CH	820	-1.0	13.018

f) C	350	-19.2	12.010
g) $H_2C=$	1030	28.5	14.026
h) -CH=	1030	13.5	13.018
j) C_2O_3 (anhydride)	7300	30.0	72.020
k) Ring Closure (3 or 4 atoms)	750	18.0	0.000
l) Ring Closure (5 or more atoms)	250	16.0	0.000

Below are the details of the calculations for each of the compounds. For this calculation of high molecular weight PDMS, we use the vinyl terminated PDMS (Mn=60,000 Da) studied in this research as the structure to model. Vinyl terminated PDMS with a number average formula weight of 60,000 Da corresponds to the following number average structure in closest integer form. The structure of PDMS is shown below:

$$CH_2=CH\text{-}Si(CH3)_2\text{-}O\text{-}[Si(CH_3)_2\text{-}O]_{807}\text{-}Si(CH_3)_2CH=CH_2$$

To apply Equation 4.1, we can first calculate the summation $\sum_i \Delta e_i$ for the numerator as follows:

$\Delta E_v = \sum_i \Delta e_i = 2*(\Delta e_g + \Delta e_h + \Delta e_a + 2*\Delta e_c) + \Delta e_b + 807*[\Delta e_a + 2*\Delta e_c + \Delta e_b]$

$= [2*(1030 + 1030 + 810 + 2*1125) + 800 + 807*[810 + 2*1125 + 800]]$ cal/mol

$= 3126060$ cal/mol

Similarly, for the denominator, we sum the molar volume contributions.

$V = \sum_i \Delta v_i = 2*(\Delta v_g + \Delta v_h + \Delta v_a + 2*\Delta v_c) + \Delta v_b + 807*[\Delta v_a + 2*\Delta v_c + \Delta v_b]$

$= [2*(28.5 + 13.5 + 0.0 + 2*33.5) + 3.8 + 807*[0.0 + 2*33.5 + 3.8]]$ cm^3/mol

$= 57357.4$ cm^3/mol

By substituting the formula weight (FW) group contribution parameters into the same formulas for ΔE_v and V, one can re-calculate the molecular weight of the compound as a cross-check to ensure key structural groups have not been omitted or double counted.

MW = $\sum_i \Delta fw_i$ = 2*(Δfw_g + Δfw_h + Δfw_a + 2*Δfw_c) + Δfw_b + 807*[Δfw_a + 2*Δfw_c + Δfw_b]

= [2*(14.026 + 13.018 + 28.090 + 2*15.034) + 16.000 + 807*[28.090 + 2*15.034 + 16.000] Da

= 60031.91 g/mol, which is consistent with the M_n of 60,000 Da of the structure.

$\delta = \sqrt{\frac{\Delta E_v}{V}}$ = (3126060 cal/mol / 57357.4 cm3/mol)$^{0.5}$ = 7.38 (cal/cm^3)$^{0.5}$

This value is in good agreement with literature values between 7.3 and 7.7 (cal/cm^3)$^{0.5}$.[219-220]

For this calculation of γ-GPS:

ΔE_v = $\sum_i \Delta e_i$ =Δe_d + Δe_b + Δe_e + Δe_k + Δe_d + Δe_b + 3∗Δe_d + Δe_a + 3∗(Δe_b + Δe_c)

= [1180 + 800 + 820 + 750 + 1180 + 800 + 3*1180 + 810 + 3*(800 + 1125)] cal/mol

= 15655 cal/mol

V = $\sum_i \Delta v_i$ = Δv_d + Δv_b + Δv_e + Δv_k + Δv_d + Δv_b + 3∗Δv_d + Δv_a + 3∗(Δv_b + Δv_c)

= [16.1 + 3.8 + -1.0 + 18.0 + 16.1 + 3.8 + 3*16.1 + 0.0 + 3*(3.8 + 33.5)] cm^3/mol

= 217 cm^3/mol

MW = $\sum_i \Delta fw_i$ = Δfw_d + Δfw_b + Δfw_e + Δfw_k + Δfw_d + Δfw_b + 3∗Δfw_d + Δfw_a + 3∗(Δfw_b + Δfw_c)

= [14.027 + 16.000 + 13.018 + 0.000 + 14.027 + 16.000 + 3*14.027 + 28.090 + 3*(16.000 + 15.034)] Da

= 236.345 Da, which agrees with the published formula weight for γ-GPS.

$\delta = \sqrt{\frac{\Delta E_v}{V}}$ = (15655 cal/mol / 217 cm3/mol)$^{0.5}$ = 8.49 (cal/cm^3)$^{0.5}$

For this calculation of SA silane:

$\Delta E_v = \sum_i \Delta e_i = \Delta e_j + \Delta e_d + \Delta e_e + \Delta e_l + 3*\Delta e_d + \Delta e_a + 3*(\Delta e_b + \Delta e_c)$

= [7300 + 1180 + 820 + 250 + 3*1180 + 810 + 3*(800 + 1125)]cal/mol

= 19675 cal/mol

$V = \sum_i \Delta v_i = \Delta v_j + \Delta v_d + \Delta v_e + \Delta v_l + 3*\Delta v_d + \Delta v_a + 3*(\Delta v_b + \Delta v_c)$

= [30.0 + 16.1 – 1.0 + 16.0 + 3*16.1 + 0.0 + 3*(3.8 + 33.5)] cm^3/mol

= 221.3 cm^3/mol

MW = $\sum_i \Delta fw_i = \Delta fw_j + \Delta fw_d + \Delta fw_e + \Delta fw_l + 3*\Delta fw_d + \Delta fw_a + 3*(\Delta fw_b + \Delta fw_c)$

= [72.0 +14.027 + 13.018 + 0.000 + 3*14.027 + 28.090 + 3*(16.000 + 15.034)] Da

= 262.33 Da, which agrees with the published formula weight for 3-(trimethoxysilyl) propylsuccinic anhydride.

$\delta = \sqrt{\frac{\Delta E_v}{V}}$ = (19675 cal/mol / 221.3 cm3/mol)$^{0.5}$ = 9.43 (cal/cm^3)$^{0.5}$

4.3.3 Buried Nylon/Silicone (with or without Adhesion Promoters) Interface: SFG C=O Stretching Signal

Figure 4.3 displays SFG spectra collected from the buried interfaces of nylon with various silicone samples in the C=O stretching frequency region. Before curing, the features of these collected SFG spectra from different interfaces between nylon and silicones with and without adhesion promotion silanes show a similar band around 1635 - 1640 cm^{-1}, assigned to the stretching mode of the amide C=O groups in the nylon backbone.[42,43] The PPP/SSP signal intensity ratios of this peak in the three spectra are also comparable, indicating the average orientations of the amide C=O groups are similar at different nylon/silicone interfaces. The SFG spectra collected before curing are also similar to those collected from the nylon/air interface.[46,47]

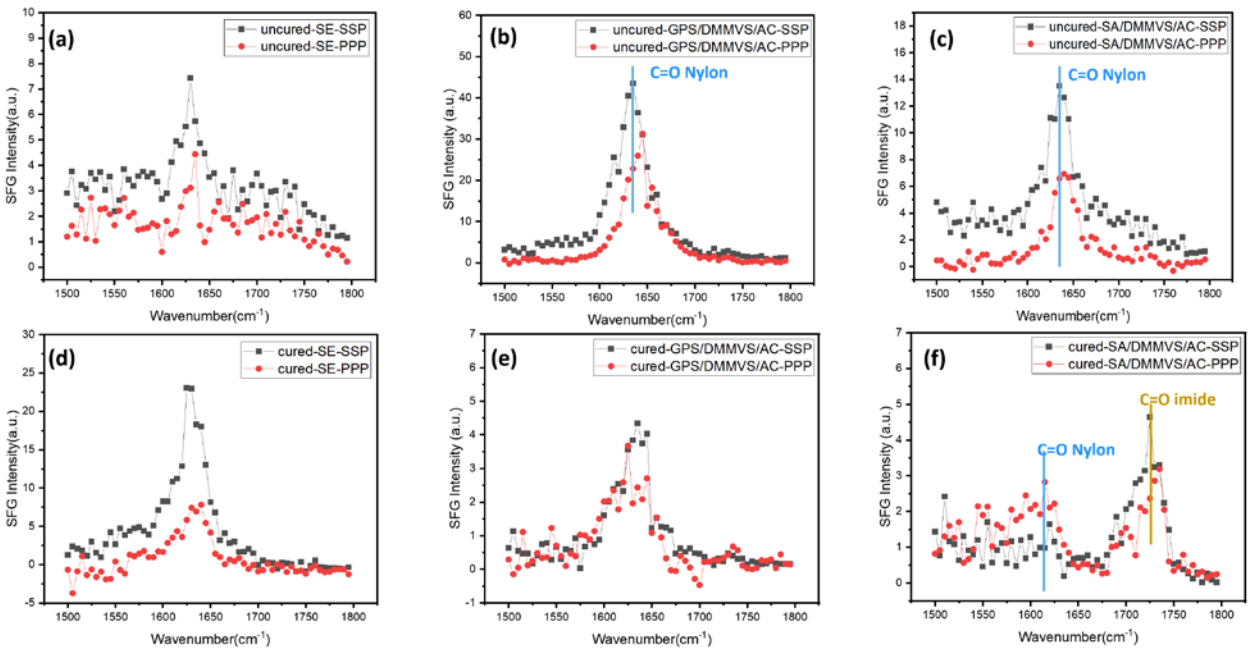

Figure 4.3 SFG spectra in the C=O stretching frequency region collected from buried interfaces between nylon and silicone with different adhesion promoter samples: (a) uncured neat silicone; (b) uncured GPS/DMMVS/AC silicone; (c) uncured SA/DMMVS/AC silicone; (d) cured neat silicone; (e) cured GPS/DMMVS/AC silicone; (f) cured SA/DMMVS/AC silicone. Black and red spectra are SFG SSP and PPP spectra, respectively.

After curing, the SFG spectra collected from the three nylon/silicone interfaces vary substantially. For the nylon/neat silicone interface, the SFG amide C=O signals were detected, but with a different PPP/SSP ratio from that measured from SFG spectra collected from the interface before curing. This agrees with the fact that the nylon amide C=O groups did not react with silicone at the interface, which is reasonable because in the neat silicone there is no reactive component which can react with the nylon amide C=O groups. The different intensity ratio shows that the C=O orientations changed after curing at the interface, which may be caused by the annealing effect on the C=O groups at the interface, or different interactions between interfacial C=O groups and uncured as well as cured (cross-linked) PDMS molecules. For the nylon/GPS/DMMVS/AC silicone interface, the amide C=O signals still dominate the collected SFG spectra, which is consistent with the results obtained from the SFG studies in the N-H stretching frequency region

discussed above. The epoxy groups of the γ-GPS silane could only react with the nylon amine NH_2 end groups but not the amide NH backbone groups because no intermediate byproduct water molecules could be formed from the above reaction to facilitate the hydrolysis reaction to produce NH_2 groups from nylon amide groups. Therefore, the nylon backbone C=O groups would not participate in the reaction, leading to no significant changes in the bands observed in the carbonyl C=O stretching frequency region in the SFG spectra from the nylon/GPS/DMMVS/AC silicone interface before and after curing. In contrast, for the nylon/SA/DMMVS/AC silicone interface, a new peak centered around 1725 cm^{-1} was detected, which could be assigned to the imide group and/or the carboxylic acid group – the products of the interfacial reaction between nylon and SA as shown in **Scheme 4.2** above.[47] Besides this new peak, the original nylon amide C=O signal was barely observed after curing, with much weaker intensity. The decreased SFG amide C=O signal reveals that the nylon NH groups were involved in the interfacial reaction, as we proposed above. The presence of the SFG signal of the reaction products (imide and carboxylic acid), the absence of the reactant nylon amide NH groups in backbone, and the greatly decreased nylon amide I signal are well correlated with each other.

The combined SFG studies in the N-H and C=O stretching frequency regions better elucidated the reaction mechanisms between nylon and silicones with different silane adhesion promoters proposed in **Scheme 4.2**. At the nylon/SA/DMMVS/AC silicone interface, the nylon NH_2 end groups reacted with the silane SA groups first, producing imide groups and water as by-product. Secondly, the water molecules hydrolyzed the exposed amide NH groups to generate additional NH_2 groups that reacted with the excess SA groups at the interface. The above reactions produced new C=O moieties (imide group and carboxylic acid) at the interface, leading to the detection of the 1725 cm^{-1} peak. These reactions consumed interfacial nylon NH_2 end groups and backbone

amide groups, resulting in the disappearance of the SFG N-H stretching signal and the substantially decreased amide C=O signal. At the nylon/GPS/DMMVS/AC silicone interface, the silane epoxy end groups reacted with the nylon NH_2 groups, without generating water molecules. Therefore, there was no additional NH_2 groups which could react with the excess epoxy groups in the silicone system. Such an interfacial reaction led to the substantial decrease of the SFG N-H stretching signal and no obvious change in the amide C=O stretching spectral features and relative intensity ratio of the SSP and PPP signals.

It is interesting to observe that the C=O stretching signal intensities increased after curing for the SFG spectra collected from the nylon/neat silicone interface, but decreased for the nylon/GPS/DMMVS/AC silicone interface. For the nylon/neat silicone interface, curing has an annealing effect for nylon, which may lead to a more ordered interfacial C=O structure, resulting in increased SFG C=O signal intensity. For the nylon/GPS/DMMVS/AC silicone interface, during the curing process, in addition to the participation of silanes in the chemical reactions to form covalent bonds at the interface, diffusion of silanes into the nylon substrate could occur, followed by self-condensation to form an interpenetrated network across the nylon/GPS/DMMVS/AC silicone interface. This greatly reduced the ordering at the interface, leading to substantially decreased SFG C=O signal intensity, as observed (**Figures 4.3b** and **4.3e**). Although the C=O groups are more disordered at the cured nylon/GPS/DMMVS/AC silicone interface, the average orientation of the C=O groups is similar to that before curing, but with a broader orientation distribution, resulting in a similar PPP/SSP signal intensity ratio but greatly reduced signal intensities after curing.

4.3.4 Adhesion Test Results

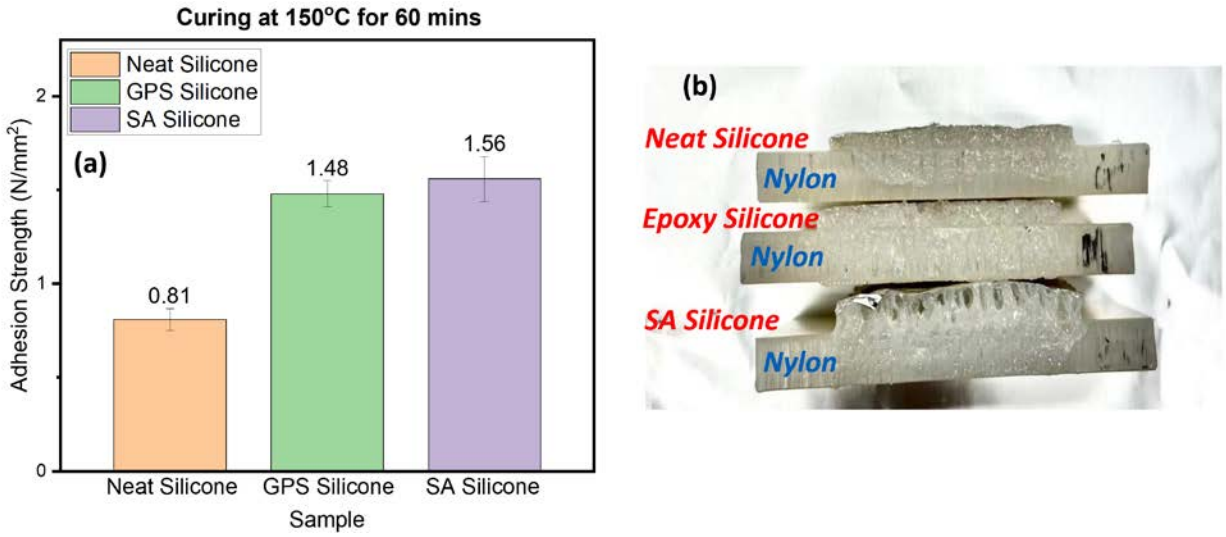

Figure 4.4 (a) Adhesion strengths measured from different nylon/silicone interfaces; (b) Photos of the cross sections of different silicone systems.

Covalent bonding offers one of the strongest and most robust molecular interactions. Forming covalent bonds at the interface between a substrate and an adhesive is expected to improve adhesion strength and durability, provided the bond is irreversible under relevant environmental aging conditions. Here adhesion tests were conducted and the results are shown in **Figure 4.4,** together with photos of the cross sections of different silicone systems in contact with nylon. The following results can be obtained from the adhesion testing results:

（1） Compared to the adhesion strength measured at the nylon/neat silicone interface, the addition of small amount of reactive adhesion promoting silane molecules to silicone enhances the adhesion strength between nylon and silicone (83% improvement with the addition of γ-GPS silane and 93% improvement with the addition of SA silane to silicone). The adhesion promotion mechanism of the silane molecules is partially attributed to the formation of covalent bonds at interface by interfacial reactions observed by the SFG analysis, evidenced by the observation of the SFG imide or/and carboxylic acid signal and the decreased SFG N-H signal. As discussed

above, interpenetration at the interface may also contribute the adhesion enhancement.

（2） For the adhesion promoters SA silane and γ-GPS silane, the difference in measured adhesion strength is small, which may suggest the main determinant of interfacial adhesion strength is from the reactions involving the amine NH_2 end groups of the nylon substrate. This result verifies the above explanation of our SFG results and the proposed reaction schemes.

Figure 4.4b shows that in the sample cross-section photo of the nylon/SA/DMMVS/AC silicone interface, some holes caused by gas bubbles were observed in the silicone adhesives after curing, which were not observed in nylon interfaces with neat silicone or GPS/DMMVS/AC silicone. Since all the samples had the same sample preparation (including the same de-gas) procure, the initial amount of gas (air) trapped in all three silicone materials should be similar before curing. While there can be many sources of void formation while curing the samples at 150 ^{o}C, we will note that the unique level of voiding in SA/DMMVS/AC silicone is consistent with a mechanism that involves water vapor generation from the interfacial reaction between nylon and SA/DMMVS/AC silicone shown in **Scheme 4.2**. Although nucleation and growth of voids during peeling can affect measured adhesion strength values upon peeling of soft adhesives like pressure sensitive adhesives, [93-94] we note that these voids were formed in the SA silicone sample during the curing process, rather than being formed during the peeling process. In all three samples shown in **Figure 4.4**, the level of bulk deformation was quite extensive and observed to be qualitatively similar despite the difference in initial bulk morphology of the cured SA/DMMVS/AC sample. Importantly, the nylon/ silicone adhesive interface exhibited adhesive failure for all three samples, cleanly detaching with no visible silicone residue on the substrate in the peeled region, despite the relatively large deformations in the bulk arising from the soft, compliant nature of these elastomers. Therefore, these measured adhesion strength values (within experimental error limits)

are expected to still be indicative of relative differences in the strength of intrinsic interfacial interactions present in the three samples, although the absolute magnitudes of the measured peel strength values are certain to contain large contributions from the bulk energy dissipation incurred during peeling.

4.4 Conclusion

SFG spectroscopy was successfully utilized to probe interfacial chemical reactions between nylon and two silicone adhesives with different adhesion promoters: silane molecules with SA and epoxy end groups respectively, in situ at the buried solid/solid interfaces. Two different interfacial reaction mechanisms were deduced from the observed SFG results. At the nylon/SA/DMMVS/AC silicone interface, after curing the nylon N−H stretching signals disappeared in both the SSP and PPP spectra, consistent with nylon reacting with the SA groups of the SA silane molecules at the buried nylon/SA/DMMVS/AC silicone interface, while the nylon C=O stretching signals at ~1635 cm^{-1} substantially decreased. At the same time, a new peak at 1725 cm^{-1} was observed from the reaction products of imide and carboxylic acid groups at the interface. A two-step reaction is thought to occur at the nylon/SA/DMMVS/AC silicone interface, with SA groups reacting with both nylon NH_2 end groups and amide NH groups in the nylon backbone to form carboxylic acid and imide functionalities.

At the nylon/GPS/DMMVS/AC silicone interface, interfacial chemical reactions between the nylon NH_2 end groups and epoxy silane were detected. The SFG N−H stretching signals of nylon dramatically decreased but did not disappear in both SSP and PPP spectra. We believe that the nylon NH_2 end groups reacted, but the nylon amide N-H groups in the backbone did not participate in the reaction which can be confirmed by the detected SFG C=O stretching signals. The C=O stretching signals of nylon at ~1635 cm^{-1} remained intact after the interfacial reaction (after

curing), indicating that the nylon amide groups were not involved in the interfacial chemical reaction between nylon and GPS/DMMVS/AC silicone. Although the interfacial chemical reaction mechanisms are different at the nylon/SA/DMMVS/AC silicone and nylon/GPS/DMMVS/AC silicone interfaces, the reactions enhanced interfacial adhesion strengths of both silicone adhesives to nylon by the formation of covalent bonds at the buried nylon/silicone interfaces.

SFG is a unique technique which can probe molecular interactions at buried solid/solid interfaces in situ nondestructively. We have applied SFG to study chemical reactions at various interfaces including polymer interfaces such as nylon/polyethylene interface, [45-47] poly(ethylene vinyl alcohol) (EVOH)/polyethylene interface,[95] PET/silicone interface, [48, 96-98] and primer/sealant interface,[74] demonstrating that SFG is a powerful tool to elucidate interfacial chemical reaction mechanisms in situ in real time. To the best of our knowledge, this is the first time to directly characterize interfacial reactions at the nylon/silicone adhesive interface in situ. The combined SFG study and adhesion measurement reported here shed light on the adhesion mechanisms at the nylon/silicone interfaces, revealing the effects of silane adhesion promoters on the enhancement of adhesion strength.

4.5 References

1. Insights, F. B. Adhesives and Sealants Market Size, Share & COVID-19 Impact Analysis, By Adhesive [Technology (Water-Based, Solvent-Based, Hot-Melt, Reactive), Application (Paper & Packaging, Building & Constructuion, Woodworking, Consumer/DIY, Automotive & Transportation, Leather & Footwear)], By Sealant [Resin (Silicone, Polyurethane, Emulsion, Polysulfide), Application (Building & Construction, Automotive & Transportation, Consumer), and Regional Forecasts, 2021-20]. https://www.fortunebusinessinsights.com/industry-reports/adhesives-and-sealants-market-101715.
2. Goff, D.; Yuan, E.; Long, H.; Neuhaus, H., Polymers for Electronic Packaging and Interconnection (Am. Chem. Soc., Symp. Ser. 407) ed JH Lupinski, RS Moore. Washington, DC: American Chemical Society) p: 1989.
3. Hampshire, W.; Dostal, C., *Electronic Materials Handbook, Volume 1;* CRC Press, **1989**.
4. Wong, C., High-Performance Silicone Gel as Integrated-Circuit-Device Chip Protection: Cure Study and Electrical Reliability. ACS Publications: 1989.

5. Teisala, H.; Baumli, P.; Weber, S. A.; Vollmer, D.; Butt, H.-J. r., Grafting Silicone at Room Temperature—a Transparent, Scratch-resistant Nonstick Molecular Coating. *Langmuir* **2020,** *36* (16), 4416-4431.
6. Kinloch, A., Adhesion and adhesives: "science and technology" eng in. London: Chapman and Hall: 1987.
7. Yacobi, B.; Martin, S.; Davis, K.; Hudson, A.; Hubert, M., Adhesive bonding in microelectronics and photonics. *Journal of applied physics* **2002,** *91* (10), 6227-6262.
8. Ahn, D.; Shephard, N. E.; Rolley, P. A.; McMillan, C. S., Correlating adhesion with local composition at silicone elastomer-polymer interfaces. *Polym. Prepr.***2005,** *46* (1).
9. Hall, J. R.; Westerdahl, C. A.; Devine, A. T.; Bodnar, M. J., Activated gas plasma surface treatment of polymers for adhesive bonding. *J. Appl. Polym. Sci.* **1969,** *13* (10), 2085-2096.
10. O'Neill, L.; Shephard, N.; Leadley, S.; O'Hare, L.-A., Atmospheric pressure plasma polymerised primer to promote adhesion of silicones. *The journal of adhesion* **2008,** *84* (6), 562-577.
11. Mine, K.; Nishio, M.; Sumimura, S., Heat curable organopolysiloxane compositions containing adhesion additives. Google Patents: 1977.
12. Schulz, J. R., Self-adhering silicone compositions and preparations thereof. Google Patents: 1978.
13. Gellman, A.; Naasz, B.; Schmidt, R.; Chaudhury, M.; Gentle, T., Secondary neutral mass spectrometry studies of germanium-silane coupling agent-polymer interphases. *J. Adhes. Sci. Technol.* **1990,** *4* (1), 597-601.
14. Gentle, T.; Schmidt, R.; Naasz, B.; Gellman, A.; Gentle, T., Organofunctional silanes as adhesion promoters: direct characterization of the polymer/silane interphase. *J. Adhes. Sci. Technol.* **1992,** *6* (2), 307-316.
15. Suzuki, T.; Kasuya, A., Adhesion of addition-reaction type silicone elastomers. *J. Adhes. Sci. Technol.* **1989,** *3* (1), 463-473.
16. Gray, T. E.; Lutz, M. A., Curable organopolysiloxane compositions with improved adhesion. Google Patents: 1997.
17. Ahn, D.; Rolley, P. A., Adhesives having improved chemical resistance and curable silicone compositions for preparing the adhesives. Google Patents: 2006.
18. Walker, P., Organosilanes as adhesion promoters. *J. Adhes. Sci. Technol.* **1991,** *5* (4), 279-305.
19. Roth, J.; Albrecht, V.; Nitschke, M.; Bellmann, C.; Simon, F.; Zschoche, S.; Michel, S.; Luhmann, C.; Grundke, K.; Voit, B., Surface functionalization of silicone rubber for permanent adhesion improvement. *Langmuir* **2008,** *24* (21), 12603-12611.
20. Bagiatis, V.; Critchlow, G.; Price, D.; Wang, S., The effect of atmospheric pressure plasma treatment (APPT) on the adhesive bonding of poly (methyl methacrylate)(PMMA)-to-glass using a polydimethylsiloxane (PDMS)-based adhesive. *Int. J. Adhes. Adhes.* **2019,** *95*, 102405.
21. Xiong, L.; Chen, P.; Zhou, Q., Adhesion promotion between PDMS and glass by oxygen plasma pre-treatment. *J. Adhes. Sci. Technol.* **2014,** *28* (11), 1046-1054.
22. Ohkubo, Y.; Endo, K.; Yamamura, K., Adhesive-free adhesion between heat-assisted plasma-treated fluoropolymers (PTFE, PFA) and plasma-jet-treated polydimethylsiloxane (PDMS) and its application. *Scientific reports* **2018,** *8* (1), 1-11.
23. Chau, K.; Millare, B.; Lin, A.; Upadhyayula, S.; Nuñez, V.; Xu, H.; Vullev, V. I., Dependence of the quality of adhesion between poly (dimethylsiloxane) and glass surfaces on the composition of the oxidizing plasma. *Microfluidics and Nanofluidics* **2011,** *10* (4), 907-917.

24. Lutz, M. A.; Gentle, T. E.; Perz, S. V.; Owen, M. J., Novel silane adhesion promoters for hydrosilylation cure systems. In *Silanes and Other Coupling Agents*, CRC Press: 2020; pp 3-13.
25. Cai, D.; Neyer, A., Cost-effective and reliable sealing method for PDMS (PolyDiMethylSiloxane)-based microfluidic devices with various substrates. *Microfluidics and nanofluidics* **2010,** *9* (4), 855-864.
26. Shen, Y., Revisiting the basic theory of sum-frequency generation. *J. Chem. Phys.J. Chem. Phys.* **2020,** *153* (18), 180901.
27. Roy, S.; Freiberg, S.; Leblanc, C.; Hore, D. K., Surface structure of acrylate polymer adhesives. *Langmuir* **2017,** *33* (8), 1763-1768.
28. Li, B.; Zhou, J.; Xu, X.; Yu, J.; Shao, W.; Fang, Y.; Lu, X., Solvent quality affects chain conformational order at the polymer surface revealed by sum frequency generation vibrational spectroscopy. *Polymer* **2013,** *54* (7), 1853-1859.
29. Yu, T.; Zhou, G.; Hu, X.; Ye, S., Transport and organization of cholesterol in a planar solid-supported lipid bilayer depend on the phospholipid flip-flop rate. *Langmuir* **2016,** *32* (44), 11681-11689.
30. Tan, J.; Zhang, J.; Luo, Y.; Ye, S., Misfolding of a Human Islet Amyloid Polypeptide at the Lipid Membrane Populates through β-Sheet Conformers without Involving α-Helical Intermediates. *Journal of the American Chemical Society* **2019,** *141* (5), 1941-1948.
31. Lovering, K. A.; Bertram, A. K.; Chou, K. C., Transient phase of ice observed by sum frequency generation at the water/mineral interface during freezing. *J. Phys. Chem. letters* **2017,** *8* (4), 871-875.
32. Nonkumwong, J.; Erasquin, U. J.; Sy Piecco, K. W.; Premadasa, U. I.; Aboelenen, A. M.; Tangonan, A.; Chen, J.; Ingram, D.; Srisombat, L.; Cimatu, K. L. A., Successive Surface Reactions on Hydrophilic Silica for Modified Magnetic Nanoparticle Attachment Probed by Sum-Frequency Generation Spectroscopy. *Langmuir* **2018,** *34* (43), 12680-12693.
33. Obiles, R.; Premadasa, U. I.; Cudia, P.; Erasquin, U. J.; Berger, J. M.; Martinez, I. S.; Cimatu, K. L. A., Insights on the Molecular Characteristics of Molecularly Imprinted Polymers as Monitored by Sum Frequency Generation Spectroscopy. *Langmuir* **2019,** *36* (1), 180-193.
34. Xiao, M.; Jasensky, J.; Gerszberg, J.; Chen, J.; Tian, J.; Lin, T.; Lu, T.; Lahann, J.; Chen, Z., Chemically immobilized antimicrobial peptide on polymer and self-assembled monolayer substrates. *Langmuir* **2018,** *34* (43), 12889-12896.
35. Chen, X.; Sagle, L. B.; Cremer, P. S., Urea orientation at protein surfaces. *Journal of the American Chemical Society* **2007,** *129* (49), 15104-15105.
36. Peng, Q.; Chen, J.; Ji, H.; Morita, A.; Ye, S., Origin of the overpotential for the oxygen evolution reaction on a well-defined graphene electrode probed by in situ sum frequency generation vibrational spectroscopy. *Journal of the American Chemical Society* **2018,** *140* (46), 15568-15571.
37. Ye, H.; Abu-Akeel, A.; Huang, J.; Katz, H. E.; Gracias, D. H., Probing organic field effect transistors in situ during operation using SFG. *Journal of the American Chemical Society* **2006,** *128* (20), 6528-6529.
38. Zhang, C.; Parada, G. A.; Zhao, X.; Chen, Z., Probing Surface Hydration and Molecular Structure of Zwitterionic and Polyacrylamide Hydrogels. *Langmuir* **2019,** *35* (41), 13292-13300.
39. Perera, H. G.; Lu, T.; Fu, L.; Zhang, J.; Chen, Z., Probing the Interfacial Interactions of Monoclonal and Bispecific Antibodies at the Silicone Oil–Aqueous Solution Interface by Using Sum Frequency Generation Vibrational Spectroscopy. *Langmuir* **2019,** *35* (44), 14339-14347.

40. Zuo, B.; Inutsuka, M.; Kawaguchi, D.; Wang, X.; Tanaka, K., Conformational relaxation of poly (styrene-co-butadiene) chains at substrate interface in spin-coated and solvent-cast films. *Macromolecules* **2018,** *51* (6), 2180-2186.
41. Nguyen, H. K.; Sugimoto, S.; Konomi, A.; Inutsuka, M.; Kawaguchi, D.; Tanaka, K., Dynamics gradient of polymer chains near a solid interface. *ACS Macro Letters* **2019,** *8* (8), 1006-1011.
42. Bhattacharyya, D.; Montenegro, A.; Dhar, P.; Mammetkuliyev, M.; Pankow, R. M.; Jung, M. C.; Thompson, M. E.; Thompson, B. C.; Benderskii, A. V., Molecular orientation of poly-3-hexylthiophene at the buried interface with fullerene. *J. Phys. Chem. letters* **2019,** *10* (8), 1757-1762.
43. Lu, X.; Zhang, C.; Ulrich, N.; Xiao, M.; Ma, Y.-H.; Chen, Z., Studying polymer surfaces and interfaces with sum frequency generation vibrational spectroscopy. *Anal. Chem.***2017,** *89* (1), 466-489.
44. Xiao, M.; Lu, T.; Lin, T.; Andre, J. S.; Chen, Z., Understanding Molecular Structures of Buried Interfaces in Halide Perovskite Photovoltaic Devices Nondestructively with Sub-Monolayer Sensitivity Using Sum Frequency Generation Vibrational Spectroscopy. *Advanced Energy Materials* **2020,** *10* (26), 1903053.
45. Xiao, M.; Mohler, C.; Tucker, C.; Walther, B.; Lu, X.; Chen, Z., Structures and adhesion properties at polyethylene/silica and polyethylene/nylon interfaces. *Langmuir* **2018,** *34* (21), 6194-6204.
46. Li, B.; Andre, J. S.; Chen, X.; Walther, B.; Paradkar, R.; Feng, C.; Tucker, C.; Mohler, C.; Chen, Z., Probing molecular behavior of carbonyl groups at buried nylon/polyolefin interfaces in situ. *Langmuir* **2020,** *36* (38), 11349-11357.
47. Li, B.; Andre, J. S.; Chen, X.; Walther, B.; Paradkar, R.; Feng, C.; Tucker, C.; Mohler, C.; Chen, Z., Observing a chemical reaction at a buried solid/solid interface in situ. *Anal. Chem.***2020,** *92* (20), 14145-14152.
48. Lin, T.; Wu, Y.; Santos, E.; Chen, X.; Ahn, D.; Mohler, C.; Chen, Z., Molecular Insights into Adhesion at a Buried Silica-Filled Silicone/Polyethylene Terephthalate Interface. *Langmuir* **2020,** *36* (49), 15128-15140.
49. Ge, A.; Inoue, K.-i.; Ye, S., Probing the electrode–solution interfaces in rechargeable batteries by sum-frequency generation spectroscopy. *J. Chem. Phys.J. Chem. Phys.* **2020,** *153* (17), 170902.
50. Peng, Q.; Qiao, Y.; Kannari, K.; Ge, A.; Inoue, K.-i.; Ye, S., In situ spectroscopic investigations of electrochemical oxygen reduction and evolution reactions in cyclic carbonate electrolyte solutions. *J. Phys. Chem. C* **2020,** *124* (29), 15781-15792.
51. Zhang, J.; Yang, W.; Tan, J.; Ye, S., In situ examination of a charged amino acid-induced structural change in lipid bilayers by sum frequency generation vibrational spectroscopy. *Physical Chemistry Chemical Physics* **2018,** *20* (8), 5657-5665.
52. Sun, V.; Jarisz, T. A.; Wunsch, L.; Hore, D. K., Monitoring early stages of bacterial adhesion at silica surfaces through image analysis. *Langmuir* **2020,** *36* (8), 2120-2128.
53. Zhang, F.; Li, X.; Ma, Y.; Wang, C.; Hu, P.; Wang, F.; Lu, X., Illustrating Interfacial Interaction between Honey Bee Venom Phospholipase A2 and Supported Negatively Charged Lipids with Sum Frequency Generation and Laser Scanning Confocal Microscopy. *Langmuir* **2020,** *36* (11), 2946-2953.

54. Wang, C.; Luo, Y.; Li, X.; Zhang, F.; Wang, F.; Han, X.; Wang, T.; Beke-Somfai, T. s.; Lu, X., Revealing molecular-level interaction between a polymeric drug and model membrane via sum frequency generation and microfluidics. *Langmuir* **2020,** *36* (6), 1615-1622.
55. Chen, C.; Wang, J.; Chen, Z., Surface restructuring behavior of various types of poly (dimethylsiloxane) in water detected by SFG. *Langmuir* **2004,** *20* (23), 10186-10193.
56. Chen, C.; Wang, J.; Loch, C. L.; Ahn, D.; Chen, Z., Demonstrating the feasibility of monitoring the molecular-level structures of moving polymer/silane interfaces during silane diffusion using SFG. *Journal of the American Chemical Society* **2004,** *126* (4), 1174-1179.
57. Loch, C. L.; Ahn, D.; Chen, C.; Chen, Z., Polymer-silane interactions probed by sum frequency generation vibrational spectroscopy. *The Journal of Adhesion* **2005,** *81* (3-4), 319-345.
58. Loch, C. L.; Ahn, D.; Chen, Z., Sum frequency generation vibrational spectroscopic studies on a silane adhesion-promoting mixture at a polymer interface. *J. Phys. Chem. B* **2006,** *110* (2), 914-918.
59. Guo, R.; Li, B.; Lu, T.; Lin, T.; Andre, J.; Zhang, C.; Zhi, L.; Chen, Z., Molecular Orientations at Buried Conducting Polymer/Graphene Interfaces. *Macromolecules* **2021,** *54* (9), 4050-4060.
60. Lin, T.; Guo, W.; Guo, R.; Chen, Z., Probing Biological Molecule Orientation and Polymer Surface Structure at the Polymer/Solution Interface In Situ. *Langmuir* **2020,** *36* (26), 7681-7690.
61. Ahn, D.; Dhinojwala, A., Sum frequency generation vibrational spectroscopy of silicone surfaces & interfaces. In *Silicone surface science*, Springer: 2012; pp 23-58.
62. Zhang, C.; Chen, Z., Quantitative molecular level understanding of ethoxysilane at poly (dimethylsiloxane)/polymer interfaces. *Langmuir* **2013,** *29* (2), 610-619.
63. Zhang, C.; Shephard, N. E.; Rhodes, S. M.; Chen, Z., Headgroup effect on silane structures at buried polymer/silane and polymer/polymer interfaces and their relations to adhesion. *Langmuir* **2012,** *28* (14), 6052-6059.
64. Shen, Y. J. N., Surface properties probed by second-harmonic and sum-frequency generation. **1989,** *337* (6207), 519-525.
65. Bain, C. D., Sum-frequency vibrational spectroscopy of the solid/liquid interface. *J. Chem. Soc., Faraday Trans.* **1995,** *91* (9), 1281-1296.
66. Gracias, D.; Chen, Z.; Shen, Y.; Somorjai, G. J. A. o. c. r., Molecular characterization of polymer and polymer blend surfaces. Combined sum frequency generation surface vibrational spectroscopy and scanning force microscopy studies. **1999,** *32* (11), 930-940.
67. Wei, X.; Zhuang, X.; Hong, S.-C.; Goto, T.; Shen, Y., Sum-frequency vibrational spectroscopic study of a rubbed polymer surface. *Phys. Rev. Lett.* **1999,** *82* (21), 4256.
68. Buck, M.; Himmelhaus, M., Vibrational spectroscopy of interfaces by infrared–visible sum frequency generation. *Journal of Vacuum Science & Technology A: Vacuum, Surfaces, and Films* **2001,** *19* (6), 2717-2736.
69. Chen, Z.; Shen, Y.; Somorjai, G. A. J. A. r. o. p. c., Studies of polymer surfaces by sum frequency generation vibrational spectroscopy. **2002,** *53* (1), 437-465.
70. Chen, Z., Understanding surfaces and buried interfaces of polymer materials at the molecular level using sum frequency generation vibrational spectroscopy. *Polym. Int.* **2007,** *56* (5), 577-587.
71. Chen, Z., Investigating buried polymer interfaces using sum frequency generation vibrational spectroscopy. *Prog. Polym. Sci.* **2010,** *35* (11), 1376-1402.
72. Shen, Y. J. A. r. o. p. c., Phase-sensitive sum-frequency spectroscopy. **2013,** *64*, 129-150.

73. Lu, X.; Zhang, C.; Ulrich, N.; Xiao, M.; Ma, Y.-H.; Chen, Z. J. A. c., Studying polymer surfaces and interfaces with sum frequency generation vibrational spectroscopy. **2017,** *89* (1), 466-489.
74. Zhang, S.; Andre, J. S.; Hsu, L.; Toolis, A.; Esarey, S. L.; Li, B.; Chen, Z., Nondestructive in situ detection of chemical reactions at the buried interface between polyurethane and isocyanate-based primer. *Macromolecules* **2020,** *53* (22), 10189-10197.
75. Guo, W.; Xu, S.; Reichart, T. M.; Xiao, M.; Lu, T.; Mello, C.; Chen, Z., Probing Molecular Interactions between Surface-Immobilized Antimicrobial Peptides and Lipopolysaccharides In Situ. *Langmuir* **2020,** *36* (41), 12383-12393.
76. Enlow, E. M.; Kennedy, J. L.; Nieuwland, A. A.; Hendrix, J. E.; Morgan, S. L., Discrimination of nylon polymers using attenuated total reflection mid-infrared spectra and multivariate statistical techniques. *Appl. Spectrosc.***2005,** *59* (8), 986-992.
77. Czarnecki, M. A.; Wu, P.; Siesler, H. W., 2D FT-NIR and FT-IR correlation analysis of temperature-induced changes of nylon 12. *Chem. Phys. Lett.* **1998,** *283* (5-6), 326-332.
78. Kim, G.; Gurau, M.; Kim, J.; Cremer, P. S., Investigations of lysozyme adsorption at the air/water and quartz/water interfaces by vibrational sum frequency spectroscopy. *Langmuir* **2002,** *18* (7), 2807-2811.
79. Clarke, M. L.; Wang, J.; Chen, Z., Conformational changes of fibrinogen after adsorption. *J. Phys. Chem. B* **2005,** *109* (46), 22027-22035.
80. Petrova, T.; Okovytyy, S.; Gorb, L.; Leszczynski, J., Computational Study of the Aminolysis of Anhydrides: Effect of the Catalysis to the Reaction of Succinic Anhydride with Methylamine in Gas Phase and Nonpolar Solution. *J. Phys. Chem. A* **2008**, 112, 5224-5235.
81. de Gooijer, J. M.; Scheltus, M.; Lösch, H. W.; Staudt, R.; Meuldijk, J.; Koning, C. E., End Group Modification of Polyamide-6 in Supercritical and Subcritical Fluids: Part 1: Amine End Group Modification with Succinic Anhydride. *J. Supercrit. Fluids* **2004**, 29, 129-152.
82. Triacca, V.; Ziaee, S.; Barlow, J.; Keskkula, H.; Paul, D., Reactive compatibilization of blends of nylon 6 and ABS materials. *Polymer* **1991,** *32* (8), 1401-1413.
83. Tyurina, T. G.; Kryuk, T. V.; Kudryavtseva, T. A., Amidation Kinetics of Succinic Anhydride by Amine-Containing Drugs. *J. Phys. Conf. Ser.* **2020**, 1658, 012063.
84. Kas'yan, L. I.; Serbin, A. V.; Kas'yan, A. O.; Karpenko, D. V.; Golodaeva, E. A., Reactions of Bi-, Tri-, and Tetracyclic Amines with Succinic Anhydride. Russ. *J. Org. Chem.* **2008**, 44, 340-347.
85. Maréchal, P.; Coppens, G.; Legras, R.; Dekoninck, J.-M., Amine/Anhydride Reaction Versus Amide/Anhydride Reaction in Polyamide/Anhydride Carriers. *J. Polym. Sci., Part A: Polym. Chem.* **1995**, *33*, 757-766.
86. Brace, N. O.; Mull, S. G., New Succinamic Acids, -Γ-Lactones, and -Succinimides from (3-Perfluoroalkyl-2-Iodoalkyl)Succinic Acid Anhydrides and Amines: Highly Surface Active Amphiphiles. *J. Fluorine Chem.* **2006**, *127*, 108-125.
87. Eichhorn, K. J.; Lehmann, D.; Voigt, D., Characterization of low molecular weight carboxyl-terminated polyamides obtained by reactive extrusion of polyamide 6 with trimellitic anhydride. *J. Appl. Polym. Sci.* **1996,** *62* (12), 2053-2060.
88. Riccardi, C. C.; Williams, R. J., A kinetic scheme for an amine-epoxy reaction with simultaneous etherification. *J. Appl. Polym. Sci.* **1986,** *32* (2), 3445-3456.
89. Mijovic, J.; Wijaya, J., Reaction kinetics of epoxy/amine model systems. The effect of electrophilicity of amine molecule. *Macromolecules* **1994,** *27* (26), 7589-7600.

90. Wang, X.; Gillham, J. K., Competitive primary amine/epoxy and secondary amine/epoxy reactions: Effect on the isothermal time-to-vitrify. *J. Appl. Polym. Sci.* **1991,** *43* (12), 2267-2277.
91. Macosko, C. W.; Jeon, H. K.; Hoye, T. R., Reactions at polymer–polymer interfaces for blend compatibilization. *Prog. Polym. Sci.* **2005,** *30* (8-9), 939-947.
92. Fedors, R. F., A method for estimating both the solubility parameters and molar volumes of liquids. *Polymer Engineering & Science* **1974,** *14* (2), 147-154.
93. Crosby, A.; Shull, K.; Lin, Y.; Hui, C.-Y., Rheological properties and adhesive failure of thin viscoelastic layers. *J. Rheol.* **2002,** *46* (1), 273-294.
94. Lakrout, H.; Creton, C.; Ahn, D.; Shull, K. R., Influence of molecular features on the tackiness of acrylic polymer melts. *Macromolecules* **2001,** *34* (21), 7448-7458.
95. Andre, J. S.; Li, B.; Chen, X.; Paradkar, R.; Walther, B.; Feng, C.; Tucker, C.; Mohler, C.; Chen, Z., Interfacial reaction of a maleic anhydride grafted polyolefin with ethylene vinyl alcohol copolymer at the buried solid/solid interface. *Polymer* **2021,** *212*, 123141.
96. Vázquez, A. V.; Shephard, N. E.; Steinecker, C. L.; Ahn, D.; Spanninga, S.; Chen, Z., Understanding molecular structures of silanes at buried polymer interfaces using sum frequency generation vibrational spectroscopy and relating interfacial structures to polymer adhesion. *J. Colloid Interface Sci.* **2009,** *331* (2), 408-416.
97. Vazquez, A. V.; Boughton, A. P.; Shephard, N. E.; Rhodes, S. M.; Chen, Z., Molecular structures of the buried interfaces between silicone elastomer and silane adhesion promoters probed by sum frequency generation vibrational spectroscopy and molecular dynamics simulations. *Appl. Mater. InterfacesACS Appl. Mater. Interfaces***2010,** *2* (1), 96-103.
98. Vázquez, A. V.; Holden, B.; Kristalyn, C.; Fuller, M.; Wilkerson, B.; Chen, Z., Surface and buried interfacial structures of epoxy resins used as underfills studied by sum frequency generation vibrational spectroscopy. *Appl. Mater. InterfacesACS Appl. Mater. Interfaces***2011,** *3* (5), 1640-1651.

Chapter 5 Elucidating the Changes in Molecular Structure at the Buried Interface of RTV Silicone Elastomers during Curing

The contents of this chapter are adopted from a manuscript entitled “Elucidating the Changes in Molecular Structure at the Buried Interface of RTV Silicone Elastomers during Curing” which was recently submitted for publication. This manuscript was finished by Ting Lin, Yuchen Wu, Elizabeth Santos, Xiaoyun Chen, Frederic Gubbels, Nick Shephard, Carol Mohler, Dongchan Ahn, Tzu-Chi Kuo, Zhan Chen.

5.1 Introduction

As discussed in the previous chapters, silicone elastomers are one of the most widely used polymeric sealants in many important industrial and other applications, due to their excellent mechanical properties, outstanding high-temperature resistance, and excellent chemical stability.[1-4] Silicone elastomers can withstand harsh environmental conditions, reducing the need for frequent replacement of sealant and thus minimizing waste. According to a market research report published by Grand View Research, the global silicone market size was valued at USD 15.3 billion in 2020 and is expected to grow at a compound annual growth rate (CAGR) of 4.9% from 2021 to 2028.[5].

In the above chapters, we presented our research on addition cured silicone systems, which require high temperatures for curing. Room-temperature vulcanized (RTV) silicone another major sub-categories of the silicone elastomer. Curing of RTV silicone to form an adhesive seal involves the formation of crosslinked networks through chemical reactions between silanol groups and other reactive groups in formulated products such as alkoxysilanes or acetoxysilanes. During curing, in addition to the bulk structural changes, the interfacial molecular structure of RTV silicone may also undergo significant transformations which can affect the interlayer adhesion. It is vital to determine any molecular-level changes at the interface that occur during curing in order to correlate interfacial structure to interfacial properties.

One of the critical aspects of RTV silicone curing is the reaction involving reactive hydroxyl (-OH) groups, wherein the hydroxyl groups play a vital role for crosslinking. The origin of these hydroxyl groups in bulk has been extensively investigated. Several studies have suggested that they can come from various sources, such as moisture, alcohol, or reactive silanes, which are either from the silicone bulk formulation or the ambient environment.[3, 6-8] However, the primary source of hydroxyl groups at the substrate/silicone interface and their role in interfacial reactions are not well understood.

There are multiple sources of interfacial hydroxyl groups in the silicone samples as well as the substrates to which silicone adhesives adhere. Glass is a commonly used substrate or adherent of silicone adhesive or sealant. In this study, silica substrate was used as a model of glass. Silica surface can have silanol groups, which contain hydroxyl functionalities.[9-11] Also, silica surface is hydrophilic, which can strongly adsorb water on the surface. These hydroxyl groups can act as active sites for various interfacial chemical reactions to occur and can participate in surface

modification processes. Hydroxyl groups at the interface during the curing process can also originate from the silicone formulation present at the interface and the hydroxyl groups in the silicone bulk which have diffused to the interface. In addition, water moisture in the environment may diffuse to the interface directly or through the silicone bulk.

To understand the molecular adhesion mechanisms of RTV silicone adhesives, it is necessary to elucidate the interfacial molecular structural transformations and the origins of interfacial reactive hydroxyl groups during silicone curing. Such knowledge can help to optimize the curing conditions and develop new formulations with improved adhesion along with better bulk properties such as enhanced thermal and chemical resistance. To our knowledge, there are very few studies which reveal the interfacial change of RTV silicone and identify the primary reacting source of interfacial hydroxyl groups.

In this research, we elucidated the interfacial molecular structural changes and the origins of interfacial reactive hydroxyl groups in RTV silicone during curing. We investigated the interfacial molecular structures of RTV silicone at different stages of curing using SFG, supplemented by other surface-sensitive analytical techniques. Our findings provide insight into the fundamental curing chemistry of RTV silicone and help enable the development of new RTV adhesives and sealants with improved performance and durability. This research demonstrates that SFG is able to detect chemical and structural changes occurring at buried interfaces between silicone adhesives and substrates under different curing and humidity conditions.

5.2 Materials and Methods

5.2.1 Materials and sample preparation

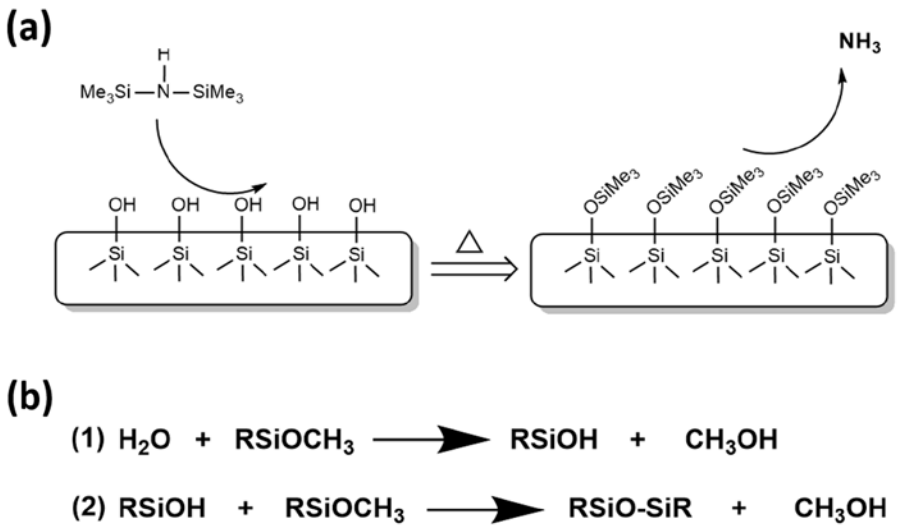

Scheme 5.1 (a) silylation reaction of silica substrate, and (b) condensation curing reaction

In this study, silica right-angle prisms were utilized as silica substrates, while a model sealant (Model Sealant A or MSA) was used to study the RTV condensation cure silicone. The major components of MSA are: trimethoxysilyl terminated polydimethylsiloxane (53%), calcium carbonate (43%), silanes for crosslinking and adhesion enhancement (3%), and diisopropoxy-bis ethylacetoacetato titanate as Ti catalyst (1%).

In addition to the studies on MSA/silica interface, studies on MSA/silylated silica interface were also performed.[12] For silylation experiments, the -OH terminal groups on silica substrates were silylated using hexamethyldisilazane (HMDS) as described in the literature.[12] The schematic showing the silylation reaction is presented in **Scheme 5.1a.** HMDS is a commonly used silylating agent due to its reactivity and the ability to create stable silyl ethers under mild conditions. Additionally, extra HMDS was removed from the reaction product mixture by rinsing with ethanol and nitrogen flow drying, in order not to interfere with the subsequent analysis. Following the silylation, several methods were employed to characterize and verify the silylation reaction including water contact angle, SFG and XPS. SFG was then used to study the molecular details of the interface between MSA and silylated silica.

The curing reaction of RTV silicone in this work is shown in **Scheme 5.1b**.[13-14] The moisture from the ambient environment hydrolyzes trimethoxy end groups of PDMS polymer and forms silanol terminated PDMS polymer. The produced silanol PDMS reacts with trimethoxy terminated PDMS for curing. Besides the major curing reaction, the silanol PDMS also reacts with the small number of methoxy groups from silane molecules in the system

5.2.2 Experimental Methods

5.2.2.1 SFG Experiment

A series of time-dependent SFG experiments were performed on condensation cured silicone samples with different curing conditions. In order to mimic the real-life applications of RTV silicone adhered on glass and provide more in-depth scientific insight on the interfacial silicone interaction, silica substrate was selected in this set of experiments. The goal of these SFG experiments was to study the changes of the interfacial molecular structure of RTV silicone that occurred during the curing process and to identify the primary reacting source of hydroxyl groups at interface.

The details of the SFG theory and SFG results have been discussed in the previous chapters and extensively presented in the literature,[15-42] thus we will not repeat them here. Previously, our group has studied several silicone systems using SFG;[34,35,37,39] Some of such studies were discussed above in this thesis. In this study, SFG experiments were conducted using a picosecond SFG system (EKSPLA, Lithuania) which was described above and presented in detail in previous publications.[15, 21, 43-46] Briefly, the system generates two input laser beams: a frequency tunable IR beam (2.3 - 10 μm) and a frequency fixed visible beam (532 nm). The two beams overlapped at the buried silica/silicone interface (with input angles of 54^{o} and 60^{o} relative to the surface normal, respectively), both spatially and temporally, to generate an output beam with the sum frequency

of the two input beams. The overlapped beam size at the sample interface was approximately 0.5 mm in diameter. The SFG signals were collected by a monochromator and a photomultiplier tube to produce vibrational SFG spectra. The intensity of the SFG signal is directly proportional to the square of the second-order nonlinear optical susceptibility, $\chi^{(2)}$, of the sample, which is the macroscopic average of the hyperpolarizability (β) of the surface or interfacial molecules. The sub-monolayer surface/interfacial specificity of the SFG technique is due to the selection rule of a second-order nonlinear optical process, as extensively reported in the previous publications.[47-57]

In this study, SFG spectra in the C-H stretching frequency region (2750 – 3000 cm^{-1}) were collected from silica/silicone interfaces. Each SFG spectrum shown below is the average of at least five scans. The silica prisms were cleaned using piranha solution (mixture of sulfuric acid and hydrogen peroxide) and air plasma for 3 minutes in a PE-25-JW plasma oven (Plasma Etch) before use. A thick semi-opaque film of silicone was applied to the silica substrate using a scraper. The silicone film was approximately 5 mm thick, which prevented the generation of SFG signals from the air/silicone interface on the opposite side. Both SSP (S-polarized sum frequency beam, S-polarized visible beam, P-polarized IR beam) and PPP polarization combinations of the input and output beams were utilized for SFG spectra collection. **Scheme 5.2a** shows the SFG sample geometry. More details of SFG data and orientation analysis are presented below.

5.2.2.2 X-Ray Photoelectron Spectroscopy (XPS) Experiment

XPS measurements were made using an Axis Ultra XPS system (Kratos Analytical Ltd, UK) to confirm the successful conversion of the hydroxyl groups into trimethyl groups on the silica substrate after silylation. The sample spot size probed by XPS was 700 μm × 300 μm. To generate the x-ray for XPS experiments, an 8 mA emission current and 14 kV high voltage were used. For the survey scan, 160 eV pass energy was used. XPS samples were prepared in the same

fashion as those studied using SFG and water contact angle measurement. Data was analyzed using CasaXPS software (version 2.3.22PR1.0).

5.2.2.3 Water Contact Angle Experiment

A CAM 100 optical contact angle goniometer (KSV Instruments, Finland) was used to measure static water contact angles on the silica surface before and after silylation reaction to characterize the outcome of surface modification. Samples used for contact angle measurements were also used in SFG study after nitrogen flow drying.

5.2.2.4 Adhesion Strength Test

The mechanical adhesion between interfaces was determined by employing the ASTM D3163 standard method, using a lap shear setup as shown in **Scheme 5.2b**.[58-59] The microscope slides used in the tests had an average overlap of 25 mm x 50mm with 5mm thickness of silicone. The tests took place at ambient temperature, utilizing an Instron 5544 mechanical testing device (Instron Co., Norwood, MA). Upon the lap shear samples reaching their breaking point at the interface, a sharp decrease in shear force was observed and documented as the adhesive strength.

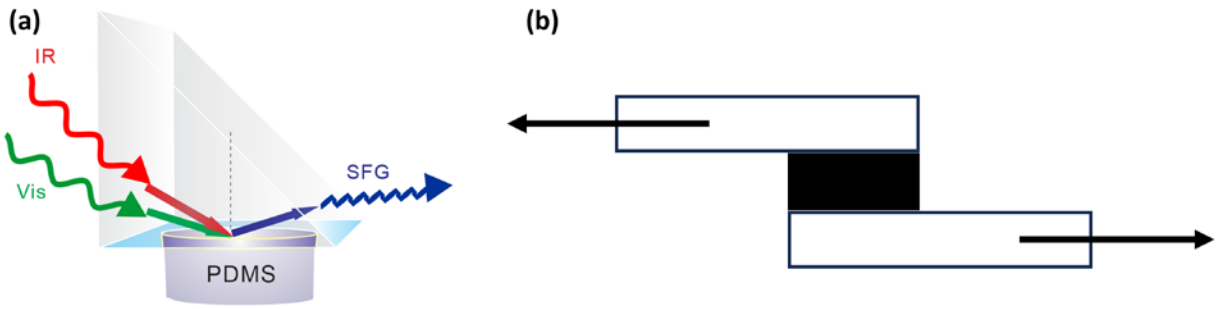

Scheme 5.2 (a) SFG sample geometry, (b) lap shear adhesion test sample geometry (not to scale)

5.2.3 SFG Data Analysis Method

Methods for SFG quantitative data analysis have been extensively published.[255-258] In this study, the Fresnel coefficient for χ_{yyz} is 3.43. The $\chi_{eff}^{(2)}$ of PPP has four terms: χ_{xxz}, χ_{xzx}, χ_{zxx}, χ_{zzz} and the Fresnel coefficients for each term are 0.15, 0.09, 0.12, and 3.88, respectively. As a result, the contributions of χ_{xxz}, χ_{xzx}, χ_{zxx} to the signal are usually small, and the signal contribution of χ_{zzz} can dominate the ppp signals. In order to simplify the data analysis, here we only consider the χ_{zzz} term for the ppp spectrum in the following data analysis.

In our RTV silicone system, there are trimethoxy groups from the silicone matrix and silane additives. To simplify the data analysis, here, the methoxy groups were treated as independent groups and each methoxy group adopts a C3v symmetry. Therefore, the methoxy orientation we deduced here is the average orientation of all the independent methoxy groups at the silicone/silica interface.

For the C-H symmetric stretching methoxy signal:

$$\chi_{xxz,s} = \chi_{yyz,s} = \frac{1}{2} N_s \beta_{ccc} [\cos\theta(1+r) - \cos^3\theta(1-r)] \quad (4)$$

$$\chi_{zzz,s} = N_s \beta_{ccc} [r\cos\theta + \cos^3\theta(1-r)] \quad (5)$$

Where N_s is the surface number density of the functional groups under study, β_{ccc} is a hyperpolarizability component of a single methoxy group C–H symmetric stretching mode, r is the ratio of β_{aac}/β_{ccc}, θ is the tilt angle of the principal vector v of the entire $SiO(CH_3)$ group versus the surface normal. The detailed tilt angle was demonstrated in **Figure 5.1**. It has been reported that the ratio of β_{aac}/β_{ccc} is around 1.7 for a methoxy group.[5]

By taking the ratio of equations (4) and (5), the N_s and β_{ccc} were canceled. Here we can correlate the χ_{xxz}/χ_{zzz} ratio to the tilt angle of methoxy group. After considering the Fresnel coefficient in

equation (3), the relationship between the tilt angle of the transition dipole vector v and the measured χ_{ssp}/χ_{ppp} ratio can be deduced and is shown in **Figure 5.2**.

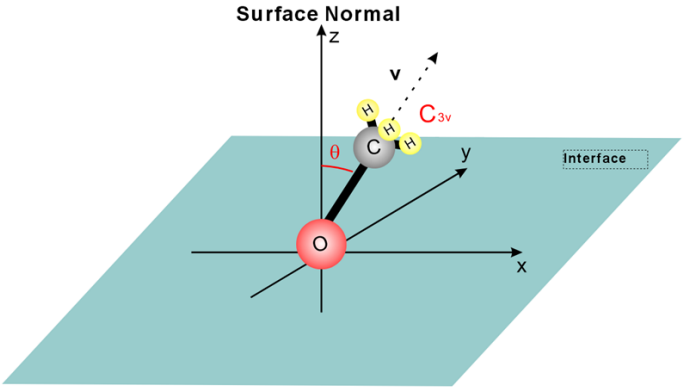

Figure 5.1 Schematic showing a methoxy group and the coordinate system chosen for orientation analysis. The methoxy group adopts a C3v symmetry. The xyz coordinate demonstrates the lab coordination frame. Θ is tilt angle of the vector v of the SiOCH3 group.

Figure 5.1 shows the orientation of a methoxy group at the MSA silicone/silica interface. Note that θ is the tilt angle used to describe the methoxy orientation, which is the angle between the z axis (surface normal) and the vector v (the principal axis of the OCH_3 group or the direction of the C-O bond). The "lying down" orientation of -OCH_3 indicates a large tilt angle θ, while the "standing up" orientation indicates a small tilt angle.

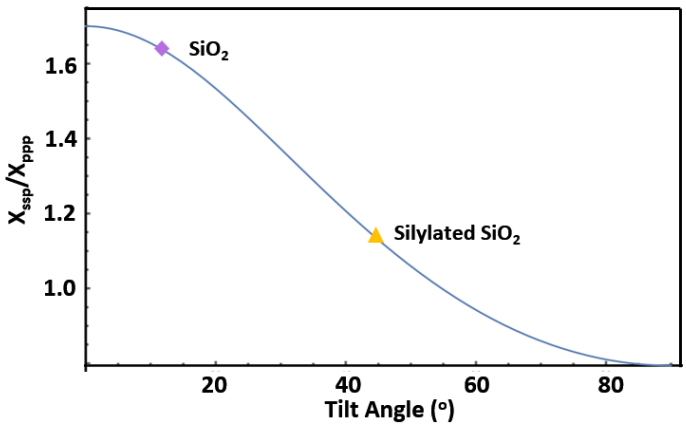

Figure 5.2 χ_{ssp}/χ_{ppp} ratio as a function of the tilt angle of the net transition dipole of the methoxy C-H symmetric stretching (with respect to the surface normal)

5.3 Results and Discussion

5.3.1 Time-dependent Methoxy SFG Results

For the condensation cured silicone, methoxy groups in the silicone formulation participate in multiple reactions including the curing reactions in the bulk and interfacial reactions to form covalent bonds. The change of SFG methoxy signal at interface is a good indicator to monitor the interfacial chemical reaction and curing reaction of silicone matrix. SFG ssp and ppp spectra were collected from the MSA silicone/silica interface as a function of curing time (under the ambient condition at room temperature), shown in **Figure 5.3**. The fitting results are also shown in the same figure and the fitting parameters are listed in **Table 5.1**. According to the spectral fitting results, peaks centered at ~2815, ~2840, ~2910, ~2935, and ~2960 cm^{-1} were detected in the SFG spectra. The 2840 cm^{-1} peak is assigned to the symmetric C-H stretching signal of the methoxy groups. The 2910 cm^{-1} peak is assigned to the symmetric C-H stretching signal of the Si-CH_3. The 2935 and 2960 cm^{-1} peaks are assigned to the asymmetric C-H stretching signal of the methylene (e.g. from Ti catalysts or silane) and methyl groups (e.g., from silicone Si-CH_3 or methoxy O-CH_3), respectively.[34, 36-38] The 2935 cm^{-1} peak may also be contributed by the methyl Fermi resonance.

The 2815 cm^{-1} peak can be assigned to the C-H stretching signal of Ti catalyst in the MSA formula. More details about the assignment of the 2815 cm^{-1} peak can be found in **Section 5.3.5**.

Table 5.1 Fitting parameters of the time-dependent SFG spectra collected from the MSA/silica interface before silylation as shown in Figure 5.3

0 hour-SSP			**0 hour-PPP**			
ωi (cm^-	Γi (cm^-	Aq	ωi (cm^-	Γi (cm^-	Aq	assignment
2815	14.3	0.21	2815	14.3	0.07	TDIDE
2842	14.2	0.75	2842	14.2	0.47	s O-CH_3
2935	18.3	0.84	2935	18.3	0.68	as
2960	13.5	-0.63	2960	13.5	-0.54	as Si-CH_3/O-
3 hour-SSP			**3 hour-PPP**			
ωi (cm^-	Γi (cm^-	Aq	ωi (cm^-	Γi (cm^-	Aq	assignment
2815	14.3	0.18	2815	14.3	0.13	TDIDE
2842	14.2	0.67	2842	14.2	0.39	s O-CH_3
2935	18.3	0.80	2935	18.3	0.59	as
2960	13.5	-0.74	2960	13.5	-0.48	as Si-CH_3/O-
6 hour-SSP			**6 hour-PPP**			
ωi (cm^-	Γi (cm^-	Aq	ωi (cm^-	Γi (cm^-	Aq	assignment
2815	14.3	0.17	2815	14.3	0.08	TDIDE
2842	14.2	0.67	2842	14.2	0.40	s O-CH_3
2935	18.3	0.80	2935	18.3	0.65	as
2960	13.5	-0.72	2960	13.5	-0.57	as Si-CH_3/O-
10 hour-SSP			**10 hour-PPP**			
ωi (cm^-	Γi (cm^-	Aq	ωi (cm^-	Γi (cm^-	Aq	assignment
2815	14.3	0.13	2815	14.3	0.09	TDIDE
2842	14.2	0.64	2842	14.2	0.42	s O-CH_3
2935	18.3	0.79	2935	18.3	0.61	as
2960	13.5	-0.79	2960	13.5	-0.52	as Si-CH_3/O-
23 hour-SSP			**23 hour-PPP**			
ωi (cm^-	Γi (cm^-	Aq	ωi (cm^-	Γi (cm^-	Aq	assignment
2815	14.3	0.005	2815	14.3	0.06	TDIDE
2842	14.2	0.25	2842	14.2	0.16	s O-CH_3
2935	18.3	0.23	2935	18.3	0.15	as
2960	13.5	-0.68	2960	13.5	-0.55	as Si-CH_3/O-

As shown in **Figure 5.3**, during the time-dependent curing process, the SFG peak features and the peak positions remain the same. However, the overall intensities of various peaks in the spectra consistently decrease with cure time. The spectral fits indicate the C-H symmetric

stretching SSP/PPP signal ratio of the methoxy groups is not significantly time dependent. Since this ratio is related to the cosine function of the tilt angle (see equations (4) and (5) above in **Section 5.2.3**), we conclude that the orientation of the interfacial methoxy is similar at various times during the curing process. Note the SFG signal intensity is influenced by both the functional group orientation and/or surface coverage of the molecules. Because the orientation of methoxy groups at the interface does not change substantially as a function of curing time, we believe that the overall methoxy SFG signal intensity decrease is related to the reduced interfacial coverage, due to the consumption of the interfacial methoxy groups by interfacial reactions. To verify this interpretation, a quantitative analysis was conducted for orientation determination. The tilt angles of the methoxy groups at different curing times were deduced and presented in **Table 5.2**. The tilt angle of the interfacial methoxy group at the MSA silicone/silica interface during the first 23 hours of curing ranged from 6.3° to 17.7°, indicating that the methoxy groups more or less stand up at the interface. This may be caused by the favorable interaction between interfacial methoxy groups and the hydroxyl groups on silica surface, which facilitates the later interfacial chemical reactions. When there are hydroxyl groups at the interface, methoxy groups could be continuously hydrolyzed and consumed, providing driving force for the excessive methoxy groups to migrate to the interface from silicone bulk and stand up at the interface. A more detailed discussion will be presented below with the comparison to the results obtained from the control experiments.

Table 5.2 Tilt angles of methoxy group at SiO_2/MSA interface with various curing times

Time stamp	0 hour	3 hours	6 hours	10 hours	23 hours
$X_{SSP/PPP}$	1.60	1.66	1.68	1.55	1.59
Tilt angle (°)	13.7	8.0	6.3	17.7	15.4

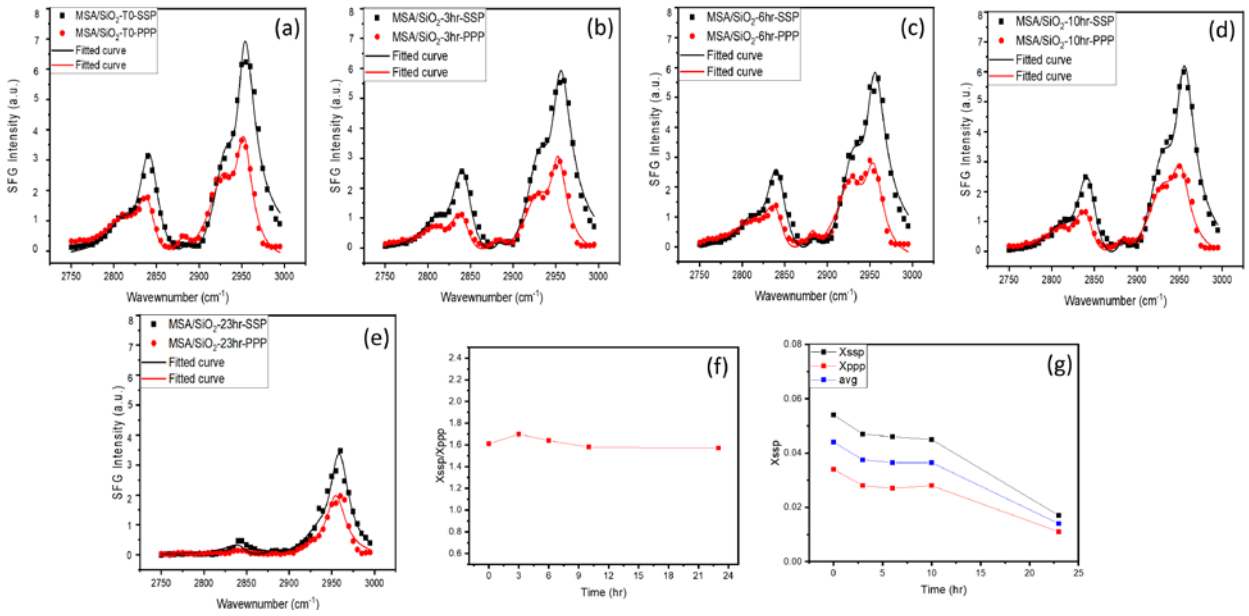

Figure 5.3 SFG SSP (black) and PPP (red) spectra collected from the MSA/silica interface as a function of curing time of (a) 0 h, (b) 3 h, (c) 6 h, (d) 10 h, (e) 23 h. Dots: experimental data. Lines: fitting results. (f) Time-dependent SFG χ_{ssp}/χ_{ppp} ratio. (g) The time-dependent χ_{ssp}, χ_{ppp}, and the averaged values.

The above observed time-dependent reduction of interfacial methoxy groups may be caused by reactions between methoxy and hydroxyl groups on silica surface and/or water moisture in the environment. To understand whether silica surface hydroxyl or moisture plays a dominating role in reacting with interfacial methoxy groups, the silica surface hydroxyl groups were decreased or eliminated through surface silylation (**Scheme 5.1a**). The effectiveness of the surface silylation treatment was investigated using multiple characterization techniques.

5.3.2 Silylated Time-dependent Methoxy SFG Results

Figure 5.4 displays the XPS spectra collected from both untreated and treated silica substrates. In the survey spectra (a) and (b), no nitrogen 1s signal was observed in the 307~400 eV region, indicating that there is no nitrogen contamination before silylation and no HMDS left on the

surface after silylation. On both silica surfaces, signature peaks for O 1s, C 1s, Si 2s, and Si 2p were observed in the XPS spectra at 529, 282, 151, 100 eV, respectively. The qualitative analysis was conducted on XPS spectra to observe changes of surface compositions by comparing the peak intensities of Si and C before and after silylation. Both the Si and C peak intensities increase on the silylated silica surface, confirming the replacement of surface Si-OH groups by Si-$(CH_3)_3$ groups.

SFG was also utilized to examine the surface change after silylation (**Figure 5.4c**). Before silylation, O-H stretching signal dominated the SFG spectrum collected from the silica surface while no C-H stretching signal was detected. There appear to be no CH groups present at the untreated silica surface but OH groups are well represented. Strong Si-$(CH_3)_3$ SFG signal was detected while SFG O-H signal disappeared after the silylation treatment on silica surface, indicating the successful silylation reaction. Water contact angle measurements on silica surfaces were performed as well to confirm the successful silylation of the silica surface (**Figure 5.4d**). Before silylation, the surface had a low contact angle and the water droplet could well spread on the surface, indicating a very hydrophilic surface. After silylation, a much higher contact angle was observed, showing that the silica became more hydrophobic. These observations from three different analytical techniques confirm the successful silylation treatment on silica and rule out the possibility of any leftover HMDS on the silica surface which could affect the silicone interfacial behavior.

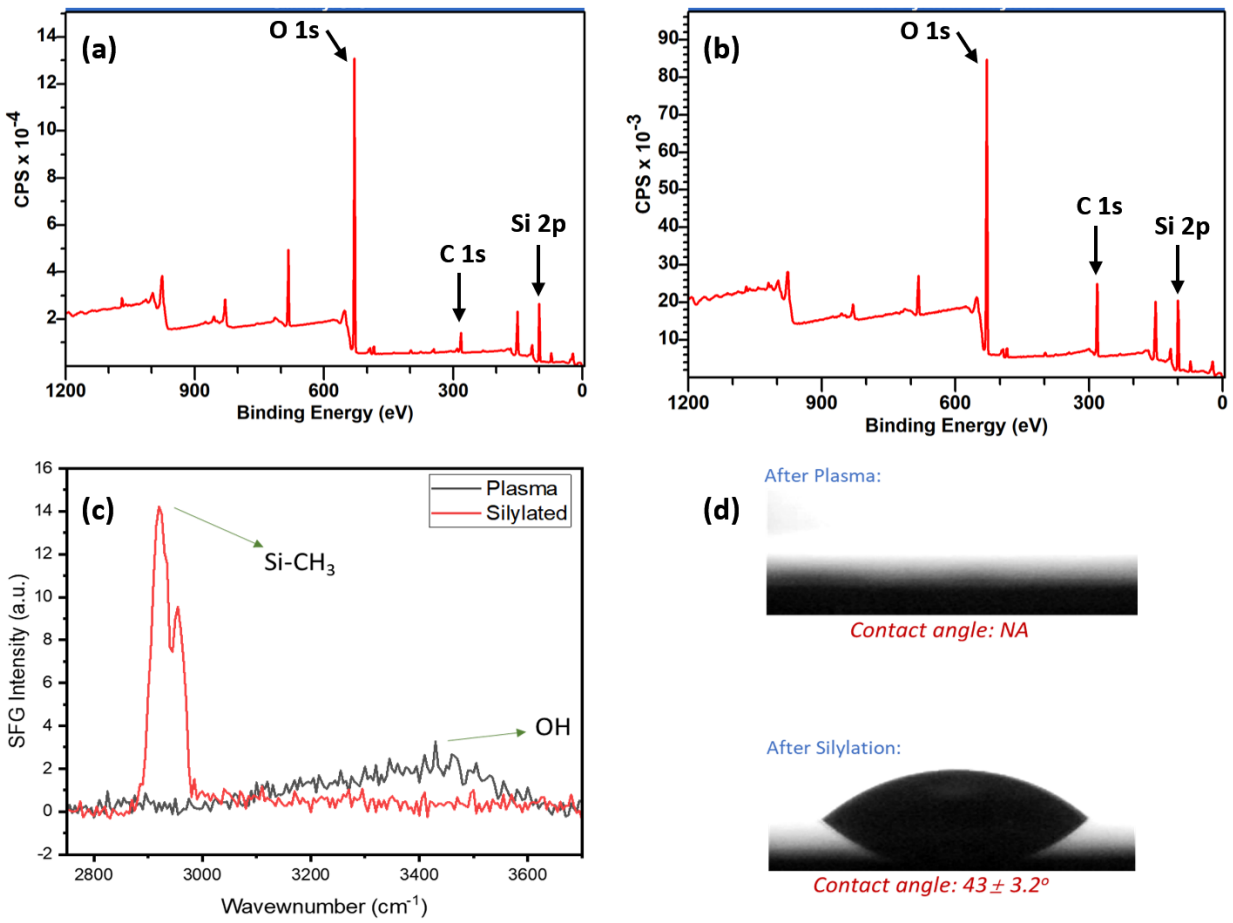

Figure 5.4 XPS spectra collected from the silica substrates (a) before and (b) after silylation, (c) SFG spectra before and after silylation, (d) water contact angle results before and after silylation.

Figure 5.5 displays the SFG spectra collected from the interface between MSA and silica after silylation as a function of curing time. The fitting results are also shown in the same figure and the fitting parameters are listed in **Table 5.3**. The initial T0 SFG spectra collected from the MSA/silylated silica interface (**Figure 5.5a**) exhibit different features from those collected from the MSA/unsilylated (or bare) silica interface (**Figure 5.3a**). Besides the 2840 cm^{-1} methoxy C-H symmetric stretching signal, **Figure 5.5a** also shows a strong peak centered at ~2910 cm^{-1}, which can be assigned to the symmetric C-H stretching signal of silicone Si-CH_3 groups or the Si-CH_3 groups on silica due to silylation. Another strong peak centered at ~2960 cm^{-1} was also observed,

which is assigned to the C-H asymmetric stretching mode of the methyl groups. This peak can be contributed from methyl groups from silica surface silylation, silicone Si-CH_3, and/or methoxy groups in silicone, therefore we cannot use the intensity ratio of this peak and the ~2910 cm^{-1} peak to deduce silicone Si-CH_3 or silica silylated Si-CH_3 orientation.

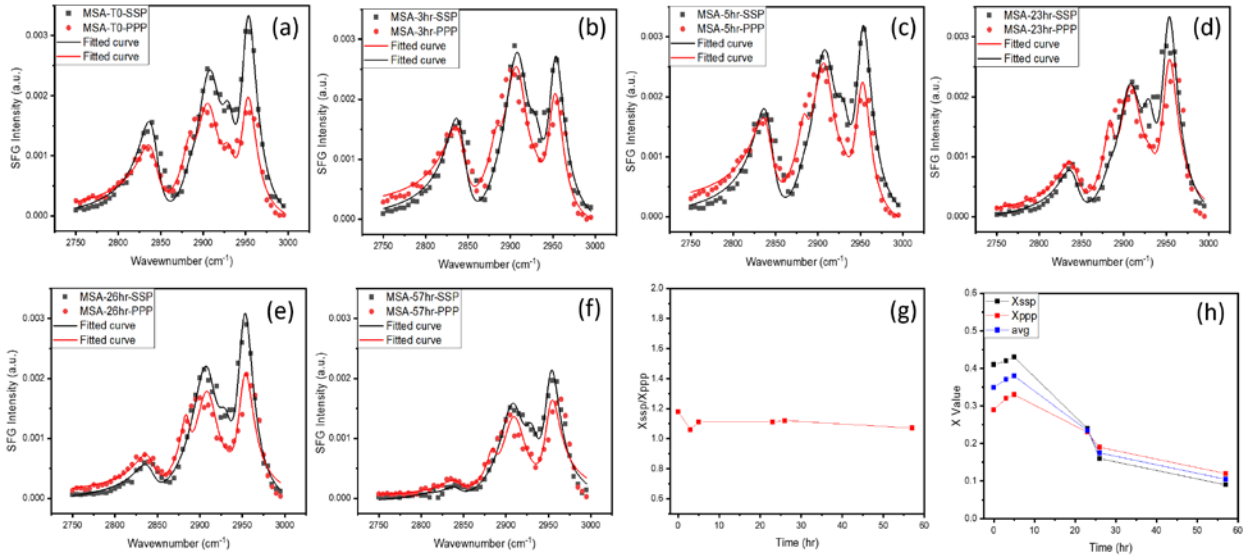

Figure 5.5 SFG spectra collected from the MSA/silylated silica interface as a function of curing time: (a) 0 hr; (b) 3 hr; (c) 5 hr; (d) 23 hr; (e) 26 hr; (f) 57 hr; (g) Time-dependent SFG χ_{ssp}/χ_{ppp} ratio; (j) The time-dependent χ_{ssp}, χ_{ppp}, and the averaged values

The methoxy orientation at the MSA/silylated silica interface can be deduced using the same method as presented in **section 5.2.3**. It was found that the methoxy tilt angle falls in a narrow range from 38.5° to 50.1°, which is different from the tilt angle of methoxy groups at the MSA/unsilylated silica interface (6.3° to 17.7°) reported above. This demonstrates that the overall tilt angle increased and interfacial methoxy groups adapted a more lying down orientation at the interface after silylation. Presumably, the silylated silica surface is more hydrophobic which should have more favorable hydrophobic-hydrophobic interactions with methoxy, leading to a more stand-up methoxy orientation. However, in this case, we observed an opposite trend. In our

previous work, we found that alkoxy silane additives are less compatible with addition cured silicone matrix, and thus tend to segregate to the interface.[35, 37] Such silane molecules are highly interface active and could substantially cover the interface with only small amount of silane in the bulk. In methoxy terminated RTV silicone system, when methoxy silane molecules segregate to an untreated (unsilylated) silica/silicone interface, the methoxy groups tend to interact with the hydrophilic hydroxyl group to participate in the interfacial reaction. Therefore, methoxy adapts a stand-up orientation at interface. This can be understood because with an oxygen atom in methoxy, it is more hydrophilic compared to a regular methyl group (Si-CH_3 or C-CH_3). This should also be true at the MSA/silica interface when PDMS is terminated with trimethoxysilyl functionality. However, the methoxy of silanes or methoxy of PDMS likely cannot favorably interact with silylated silica (with Si-CH_3 groups). As a result, interfacial methoxy groups lie down more at the interface after silylation. **Figure 5.6** shows the schematic of molecular interactions at the interfaces between silicone and native (unsilylated) as well as silylated silica surfaces.

Before silylation, the SFG methoxy SSP/PPP intensity ratio was found to be similar at different curing times, demonstrating similar methoxy orientations during the curing process (see **Figure 5.3**). However, the overall SFG methoxy intensity decreased as a function of time, even with the first three hours, due to the interfacial reaction between methoxy and silica hydroxyl groups or water moisture at the interface during the on-going curing process. After silica silylation was performed to remove the silica surface hydroxyl groups, SFG spectral features and intensities remained similar at different times in the first 5 hours, indicating the absence of time-dependent molecular structure change or reaction at the interface during this period of time. For the first 5 hours, the interfacial molecular structure change observed at the silica (without silylation) interface

must be due to the interfacial –OH, not the bulk –OH from water in ambient condition, otherwise the methoxy signals from the silica with silylation should have decreased as well.

Table 5.3 Fitting parameters of the time-dependent SFG spectra collected from the MSA/silica interface after silylation as shown in Figure 5.5

0 hour-SSP			**0 hour-PPP**			
ωi	Γi (cm^-	Aq	ωi (cm^-	Γi (cm^-	Aq (a.u.)	assignment
2815	14.3	0.016	2815	14.3	0.036	TDIDE
2842	14.2	0.41	2842	14.2	0.29	as O-CH_3
2935	18.3	0.73	2910	18.3	0.64	as
2960	11.5	-0.54	2960	11.5	-0.42	as Si-
3 hour-SSP			**3 hour-PPP**			
ωi	Γi (cm^-	Aq	ωi (cm^-	Γi (cm^-	Aq (a.u.)	assignment
2815	14.3	0.015	2815	14.3	0.025	TDIDE
2842	14.2	0.42	2842	14.2	0.32	as O-CH_3
2935	18.3	0.82	2935	18.3	0.77	as
2960	11.5	-0.46	2960	11.5	-0.43	as Si-
5 hour-SSP			**5 hour-PPP**			
ωi	Γi (cm^-	Aq	ωi (cm^-	Γi (cm^-	Aq (a.u.)	assignment
2815	14.3	0.013	2815	14.3	0.023	TDIDE
2842	14.2	0.43	2842	14.2	0.33	as O-CH_3
2935	18.3	0.79	2910	18.3	0.77	as
2960	11.5	-0.51	2960	11.5	-0.45	as Si-
23 hour-SSP			**23 hour-PPP**			
ωi	Γi (cm^-	Aq	ωi (cm^-	Γi (cm^-	Aq (a.u.)	assignment
2815	14.3	0.016	2815	14.3	0.031	TDIDE
2842	14.2	0.24	2842	14.2	0.23	as O-CH_3
2935	18.3	0.67	2910	18.3	0.74	as
2960	11.5	-0.53	2960	11.5	-0.46	as Si-
26 hour-SSP			**26 hour-PPP**			
ωi	Γi (cm^-	Aq	ωi (cm^-	Γi (cm^-	Aq (a.u.)	assignment
2815	14.3	0.012	2815	14.3	0.033	TDIDE
2842	14.2	0.16	2842	14.2	0.19	as O-CH_3
2935	18.3	0.68	2910	18.3	0.67	as
2960	11.5	-0.54	2960	11.5	-0.42	as Si-
57 hour-SSP			**57 hour-PPP**			
ωi	Γi (cm^-	Aq	ωi (cm^-	Γi (cm^-	Aq (a.u.)	assignment
2815	14.3	0.011	2815	14.3	0.032	TDIDE
2842	14.2	0.09	2842	14.2	0.12	as O-CH_3
2935	18.3	0.60	2910	18.3	0.60	as
2960	11.5	-0.41	2960	11.5	-0.34	as Si-

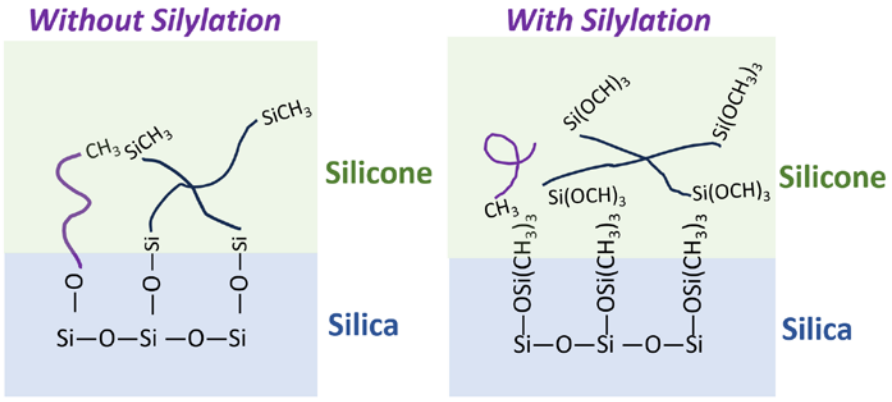

Figure 5.6 Schematic of molecular interactions on (left) native (unsilylated) and (right) silylated silica surfaces

This comparison demonstrates that the primary source of reacting hydroxyl group at the interfacial region for the initial several hours of curing is more likely from the substrate instead of the ambient moisture. Later after water (moisture) molecules diffuse to the interface, further interfacial reaction can consume more methoxy groups. This may explain why at the silicone/unsilylated silica interface (**Figure 5.3**), the SFG methoxy signal decreased in the first three hours (reacted with hydroxyl groups on silica), only slightly decreased between 3 and 10 hours (the silica surface hydroxyl groups already reacted and almost no interfacial reaction with methoxy occurred), and substantially decreased again after 10 hours (reacted with moisture diffused from environment – it took some time for moisture to diffuse to the interface from the environment). Further evidence supporting this hypothesis will be presented below

5.3.3 Humidity Comparison on Methoxy SFG Results

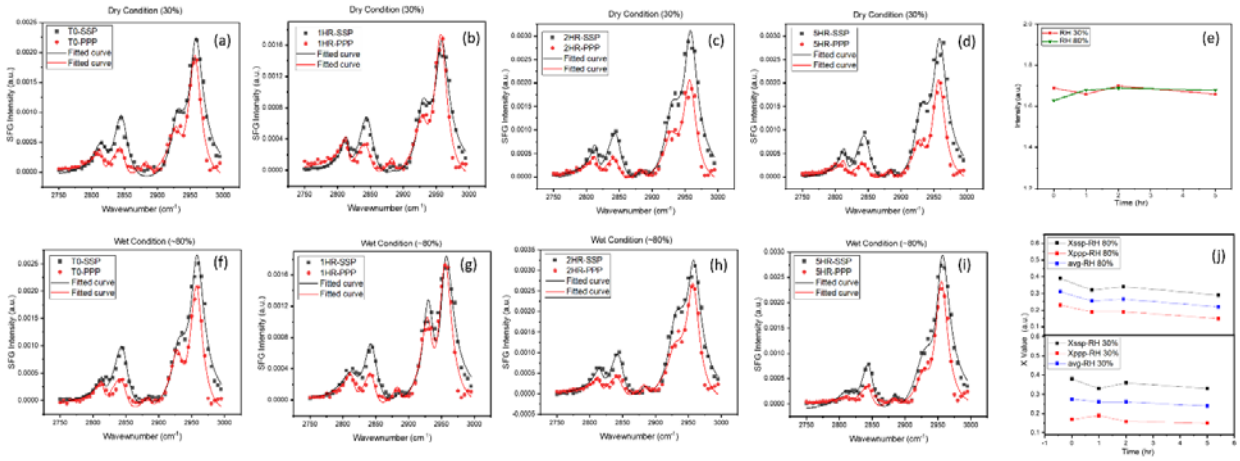

Figure 5.7 SFG spectra collected from the MSA/silica interface as a function of time when cured at different humidity levels: exposure of (a) 0 hr; (b) 1 hr; (c) 2 hr; (d) 5 hr to 30% humidity level; (f) 0 hr; (g) 1 hr; (h) 2 hr; (i) 5 hr to 80% humidity level; (e) Time-dependent SFG χ_{ssp}/χ_{ppp} ratio at 30% and 80% humidity levels. (j) Time-dependent χ_{ssp}, χ_{ppp}, and the averaged values at 30% and 80% humidity levels.

To further verify this hypothesis, humidity control experiments were conducted in 30% and 80% relative humidity environments. If the interfacial -OH groups (from silica) are the primary sources for the interfacial methoxy reactions instead of the -OH groups from the ambient moisture, the molecular structure change reflected in the SFG spectra (e.g., reduction of the methoxy signal) should be the same at different humidity levels. **Figure 5.7** shows that the SFG spectra collected from MSA/unsilylated silica interface exposed to different relative humidities. The fitting results are also shown in the same figure and the fitting parameters are listed in **Table 5.4**. The results exhibit similar features including peak positions, widths, and intensities in the first three to five hours, indicating that ambient moisture is not the primary source of –OH for methoxy interfacial reactions initially. By five hours, the interfacial -OH groups provided by the silica substrate surface were fully reacted and substantial water molecules could gradually diffuse to the interface, and start to participate in the interfacial reactions.

Table 5.4 Fitting parameters of the time-dependent SFG spectra collected from the MSA/silica interface before silylation at different humidity levels (30% and 80%)

0 hour-SSP (RH 30%)			**0 hour-PPP (RH 30%)**			
ωi	Γi (cm^{-}	Aq	ωi (cm^{-}	Γi (cm^{-}	Aq (a.u.)	assignment
2815	14.3	0.06	2815	14.3	0.05	TDIDE
2842	14.2	0.38	2842	14.2	0.17	as O-CH_3
2935	10.1	0.42	2935	10.1	0.23	as
2960	11.5	-0.41	2960	11.5	-0.49	as Si-
1 hour-SSP (RH 30%)			**1 hour-PPP (RH 30%)**			
ωi	Γi (cm^{-}	Aq	ωi (cm^{-}	Γi (cm^{-}	Aq (a.u.)	assignment
2815	14.3	0.06	2815	14.3	0.06	TDIDE
2842	14.2	0.33	2842	14.2	0.19	as O-CH_3
2935	10.1	0.41	2935	10.1	0.21	as
2960	11.5	-0.34	2960	11.5	-0.45	as Si-
2 hour-SSP (RH 30%)			**2 hour-PPP (RH 30%)**			
ωi	Γi (cm^{-}	Aq	ωi (cm^{-}	Γi (cm^{-}	Aq (a.u.)	assignment
2815	14.3	0.07	2815	14.3	0.06	TDIDE
2842	14.2	0.36	2842	14.2	0.16	as O-CH_3
2910	18.3	0.13	2910	18.3	0.11	s Si-CH_3
2935	10.1	0.40	2935	10.1	0.20	as
2960	11.5	-0.46	2960	11.5	-0.45	as Si-
5 hour-SSP (RH 30%)			**5 hour-PPP (RH 30%)**			
ωi	Γi (cm^{-}	Aq	ωi (cm^{-}	Γi (cm^{-}	Aq (a.u.)	assignment
2815	14.3	0.07	2815	14.3	0.05	TDIDE
2842	14.2	0.33	2842	14.2	0.15	as O-CH_3
2935	10.1	0.37	2935	10.1	0.20	as
2960	11.5	-0.44	2960	11.5	-0.51	as Si-
T0-SSP (RH 80%)			**T0-PPP (RH 80%)**			
ωi	Γi (cm^{-}	Aq	ωi (cm^{-}	Γi (cm^{-}	Aq (a.u.)	assignment
2815	14.3	0.04	2815	14.3	0.04	TDIDE
2842	14.2	0.39	2842	14.2	0.23	as O-CH_3
2935	10.1	0.39	2935	10.1	0.23	as
2960	11.5	-0.45	2960	11.5	-0.51	as Si-
1 hour-SSP (RH 80%)			**1 hour-PPP (RH 80%)**			
ωi	Γi (cm^{-}	Aq	ωi (cm^{-}	Γi (cm^{-}	Aq (a.u.)	assignment
2815	14.3	0.09	2815	14.3	0.07	TDIDE
2842	14.2	0.32	2842	14.2	0.19	as O-CH_3
2935	10.1	0.27	2935	10.1	0.22	as
2960	11.5	-0.40	2960	11.5	-0.45	as Si-
2 hour-SSP (RH 80%)			**2 hour-PPP (RH 80%)**			
ωi	Γi (cm^{-}	Aq	ωi (cm^{-}	Γi (cm^{-}	Aq (a.u.)	assignment
2815	14.3	0.07	2815	14.3	0.05	TDIDE
2842	14.2	0.34	2842	14.2	0.19	as O-CH_3
2935	10.1	0.45	2935	10.1	0.25	as

2960	11.5	-0.42	2960	11.5	-0.50	as Si-
5 hour-SSP (RH 80%)			**5 hour-PPP (RH 80%)**			
ωi	Γi (cm^{-}	Aq	ωi (cm^{-}	Γi (cm^{-}	Aq (a.u.)	assignment
2815	14.3	0.11	2815	14.3	0.04	TDIDE
2842	14.2	0.29	2842	14.2	0.15	as O-CH_3
2935	10.1	0.37	2935	10.1	0.21	as
2960	11.5	-0.46	2960	11.5	-0.55	as Si-

5.3.4 Adhesion Results

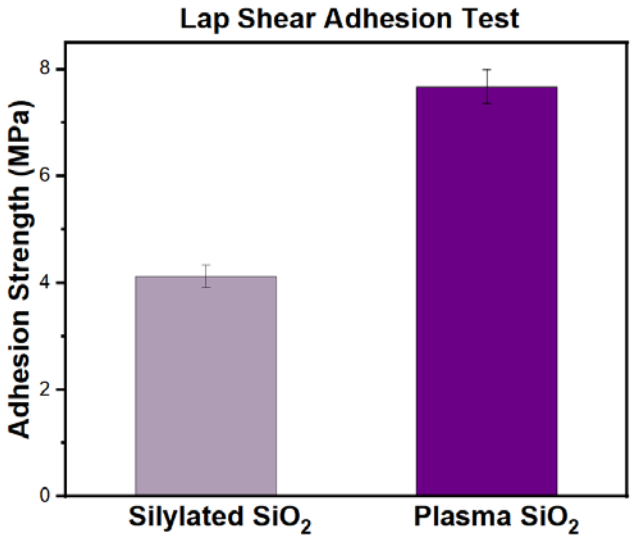

Figure 5.8 Adhesion strength on silica substrate with and without silylation

The lap shear adhesion test was conducted on the fully cured silicone samples to correlate the results obtained from the interfacial structure study presented above to those from the property (adhesion) measurements. The adhesion results are shown in **Figure 5.8**. Compared to the silylated silica substrate, the silica without silylation treatment shows a significant enhancement in the adhesion strength. According to the interfacial structure and composition probed by SFG and XPS, we believe the enhancement originates from more reaction sites (more hydroxyl groups) at the interface, leading to more covalent bonds formed at the interface by interfacial chemical reaction.

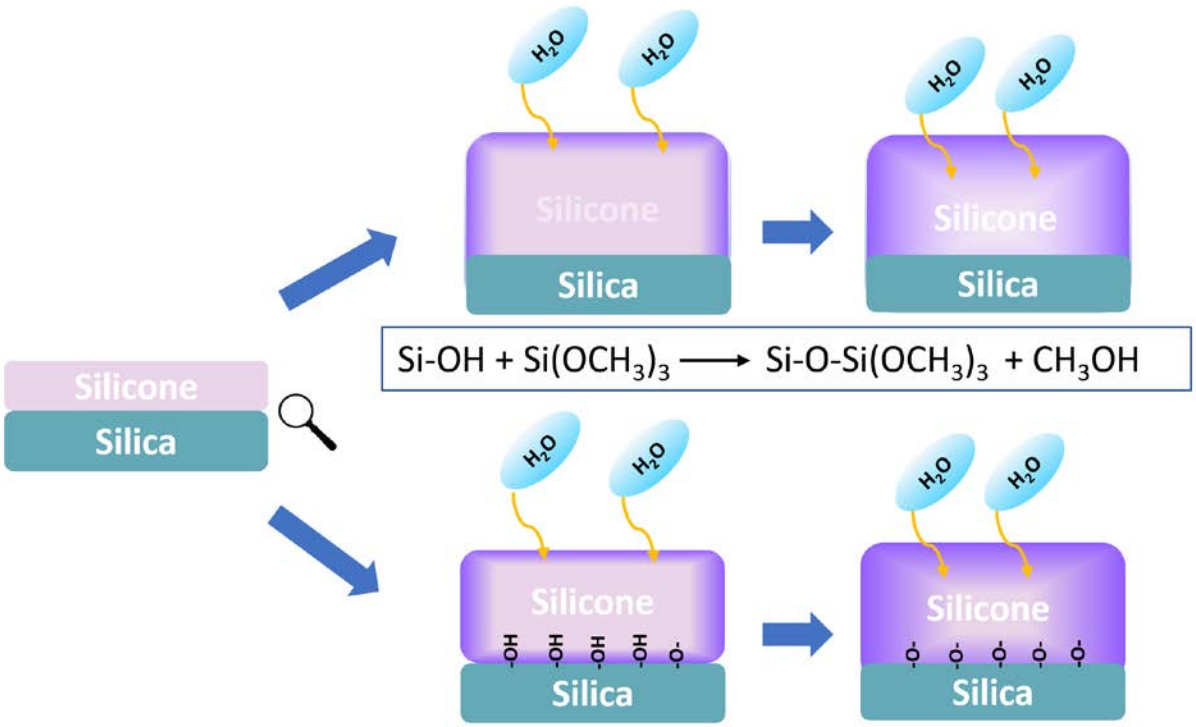

Figure 5.9 Schematic of the curing process of RTV silicone. Initially curing occurs using the hydroxyl groups because it takes some time for moisture to diffuse to the interface. Top right: silylated silica/silicone interface. Bottom right: silica/silicone interface. Different objects in the figure were not drawn to scale.

The curing mechanism at the interfacial region is depicted in **Figure 5.9**. It is well known that ambient moisture triggers the curing reaction of RTV silicone and provides hydroxyl group which reacts with methoxy terminated RTV silicone. However, this is likely not the case for the interfacial region. The interfacial hydroxyl from the substrate is the primary source of the curing and interfacial reactions initially. Even though the water permeability of silicone is quite high, there would be a crust layer formed in the outside region of silicone during curing. The region underneath the crust layer contains unreacted methoxy groups which could capture the water and slow down the water migration process to the interface. Therefore, there is no moisture hydroxyl at the interface for the first several hours (**Figure 5.9**). The interfacial hydroxyl groups are crucial for silicone curing and interfacial reaction, which can form covalent bonds between silicone matrix

and the substrate. As a result, stronger adhesion strength can be obtained if there are more interfacial hydroxyl groups on the surface. Later on, as the crust layer propagates to the interfacial region, moisture hydroxyl groups could play a more significant role for the interfacial curing. This aligns well with the results obtained by other researchers using NMR.[60]

5.3.5 Peak Assignment of Ti Catalyst

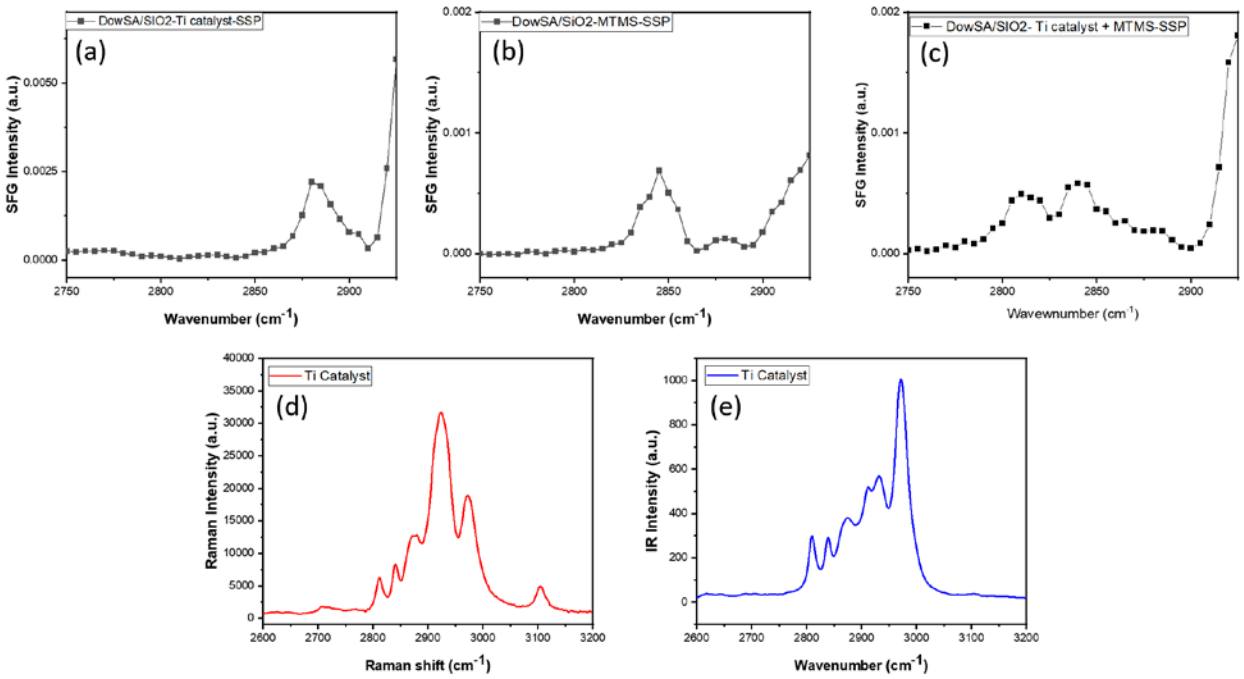

Figure 5.10 SFG spectrum from the MSA (with Ti catalyst but without MTMS)/silica interface (a), SFG spectrum from the MSA (wih MTMS but without Ti catalyst)/silica interface (b), SFG spectrum from the MSA (with both Ti catalyst and MTMS)/silica interface (c), Raman spectrum of Ti catalyst (d), IR spectrum of Ti catalyst (e).

The SFG spectra displayed in **Figures 5.3** and **5.7** show a peak centered around 2815 cm^{-1}. We believe that this signal can be contributed by Ti catalyst and/or MTMS. **Figures 5.10a** and **5.10b** show that the 2815 cm^{-1} signal was not detected from the MSA/silica interface when MSA only contains Ti catalyst or MTMS. However, a peak at 2815 cm^{-1} was detected from the MSA/silica

interface when MSA contains both Ti catalyst and MTMS (**Figure 5.10c**). Both Raman and IR spectra from Ti catalyst show the 2815 cm^{-1} signal (**Figures 5.10d** and **5.10e**), while this signal was not observed from the IR or Raman spectra from MTMS (not shown). Therefore, we assigned the 2815 cm^{-1} peak to Ti catalysts, the detection of which by SFG requires the addition of the MTMS to the silicone adhesive as well. More detailed assignment of this peak is beyond the scope of this research, which will be reported in our future work.

5.4 Conclusion

SFG has been successfully applied to study adhesion mechanisms of condensation cured silicone materials to glass, modeled by silica. Our time-dependent in situ SFG experiments revealed that the condensation cured silicone samples undergo interfacial changes (especially for methoxy groups) during the curing process. Such observed interfacial changes indicated that the primary reacting source of interfacial hydroxyl groups in these materials for initial curing (3 to 5 hours) was the hydroxyl groups on the substrate surface, rather than the hydroxyl groups on the silicone itself or from environmental moisture. Such interfacial hydroxyl groups reacted with methoxy groups in silicone to form covalent bonds at the interface. At longer cure times moisture from the environment may diffuse into the interface to cause further interfacial reactions.

The results of this research further validate the usefulness of SFG as a unique and effective method for examining buried solid/solid interfaces — like the ones between silicone and silica substrates —at the molecular level, in real-time during curing and other processes. Insights gained from the study enhance our understanding of the relationship between changes in the interfacial molecular structure and the characteristics and functionality of the condensation cured silicone. This important understanding will assist in the design and development of RTV silicone materials with superior performance qualities for a variety of applications in the future.

5.5 References

1. Jurásková, A.; Møller Olsen, S.; Dam-Johansen, K.; Brook, M. A.; Skov, A. L., Reliable Condensation Curing Silicone Elastomers with Tailorable Properties. *Molecules* **2021**, *26*, 82.
2. Shit, S. C.; Shah, P., A Review on Silicone Rubber. *Natl. Acad. Sci. Lett.* **2013**, *36*, 355-365.
3. Jurásková, A.; Dam-Johansen, K.; Olsen, S. M.; Skov, A. L., Factors Influencing Mechanical Long-Term Stability of Condensation Curing Silicone Elastomers. *J. Polym. Res.* **2020**, *27*, 341.
4. Leow, M. E. L.; Pho, R. W. H., RTV Silicone Elastomers in Hand Prosthetics: Properties, Applications and Techniques. *Prosthet. Orthot. Int.* **1999**, *23*, 169-173.
5. Research, G. V. *Silicone Market Size, Share & Trends Analysis Report by Product (Fluids, Gels, Resins, Elastomers), by End-Use (Electronics, Transportation, Construction, Healthcare, Industrial Processes, Energy), by Region, and Segment Forecasts, 2023 - 2030*; 2022.
6. De Buyl, F.; Comyn, J.; Shephard, N. E.; Subramaniam, N. P., Kinetics of Cure, Cross Link Density and Adhesion of Water-Reactive Alkoxysilicone Sealants. *J. Adhes. Sci. Technol.* **2002**, *16*, 1055-1071.
7. Ghanbari, K.; Ehsani, M.; Jannesari Ladani, A.; Mohseni, M.; Ghaffari, M., Thermoanalytical Study of Siloxane-Polyurethane Thermosets: Kinetic Deconvolution of Overlapping Heterogeneous Curing Reactions. *Prog. Org. Coat.* **2017**, *112*, 234-243.
8. Ye, H.; Gu, Z.; Gracias, D. H., Kinetics of Ultraviolet and Plasma Surface Modification of Poly(Dimethylsiloxane) Probed by Sum Frequency Vibrational Spectroscopy. *Langmuir* **2006**, *22*, 1863-1868.
9. Tsige, M.; Soddemann, T.; Rempe, S. B.; Grest, G. S.; Kress, J. D.; Robbins, M. O.; Sides, S. W.; Stevens, M. J.; Webb III, Interactions and Structure of Poly (Dimethylsiloxane) at Silicon Dioxide Surfaces: Electronic Structure and Molecular Dynamics Studies. *Chem. Phys.* **2003**, *118*, 5132-5142.
10. Wang, B.; Hu, J.; Liu, K.; Zhang, L.; Jiang, H.; Li, C., Reinforcement Mechanism of Silica Surface Hydroxyl: The Opposite Effect. *Appl. Surf. Sci.* **2023**, *623*, 157000.
11. Liu, J.; Wu, S.; Zou, M.; Zheng, X.; Cai, Z., Surface Modification of Silica and Its Compounding with Polydimethylsiloxane Matrix: Interaction of Modified Silica Filler with Pdms. *Iran. Polym. J.* **2012**, *21*, 583-589.
12. He, X. W.; Widmaier, J. M.; Herz, J. E.; Meyer, G. C., Competition between Polycondensation of A,Ω-Dihydroxy Polydimethylsiloxane and Its Condensation with Alkoxy Silane: A Kinetic Approach. *Eur. Polym. J.* **1988**, *24*, 1145-1148.
13. Tarasenkov, A. N.; Parshina, M. S.; Goncharuk, G. P.; Borisov, K. M.; Golubev, E. K.; Meshkov, I. B.; Cherkaev, G. V.; Shevchenko, V. G.; Ponomarenko, S. A.; Muzafarov, A. M., Thioether-Containing Zirconium(Alkoxy)Siloxanes: Synthesis and Study of Dielectric and Mechanical Properties of Silica-Filled Polydimethylsiloxane Compositions Cured by Them. *Polymers* **2023**, *15*, 3361.
14. Chen, Z., Investigating Buried Polymer Interfaces Using Sum Frequency Generation Vibrational Spectroscopy. *Prog. Polym. Sci.* **2010**, *35*, 1376-1402.
15. Bain, C. D., Sum-Frequency Vibrational Spectroscopy of the Solid/Liquid Interface. *J. Chem. Soc., Faraday Trans.* **1995**, *91*, 1281-1296.

16. Chen, C.; Wang, J.; Even, M. A.; Chen, Z., Sum Frequency Generation Vibrational Spectroscopy Studies on “Buried” Polymer/Polymer Interfaces. *Macromolecules* **2002**, *35*, 8093-8097.

17. Shen, Y., Surface Properties Probed by Second-Harmonic and Sum-Frequency Generation. *Nature* **1989**, *337*, 519-525.

18. Wu, Y.; Wang, T.; Gao, J.; Zhang, L,; Fay, J. D. B.; Hirth, S.; Hankett, J.; Chen, Z. Molecular Behavior of 1-K Polyurethane Adhesive at Buried Interfaces: Plasma Treatment, Annealing, and Adhesion. *Langmuir* **2023**, *39*, 3273–3285.

19. Buck, M.; Himmelhaus, M., Vibrational Spectroscopy of Interfaces by Infrared–Visible Sum Frequency Generation. *J. Vac. Sci. Technol.* **2001**, *19*, 2717-2736.

20. Fang, Y.; Li, B.; Yu, J.; Zhou, J.; Xu, X.; Shao, W.; Lu, X., Probing Surface and Interfacial Molecular Structures of a Rubbery Adhesion Promoter Using Sum Frequency Generation Vibrational Spectroscopy. *Surf. Sci.* **2013**, *615*, 26-32.

21. Zuo, B.; Zhou, H.; Davis, M. J. B.; Wang, X.; Priestley, R. D., Effect of Local Chain Conformation in Adsorbed Nanolayers on Confined Polymer Molecular Mobility. *Phys. Rev. Lett.***2019**, *122*, 217801.

22. Zhang, C.; Wang, J.; Khmaladze, A.; Liu, Y.; Ding, B.; Jasensky, J.; Chen, Z., Examining Surface and Bulk Structures Using Combined Nonlinear Vibrational Spectroscopies. *Opt. Lett.* **2011**, *36*, 2272-2274.

23. Ding, B.; Panahi, A.; Ho, J.-J.; Laaser, J. E.; Brooks, C. L., III; Zanni, M. T.; Chen, Z., Probing Site-Specific Structural Information of Peptides at Model Membrane Interface in Situ. *J. Am. Chem. Soc.* **2015**, *137*, 10190-10198.

24. Ye, H.; Abu-Akeel, A.; Huang, J.; Katz, H. E.; Gracias, D. H., Probing Organic Field Effect Transistors in Situ During Operation Using Sfg. *J. Am. Chem. Soc.* **2006**, *128*, 6528-6529.

25. Gracias, D. H.; Chen, Z.; Shen, Y. R.; Somorjai, G. A., Molecular Characterization of Polymer and Polymer Blend Surfaces. Combined Sum Frequency Generation Surface Vibrational Spectroscopy and Scanning Force Microscopy Studies. *Acc. Chem. Res.* **1999**, *32*, 930-940.

26. Inutsuka, M.; Haraguchi, M.; Ozawa, M.; Yamada, N. L.; Tanaka, K., Adhesion Control of Elastomer Sheet on the Basis of Interfacial Segregation of Hyperbranched Polymer. *ACS Macro Lett.***2019**, *8*, 267-271.

27. Sugimoto, S.; Inutsuka, M.; Kawaguchi, D.; Tanaka, K., Reorientation Kinetics of Local Conformation of Polyisoprene at Substrate Interface. *ACS Macro Lett.***2018**, *7*, 85-89.

28. Hong, Y.; Bao, S.; Xiang, X.; Wang, X., Concentration-Dominated Orientation of Phenyl Groups at the Polystyrene/Graphene Interface. *ACS Macro Lett.***2020**, *9*, 889-894.

29. Yamamoto, S.; Kuwahara, R.; Aoki, M.; Shundo, A.; Tanaka, K., Molecular Events for an Epoxy–Amine System at a Copper Interface.ACS Appl. Polym. Mater. **2020**, *2*, 1474-1481.

30. Wan, Z.; Azam, M. S.; Wyatt, S.; Ramsay, K.; Korner, J. L.; Elvira, K. S.; Padmawar, R.; Varela, D.; Hore, D. K., Algae Adhesion onto Silicone Is Sensitive to Environment-Induced Surface Restructuring. *Langmuir* **2021**, *37*, 9597-9604.

31. Cai, C.; Azam, M. S.; Hore, D., Temperature-Dependent Chemical Functional Group Reorientation at Silicone Surfaces. *J. Phys. Chem. C* **2021**, *125*, 22214-22222.

32. Ding, B.; Jasensky, J.; Li, Y.; Chen, Z., Engineering and Characterization of Peptides and Proteins at Surfaces and Interfaces: A Case Study in Surface-Sensitive Vibrational Spectroscopy. *Acc. Chem. Res.* **2016**, *49*, 1149-1157.

33. Zhang, C.; Shephard, N. E.; Rhodes, S. M.; Chen, Z., Headgroup Effect on Silane Structures at Buried Polymer/Silane and Polymer/Polymer Interfaces and Their Relations to Adhesion. *Langmuir* **2012**, *28*, 6052-6059.

34. Lin, T.; Wu, Y.; Santos, E.; Chen, X.; Kelleher-Ferguson, J.; Tucker, C.; Ahn, D.; Mohler, C.; Chen, Z., Probing Covalent Interactions at a Silicone Adhesive/Nylon Interface. *Langmuir* **2022**, *38*, 2590-2600.

35. Wang, J.; Wloch, G.; Lin, T.; Chen, Z., Investigating Thin Silicone Oil Films Using Four-Wave Mixing Spectroscopy and Sum Frequency Generation Vibrational Spectroscopy. *Langmuir* **2021**, *37*, 14540-14549.

36. Lin, T.; Wu, Y.; Santos, E.; Chen, X.; Ahn, D.; Mohler, C.; Chen, Z., Molecular Insights into Adhesion at a Buried Silica-Filled Silicone/Polyethylene Terephthalate Interface. *Langmuir* **2020**, *36*, 15128-15140.

37. Loch, C. L.; Ahn, D.; Chen, C.; Chen, Z., Polymer-Silane Interactions Probed by Sum Frequency Generation Vibrational Spectroscopy. *J Adhes.* **2005**, *81*, 319-345.

38. Vázquez, A. V.; Shephard, N. E.; Steinecker, C. L.; Ahn, D.; Spanninga, S.; Chen, Z., Understanding Molecular Structures of Silanes at Buried Polymer Interfaces Using Sum Frequency Generation Vibrational Spectroscopy and Relating Interfacial Structures to Polymer Adhesion. *J. Colloid Interface Sci.* **2009**, *331*, 408-416.

39. Vázquez, A. V.; Boughton, A. P.; Shephard, N. E.; Rhodes, S. M.; Chen, Z., Molecular Structures of the Buried Interfaces between Silicone Elastomer and Silane Adhesion Promoters Probed by Sum Frequency Generation Vibrational Spectroscopy and Molecular Dynamics Simulations. *ACS Appl. Mater. Interfaces* **2010**, *2*, 96-103.

40. Vázquez, A. V.; Holden, B.; Kristalyn, C.; Fuller, M.; Wilkerson, B.; Chen, Z., Surface and Buried Interfacial Structures of Epoxy Resins Used as Underfills Studied by Sum Frequency Generation Vibrational Spectroscopy. *ACS Appl. Mater. Interfaces* **2011**, *3*, 1640-1651.

41. Loch, C. L.; Ahn, D.; Vázquez, A. V.; Chen, Z., Diffusion of One or More Components of a Silane Adhesion-Promoting Mixture into Poly (Methyl Methacrylate). *J. Colloid Interface Sci.* **2007**, *308*, 170-175.

42. Lu, X.; Li, B.; Zhu, P.; Xue, G.; Li, D., Illustrating Consistency of Different Experimental Approaches to Probe the Buried Polymer/Metal Interface Using Sum Frequency Generation Vibrational Spectroscopy. *Soft Matter* **2014**, *10*, 5390-5397.

43. Chen; Wang, J.; Even, M. A.; ChenChen, Z., Sum Frequency Generation Vibrational Spectroscopy Studies on "Buried" Polymer/Polymer Interfaces. *Macromolecules* **2002**, *35*, 8093-8097.

44. Zhang, C.; Chen, Z., Quantitative Molecular Level Understanding of Ethoxysilane at Poly(Dimethylsiloxane)/Polymer Interfaces. *Langmuir* **2013**, *29*, 610-619.

45. Lu, X.; Clarke, M. L.; Li, D.; Wang, X.; Xue, G.; Chen, Z., A Sum Frequency Generation Vibrational Study of the Interference Effect in Poly(N-Butyl Methacrylate) Thin Films Sandwiched between Silica and Water. *J. Phys. Chem. C* **2011**, *115*, 13759-13767.

46. Lambert, A. G.; Davies, P. B.; Neivandt, D. J., Implementing the Theory of Sum Frequency Generation Vibrational Spectroscopy: A Tutorial Review. *Appl. Spectrosc. Rev.* **2005**, *40*, 103-145.

47. Guyot-Sionnest, P., Coherent Processes at Surfaces: Free-Induction Decay and Photon Echo of the Si-H Stretching Vibration for H/Si(111). *Phys. Rev. Lett.***1991**, *66*, 1489-1492.

48. Zhuang, X.; Miranda, P. B.; Kim, D.; Shen, Y. R., Mapping Molecular Orientation and Conformation at Interfaces by Surface Nonlinear Optics. *Phys. Rev. B* **1999**, *59*, 12632-12640.

49. Richter, L. J.; Petralli-Mallow, T. P.; Stephenson, J. C., Vibrationally Resolved Sum-Frequency Generation with Broad-Bandwidth Infrared Pulses. *Opt. Lett.* **1998**, *23*, 1594-1596.

50. Superfine, R.; Huang, J. Y.; Shen, Y. R., Phase Measurement for Surface Infrared–Visible Sum-Frequency Generation. *Opt. Lett.* **1990**, *15*, 1276-1278.

51. Lagutchev, A.; Hambir, S. A.; Dlott, D. D., Nonresonant Background Suppression in Broadband Vibrational Sum-Frequency Generation Spectroscopy. *J. Phys. Chem. C* **2007**, *111*, 13645-13647.

52. Moad, A. J.; Simpson, G. J., A Unified Treatment of Selection Rules and Symmetry Relations for Sum-Frequency and Second Harmonic Spectroscopies. *J. Phys. Chem. B* **2004**, *108*, 3548-3562.

53. Perry, A.; Neipert, C.; Space, B.; Moore, P. B., Theoretical Modeling of Interface Specific Vibrational Spectroscopy: Methods and Applications to Aqueous Interfaces. *Chem. Rev.* **2006**, *106*, 1234-1258.

54. Hirose, C.; Akamatsu, N.; Domen, K., Formulas for the Analysis of Surface Sum-Frequency Generation Spectrum by Ch Stretching Modes of Methyl and Methylene Groups. *J. Phys. Chem.* **1992**, *96*, 997-1004.

55. Geiger, F. M., Second Harmonic Generation, Sum Frequency Generation, and X(3): Dissecting Environmental Interfaces with a Nonlinear Optical Swiss Army Knife. *Annu. Rev. Phys. Chem.* **2009**, *60*, 61-83.

56. Lin, T.; Guo, W.; Guo, R.; Chen, Z., Probing Biological Molecule Orientation and Polymer Surface Structure at the Polymer/Solution Interface in Situ. *Langmuir* **2020**, *36*, 7681-7690.

57. Kendall, K., Crack Propagation in Lap Shear Joints. *J. Phys. D: Appl. Phys.* **1975**, *8*, 512.

58. Da Silva, L. F. M.; Rodrigues, T. N. S. S.; Figueiredo, M. A. V.; de Moura, M. F. S. F.; Chousal, J. A. G., Effect of Adhesive Type and Thickness on the Lap Shear Strength. *J Adhes.* **2006**, *82*, 1091-1115.

59. Knipe, J. M.; Sirrine, J.; Sawvel, A. M.; Mason, H. E.; Lewicki, J. P.; Sun, Y.; Glascoe, E. A.; Sharma, H. N., In Situ Curing Kinetics of Moisture-Reactive Acetoxysiloxane Sealants. *Ind. Eng. Chem. Res.* **2019**, *58*, 17266-17276.

Chapter 6 Analysis of Accelerated Weather Aging Effect on Polyethylene with Varied Densities Using a Combination of Analytical Techniques

The contents presented in this chapter were adopted from a submitted manuscript entitled "Analysis of Accelerated Weather Aging Effect on Polyethylene with Varied Densities Using a Combination of Analytical Techniques". The research related to ATR-FTIR, water contact angle, and nanoindentation measurements were performed by a graduate student in our lab, Shuqing Zhang. I performed research related to Raman and GIXRD measurements.

6.1 Introduction

Plastics, owing to their cost-effectiveness, easy handling, and lightweight nature, have been universally integrated into diverse applications, enhancing living standards.[1-3] However, a flip side exists: post-consumption, plastics contribute significantly to global municipal waste.[4-6] Alarmingly, with annual plastic production surpassing 300 million tons since 2014, environmental plastic build-up is escalating.[7,8] On the global front, a tiny fraction of plastic waste is repurposed,[9-13] and a majority either ends up in landfills or contaminates natural habitats, heralding environmental and sustainability challenges.[14] Investigating plastic degradation processes can unveil the repercussions of these decomposed materials, guiding mitigation approaches.

Polyethylene (PE) stands out as one of the most produced and versatile plastics globally, catering to various applications.[15-18] Derived from polyolefin, its intrinsic traits—large molecular structure, hydrophobic nature, and absence of vulnerable functional groups—grant it durability and resistance to biological interactions.[19,20] These properties, while advantageous for applications like automotive components and pipework,[21,22] complicate its disposal post-usage. A number of

studies have delved into PE's degradation behavior under diverse conditions.[20,23-30] Notably, photooxidation has been identified as an effective accelerator for PE degradation and has been a research hotspot for decades.[31-37] In theory, pure PE should repel photooxidative degradation due to its hydrocarbon configuration's resilience against the majority of the sun's spectrum. However, the production process can introduce imperfections and contaminants, predisposing PE to degradation.

Although the UV-induced deterioration of PE has been rigorously studied, most research in photooxidation has zoomed in on model PE variants or specific commercial products without extensive material profiling. Establishing a definitive link between PE attributes and degradation outcomes is vital for understanding the environmental implications and guiding producers towards eco-friendly products. This research's distinction lies in its focus on a wide spectrum of PE types tailored for packaging, encompassing HDPE and LLDPE, fashioned into diverse physical and chemical forms. Subjecting these to simulated solar radiation, the study demonstrates the UV degradation effects and subsequent weathering mechanisms. A suite of analytical methods—including water contact angle measurements, ATR-FTIR, Raman microscopy, GIXRD, and nano-indentation—was deployed to evaluate the PE variants post UV-exposure. The study, through its methodological arsenal, sheds light on the transformative structural dynamics of PE under UV influence over time. The integrative approach provides an all-rounded perspective on PE photooxidation due to solar activity. This research not only uncovers PE's degradation patterns but also underscores the environmental implications, empowering industries to innovate less environmentally detrimental plastics.

6.2 Materials and Methods

6.2.1 Materials and Sample Preparation

All the polyethylene (HDPE and LLDPE) samples in the form of plaques and films were provided by The Dow Chemical Company. **Table 6.1** lists detailed characteristics of the samples used in this study with information on density, melt index, and thickness.

Table 6.1 Polyethylene sample information

Generic Label	Architecture	Generic description	Density (g/cm^3)	Melt Index (g/10 min at 190 °C)	Thickness (mm)
G	Plaque	HDPE	0.9573	1.4	~3
H	Plaque	HDPE	0.9555	1.5	~3
J	Plaque	LLDPE	0.9159	0.94	~3
K	Plaque	LLDPE	0.9145	0.98	~3
L	Plaque	LLDPE	0.9214	0.95	~3
Generic Label	**Architecture**	**Generic description**	**Density (g/cm^3)**	**Melt Index (g/10 min at 190 °C)**	**Thickness (mil/μm)**
#5	Film	LLDPE	0.923	1	3/75
#6	Film	HDPE	0.9646	0.91	3/75

The aging technique utilized was the ISO 4892 cycle 4, which incorporates UV, heat, and moisture factors, executed in the SUNTEST XXL chamber from ATLAS MTS LLC. This approach is believed to expedite the aging process by about four to five times compared to outdoor aging in southern Florida, based on equivalent UV dosage assessments. Polyethylene specimens underwent simulated solar aging for varied durations, either two or four weeks, prior to analysis.

6.2.2 Experimental Methods

6.2.2.1 ATR-FTIR Experiments

ATR-FTIR spectra were collected using a Nicolet iS50 (Thermo Scientific) spectrometer controlled by OMNIC software from the polyethylene material in contact with the ATR crystal. Samples were characterized at a 4 cm^{-1} resolution within the range of 4000 to 600 cm^{-1}. By detecting the change at distinct bands at different times, ATR-FTIR is capable of describing the species formed throughout the process. Carbonyl index and vinyl index are commonly used as indicators to quantitively evaluate the photooxidation process of polyethylene samples and will be applied in this study. Multiple methods of calculating the carbonyl index and vinyl index have been reported and are yet to be unified, but typically are based on a ratio of carbonyl or vinyl peak to a reference peak.[7, 38-43] In this study, the carbonyl index was calculated as the maximum absorption in the carbonyl range (around 1714 cm^{-1}) relative to the reference methylene absorbance around 730 cm^{-1} as described in the literature,[44] based on the average values gained from repeated tests on each sample. The vinyl index was evaluated as the absorbance around 909 cm^{-1} to that of the same reference methylene absorbance.

6.2.2.2 Raman spectroscopy

All the Raman spectra were collected by a Leica optical microscope equipped Renishaw inVia Raman spectrophotometer. The Raman system uses a 785 nm laser, a 1800 lines/mm grating, a 65 micron slit, and a RenCam CCD detector. The spectra were obtained with extended mode (200 – 3800 cm^{-1}). Raman spectroscopy was utilized to characterize the photodegradation of above HDPE and LLDPE samples after simulated weather aging. Raman spectra can provide insightful microscopic structure information in the chemicrystallization during the degradation process.

6.2.2.3 Grazing incident X-ray diffraction (GIXRD)

A Rigaku Ultima IV diffractometer with grazing incident mode was used to obtain GIXRD results. The diffractometer was equipped with a 2.2 kW and 0.4 x 12 mm focus size Cu K-alpha radiation long-fine focus tube, a 285 mm radius and 0.0001^{o} minimum step size goniometer, and a D/teX-ULTRA scintillation detector. Calibration was conducted before data collection. The detection depth of GIXRD is in the magnitude of nanometer and can be considered a surface-sensitive crystallinity characterization technique to provide complementary results to Raman.

6.2.2.4 Nanoindentation tests

Nanoindentation is considered a powerful method to measure the mechanical properties of polymer materials.[45-47] Here, nanoindentation tests were conducted using the Hysitron TI 950 TriboIndenter (Bruker, Eden Prairie, MN) with an optical camera for viewing the surface structures in high-resolution and defining areas to be indented. Tests were controlled by TriboScan9 software. A Berkovich indentation probe with a triangular base was used for depth-sensing indentation (lift height 25 nm). Before nanoindentation experiments, samples were glued onto circular AFM specimen discs (Ted Pella Inc., Redding, CA) and mounted on the intender stage which transfers samples back and forth between optics and probes. The device was calibrated before indentation experiments to ensure the probe was at the desired location during the tests. The experiments were performed in ambient conditions. Each sample was indented 18 times in different locations by setting up two 3 × 3 grids using array pattern with a load range of 0-100 μN. The reduced elastic modulus was obtained from each indentation process, and Young's modulus can be deduced by the Oliver and Pharr method.[48] Parameters needed for calculations were obtained from previous literature.[49-51]

6.2.2.5 Water contact angle

Water contact angles were measured on the polyethylene material surfaces with a CAM 100 contact angle goniometer (KSV Instruments) to assess the hydrophilicity. At least contact angles for five water drops were measured on each sample, and multiple samples of the same type were tested to obtain the error bar for each data.

6.3 Results and Discussion (Ting Lin's work)

6.3.1 Raman spectroscopy

Raman spectra were collected and processed before the data interpretation. The data processing included baseline correction, standard normal variate transformation and normalization by the intensity of the CH_2 twisting band at 1298 cm^{-1}. The peaks at 1080 and 1418 cm^{-1} are assigned to the C-C stretching mode of the amorphous chains and combination of CH_2 bending and wagging vibrational mode of crystalline (orthorhombic) chains, respectively.[53-57]

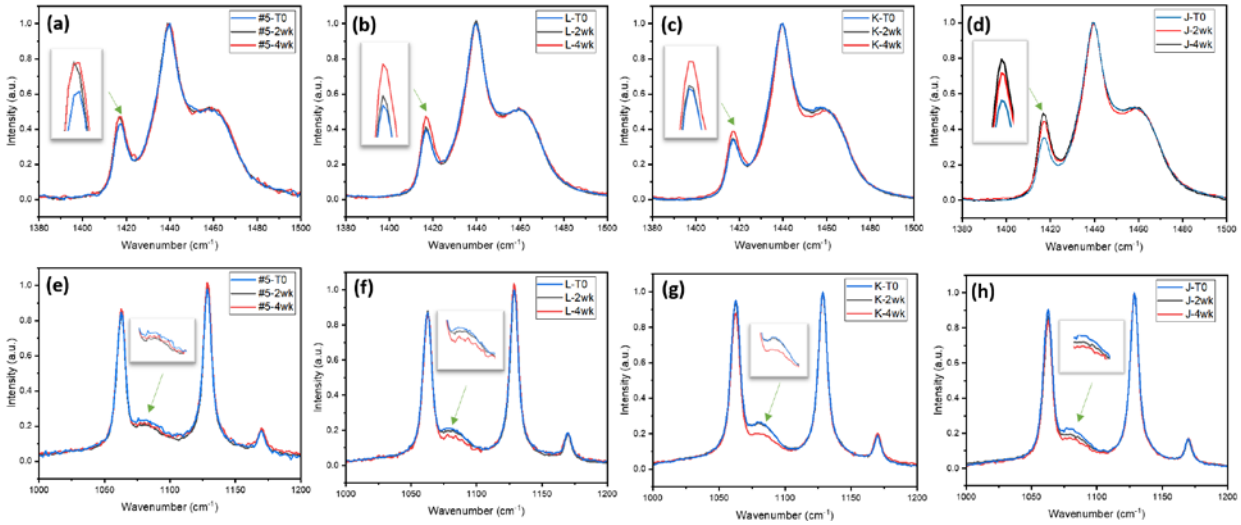

Figure 6.1 Raman results of various LLDPE samples in pristine condition, after two and four weeks of simulated weather aging. a) LLDPE #5 crystalline region, b) LLDPE L crystalline region, c) LLDPE K crystalline region, d) LLDPE J crystalline region, e) LLDPE #5 amorphous region, f) LLDPE L amorphous region, g) LLDPE K amorphous region, h) LLDPE J amorphous region.

Figure 6.1 represents the Raman results of LLDPE samples in the crystalline (a, b, c, d) frequency region and the amorphous (e, f, g, h) frequency region. The peak at 1418 cm^{-1} refers to the crystalline form of PE, which increased in its intensity from pristine condition to two weeks and then to four weeks of UV exposure. This marks the increased degree of crystallinity as the result of the proceeding of photooxidation. On the other hand, signals at around 1080 cm^{-1} representing the amorphous region show a downward trend with UV exposure time, which means that the amorphous region is reduced by aging, well correlated to the crystalline region results.

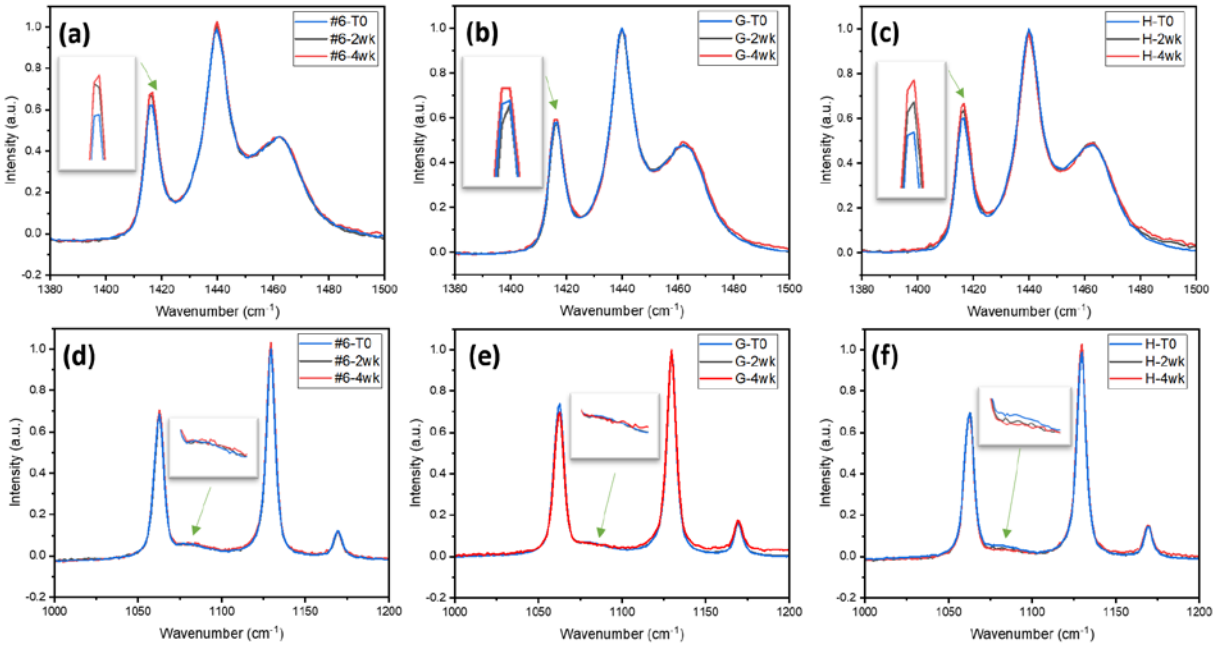

Figure 6.2 Raman results of various HDPE samples in pristine condition, after two and four weeks of UV exposure. a) HDPE #6 crystalline region, b) HDPE G crystalline region, c) HDPE H crystalline region, d) HDPE #6 amorphous region, e) HDPE G amorphous region, f) HDPE H amorphous region.

The Raman spectra collected from HDPE samples in the crystalline region and the amorphous region are shown in **Figure 6.2**. The results obtained from these spectra are also summarized in **Figure 6.3**. For the HDPE sample set, the same trend of changes after UV exposure was observed

as that of LLDPE samples. As the UV exposure time increases, the crystalline signal at 1416 cm^{-1} increases and the amorphous signal at 1080 cm^{-1} decreases.

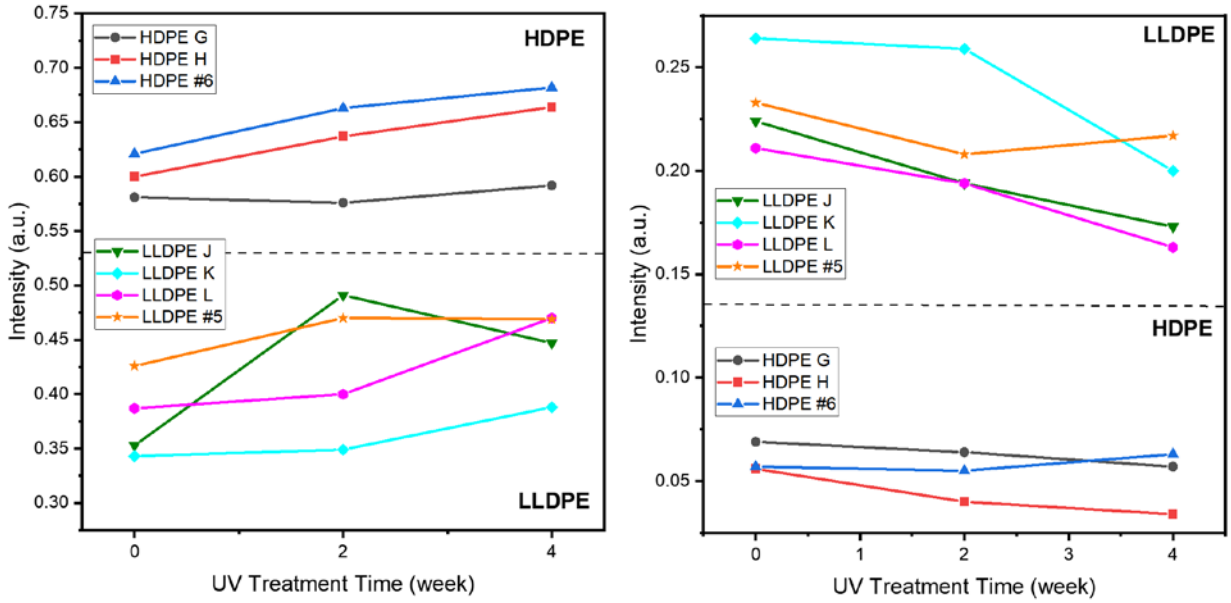

Figure 6.3 Raman intensity change of various samples as a function of the UV exposure time in the crystalline region (left) and the amorphous region (right).

Figure 6.3 quantitatively compared the Raman signal intensities detected in the crystalline frequency region and the amorphous frequency region of different samples. Overall, the change of the Raman signal from the crystalline region is opposite to the change of the Raman signal from the amorphous region for all the samples. The intensity change in crystallinity and amorphous is more obvious on LLDPE than HDPE, which indicates the amorphous domain is more vulnerable to attack by UV photon as reported by other researchers.[56]

6.3.2 Grazing incident X-ray diffraction (GIXRD)

To further verify the degree of crystallinity induced by UV photodegradation, GIXRD was applied to characterize the surface crystallinity change.

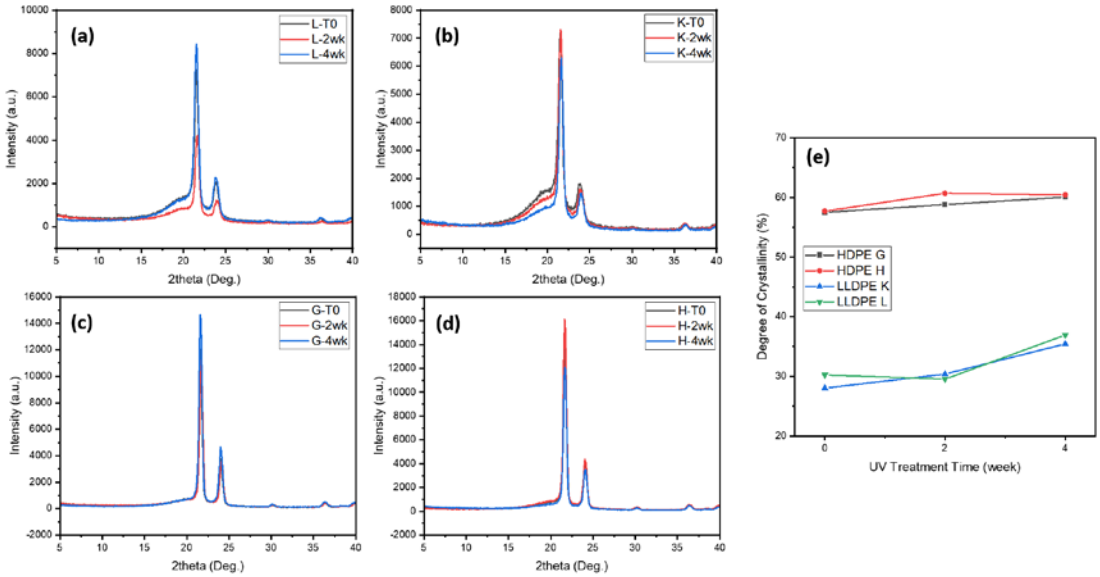

Figure 6.4 GIXRD results of various PE samples in pristine condition, after two and four weeks of UV exposure. a) LLDPE L, b) LLDPE K, c) HDPE G, d) HDPE H, e) Summary of crystallinity change trend probed by GIXRD.

The XRD pattern is utilized to analyze how the different timespans of UV photodegradation affect various PE with different densities. All the XRD results demonstrate two sharp diffraction peaks at 21.6^{o} and 24.5^{o}, indicating the semicrystalline structure in both HDPE and LLDPE samples. These two diffraction signals can be assigned to (110) and (200) lattice planes of PE, respectively. The broad band diffraction peak centered at 20.2^{o} is the signal contributed by the amorphous content of PE, which is stronger in LLDPE and weaker in HDPE samples. The calculation methods based on XRD results were well developed and demonstrated by many researchers.[58-60] Here, the degree of crystallinity in various PE samples with different UV treatments was calculated using the published method. The trend of crystallinity in PE was shown in **Figure 6.4.** The overall trend observed by GIXRD is the same as Raman results: There is an increasing degree of crystallinity in both LLDPE and HDPE along with the UV treatment, and the crystallinity increases as the increase of UV treatment time. Similar to Raman, the GIXRD results indicate that there is more obvious change in LLDPE than HDPE in terms of crystallinity. Again,

this can be explained by the fact that LLDPE has more amorphous content and is more vulnerable to be attacked by UV photon to trigger the photodegradation reactions including chain scission.[61] Oxygen is necessary for photodegradation reaction and can diffuse across amorphous domains relatively freely but restricted within the more condensed crystalline domain. As a result, the previously entangled polymer chains in amorphous domains are released and tend to crystallize near the existing crystal.

6.4 Results and Discussion (Shuqing Zhang's work)

6.4.1 ATR-FTIR

ATR-FTIR monitors the change in functional groups of polyethylene samples by simulated solar exposure. UV effects on the HDPE and LLDPE films are shown in **Figure 6.5**. The signals detected from the 3100 – 3800 cm^{-1} are assigned to the O-H stretching modes, the C=O signals are detected in the 1600 – 1800 cm^{-1} region while the peak around 910 cm^{-1} is due to the vinyl groups. Their changes in intensity were studied as an indication of the photooxidation progression.

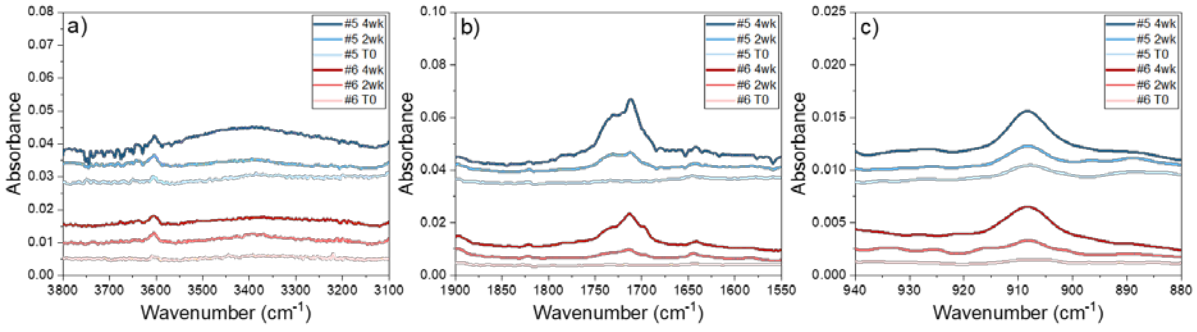

Figure 6.5 ATR-FTIR of LLDPE film #5 and HDPE film #6 in pristine condition (T0), after two and four weeks of simulated solar exposure. (a: 3100-3800 cm^{-1}, b: 1550-1900 cm^{-1}, c: 880-940 cm^{-1})

Increases in peak intensity were observed from the three wavenumber regions in **Figure 6.5**, as a result of hydroxyl groups, carbonyl groups, and vinyl groups generated by simulated solar exposure. This result is consistent with the increasing hydrophilicity measured by water contact angles, as the amount of polar groups is increased upon UV aging. The formation of terminal vinyl groups was caused by the chain scission of its backbone.[40] In addition, both LLDPE and HDPE film samples were changed in their chemical structures as a function of time by exposure. Their changes are quantified by the carbonyl indices shown in **Figure 6.6**, where increases in the values are observed along the exposure time. Both LLDPE films and HDPE films experienced a sharp increase in carbonyl indices after two weeks (from two weeks to four weeks), indicating longer simulated solar exposure led to a greater number of groups generated. **Figure 6.6** also displays the vinyl indices of the films. Overall, the vinyl index increases after simulated solar exposure.

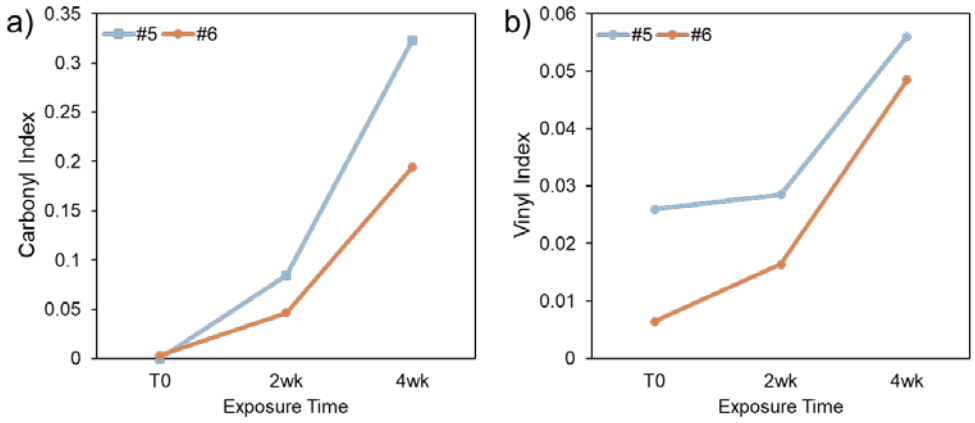

Figure 6.6 Carbonyl index (a) and vinyl index (b) of LLDPE film #5 and HDPE film #6 in pristine condition (T0), after two and four weeks of simulated solar exposure.

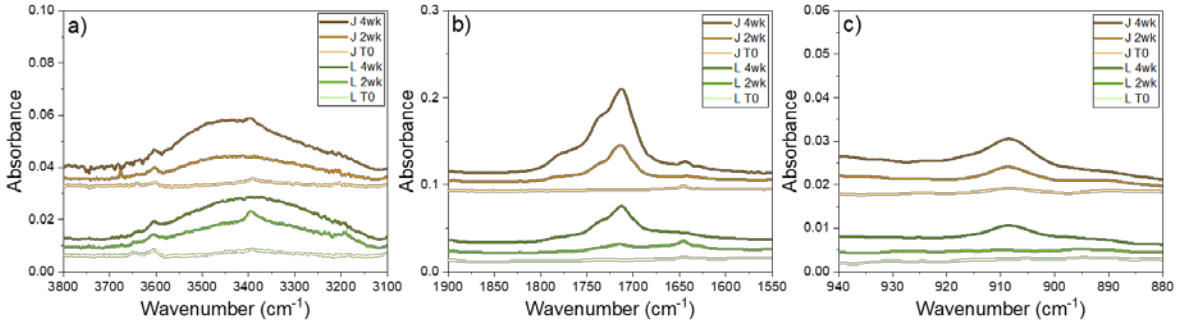

Figure 6.7 ATR-FTIR of LLDPE plaques J, L in pristine condition (T0), after two and four weeks of simulated solar exposure. (a: 3100-3800 cm^{-1}, b: 1550-1900 cm^{-1}, c: 880-940 cm^{-1})

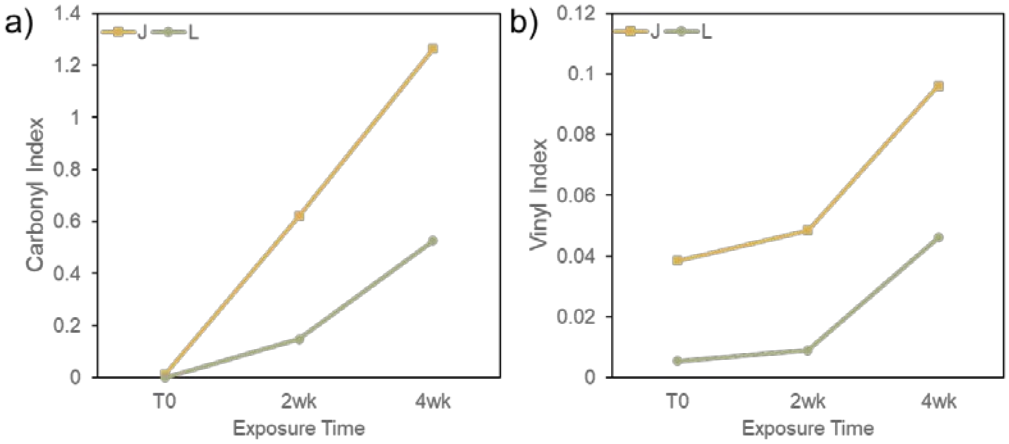

Figure 6.8 Carbonyl index (a) and vinyl index (b) of LLDPE plaques in pristine condition, after two and four weeks of simulated solar exposure.

Apart from thin films, rigid plaques were also tested after undergoing UV irradiation for different lengths of time. **Figure 6.7** depicts the results of two types of LLDPE plaques. Simulated solar exposure also changed the functional groups in them. The increase in peaks reflects that the degradation of LLDPE plaques proceeded as a function of time. The results indicate that LLDPE plaques of J with a lower density (0.9159 g/cm^3) degraded faster than those of L (0.9214 g/cm^3), which could also be seen from their carbonyl indices as shown in **Figure 6.8**. **Figure 6.8** also shows that the overall trend of the vinyl index increases after simulated solar exposure.

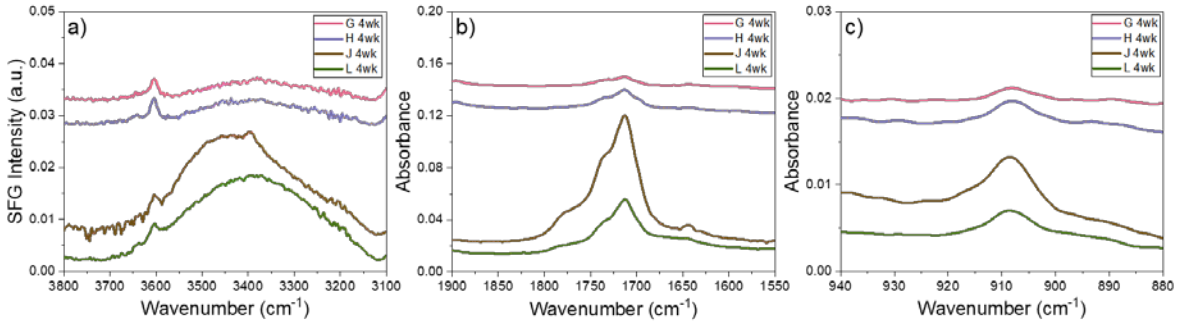

Figure 6.9 ATR-FTIR of HDPE plaques G, H and LLDPE plaques J, L undergoing four weeks of simulated solar exposure. (a: 3100-3800 cm^{-1}, b: 1550-1900 cm^{-1}, c: 880-940 cm^{-1})

Figure 6.9 compares HDPE plastic plaques with LLDPE plaques undergoing four weeks of UV aging. It was found that both LLDPE plaques exhibit stronger peaks in the three regions compared to HDPE samples. As indicators of chain scission induced by photooxidation,[7, 40] the increases of carbonyl groups and vinyl groups are normalized to carbonyl index and vinyl index to evaluate the degree of chemical oxidation as listed in **Table 6.2** LLDPE plaques J and L both show higher carbonyl indices and vinyl indices than HDPE plaques G and H. In general, LLDPE plaques show a higher degree of degradation than HDPE after being exposed to UV radiation for the same length of time. This is because compared to HDPE, more branches in LLDPE led to polymer chains not being closely packed and a reduced degree of crystallinity. A lower crystallinity increases oxygen permeability and therefore shows an increased sensitivity to photooxidation.

Table 6.2 Summary of change in carbonyl index and vinyl index for plaques after 4 weeks of simulated solar exposure

	G (0.9573 g/cm^3)	H (0.9555 g/cm^3)	J (0.9159 g/cm^3)	L (0.9214 g/cm^3)
Carbonyl Index	0.135	0.145	1.252	0.526
Vinyl Index	0.018	0.016	0.058	0.041

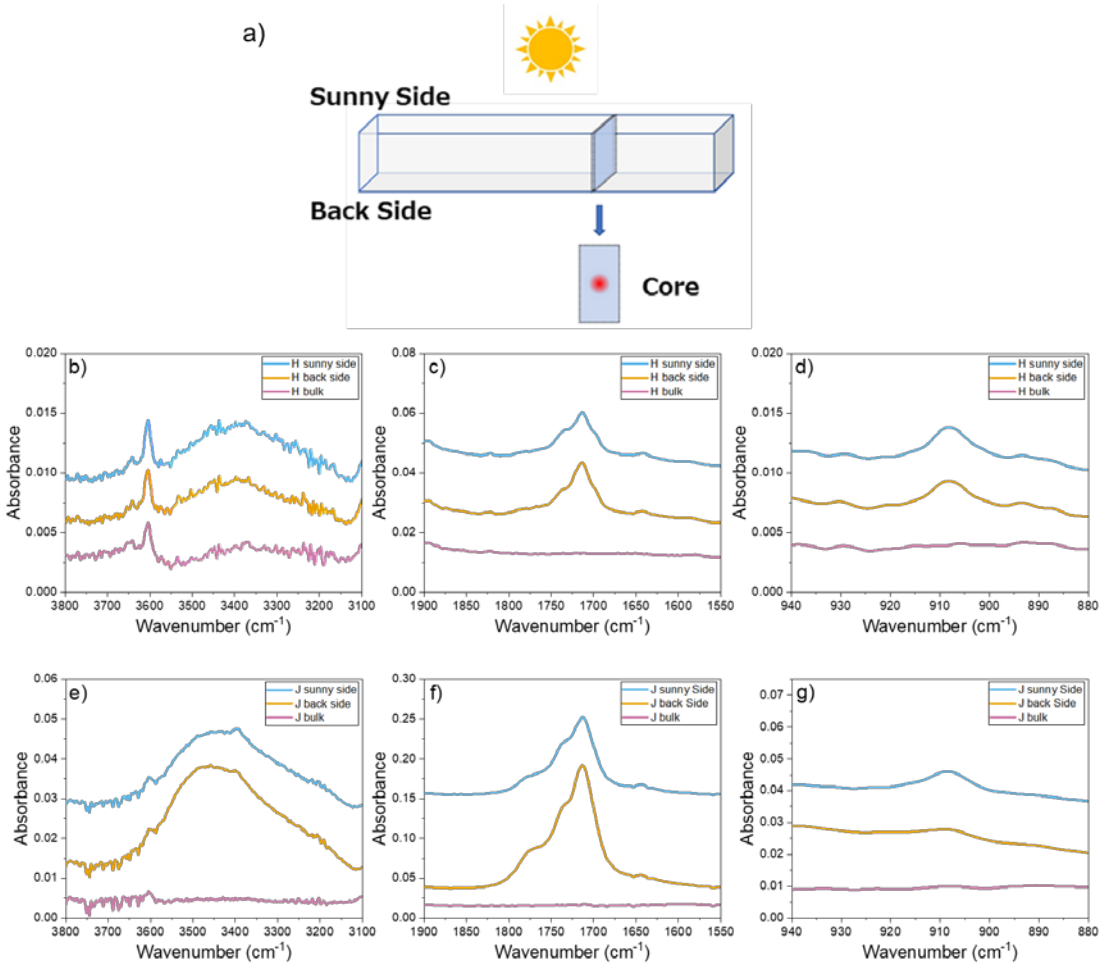

Figure 6.10 a) Schematic of different sample locations for testing. ATR-FTIR of HDPE plaques H (b, c, d) and LLDPE J (e, f, g) undergoing four weeks of simulated solar exposure at different locations. (b, e: 3100-3800 cm^{-1}, c, f: 1550-1900 cm^{-1} d, g: 880-940 cm^{-1})

Furthermore, a comparison was made between different locations of plaques on ATR-FTIR (**Figure 6.10**). Sunny sides represent the side towards the UV source, while the back sides mean the one away from the light source. Based on the intensity of peaks, the core part of both LLDPE and HDPE plaque samples with nominal thickness of 3 mm was less likely affected by UV exposure. Degradation processes are subject to diffusion-limited oxidation phenomena,[52] oxygen present in the core part of the polyethylene samples is believed to be much less than in the surface

region. The depth and oxygen permeability of the material will be factors that lead to different oxidation results.

The back sides away from UV sources were also degraded to varying degrees, and the signals of oxidation products are even stronger than those of sunny sides. This indicates that the oxidation rate on the back side is possibly faster than on the sunny sides. It may be due to the difference in adsorbed water amount between the two sides of the sample resulting from the UV exposure where water was sprayed onto specimens for 18 mins in every 120 mins duration. The adsorbed water amount on the sunny side may be less compared to the back side, as the rate of evaporation is faster on the side of direct exposure to UV light. This will be further studied in future works.

We also performed water contact angle measurements on selected PE surfaces before and after the UV exposure. The results are presented in **Figure 6.12**, which show that the PE surfaces become more hydrophilic after the UV exposure, due to the surface photooxidation caused by UV irradiation. Such results are well correlated to the ATR-FTIR data presented above.

6.4.2 Nanoindentation

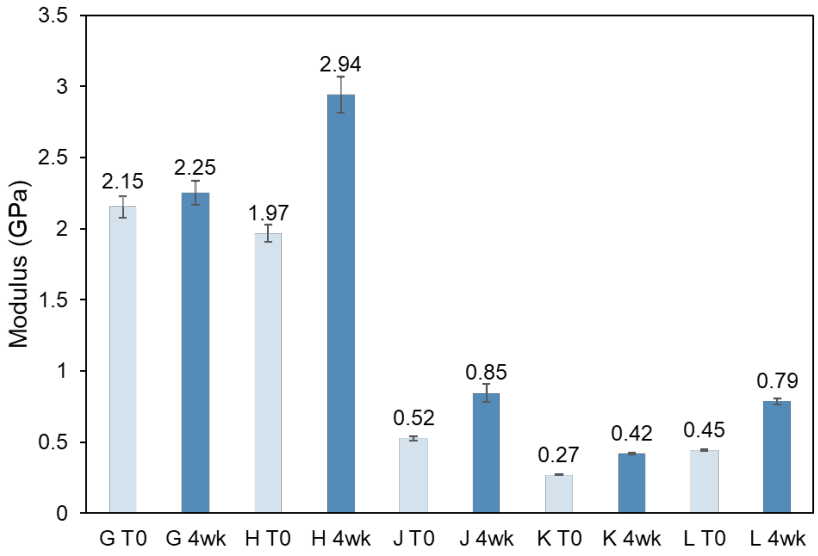

Figure 6.11 Nanoindentation results: plaques G, H, J, K, L in pristine condition and after four weeks of simulated solar exposure.

The mechanical properties of polyethylene plaques before and after four weeks of simulated solar exposure were measured by nanoindentation tests (**Figure 6.11**). The values shown in the figure are averaged based on 18 data sets with error bars presented. By comparing HDPE and LLDPE samples, the moduli of all HDPE plaques G and H are around 2 GPa and above, much greater than the three types of LLDPE plaques tested J, K and L, which is likely because of the difference in their crystalline regions. Specifically, HDPE molecules with little branching are easier to pack and tend to form more crystalline regions, and therefore contributed to higher modulus values. According to our XRD results, both HDPE and LLDPE samples are dominated by the signals contributed from crystal (110) and (200) lattice planes, indicating that the crystal forms are the same for the two types of polyethylene samples while the main difference is only on the degree of crystallinity. Compared to the untreated samples, those experiencing four weeks of UV aging generally show an increasing trend in modulus, except for sample G with no significant increase. In general, the increased moduli could be explained by the increased crystallinity of polyethylene caused by UV treatment, as UV irradiation led to chain scission of polyethylene with

shorter chains formed and facilitated the formation of crystalline regions. However, sample G is possibly less affected by simulated solar exposure than others, likely due to its highest density. The change is subtle that it did not show an obvious increase on nanoindentation tests. This corresponds to **Figure 6.9** of ATR-FTIR data, where sample G shows the smallest change in carbonyl groups in comparison to the other three types of plaques. The trend is also similar to the trend in the Raman results regarding the change in crystallization. **Figure 6.3** shows that sample G has the least crystallinity change among all the PE plaques.

6.4.3 Water Contact Angle Measurement

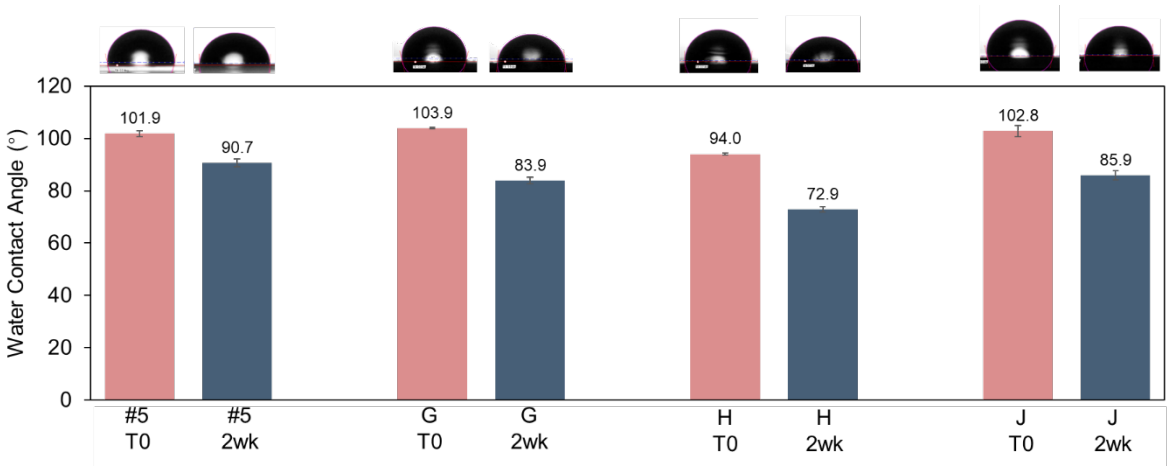

Figure 6.12 Water contact angle measurement results

We also performed water contact angle measurements on selected PE surfaces before and after the UV exposure. The results (**Figure 6.12**) were used to compare the hydrophilicity of polyethylene samples before and after two weeks of simulated solar exposure. Pristine polyethylene samples are hydrophobic inherently due to their simple hydrocarbon structures, evidenced by their water contact angles above 90 degrees before UV aging. After two weeks of UV aging, all of the polyethylene samples, regardless of their architectures or types, show a

downward trend in their water contact angles, revealing the increased hydrophilicity of the plastic surface after UV aging. This change indicates the effect of photooxidation caused by the UV exposure on the surface of polyethylene samples. Photooxidation introduced oxygen-containing hydrophilic functional groups to the surface and therefore resulted in a more hydrophilic plastic surface. The water contact angle measuresment results are well correlated to the ATR-FTIR data presented above.

6.5 Further Discussion

As we presented above, we have extensively investigated the simulated weathering effect on several different polyethylene samples using a variety of analytical tools. It is worth noting that various analytical tools adopted in this research have varied surface sensitivities, thus they may probe varied sample regions. However, as presented above, similar trends were found when studying a sample with different analytical techniques. Therefore here we want to compare the results obtained from different analytical methods in more detail. To facilitate the understanding of the weather effects, we only compare the samples at time zero and four weeks.

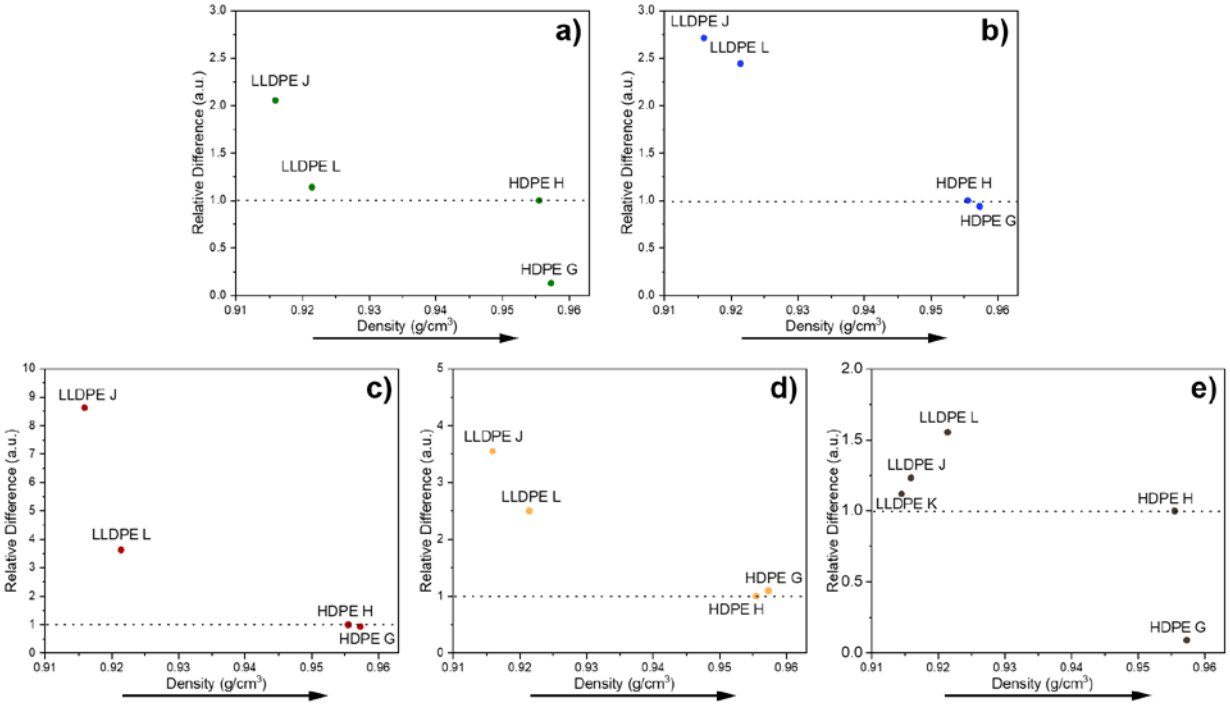

Figure 6.13 Summary of the normalized difference between 4-week aged and pristine polyethylene samples: a) Raman deduced crystallinity, b) GIXRD deduced crystallinity, c) Carbonyl index, d) Vinyl index, e) Nanoindentation.

Figure 6.13 displays the differences between the 4-week aged and pristine polyethylene samples, aiming for a more detailed connection between different techniques applied in this study to depict a more complete picture of the polyethylene degradation process. To better reflect the relative difference between varied polyethylene samples, all the data were normalized with the following method: For the results obtained from all the analytical techniques, the difference value in sample H aged in 4 weeks compared to time zero was normalized to 1 as a defined benchmark. The results of all other samples were calculated based on this benchmark. It is worth noting that the data normalized in **Figure 6.13 a-d** were based on the difference between 4-week aged and time zero data, whereas in **Figure 6.13 e**, the difference between the 4-week data and time zero data versus the time zero data for each sample is shown.

It can be observed from **Figure 6.13** that the results of LLDPE samples obtained from all the analytical techniques applied in this study exhibit higher difference values compared to those from HDPE samples. As we discussed above, a limited number of branches exist in an HDPE sample, while many more branches were introduced into an LLDPE sample during the polymerization process, giving rise to a significant decrease in density and crystallinity for LLDPE. The presence of more tertiary carbons and more amorphous contents in LLDPE allows for increased oxygen permeability and relatively low stability of LLDPE. Hence, LLDPE was more significantly affected by photooxidation, reflected by the increased carbonyl C=O groups and vinyl C=C bonds as the reaction products, leading to the increase of the carbonyl index and vinyl index. This was also shown by the increased crystallinity induced by chain scission, resulting in the increased signal from the crystalline phase in Raman scattering and the increased crystallinity measured by GIXRD. The increase in crystallinity corresponds to the increased modulus observed from the nanoindentation experiments. Sample J with the lowest density shows the most distinct changes in **Figures 6.13 a-d.** For the nanoindentation test, Sample J did not exhibit the largest change. It is possible that for this nanoindentation setup, a longer period of aging is needed to better differentiate the difference between LLDPE samples or perhaps the nanoindentation method is not sensitive enough to detect the microstructural changes. It is also worth noting that **Figure 6.13e** compares the modulus change ratio. If we compare the modulus change value instead of the ratio, samples J and L have similar values.

Quantitatively, the effect of simulated solar exposure can be correlated to PE density. **Figure 6.1** shows that the density of various PE samples follows the trend of G (0.9573) > H (0.9555) >> L (0.9214) >J (0.9159). **Figure 6.13** shows that the Raman scattering result follows G < H < L < J. The GIXRD, carbonyl index, and vinyl index changes all suggest G ≈ H < L < J,

while the nanoindentation data indicates G < H < L > J. Clearly, except for the nanoindentation result of sample J, which was explained above, all the results demonstrated that the effect of simulated solar exposure on PE increases when the PE density decreases. For HDPE samples G and H, the similar changes of the GIXRD, carbonyl index, and vinyl index results indicate that likely solar exposure leads to a similar effect on the G and H samples while the Raman results which reflected both the surface and bulk changes follows the above rule: the lower the density, the larger the change. Further discussions on the PE crystallinity measured by using Raman and GIXRD are presented below.

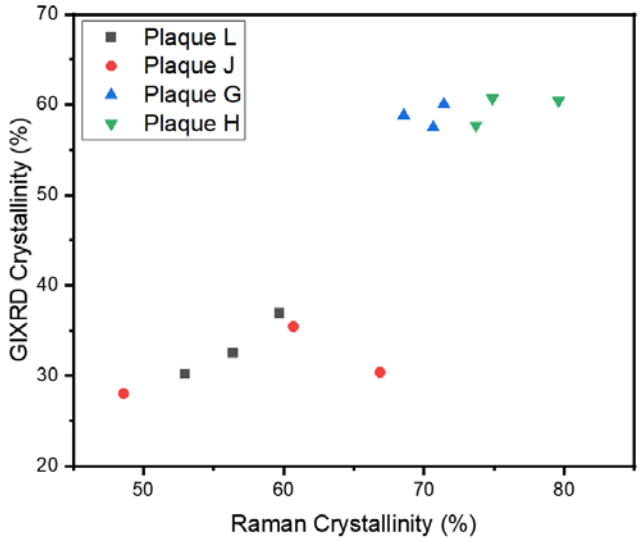

Figure 6.14 Correlations of the crystallinities measured from different samples with GIXRD and Raman spectroscopy.

Figure 6.14 shows the correlations of the crystallinities measured from different samples with GIXRD and Raman spectroscopy. The crystallinity determination method for GIXRD data was presented above in the experimental section. A published method was used to determine the crystallinities of various samples from Raman spectra.[62-65] This method uses the peak intensities of the 1418 cm^{-1} peak and the twist band at around 1300 cm^{-1}.[65] **Figure 6.14** shows that the crystallinities of various samples deduced by GIXRD are lower than those determined by Raman.

This is due to the fact that in GIXRD, the amorphous broad peaks overlap with the crystalline peaks and it inevitably underfits the crystalline signal and underestimates the crystallinity phase region. It is worth noting that the two crystallinity characterization techniques, Raman and GIXRD, demonstrated different sensitivities in distinguishing crystallinity change in the sample. In **Figure 6.14**, the Raman crystallinity difference on the same set of samples is larger than that measured with GIXRD. Therefore, Raman may be a better technique to analyze the crystallinity change by photodegradation. As presented above, it is also worth noting that GIXRD has a much better surface sensitivity which probes the surface crystallinity. Nevertheless, the trends of the overall changes observed by GIXRD and Raman are more or less similar – That is - the PE samples have an increased degree of crystallinity after longer photodegradation treatment.

Both the amount of crystalline regions and the crystal sizes could affect the intensity and shape of XRD signals. We believe that the crystalline domains also experienced some changes during the simulated weathering process, which is beyond the scope of this paper.

6.6 Conclusion

In this study, various polyethylene samples subjected to artificial solar exposure were analyzed using multiple methods. The water contact angle test displayed an increase in hydrophilicity for both LLDPE and HDPE samples post UV exposure, indicating the formation of more polar groups during degradation. ATR-FTIR results supported the observation that the polyethylene samples developed more unsaturated and polar structures, like hydroxyl and carbonyl groups, over time. Interestingly, samples with lesser densities had a more rapid degradation, evidenced by carbonyl and vinyl indices. The depth of photooxidation varied from the exterior to the inner parts, possibly due to differences in oxygen contents at different sample locations. Raman spectroscopy revealed that the polyethylene's crystallinity rose over exposure time, while its non-crystalline portions

reduced, making them more prone to damage. The GIXRD method further confirmed this change in crystallinity on the surface, with LLDPE samples undergoing a more pronounced shift than HDPE, possibly due to their initial non-crystalline content before exposure. After four weeks of simulated sunlight exposure, samples analyzed by nanoindentation showed increased moduli, suggesting more brittleness in the crystalline areas resulting from photooxidation. Macro-level mechanical findings mirrored molecular-level data from Raman and GIXRD, reflecting the ongoing degradation of the polyethylene surfaces. Findings from various methods were interconnected to enhance understanding of the degradation process. Overall, here the research using multiple analytical methods provided a more detailed comparison and understanding of how different polyethylene materials degrade, benefiting future polyethylene production and development.

6.7 References

1. Hopewell, J.; Dvorak, R.; Kosior, E. Plastics recycling: challenges and opportunities. *Philos Trans R Soc Lond B Biol Sci* **2009,** 364 (1526), 2115-2126.
2. Millican, J. M.; Agarwal, S. Plastic Pollution: A Material Problem? *Macromolecules* **2021,** 54 (10), 4455-4469.
3. Shang, J.; Chai, M.; Zhu, Y. Photocatalytic degradation of polystyrene plastic under fluorescent light. *Environ. Sci. Technol.* **2003,** 37 (19), 4494-4499.
4. Ghosh, S. K.; P, A. Plastics in municipal solid waste: What, where, how and when? *Waste Manag Res* **2019,** 37 (11), 1061-1062.
5. Lettieri, P.; Al-Salem, S. M., Thermochemical Treatment of Plastic Solid Waste. In *Waste*, 2011; pp 233-242.
6. Vyas, D.; Dave, U.; Parekh, H. In *Plasma pyrolysis: an innovative treatment to solid waste of plastic material*, National conference on recent trends in engineering & technology, NCRTET, Gujarat, 2011; 2011.
7. Bayo, J.; Rojo, D.; Olmos, S. Weathering indices of microplastics along marine and coastal sediments from the harbor of Cartagena (Spain) and its adjoining urban beach. *Mar. Pollut. Bull.* **2022,** 178, 113647.
8. Lebreton, L. C. M.; van der Zwet, J.; Damsteeg, J. W.; Slat, B.; Andrady, A.; Reisser, J. River plastic emissions to the world's oceans. *Nat. Commun.* **2017,** 8, 15611.
9. Al-Maaded, M.; Madi, N. K.; Kahraman, R.; Hodzic, A.; Ozerkan, N. G. An Overview of Solid Waste Management and Plastic Recycling in Qatar. *J. Polym. Environ.* **2011,** 20 (1), 186-194.

10. Chamas, A.; Moon, H.; Zheng, J.; Qiu, Y.; Tabassum, T.; Jang, J. H.; Abu-Omar, M.; Scott, S. L.; Suh, S. Degradation Rates of Plastics in the Environment. *ACS Sustain. Chem. Eng.* **2020,** 8 (9), 3494-3511.
11. Geyer, R.; Jambeck, J. R.; Law, K. L. Production, use, and fate of all plastics ever made. *Science advances* **2017,** 3 (7), e1700782.
12. Lebreton, L.; Andrady, A. Future scenarios of global plastic waste generation and disposal. *Palgrave Commun.* **2019,** 5 (1), 1-11.
13. Shen, L.; Worrell, E., Plastic Recycling. In *Handbook of Recycling*, 2014; pp 179-190.
14. Iovino, R.; Zullo, R.; Rao, M. A.; Cassar, L.; Gianfreda, L. Biodegradation of poly(lactic acid)/starch/coir biocomposites under controlled composting conditions. *Polym. Degrad. Stab.* **2008,** 93 (1), 147-157.
15. Brewis, D.; Briggs, D. Adhesion to polyethylene and polypropylene. *Polymer* **1981,** 22 (1), 7-16.
16. Demirors, M., The history of polyethylene. In *100+ Years of Plastics. Leo Baekeland and Beyond*, ACS Publications: 2011; pp 115-145.
17. McDaniel, M. P.; DesLauriers, P. J., Ethylene Polymers, HDPE. In *Kirk-Othmer Encyclopedia of Chemical Technology*, 2015; pp 1-40.
18. Pathak, V. M.; Navneet. Review on the current status of polymer degradation: a microbial approach. *Bioresources and Bioprocessing* **2017,** 4 (1), 1-31.
19. Harshvardhan, K.; Jha, B. Biodegradation of low-density polyethylene by marine bacteria from pelagic waters, Arabian Sea, India. *Mar. Pollut. Bull.* **2013,** 77 (1-2), 100-106.
20. Restrepo-Flórez, J.-M.; Bassi, A.; Thompson, M. R. Microbial degradation and deterioration of polyethylene – A review. *International Biodeterioration & Biodegradation* **2014,** 88, 83-90.
21. Sanchis, R.; Fenollar, O.; García, D.; Sánchez, L.; Balart, R. Improved adhesion of LDPE films to polyolefin foams for automotive industry using low-pressure plasma. *International journal of adhesion and adhesives,* **2008**, 28(8), 445-451.
22. Chirayil, C. J.; Joy, J.; Maria, H. J.; Krupa, I.; Thomas, S.. Polyolefins in automotive industry. *Polyolefin Compounds and Materials: Fundamentals and Industrial Applications,* **2016** 265-283.
23. Fayolle, B.; Colin, X.; Audouin, L.; Verdu, J. Mechanism of degradation induced embrittlement in polyethylene. *Polym. Degrad. Stab.* **2007,** 92 (2), 231-238.
24. Feuilloley, P.; César, G.; Benguigui, L.; Grohens, Y.; Pillin, I.; Bewa, H.; Lefaux, S.; Jamal, M. Degradation of Polyethylene Designed for Agricultural Purposes. *J. Polym. Environ.* **2005,** 13 (4), 349-355.
25. Gardette, M.; Perthue, A.; Gardette, J.-L.; Janecska, T.; Földes, E.; Pukánszky, B.; Therias, S. Photo- and thermal-oxidation of polyethylene: Comparison of mechanisms and influence of unsaturation content. *Polym. Degrad. Stab.* **2013,** 98 (11), 2383-2390.
26. Mendes, A. A.; Cunha, A. M.; Bernardo, C. A. Study of the degradation mechanisms of polyethylene during reprocessing. *Polym. Degrad. Stab.* **2011,** 96 (6), 1125-1133.
27. Mierzwa-Hersztek, M.; Gondek, K.; Kopeć, M. Degradation of Polyethylene and Biocomponent-Derived Polymer Materials: An Overview. *J. Polym. Environ.* **2019,** 27 (3), 600-611.
28. Montazer, Z.; Habibi Najafi, M. B.; Levin, D. B. Challenges with Verifying Microbial Degradation of Polyethylene. *Polymers (Basel)* **2020,** 12 (1), 123.

29. Park, D.; Hwang, E.; Kim, J.; Choi, J.; Kim, Y.; Woo, H. Catalytic degradation of polyethylene over solid acid catalysts. *Polym. Degrad. Stab.* **1999,** 65 (2), 193-198.
30. Sugimoto, M.; Shimada, A.; Kudoh, H.; Tamura, K.; Seguchi, T. Product analysis for polyethylene degradation by radiation and thermal ageing. *Radiat. Phys. Chem.* **2013,** 82, 69-73.
31. Gauthier, E.; Nikolić, M.; Truss, R.; Laycock, B.; Halley, P. Effect of soil environment on the photo-degradation of polyethylene films. *J. Appl. Polym. Sci.* **2015,** 132 (39),
32. Martínez-Romo, A.; Mota, R. G.; Bernal, J. S.; Reyes, C. F.; Candelas, I. R. In *Effect of ultraviolet radiation in the photo-oxidation of High Density Polyethylene and Biodegradable Polyethylene films*, Journal of Physics: Conference Series, 2015; IOP Publishing: 2015; p 012026.
33. Menzel, T.; Meides, N.; Mauel, A.; Mansfeld, U.; Kretschmer, W.; Kuhn, M.; Herzig, E. M.; Altstadt, V.; Strohriegl, P.; Senker, J.; Ruckdaschel, H. Degradation of low-density polyethylene to nanoplastic particles by accelerated weathering. *Sci. Total Environ.* **2022,** 826, 154035.
34. Rabek, J. F., *Photodegradation of polymers: physical characteristics and applications*. Springer Science & Business Media: 2012.
35. Rodriguez, A. K.; Mansoor, B.; Ayoub, G.; Colin, X.; Benzerga, A. A. Effect of UV-aging on the mechanical and fracture behavior of low density polyethylene. *Polym. Degrad. Stab.* **2020,** 180, 109185.
36. Tidjani, A. Comparison of formation of oxidation products during photo-oxidation of linear low density polyethylene under different natural and accelerated weathering conditions. *Polym. Degrad. Stab.* **2000,** 68 (3), 465-469.
37. White, J. R.; Shyichuk, A. V. Macromolecular scission and crosslinking rate changes during polyolefin photo-oxidation. *Polym. Degrad. Stab.* **2007,** 92 (7), 1161-1168.
38. Almond, J.; Sugumaar, P.; Wenzel, M. N.; Hill, G.; Wallis, C. Determination of the carbonyl index of polyethylene and polypropylene using specified area under band methodology with ATR-FTIR spectroscopy. *e-Polymers* **2020,** 20 (1), 369-381.
39. Focke, W. W.; Mashele, R. P.; Nhlapo, N. S. Stabilization of low-density polyethylene films containing metal stearates as photodegradants. *Journal of Vinyl and Additive Technology* **2011,** 17 (1), 21-27.
40. Grause, G.; Chien, M.-F.; Inoue, C. Changes during the weathering of polyolefins. *Polym. Degrad. Stab.* **2020,** 181, 109364.
41. Gulmine, J.; Janissek, P.; Heise, H.; Akcelrud, L. Degradation profile of polyethylene after artificial accelerated weathering. *Polym. Degrad. Stab.* **2003,** 79 (3), 385-397.
42. Herath, A.; Salehi, M. Studying the combined influence of microplastics' intrinsic and extrinsic characteristics on their weathering behavior and heavy metal transport in storm runoff. *Environ. Pollut.* **2022,** 308, 119628.
43. Stangenberg, F.; Ågren, S.; Karlsson, S. Quality assessments of recycled plastics by spectroscopy and chromatography. *Chromatographia* **2004,** 59 (1), 101-106.
44. Antunes, M. C.; Agnelli, J. A. M.; Babetto, A. S.; Bonse, B. C.; Bettini, S. H. P. Abiotic thermo-oxidative degradation of high density polyethylene: Effect of manganese stearate concentration. *Polym. Degrad. Stab.* **2017,** 143, 95-103.
45. Pertin, T.; Minatchy, G.; Adoue, M.; Flory, A.; Romana, L. Investigation of nanoindentation as a fast characterization tool for polymer degradation study. *Polym. Test.* **2020,** 81, 106194.

46. Tavares, A. C.; Gulmine, J. V.; Lepienski, C. M.; Akcelrud, L. The effect of accelerated aging on the surface mechanical properties of polyethylene. *Polym. Degrad. Stab.* **2003,** 81 (2), 367-373.
47. Tranchida, D.; Piccarolo, S.; Loos, J.; Alexeev, A. Mechanical characterization of polymers on a nanometer scale through nanoindentation. A study on pile-up and viscoelasticity. *Macromolecules* **2007,** 40 (4), 1259-1267.
48. Oliver, W. C.; Pharr, G. M. An improved technique for determining hardness and elastic modulus using load and displacement sensing indentation experiments. *J. Mater. Res.* **2011,** 7 (6), 1564-1583.
49. Jee, A.-Y.; Lee, M. Comparative analysis on the nanoindentation of polymers using atomic force microscopy. *Polym. Test.* **2010,** 29 (1), 95-99.
50. Prasad, K.; Nikzad, M.; Doherty, C. M.; Sbarski, I. Predicting trends in structural and physical properties of a model polymer with embedded natural fibers: Viability of molecular dynamics studies for a bottom up design. *J. Appl. Polym. Sci.* **2019,** 136 (45), 48189.
51. Rajeshwari, P.; Dey, T. K. Novel HDPE nanocomposites containing aluminum nitride (nano) particles: Micro-structural and nano-mechanical properties correlation. *Mater. Chem. Phys.* **2017,** 190, 175-186.
52. Celina, M. C. Review of polymer oxidation and its relationship with materials performance and lifetime prediction. *Polym. Degrad. Stab.* **2013,** 98 (12), 2419-2429.
53. Bailey, R.; Hyde, A.; Kim, J. J.; McLeish, J. Raman studies on oriented, high modulus, polyethylene. *Spectrochimica Acta Part A: Molecular Spectroscopy* **1977,** 33 (12), 1053-1058.
54. Gall, M.; Hendra, P.; Peacock, C.; Cudby, M.; Willis, H. Laser-Raman spectrum of polyethylene: Part 1. Structure and analysis of the polymer. *Polymer* **1972,** 13 (3), 104-108.
55. Gall, M.; Hendra, P.; Peacock, O.; Cudby, M.; Willis, H. The laser-Raman spectrum of polyethylene: the assignment of the spectrum to fundamental modes of vibration. *Spectrochimica Acta Part A: Molecular Spectroscopy* **1972,** 28 (8), 1485-1496.
56. Hiejima, Y.; Kida, T.; Takeda, K.; Igarashi, T.; Nitta, K.-h. Microscopic structural changes during photodegradation of low-density polyethylene detected by Raman spectroscopy. *Polym. Degrad. Stab.* **2018,** 150, 67-72.
57. Schachtschneider, J.; Snyder, R. Vibrational analysis of the n-paraffins—II: normal co-ordinate calculations. *Spectrochim. Acta* **1963,** 19 (1), 117-168.
58. Patel, A. K.; Bajpai, R.; Keller, J. M.; Kumari, B.; Vatsal, V.; Saha, A. Structural, morphological and micromechanical studies on fly ash reinforced PMMA composites. *Microsystem Technologies* **2011,** 17 (12), 1755-1762.
59. Statton, W. Hand book of X-ray diffraction, emission, absorption and microscopy. *Chapter-21, McGraw-Hill, New York* **1967**, 21.21-21.19.
60. Wu, Q.; Chen, N.; Wang, Q. Crystallization behavior of melt-spun poly (vinyl alcohol) fibers during drawing process. *Journal of polymer research* **2010,** 17 (6), 903-909.
61. Craig, I. H.; White, J. R.; Kin, P. C. Crystallization and chemi-crystallization of recycled photo-degraded polypropylene. *Polymer* **2005,** 46 (2), 505-512.
62. Lin, W.; Cossar, M.; Dang, V.; Teh, J. The application of Raman spectroscopy to three-phase characterization of polyethylene crystallinity. *Polym. Test.* **2007,** 26 (6), 814-821.
63. Mutter, R.; Stille, W.; Strobl, G. Transition regions and surface melting in partially crystalline polyethylene: A raman spectroscopic study. *J. Polym. Sci., Part B: Polym. Phys.* **1993,** 31 (1), 99-105.

64. Rull, F.; Prieto, A. C.; Casado, J. M.; Sobron, F.; Edwards, H. G. M. Estimation of crystallinity in polyethylene by Raman spectroscopy. *Journal of Raman Spectroscopy* **1993,** 24 (8), 545-550.
65. Strobl, G. R.; Hagedorn, W. Raman spectroscopic method for determining the crystallinity of polyethylene. *Journal of Polymer Science: Polymer Physics Edition* **1978,** 16 (7), 1181-1193.

Chapter 7 Conclusions and Future Work

7.1 Conclusions and Future Work

This thesis research aimed to elucidate the structure–function relationships of polymer materials, focusing on the molecular structural studies on buried interfaces using SFG, and on bulk polymer materials after simulated solar exposure using a variety of analytical tools. To be more specific, this thesis provided in-depth understanding on: (1) the effect of pi-pi interactions between peptides and polymers at the solid/liquid interface in situ, providing fundamental knowledge on molecular interactions between biological molecules and polymer biomedical materials; (2) the effect of fillers and adhesion catalyst on the structure of silane adhesion promoter at the composite HTV silicone/PET interface, and adhesion promotion mechanism resulting in different adhesion performance; (3) details of the interfacial chemical reactions of various silane adhesion promoters, elucidating the adhesion promotion mechanism and developing a silane adhesion promoter selection strategy; (4) the RTV condensation silicone interfacial molecular structure change during curing and the primary sources of hydroxyl functionality participating in curing and adhesion reactions; (5) degradation mechanisms of various polyethylene materials with different properties studied by using a variety of analytical techniques.

Furthermore, this thesis demonstrated that SFG cannot only study simple model systems, but also complex ‘real life’ commercial material systems. The insights gained from the research conducted are significant for both fundamental science and practical applications. This allows a more profound understanding of the molecular mechanisms of adhesion and promotes enhanced

comprehension of commercial materials used in common industrial applications, wherein adhesion plays a vital role in ensuring quality and durability.

In Chapter 2, d8-PS was used as a model polymer to study pi-pi interactions between polymer and biological molecules with different numbers of aromatic amino acids. The investigation initially focused on a hybrid peptide alongside three mutational variations with varying quantities of aromatic amino acid residues. We observed that all the peptides and the phenyl ring of PS exhibited a comparable orientation at interface using SFG, showing similar interactions at the interface which were independent of the number of aromatic amino acids present within the peptide. This indicated that the pi-pi interaction did not play a major role. The results are similar to those obtained at the MoS_2/peptide interface studied by SFG previously.[1] In contrast, during the peptide-graphene interaction, the peptide's orientation was greatly influenced by the number of aromatic amino acids, owing to the dominance of the pi-pi interaction in steering the interactions at the interface. To further confirm the above conclusion, interactions between d8-PS and MSI-78 as well as its mutant with two less aromatic amino acids were investigated using SFG. It was found that the two peptides adopted similar orientations at the d8-PS/peptide solution interfaces, which verified that the pi-pi interaction did not play a major role in determining peptide – d8-PS interactions, otherwise the peptides should adopt different orientations, as what was observed on a graphene surface.[2]

The research in Chapter 2 discovered that the pi-pi interaction was not the dominant interaction between peptides and polystyrene. It is well known that there are many other possible interfacial interactions, examples of which include hydrophobic interactions, charge interactions, and hydrogen-bond interactions, etc. In order to provide a more complete understanding on polymer–biomolecule interactions to manipulate such interactions, it is necessary to investigate interfacial

interactions beyond the pi-pi interaction. Therefore, Research focused on such interfacial interactions can be performed in the future. For example, model peptides can be mutated systematically with different kinds of amino acids with different charges, with varied hydrophobic/hydrophilic characteristics, and with different hydrogen bond formation capabilities. SFG studies on interfaces between such peptide mutants and polymers can provide important knowledge on various interfacial interactions. Polymers with different surface structures and properties (e.g., varied charges, hydrophobicity etc.) can be used in such studies. In addition to the peptides, proteins with more complex structures can be used in such studies to further understand polymer–biomolecule interactions in the future. The feasibility of applying SFG to study molecular interactions between proteins and solid surfaces has been demonstrated extensively in our research.[3-7] The SFG results can also be correlated to those obtained from computational simulations to understand detailed structural changes of biological molecules and polymer surfaces during the interaction in the future.

Chapter 3 focused on the elucidation of interfacial structures of silicone adhesives with different additive compositions including adhesion promoters, fillers, and catalysts, and the impact of such interfacial structures on adhesion. We successfully investigated how different additives influence the structure at the buried silicone/polymer interface. To unravel the molecular mechanisms that facilitate the adhesion of silicone adhesives, we compared the adhesion data with the results on interfacial structures obtained from SFG studies. Our previous SFG studies on simpler silicone adhesive systems without fillers or adhesion catalysts indicated that methoxy groups of adhesion promoters played important roles in adhesion. Such methoxy groups could segregate to the interface with ordering before curing. Here it was found that adding fillers to the silicone formulation appeared to diminish the interfacial segregation of adhesion promoter's methoxy

groups to the silicone/polymer interface from the bulk prior to curing. This is because many silane adhesion promoters segregated to the filler/silicone interface. Our SFG studies also found that during the high temperature curing phase, these methoxy groups could migrate to the silicone/polymer interface and react with the polymer, leading to strong adhesion. The impact of adhesion catalyst on interfacial segregation of methoxy groups on adhesion promoter was also investigated. SFG results showed that the inclusion of adhesion catalyst in the silicone adhesive formulation could facilitate the methoxy interfacial segregation, particularly when silica fillers were absent. When fillers were present in the silicone matrix, the adhesion catalyst could also facilitate the systematic reorganization of methoxy groups at an elevated curing temperature, enhancing the adhesive property of the silicone. In addition to the methoxy groups, the impact of adhesion promoter γ-GPS's epoxy end group at the silicone/polymer interface on adhesion was also examined. The detection of epoxy before curing and disappearance after curing by SFG indicated that epoxy groups were involved in the interfacial chemical reactions at the silicone/polymer interface to improve adhesion.

With the knowledge acquired from Chapter 3, Chapter 4 further investigated the interfacial chemical reactions between silicone adhesives with various functional silanes as adhesion promoters and nylon substrate. SFG was used to study such interfacial chemical reactions in both C=O and N-H stretching frequency regions. Two different silane adhesion promotes, SA and GPS with different end groups were used in the study. SFG results clearly demonstrated that two silanes led to two different interfacial reactions at the silicone/nylon interface. For SA silane, a two-step reaction was observed, with SA groups reacting with nylon NH_2 end groups, then reaction product water breaking the nylon C-N bonds to produce more NH_2 groups for more reactions, leading to the formation of carboxylic acid and imide functionalities. For GPS silane, interfacial chemical

reactions between the nylon NH_2 end groups and epoxy silane were detected. Although the interfacial chemical reaction mechanisms are different between SA and GPS, the reactions enhanced interfacial adhesion strengths of both silicone adhesives to nylon by the formation of covalent bonds at the buried nylon/silicone interfaces.

For the research in Chapter 3 and 4, the adhesion promotion mechanisms of silane adhesion promoter systems were well elucidated using SFG. However, there are still unclear mechanisms related to the adherent substrates. It is important to understand the polymer substrate effects in order to further understand the adhesion mechanisms of silicone adhesives. Many possible research topics can be covered in the future. For example, it is necessary to investigate how the surface functionality and polarity of the polymer substrate affect the adhesion promotion mechanism with silicone adhesives, and how to select an optimal adhesion promoter for a polymer substrate with certain surface functionality or polarity to maximize the adhesion. It is also important to understand how the crystallinity of a polymer substrate could influence its interfacial interactions with silicone adhesion promoters. In addition to the polymer substrates, silicone adhesives can also be used to adhere to other substrates such as metals and oxides. Therefore it is also crucial to investigate molecular interactions between silicone adhesives and metal or oxide surfaces, and how adhesion promoters enhance the silicone adhesion to these surfaces.

With the well-established research in Chapters 3 and 4 on HTV silicone, Chapter 5 focused on another main category of silicone: RTV condensation silicone. In this chapter, SFG studies explored the adhesion mechanisms of condensation cured silicone adhesives to glass (modelled by silica). Time-dependent in situ SFG tests uncovered interfacial transformations (particularly for methoxy groups) during the curing process of the condensation cured silicone samples. SFG results showed that the primary reaction source for the interfacial hydroxyl groups during the initial curing

period of 3 to 5 hours was the hydroxyl groups present on the silica substrate surface, not those on the silicone itself or from ambient moisture. Such interfacial hydroxyl groups reacted with methoxy groups in silicone to establish covalent associations at the interface. Further interfacial reactions could later be induced by the diffusion of environmental moisture into the interface.

Since this was the first time to probe RTV silicone system using SFG, the research included in this thesis laid a foundation for future research on condensation cured silicone. There is still much research required to be systematically performed to understand interfacial molecular structures and interactions of such silicone systems. Similar to the future research after Chapters 3 and 4, here many different adhesion promoters can be studied to systematically understand the effect of adhesion promoters on adhesion of condensation cured silicone. Also, a verity of substrates with varied properties can be studied in addition to silica in the future.

Chapter 6 successfully investigated the structure and property changes of PE after simulated solar weathering using multiple characterization techniques. Several important conclusions can be made in this research: (1) The extent of photooxidation varied from the exterior part to the inner part of a PE sample, possibly due to the varying amounts of available oxygen at different sample locations. (2) The crystallinity of polyethylene, as revealed by Raman spectroscopy, increased with simulated solar exposure time, while its non-crystalline portions decreased, thus becoming more susceptible to damage. (3) The elevated moduli, indicating increased brittleness in the crystalline regions due to photooxidation, was detected. (4) Both LLDPE and HDPE samples became more hydrophilic after UV exposure, suggesting that the degradation process led to the creation of more polar groups. (5) ATR-FTIR analysis confirmed that the polyethylene samples formed more hydroxyl and carbonyl groups and other unsaturated and polar structures over time. Notably, more

rapid degradation was seen in samples with lower densities, as shown by certain carbonyl and vinyl indices.

Polymer waste poses a negative impact on our environment. Many different kinds of polymers in plastic wastes were found in ocean and on land. Although PE is the most produced polymer, it is necessary to study degradation mechanisms of many other polymers to understand their environmental fates. The developed methodology of using a variety of analytical tools to study PE degradation in this research is generally applicable, which can be used to study degradation of many other polymer materials in the future. Especially, more and more “green” and degradable polymers have been and will be developed to satisfy the environmental protection needs. It is important to study the degradation mechanisms of such polymers in the future.

7.2 References

1. Zou, X.; Wei, S.; Jasensky, J.; Xiao, M.; Wang, Q.; Brooks III, C. L.; Chen, Z., Molecular interactions between graphene and biological molecules. *J. Am. Chem. Soc.* **2017**, 139 (5), 1928-1936.
2. Xiao, M.; Wei, S.; Li, Y.; Jasensky, J.; Chen, J.; Brooks, C. L.; Chen, Z., Molecular interactions between single layered MoS2 and biological molecules. *Chem. Sci.* **2018**, 9 (7), 1769-1773.
3. Guo, W.; Lu, T.; Crisci, R.; Nagao, S.; Wei, T.; Chen, Z., Determination of Protein Conformation and Orientation at Buried Solid/Liquid Interfaces. *Chem. Sci.* **2023**, 14, 2999-3009.
4. Guo, W.; Xu, S.; Reichart, T. M.; Xiao, M.; Lu, T.; Mello, C.; Chen, Z., Probing Molecular Interactions between Surface-Immobilized Antimicrobial Peptides and Lipopolysaccharides in Situ. *Langmuir* **2020**, 36, 12383-12393.
5. Guo, W.; Lu, T.; Gandhi, Z.; Chen, Z., Probing Orientations and Conformations of Peptides and Proteins at Buried Interfaces. *J. Phys. Chem. Lett.* **2021**, 12, 10144-10155.
6. Lu, T.; Fu, L.; Qiu, Y.; Zhang, J.; Chen, Z., Probing Molecular Interactions of Antibody Drugs, Silicone Oil, and Surfactant at Buried Interfaces in Situ. *Anal. Chem.* **2022**, 94, 14761-14768.
7. Lu, T.; Chen, Z., Monitoring the Molecular Structure of Fibrinogen During the Adsorption Process at the Buried Silicone Oil Interface in Situ in Real Time. *J. Phys. Chem. Lett.* **2023**, 14, 3139-3145.